University of Naples Federico II
Department of Structures for Engineering and Architecture

Ph.D. Program in Structural, Geotechnical Engineering and Seismic Risk
XXXVII Cycle

Nonlinear Dynamics of Hysteretic Mechanical Systems: Theory and Applications

Raffaele Capuano

Advisor:
Prof. eng. Luciano Rosati

Co-advisor:
Dr. eng. Nicolò Vaiana

Ph.D Coordinator:
Prof. eng. Iunio Iervolino

Raffaele Capuano · `raffaele.capuano@unina.it`
Nonlinear Dynamics of Hysteretic Mechanical Systems: Theory and Applications

Ai miei genitori

Acknowledgments

I would like to express my heartfelt gratitude to Professor Luciano Rosati and Professor Nicolò Vaiana for their inspiring and warm guidance throughout my journey. Their invaluable support and profound teachings have shaped both my academic experience and personal growth. I am especially thankful for the opportunities they have provided over the years and for recognizing a potential within me that I had yet to discover. I hope to have repaid their trust in me.

Raffaele

Declaration

Raffaele Capuano hereby declares that this dissertation submitted to obtain the academic degree of Philosophiæ Doctor (Ph.D.) in Structural, Geotechnical Engineering and Seismic Risk is his own unaided work, that he has not used other than the sources indicated, and that all direct and indirect sources are acknowledged as references.

Parts of this dissertation have been published in international journals and conference proceedings.

Naples, 2024

Contents

List of Figures

List of Tables

1

CHAPTER

1

Introduction

The study of hysteretic systems has garnered significant attention across various disciplines, including physics, engineering, and material science, due to the ubiquitous presence of hysteresis in natural and engineered systems. Hysteresis, characterized by the dependence of the output not only on the current input but also on its past history, manifests in many applications ranging from magnetic and electrical systems to biological and mechanical systems. In mechanical systems, hysteresis is particularly evident in structural elements, materials, and devices, in which it influences the behavior under cyclic loading conditions. These applications underscore the critical importance of accurately modeling and predicting hysteretic behavior for designing robust systems and optimizing their performance.

Historically, a wide range of mathematical models have been developed to capture the complex dynamics of hysteresis. Phenomenological models such as those by Bouc and Wen, Preisach, and Baber-Noori have provided valuable frameworks for simulating hysteresis in mechanical systems. However, these models often exhibit significant limitations since they are typically tailored for specific types of hysteretic behaviors and may fail to be generalized for different loop shapes. Moreover, the lack of clear mechanical interpretation for many model parameters complicates their calibration, often requiring computationally intensive numerical optimization techniques. These challenges have hindered the widespread applicability of existing models in real-world scenarios.

To address these shortcomings, Vaiana and Rosati introduced a novel rate-independent hysteretic model (VRM) and subsequently improved it with the VRM+A and VRM+D formulations. These advancements offer a unified framework for modeling diverse hysteretic behaviors, including asymmetric and flag-shaped loops, with closed-form solutions and a clear mechanical interpretation of the parameters involved in the model. The differential formulation, VRM+D, further extends the model's applicability to nonlinear dynamic analyses, enabling a detailed study of stability and bifurcation phenomena in mechanical systems subjected to periodic forces.

This dissertation builds upon these recent advancements by applying the VRM+D to analyze and predict the dynamic responses of hysteretic mechanical systems. By leveraging the Poincaré map-based continuation method, a robust numerical technique, we systematically explore the steady-state dynamics, stability, and bifurcation characteristics of mechanical systems exhibiting complex hysteretic behaviors. The integration of the VRM+D and continuation methods represents a novel contribution to the field, offering a comprehensive approach to investigating the effects of hysteresis on frequency response and dynamic stability.

The novelty of this work lies in its systematic examination of how different hysteretic loop shapes influence the dynamic behavior of mechanical systems. While prior research has largely focused on symmetric or simplified hysteretic models, this study explicitly incorporates asymmetric and non-standard loop shapes, reflecting the complexities observed in real-world materials and structures. Moreover, this work extends the application of hysteresis modeling to new domains, including mechanical metamaterials and rocking systems, where hysteresis is deliberately exploited for vibration control and energy dissipation.

The thesis is organized as follows:

- Chapter 2: This chapter offers a detailed exploration of the fundamental concepts and mathematical frameworks essential to the study of dynamical systems. It is divided into three main sections: the mathematical formulation of dynamical systems, the analysis and classification of continuous-time systems, and the introduction of essential techniques such as phase portraits and nondimensionalization. The chapter is designed to progressively build a comprehensive understanding of both theoretical and applied aspects of dynamical systems.

- Chapter 3: Leveraging the principles of proportionality and additivity, this chapter delves into the analysis of linear time-invariant dynamical systems. It begins with an overview of these systems and introduces the Laplace transform, a key tool for frequency domain analysis. The chapter also covers various mathematical frameworks, including state-space and frequency domain representations, illustrating how they facilitate the study of linear dynamical systems.

- Chapter 4: Nonlinearity introduces complexities that necessitate a distinct analytical approach. This chapter provides a comprehensive overview of nonlinear dynamical systems, encompassing smooth and non-smooth nonlinear dynamical systems. Topics include the behavior of one-, two-, and three-dimensional flows, periodic solutions, Poincaré maps, and bifurcation theory. Special emphasis is placed on hysteretic mechanical systems, with discussions on their mathematical modeling, including the Vaiana-Rosati model, Poincaré map-based continuation methods, and energy components. The chapter aims to equip the reader with the tools and concepts needed to understand the results presented in the last chapter.
- Chapter 5: This chapter focuses on hysteretic mechanical systems, providing a systematic analysis of their complex dynamic responses and key characteristics. It examines the frequency response of hysteretic systems exhibiting complex behaviors and investigates the impact of asymmetry on their dynamic response. The discussion extends to the dynamic behavior of negative stiffness metamaterials, offering insights into their unique properties. Additionally, the chapter explores hysteretic rocking systems, analyzing the influence of different loop shape types on their responses, with particular attention to energy considerations. Finally, an analysis of MDoF hysteretic systems is presented, highlighting their complex hysteretic behaviors and dynamic interactions.

By means of these investigations, this thesis aims to contribute to the field of nonlinear dynamics and hysteresis modeling by offering new insights and practical methodologies for the analysis of mechanical systems exhibiting complex hysteretic behavior.

CHAPTER

2

Dynamical Systems

This chapter provides a structured exploration of the fundamental concepts and mathematical frameworks underlying the study of dynamical systems. The chapter is organized into three main sections: the mathematical formulation of dynamical systems, the analysis and classification of continuous-time systems, and fundamental techniques such as phase portraits and nondimensionalization. Each section builds progressively to offer a comprehensive understanding of both the theoretical and applied aspects of dynamical systems.

> *La filosofia è scritta in questo grandissimo libro che continuamente ci sta aperto innanzi a gli occhi (io dico l'universo), ma non si può intendere se prima non s'impara a intender la lingua e conoscer i caratteri, ne' quali è scritto. Egli è scritto in lingua matematica, e i caratteri son triangoli, cerchi, ed altre figure geometriche, senza i quali mezzi è impossibile a intenderne umanamente parola; senza questi è un aggirarsi vanamente per un oscuro laberinto.*
>
> — Galileo Galilei

Section 2.1

Definition of a Dynamical System

Definition 1 A dynamical system S (Fig. 2.1) can be formally defined as a combination of a state-space $\mathcal{X}$, a set of times $\mathcal{T}$, and a time evolution rule $\mathcal{R} : \mathcal{X} \times \mathcal{T} \to \mathcal{X}$ that defines how the system's state evolves over time [42, 46, 64].

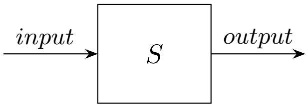

Figure 2.1. Dynamical system.

Subsection 2.1.1

Mathematical Formulation

The concept of a dynamical system is the mathematical formulation of the general scientific idea of a deterministic process. The future and past state of many physical, chemical, biological, ecological, economic, and even social systems can be predicted to some extent by knowing their present state and the laws governing their evolution. Provided that these laws remain constant over time, the behavior of such a system can be considered fully determined by its initial state. Therefore, the concept of a dynamical system includes a set of its possible states (*state-space*), a set of times, and a law governing the evolution of the states over time. We will discuss these elements separately [42, 46, 64].

Subsection 2.1.2

State-Space

All possible states of a dynamical system are characterized by the points of a certain set $\mathcal{X}$. This set is referred to as the *state-space* of the system. Indeed, specifying a point $\mathbf{x} \in \mathcal{X}$ must be sufficient not only to describe the system's current "position" but also to determine its future evolution. In various scientific disciplines, suitable state-spaces are designated, frequently referred to as *phase-space* within the framework of classical mechanics.

Example In classical mechanics, the state of a system with n Degrees-of-Freedom (DoF) is characterized by a real vector of dimension $2n$:

$$\mathbf{x} \equiv [q_1, q_2, \dots, q_n, p_1, p_2, \dots, p_n]^T ,$$

where q_i are the generalized coordinates and p_i are the corresponding generalized momenta. Therefore, in this case, $\mathcal{X} =$

$\mathbb{R}^{2n}$. If k coordinates are cyclic, $\mathcal{X} = \mathbb{S}^k \times \mathbb{R}^{2n-k}$ where $\mathbb{S}$ is the unit circle parameterized by the angle.

SUBSECTION 2.1.3

Time

The evolution of a dynamical system represents a change in the system's state over time $t \in \mathcal{T}$, where $\mathcal{T}$ is a numerical set. In general, we can distinguish two types of dynamical systems:

- Continuous-time dynamical systems $\mathcal{T} = \mathbb{R}$.
- Discrete-time dynamical systems $\mathcal{T} = \mathbb{Z}$.

Continuous-time systems hold greater relevance in engineering, while discrete-time systems emerge naturally in fields like ecology and economics, where a system's state at time t entirely determines its state at $t + 1$.

A set of times $\mathcal{T}$ may extend only into the future (for irreversible or non-invertible processes) or into both the past and the future (for reversible or invertible processes). The sequence of time instants for a reversible discrete-time process naturally corresponds to the set of all integers $\mathbb{Z}$; irreversibility corresponds to considering only non-negative integers $\mathbb{Z}^+$. Similarly, for a continuous-time process, time is represented by the set of all real numbers $\mathbb{R}$ in the reversible case, and by the set of non-negative real numbers $\mathbb{R}^+$ in the irreversible case.

SUBSECTION 2.1.4

Time Evolution Rule

The main component of a dynamical system is the time evolution rule that determines the state of the system at time t provided that the initial state is known. In the most general setting, the time evolution rule $\mathcal{R} : \mathcal{X} \times \mathcal{T} \to \mathcal{X}$ is a rule that allows us to determine the state of the system at each time t from its states at previous times. Thus, the most general time-evolution law is time dependent and has infinite memory. It is common, however, to consider only those time evolution rules that allow us to define all future states (and for reversible systems also past states) given a state at a particular time. Furthermore, it is commonly assumed that the same time evolution rule does not change with time. In other words, the result of time evolution will depend only on the initial position of the system and the duration of the evolution, but not on the time when the state of the system was initially recorded.

The most general way to specify the evolution of a system is by assuming that, for a given $t \in \mathcal{T}$, a mapping φ^t is defined on the state-space $\mathcal{X}$, where $\varphi^t : \mathcal{X} \to \mathcal{X}$, which transforms an initial state $x_0 \in \mathcal{X}$ at time t_0 into a state $x_t \in \mathcal{X}$ at time t, such that $x_t = \varphi^t x_0$. Thus, if our system was initially at a state $x \in \mathcal{X}$, after time t, it will be at a new state uniquely determined by x and t, and can therefore be denoted by $F(x, t)$. Fixing t, we obtain a transformation $\varphi^t : x \to F(x, t)$ of the state-space into itself.

The map φ^t is often referred to as the *evolution operator* of the dynamical system. It may be explicitly known, but in most general cases, it is defined indirectly and can only be calculated approximately. In the case of continuous-time dynamical systems, the family φ^t of evolution operators is called a *flow*.

Dynamical systems with an evolution operator φ^t defined for both $t \geq 0$ and $t < 0$ are called *invertible*. In such systems, the initial state x_0 fully determines not only the future states of the system but also its past behavior. However, it is also useful to consider dynamical systems in which the future behavior for $t > 0$ is completely determined by the initial state x_0 at $t = 0$, but the history for $t < 0$ cannot be uniquely reconstructed. Such systems (called *non-invertible*) are described by evolution operators defined only for $t \geq 0$ (i.e., for $t \in \mathbb{R}^+$ or $\mathbb{Z}^+$). In the case of continuous-time systems, these are called *semi-flows*.

Historically, smooth continuous-time dynamical systems appeared first because of Newton's discovery that the motions of mechanical objects can be described by second-order Ordinary Differential Equations (ODEs). More generally, many other natural and social phenomena, such as radioactive decay, chemical reactions, population growth, or dynamics of prices on the market, may be modeled with various degrees of accuracy by systems of ODEs [46]. These scenarios are within the framework of our investigation because, in almost all relevant cases, the state-space of a dynamical system has a specific structure that is respected by the time evolution rule. Different structures lead to the development of theories that focus on dynamical systems maintaining such intrinsic structures.

SECTION 2.2

Continuous-Time Dynamical Systems

A continuous-time dynamical system constitutes a mathematical model of a physical object interacting with its surrounding environment through continuous time-dependent variables [7].

It is crucial to establish a fundamental distinction between the different types of variables involved, which can be categorized into two main categories:

- *input* variables;
- *output* variables.

Input variables represent the actions exerted on the system by external agents, whereas output variables represent the aspects of the system's behavior that are of interest. As previously mentioned, a cause-effect relationship exists between these classes of variables, almost always functions of time, moderated by the time evolution rule of the system. These systems are highly significant in the context of control problems because the particular properties that characterize such mathematical models allow for their broad applications.

Subsection 2.2.1

State-Space Representation

As discussed in Section 2.1.4, for historical reasons the most common way to define a continuous-time dynamical system is through ODEs. Specifically, the dynamical systems of relevance in engineering applications are represented by a finite number of coupled first-order ODEs in the following form:

$$\begin{cases} \dot{x}_1 = f_1\left(x_1, \ldots, x_n, u_1, \ldots, u_m, t\right) \\ \dot{x}_2 = f_2\left(x_1, \ldots, x_n, u_1, \ldots, u_m, t\right) \\ \qquad\qquad \vdots \\ \dot{x}_n = f_n\left(x_1, \ldots, x_n, u_1, \ldots, u_m, t\right), \end{cases}$$

where $\dot{x}_i$ denotes the derivative of the n *state variables* x_i with respect to time variable t and u_j are the m specified input variables. The vector notation is commonly used to write these equations in a compact form as one n-dimensional first-order vector differential equation:

$$\dot{\mathbf{x}} = \mathbf{f}\left(\mathbf{x}(t), \mathbf{u}(t), t\right), \tag{2.2.1}$$

where $\mathbf{x} \in \mathbb{R}^{n\times 1}$, $\mathbf{u} \in \mathbb{R}^{m\times 1}$, and the vector function $\mathbf{f} : \mathbb{R}^n \to \mathbb{R}^n$ assumed to be sufficiently regular (differentiable). This equation is called the *state-equation* and refer to $\mathbf{x}$ as the state and $\mathbf{u}$ as the input. Sometimes another equation is associated with Eq. (2.2.1), that is:

$$\mathbf{y} = \mathbf{g}\left(\mathbf{x}(t), \mathbf{u}(t), t\right). \tag{2.2.2}$$

Here $\mathbf{y} \in \mathbb{R}^{p\times 1}$ is defined as a p-dimensional output vector that includes variables of particular interest in the analysis of the dynamical system, (e.g., variables that can be physically measured or variables that are required to behave in a specified manner). This equation is called the *output equation* and refer to Eqs. (2.2.1) and (2.2.2) together as the *state-space model*, or simply the *state model* [44].

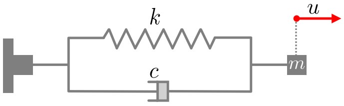

Figure 2.2. SDoF damped harmonic oscillator.

Remark

Note that, unlike the state equation, the output equation is an algebraic equation. Additionally, it is worth emphasizing that the number n of state variables constitutes the *order of the system* [7].

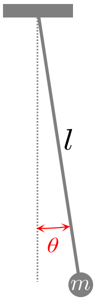

Figure 2.3. Ideal pendulum.

Example

An example of a dynamic system governed by a second-order ODE is the damped harmonic oscillator, as illustrated in Fig. 2.2. The behavior of this system is described by the following ODE:

$$m\frac{d^2u}{dt^2} + c\frac{du}{dt} + ku = 0, \tag{2.2.3}$$

where m represents the mass, c is the damping coefficient, k is the spring stiffness, and u denotes the displacement of the oscillator.

Equation (2.2.3) can be reformulated into the form presented in Eq. (2.2.1) by introducing the new variables $x_1 = u$ and $x_2 = \dot{u}$. Based on these definitions and the governing equation, the equivalent system is thus represented as follows:

$$\begin{cases} \dot{x}_1 = x_2 \\ \dot{x}_2 = -\frac{c}{m}x_2 - \frac{k}{m}x_1. \end{cases}$$

The system obtained is an example of a linear system, because all the x_i on the right-hand side appear to the first power only.

Example

Another example is provided by an ideal pendulum, as illustrated in Fig. 2.3. In this case, the state of the system is fully characterized by defining its angular displacement $\theta \pmod{2\pi}$ from the vertical position, along with the corresponding angular velocity $\dot{\theta}$. It is crucial to emphasize that the angle θ alone is inadequate for determining the future state of the pendulum.

Thus, for this mechanical system, the state-space is $\mathcal{X} = \mathbb{S} \times \mathbb{R}$, where $\mathbb{S}$ is once again the unit circle parameterized by the angle, and $\mathbb{R}$ is the real line corresponding to the set of all possible angular velocities. The set $\mathcal{X}$ can be considered as a smooth two-dimensional manifold (cylinder) in $\mathbb{R}^3$. The dynamics of an ideal pendulum is fully described by Newton's second law, resulting in the following ODE:

$$\ddot{\theta} = -\frac{g}{l} \sin \theta,$$

where l represents the length of the pendulum and g denotes the acceleration due to gravity.

At this point, if we introduce $x_1 = \theta$ and $x_2 = \dot{\theta}$ such that the pair (x_1, x_2) represents a point in the state-space $\mathcal{X} = \mathbb{S} \times \mathbb{R}^1$, the governing ODE can be rewritten in the form of Eq. (2.2.1) as:

$$\begin{cases} \dot{x}_1 = x_2 \\ \dot{x}_2 = -\frac{g}{l} \sin x_1, \end{cases}$$

where the vector field $\mathbf{f}$ is defined as:

$$\mathbf{f}(\mathbf{x}) = \begin{bmatrix} x_2 \\ -\frac{g}{l} \sin x_1 \end{bmatrix}.$$

The system obtained is an example of a nonlinear system, due to the term $\sin x_1$.

Concerning the output transformation given by Eq. (2.2.2), we can select the output variables to be the position and angular velocity of the pendulum by introducing the following expressions:

$$\begin{cases} y_1 = x_1 \\ y_2 = x_2. \end{cases}$$

Consequently, the vector field $\mathbf{g}$ can be expressed as:

$$\mathbf{g}(\mathbf{x}) = \begin{bmatrix} x_1 \\ x_2 \end{bmatrix}.$$

Section 2.3

Classification of Continuous-Time Dynamical Systems

Dynamical systems described by Eqs. (2.2.1) and (2.2.2) can be classified in different ways based on the characteristics of the vector fields $\mathbf{f}$ and $\mathbf{g}$. In particular, based on the number of *input* and *output* variables, they can be classified as:

- *Single-Input-Single-Output* (SISO): systems characterized by having a single input variable and a single output variable;
- *Multiple-Input-Multiple-Output* (MIMO): systems defined by the presence of multiple input variables and multiple output variables.

Additionally, systems can be classified based on the characteristics of the output transformation $\mathbf{g}$ into:

- *Proper systems*: for which Eq. (2.2.2) holds. A special case is that of a *static* system, i.e., a system where the function $\mathbf{g}$ does not depend on the state vector;
- *Strictly proper systems*: for which the function $\mathbf{g}$ does not depend on the input vector.

Further classification can be made between:

- *Linear systems*: defined as those systems where the functions $\dot{\mathbf{x}}(t)$ and $\mathbf{y}(t)$ are linear combinations of the components of the state and input vectors.
- *Nonlinear systems*: defined as systems that cannot be described as linear combinations of the components of the state variable vectors $\mathbf{x}(t)$ and input vectors $\mathbf{u}(t)$.

Finally, dynamical systems can be classified based on their direct time dependence into:

- *Autonomous systems*: those systems where there are no direct time dependencies;
- *Nonautonomous systems*: those systems that explicitly depend on time.

The distinction between autonomous and nonautonomous systems is fundamental in the analysis of dynamical systems, as it significantly influences their behavior and characteristics. The following subsections will delve into the characteristics of autonomous and nonautonomous systems, providing a description of each category.

SUBSECTION 2.3.1
Autonomous Systems

Definition 2 In the case where the function $\mathbf{f}$ does not explicitly depend on time, the system is classified as *autonomous* and operates within a general n-dimensional state-space [64]. The governing equation for an autonomous system is then expressed as follows:

$$\dot{\mathbf{x}} = \mathbf{f}\left(\mathbf{x}\right). \tag{2.3.1}$$

The evolution of autonomous systems is determined just by the current state of the system, without any external temporal influence. This leads to a simpler analytical framework, often allowing for the derivation of general solutions and stability assessments. The behavior of an autonomous system is invariant to shifts in the time origin, since changing the time variable from t to $t + a$ does not change the right-hand side of the state equation.

SUBSECTION 2.3.2
Nonautonomous Systems

Definition 3 In the case where the function $\mathbf{f}$ explicitly depend on time, the system is classified as *nonautonomous*. The governing equation for a nonautonomous system is formally expressed by means of a different symbol, $\mathbf{F}$, as follows:

$$\dot{\mathbf{x}} = \mathbf{F}\left(\mathbf{x}, t\right). \tag{2.3.2}$$

Nonautonomous systems incorporate time as an explicit variable, resulting in dynamics that can vary over time and depend on external inputs. This time dependence introduces additional complexity, necessitating specific approaches to fully understand the system's behavior.

The time variable introduces a state-space of one dimension higher than defined by $\mathbf{x}$. The new dimension is time, although time is not on an equal footing with $\mathbf{x}$ because time cannot be controlled. However, the higher dimensionality does allow different dynamics. For instance, in a 2D state-space, as we will see in the following chapters, chaos is not allowed because of the non-crossing theorem. However, in a driven 2D system, the extra dimension of time lifts this restriction and chaos is thus possible.

There are many ways to introduce a new variable related to time. For instance the new variable may be introduced as:

$$\begin{aligned} x_{n+1} &= t, \\ \dot{x}_{n+1} &= 1. \end{aligned}$$

On the other hand, for $\theta = \omega t$, a natural variable to describe the dynamics is:

$$\begin{aligned} x_{n+1} &= \omega t, \\ \dot{x}_{n+1} &= \omega, \end{aligned} \tag{2.3.3}$$

and the angle can be plotted as mod 2π. Both of these substitutions convert a nonautonomous flow into an autonomous one.

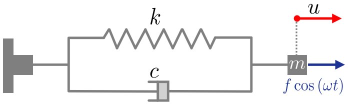

Figure 2.4. SDoF forced damped harmonic oscillator.

In the case of a harmonic forcing function, the new variable can also be:

$$\begin{aligned} x_{n+1} &= \sin(\omega t), \\ \dot{x}_{n+1} &= \omega \cos(\omega t). \end{aligned}$$

This representation has the benefit that trajectories are bounded along the new dimension, while in the first cases the trajectories are not. If $\mathbf{F}$ is an explicit function of time, then the system is *nonautonomous* with an $(n+1)$-dimensional state-space [64].

Example To address *autonomous* and *nonautonomous* equations, we examine the case of a forced damped harmonic oscillator as shown in Fig. 2.4. This system is described by the following second-order ODE:

$$m\frac{d^2u}{dt^2} + c\frac{du}{dt} + ku = f\cos(\omega t)\,, \tag{2.3.4}$$

where, u represents the displacement, m is the mass, c is the viscous damping coefficient, k is the elastic stiffness, and f and ω are the amplitude and angular frequency of the external

forcing, respectively.
We can rewrite this equation in the form described in Eq. (2.3.2) by introducing the variables $x_1 = u$ and $x_2 = \dot{u}$ as:

$$\begin{cases} \dot{x}_1 = x_2 \\ \dot{x}_2 = \frac{1}{m}\left[-cx_2 - kx_1 + f\cos(\omega t)\right], \end{cases}$$

where the nonautonomous vector fiel $\mathbf{F}(\mathbf{x}, t)$ is defined by:

$$\mathbf{F}(\mathbf{x}, t) = \begin{bmatrix} x_2 \\ \frac{1}{m}\left[-cx_2 - kx_1 + f\cos(\omega t)\right] \end{bmatrix}.$$

At this point, by introducing a new state variable $x_3 = \omega t \bmod 2\pi$ (Eq. (2.3.3)), we can express the initial set of equations as an autonomous system described by Eq. (2.3.1). In such a way, since $\dot{x}_3 = \omega$, the equivalent autonomous system is:

$$\begin{cases} \dot{x}_1 = x_2 \\ \dot{x}_2 = \frac{1}{m}\left[-cx_2 - kx_1 + f\cos(x_3)\right] \\ \dot{x}_3 = \omega, \end{cases} \tag{2.3.5}$$

and the autonomous vector field $\mathbf{f}(\mathbf{x})$ is:

$$\mathbf{f}(\mathbf{x}) = \begin{bmatrix} x_2 \\ \frac{1}{m}\left[-cx_2 - kx_1 + f\cos(x_3)\right] \\ \omega \end{bmatrix}.$$

In a more general setting, a n^{th}-order nonautonomous equation is a special case of a $(n+1)$-dimensional autonomous system. Through this substitution, we can always remove any time dependence by adding an extra dimension to the system. The main advantage of this change of variables is that it allows us to visualize a state-space with trajectories frozen in it. Otherwise, if we allowed an explicit time dependence, the vectors and trajectories would always be oscillating.

A more physical reason is that the state of the forced harmonic oscillator is truly three-dimensional; in fact, we need to know u, $\dot{u}$ and t, to predict the future, given the present, so a three-dimensional state-space is natural. The cost, however, is that some of our terminology is non-traditional. For example, the forced harmonic oscillator would traditionally be considered as a second-order linear system, whereas in this case we can consider it a third-order nonlinear system, since Eq. (2.3.5) is nonlinear, thanks to the cosine term [80].

SECTION 2.4

Phase Portraits

The fundamental idea of geometric methods, such as the phase portrait construction, is to assume that the solution for particular initial conditions is known. This solution will be composed of functions representing the position and velocity of the vector field in the state-space. At this point the solution at any instant of time will correspond to a point moving along a curve, called *trajectory*, in the *state-space* of the system. The state-space is completely filled with trajectories, since each point can serve as an initial condition. Given a system, the main goal is to draw the trajectories, and thereby extract information about the solutions.

The general form of a vector field in the state-space is given by:

$$\dot{\mathbf{x}} = \mathbf{f}\left(\mathbf{x}\right), \tag{2.4.1}$$

where $\mathbf{x}$ represents a point in the state-space, and $\dot{\mathbf{x}}$ is the velocity vector at that point. The entire phase plane is filled with trajectories, since each point can play the role of an initial condition. The strength of the graphical method lies in the fact that, in the case of a nonlinear system, it is not possible to determine the trajectories analytically, even when explicit formulas are available. For such a reason, the goal is to determine the phase portrait of a system directly from the properties of $\mathbf{f}$.

The most important features of any phase portrait are:

- Fixed-points: These points satisfy the equation $\mathbf{f}\left(\mathbf{x}\right) = \mathbf{0}$ and correspond to steady states or equilibria of the system. In terms of the original differential equation, fixed-points represent equilibrium solutions.

- Nullclines: Nullclines are defined as the curves where all the $\dot{x}_i$ are equal to zero except one. The nullclines indicate where the flow is purely in one direction.

- Closed orbits: These correspond to periodic solutions, i.e., solutions for which $\mathbf{x}\left(t+T\right) = \mathbf{x}\left(t\right)\ \forall t$, given $T > 0$.

- The arrangement of trajectories near the fixed-points and closed orbits.

- The stability or instability of the fixed-points and closed orbits. In particular, an equilibrium is defined to be stable if all sufficiently small disturbances away from it damp out in time. Conversely, unstable equilibria, in which disturbances grow in time.

Sometimes also quantitative aspects of the phase portrait are important. In these cases we solve the system in Eq. (2.4.1) by means of numerical integration. One of the most used numerical integration methods is the fourth order Runge-Kutta method (ode45).

Example Consider the following nonlinear system:

$$\begin{cases} \dot{x}_1 = x_1 + e^{-x_2} \\ \dot{x}_2 = -x_2. \end{cases} \tag{2.4.2}$$

1. To find the fixed-points of this system we impose $\mathbf{f}(\mathbf{x}) = \mathbf{0}$, for which the only solution is the point $\mathbf{x}^* \equiv [-1, 0]^T$.
2. The stability of the system is determined by noting that $x_2 \to 0$ as $t \to \infty$, since the solution to $\dot{x}_2 = -x_2$ is $x_2(t) = x_2(t=0)e^{-t}$. Hence, $e^{-x_2} \to 1$ and so in the long run, the equation for x_1 becomes $\dot{x}_1 \approx x_1 + 1$; this has exponentially growing solutions, which suggests that the fixed-point is unstable [80].
3. To obtain the nullcines we observe that the flow defined in Eq. (2.4.2) is horizontal where $\dot{x}_2 = 0$, and since $\dot{x}_2 = -x_2$, this occurs on the line $x_2 = 0$. Along this line, the flow is to the right where $\dot{x}_1 \approx x_1 + 1 > 0$, that is, where $x_1 > -1$. Similarly, the flow is vertical where $\dot{x}_1 = x_1 + e^{-x_2} = 0$, which occurs on the curve shown in Fig. 2.5. On the upper part of the curve where $x_2 > 0$, the flow is downward, since $\dot{x}_2 < 0$.

   The nullclines also partition the plane into regions where x_1 and x_2 have different signs. Even with the limited information obtained so far, we obtain a good sense of the overall flow pattern.

The phase portrait, derived by merging the insights gathered from prior analyses with the outcomes of the direct numerical computation, is provided in Fig. 2.5.

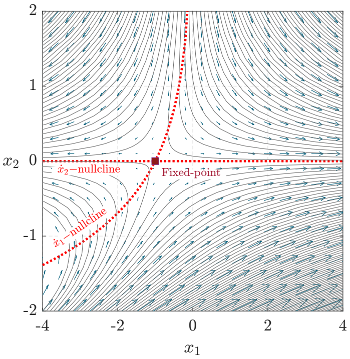

Figure 2.5. Phase portrait showing vector field, flow lines, nullclines and fixed-point [80].

SECTION 2.5

Non-dimensionalization

Non-dimensionalization is a powerful technique that can be used to simplify and parameterize problems involving physical quantities. Specifically, by eliminating the physical dimensions from an equation, one can identify which combination of parameters best describes the behavior of the solution and reduce the number of parameters in a system. Additionally, non-dimensionalization allows us to recover some intrinsic properties of a system, such as resonant frequency, length, or time constant. Through the careful application, non-dimensionalization offers great potential for understanding complex systems with multiple variables involved.

Non-dimensionalization serves as an effective approach for simplifying systems of differential equations by scaling each independent and dependent variable with respect to a characteristic unit of measurement. This process reduces the complexity of the equations while preserving their essential features, making it especially valuable in addressing physical problems often represented by ODEs. Beyond this, non-dimensionalization also finds applications in fields such as dimensional analysis and statistical normalization, where it aids in establishing comparability across diverse datasets.

A system of equations can be non-dimensionalized by following these steps:

1. Identify all independent and dependent variables;
2. Replace all variables with non-dimensional quantities based on characteristic units;
3. Divide the obtained equation by the coefficient of the highest-order derivative;
4. Choose the characteristic unit for each variable so that potential auxiliary conditions become as simple as possible;
5. Rewrite the equation in terms of new non-dimensional quantities.

It may be necessary to perform the last three steps depending on the type of problem being addressed. However, all systems require the fulfillment of the first two steps.

Example

As an example, we consider Eq. (2.3.4) which is a second-order ODE with constant coefficients, characteristic of a forced damped harmonic oscillator. By applying the previously described steps to:

$$m\frac{d^2u}{dt^2} + c\frac{du}{dt} + ku = f\cos(\omega t), \tag{2.5.1}$$

we have that:

1. The independent variable is time t, whereas the generalized displacement u is the dependent one.
2. We define the non-dimensional time τ and displacement x as:
$$\tau = \frac{t - t_r}{t_s}, \qquad x = \frac{u - u_r}{u_s}.$$
These two quantities are defined as the difference of the dimensional variable and a reference value, indicated with t_r and u_r, over a dimensional scaling factor (i.e., t_s and u_s). If we assume that the dimensional reference values are equal to zero, we obtain:
$$t = t_s\tau, \qquad u = x_s x.$$
Now if we plug these quantities into Eq. (2.5.1) the obtained ODE is:
$$\begin{aligned} m\frac{d}{dt}\left(\frac{du}{dt}\right) + c\frac{du}{dt} + ku &= f\cos(\omega t), \\ m\frac{d}{d(t_s\tau)}\left[\frac{d(x_s x)}{d(t_s\tau)}\right] + c\frac{d(x_s x)}{d(t_s\tau)} + k(x_s x) &= f\cos(\omega t_s\tau), \\ \frac{m x_s}{t_s^2}\frac{d^2x}{d\tau^2} + \frac{c x_s}{t_s}\frac{dx}{d\tau} + k x_s x &= f\cos(\omega t_s\tau). \end{aligned}$$
3. The coefficient of the highest ordered term is $\frac{m x_s}{t_s^2}$, dividing by this we obtain:
$$\frac{d^2x}{d\tau^2} + \frac{c t_s}{m}\frac{dx}{d\tau} + \frac{k t_s^2}{m}x = \frac{f t_s^2}{m x_s}\cos(\omega t_s\tau).$$
4. To determine the scaling factors t_s and x_s such that equations and potential auxiliary conditions, become as simple as possible, we can set, as an example, the coef-

ficients in front of x and $\cos(\omega t_s \tau)$ equal to one:

$$\frac{kt_s^2}{m} = 1 \rightarrow t_s = \sqrt{\frac{m}{k}} = \frac{1}{\omega_0},$$
$$\frac{ft_s^2}{mx_s} = 1 \rightarrow x_s = \frac{f_0}{k}.$$

5. The final non-dimensional equation in this case becomes dependent only on two non-dimensional parameters:

$$2\zeta = \frac{c}{\sqrt{mk}}, \qquad \Omega = \omega\sqrt{\frac{m}{k}},$$

so the final non-dimensional form of the initial ODE is:

$$\frac{d^2x}{d\tau^2} + 2\zeta\frac{dx}{d\tau} + x = \cos(\Omega\tau).$$

CHAPTER

3

Linear Dynamical Systems

I do not know what I may appear to the world, but to myself I seem to have been only a poor boy playing on the sea-shore, and diverting myself in now and then finding a smoother pebble or a prettier shell than ordinary, whilst the great ocean of truth lay all undiscovered before me.
— Sir Isaac Newton

Linear physics is the bedrock upon which all introductory physics and engineering courses are built. The power of linearity comes from proportionality and additivity. With proportionality, all systems respond in a manner proportional to the strength of the inputs. With additivity, known as the principle of linear superposition, the behavior of complicated systems can be decomposed into their fundamental elements.

This chapter delves into the analysis of linear time-invariant dynamical systems, beginning with fundamental concepts and progressing to advanced mathematical techniques. It starts with an overview of linear time-invariant systems and introduces Laplace transform, which are essential tools for analyzing system behavior in the frequency domain. Subsequent sections focus on various mathematical representations, including state-space representation and frequency domain representation, illustrating how these frameworks facilitate the analysis of linear dynamical systems.

Section 3.1

Linear Time-Invariant Dynamical Systems

For linear systems, the state model represented by Eqs. (2.2.1)-(2.2.2) takes the form:

$$\begin{cases} \dot{\mathbf{x}}(t) = \mathbf{A}(t)\mathbf{x}(t) + \mathbf{B}(t)\mathbf{u}(t) \\ \mathbf{y}(t) = \mathbf{C}(t)\mathbf{x}(t) + \mathbf{D}(t)\mathbf{u}(t). \end{cases}$$

A case of particular interest in various fields of engineering is that of Linear Time-Invariant (LTI) systems. These systems are characterized by the following equations:

$$\begin{cases} \dot{\mathbf{x}}(t) = \mathbf{A}\mathbf{x}(t) + \mathbf{B}\mathbf{u}(t) \\ \mathbf{y}(t) = \mathbf{C}\mathbf{x}(t) + \mathbf{D}\mathbf{u}(t), \end{cases} \tag{3.1.1}$$

where the matrices $\mathbf{A} \in \mathbb{R}^{n \times n}$, $\mathbf{B} \in \mathbb{R}^{n \times m}$, $\mathbf{C} \in \mathbb{R}^{p \times n}$, and $\mathbf{D} \in \mathbb{R}^{p \times m}$ are all time-invariant and defined within the matrix spaces mentioned in Section 2.2.1. These matrices are commonly referred to as the *state matrix*, *input matrix*, *output matrix*, and *feed-through matrix*, respectively [7].

Properties Due to their distinctive properties, LTI systems hold significant importance in the fields of control theory, mechanics, and a broad spectrum of engineering applications. In particular, these systems are characterized by the following properties:

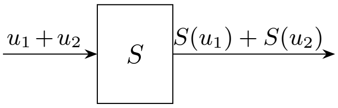

Figure 3.1. Superposition principle.

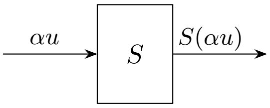

Figure 3.2. Scaling principle.

- **Superposition principle**: The response of a linear system to a linear combination of a certain number of linearly independent inputs can be obtained by summing the individual responses that each input would generate if it acted independently (Fig. 3.1):

$$S(u_1 + u_2) = S(u_1) + S(u_2).$$

- **Scaling principle**: For a linear system, scaling an input by a certain factor results in the output being scaled by the same factor (Fig. 3.2):

$$S(\alpha u) = \alpha S(u) \quad \forall \alpha \in \mathbb{R}.$$

- **Closed-form solutions**: A linear system has explicit solutions, often represented by Lagrange formulas. Specifically, the state vector $\mathbf{x}(t)$ and the output vector $\mathbf{y}(t)$ corresponding to the input $\mathbf{u}(t)$ over the time interval $(t-t_0)$ $\forall t \geq t_0$, can be explicitly determined given the state variables at time t_0 (i.e., $\mathbf{x}(t_0) = \mathbf{x}_0$). The expressions for these vectors are as follows:

  $$\mathbf{x}(t) = e^{\mathbf{A}(t-t_0)}\mathbf{x}_0 + \int_{t_0}^{t} e^{\mathbf{A}(t-\tau)}\mathbf{B}\mathbf{u}(\tau)d\tau, \tag{3.1.2}$$

  $$\mathbf{y}(t) = \mathbf{C}e^{\mathbf{A}(t-t_0)}\mathbf{x}_0 + \int_{t_0}^{t} \left[\mathbf{C}e^{\mathbf{A}(t-\tau)}\mathbf{B} + \mathbf{D}\delta(t-\tau)\right]\mathbf{u}(\tau)d\tau. \tag{3.1.3}$$

  The contribution that depends uniquely on the initial state $\mathbf{x}(t_0) = \mathbf{x}_0$ is referred to as the system's *free response*, which occurs when the input is zero for the same $\mathbf{x}_0$:

  $$\begin{cases} \mathbf{x}_l(t) = e^{\mathbf{A}(t-t_0)}\mathbf{x}_0 \\ \mathbf{y}_l(t) = \mathbf{C}e^{\mathbf{A}(t-t_0)}\mathbf{x}_0. \end{cases} \tag{3.1.4}$$

  Conversely, the contribution to the overall response that relies exclusively on the input is defined as the system's *forced response*:

  $$\begin{cases} \mathbf{x}_f(t) = \int_{t_0}^{t} e^{\mathbf{A}(t-\tau)}\mathbf{B}\mathbf{u}(\tau)d\tau \\ \mathbf{y}_f(t) = \int_{t_0}^{t} \left[\mathbf{C}e^{\mathbf{A}(t-\tau)}\mathbf{B} + \mathbf{D}\delta(t-\tau)\right]\mathbf{u}(\tau)d\tau. \end{cases}$$

  Additionally, the following matrices can also be defined:

  - *State transition matrix*: $\mathbf{\Phi}(t-t_0) := e^{\mathbf{A}(t-t_0)} \in \mathbb{R}^{n\times n}$.
  - *Impulse response matrix for the state*: $\mathbf{H}(t-t_0) := e^{\mathbf{A}(t-t_0)}\mathbf{B} \in \mathbb{R}^{n\times m}$.
  - *Output transition matrix*: $\mathbf{\Psi}(t-t_0) := \mathbf{C}e^{\mathbf{A}(t-t_0)} \in \mathbb{R}^{p\times n}$.
  - *Impulse response matrix for the output*: $\mathbf{W}(t-t_0) := \mathbf{C}e^{\mathbf{A}(t-t_0)}\mathbf{B} + \mathbf{D}\delta(t-\tau) \in \mathbb{R}^{p\times m}$.

  In such a way, the responses in Eqs. (3.1.2) and (3.1.3) can be expressed more compactly as follows:

  $$\mathbf{x}(t) = \mathbf{\Phi}(t-t_0)\mathbf{x}_0 + \int_{t_0}^{t} \mathbf{H}(t-\tau)\mathbf{u}(\tau)d\tau, \tag{3.1.5}$$

$$\mathbf{y}(t) = \mathbf{\Psi}(t - t_0)\mathbf{x}_0 + \int_{t_0}^{t} \mathbf{W}(t - \tau)\mathbf{u}(\tau)d\tau. \tag{3.1.6}$$

Further details regarding the exponential matrix $e^{\mathbf{A}t}$ introduced in the above equations can be found in Appendix A.

- **Rouché–Capelli theorem**: For a linear system of the type $\mathbf{Ax} = \mathbf{b}$, where the matrix $\mathbf{A} \in \mathbb{R}^{n\times n}$ and the vectors $\mathbf{x}, \mathbf{b} \in \mathbb{R}^{n\times 1}$:
  - There are no solutions if the rank of the incomplete matrix is less than the rank of the augmented matrix:

    $$\mathrm{rk}(\mathbf{A}) < \mathrm{rk}(\mathbf{A}|\mathbf{b}) \implies \nexists \quad \text{solutions.}$$

  - There is exactly one solution if the rank of the incomplete matrix is equal to the rank of the augmented matrix, which is also equal to the number of unknowns n:

    $$\mathrm{rk}(\mathbf{A}) = \mathrm{rk}(\mathbf{A}|\mathbf{b}) = n \implies \exists! \quad \text{solution.}$$

  - There are infinite solutions, to the order of $n - \mathrm{rk}(\mathbf{A})$, if and only if the rank of the incomplete matrix is equal to the rank of the augmented matrix, which in turn is greater than the number of unknowns n:

    $$\mathrm{rk}(\mathbf{A}) = \mathrm{rk}(\mathbf{A}|\mathbf{b}) > n \implies \exists \quad \infty^{n-\mathrm{rk}(\mathbf{A})} \quad \text{solutions.}$$

- **Stability**: A linear stationary system is stable or asymptotically stable, respectively, if and only if all its free responses are bounded or tend to zero as $t \to \infty$. If at least one of the state motions is unbounded, the system is unstable.

  To better understand the concept of stability, consider a time-invariant dynamical system with a given input $\mathbf{u}(t)$ for $t \geq 0$, an initial state $\mathbf{x}_0$, and the resulting trajectory $\mathbf{x}(t)$, referred to as the nominal motion. Additionally, consider a second trajectory, referred to as the perturbed motion, $\tilde{\mathbf{x}}(t)$, generated by the same input $\mathbf{u}(t)$ but starting from a different initial state $\tilde{\mathbf{x}}_0$.

Definition 4 The motion $\mathbf{x}(t)$ is defined as *stable* (Fig. 3.3a), in the sense of Lyapunov, if $\forall \varepsilon > 0$ there exists a $\delta(\varepsilon) > 0$ such

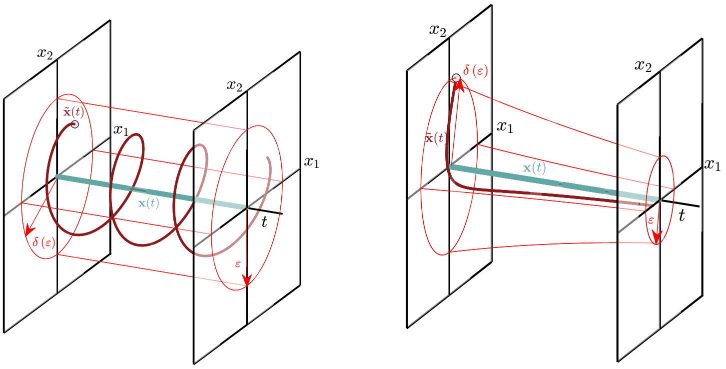

(a) (b)

Figure 3.3. Graphical representation of stable (a) and asymptotically stable (b) motion.

that for all initial states $\mathbf{x}_0$, $\tilde{\mathbf{x}}_0$ satisfying:

$$||\tilde{\mathbf{x}}_0 - \mathbf{x}_0|| < \delta(\varepsilon),$$

it turns out to be:

$$||\tilde{\mathbf{x}}(t) - \mathbf{x}(t)|| < \varepsilon \quad \forall t \geq 0.$$

Furthermore, if:

$$\lim_{t\to\infty} ||\tilde{\mathbf{x}}(t) - \mathbf{x}(t)|| = 0,$$

the motion is said to be *asymptotically stable* (Fig. 3.3b).

For a LTI system, the stability property of the motion depends just on the free response. Moreover, for this class of systems, it is noteworthy that local stability implies global stability[1].

SECTION 3.2

Laplace Transform

Laplace transform is an important mathematical tool used in the analysis of linear dynamical systems to solve linear differential equations by transforming them into algebraic equations, which are easier to solve. It is also widely used in control system analysis, signal theory, circuit analysis, and many other fields of engineering and physics. The use of Laplace transform is justi-

---

[1] A change is considered *global* if it occurs outside the *local neighborhood* of the point, where the *local neighborhood* refers to the immediate region surrounding the point under consideration.

fied by the simplification of linear differential equation analysis that results from its application.

SUBSECTION 3.2.1

Laplace Integral Transform

The Laplace integral transform, formally, represents a mathematical operation that transforms a real ODE into a complex valued algebraic one through the following integral transformation:

$$\mathcal{L}\{f(t)\} = F(s) = \int_0^\infty f(t)e^{-st}dt,$$

where $f(t)$ is the function being transformed, depending on the continuous time variable, and e^{-st} is the complex valued exponential function, with s being a complex variable specifically defined by the expression:

$$s = \sigma + i\omega,$$

where i is the imaginary unit.

In other words, the Laplace transform is an integral transformation of the real function $f(t)$, multiplied by a complex valued exponential function. The result of this operation is a function of the complex variable s, expressed as $F(s)$.

Properties There are several key properties that make Laplace transform a highly useful mathematical tool for dealing with problems related to linear dynamic systems. The following are the main ones:

- **Linearity**: Given two real functions f and g, with $\alpha,\ \beta \in \mathbb{R}$, it follows that:

  $$\mathcal{L}\left\{\alpha f(t) + \beta g(t)\right\} = \alpha F(s) + \beta G(s),$$

  where F and G are the Laplace transform of f and g, respectively.

- **Transform of the time-domain derivative**: Assuming that the function $f(t)$ is differentiable $\forall t \geq 0$, the Laplace transform of the n^{th} derivative of this function is given by:

  $$\mathcal{L}\left\{f^{(n)}(t)\right\} = s^n F(s) - \sum_{i=1}^{n} s^{n-i} f^{(i-1)}(0),$$

where s^n is the nth power, in the complex sense, of the variable s previously defined.

- **Transform of the time-domain integral**: Assuming that the function f is integrable from 0 to t, we have:

$$\mathcal{L}\left\{\int_0^t f(\tau)d\tau\right\} = \frac{1}{s}F(s).$$

- **Time-domain translation**: For any $\tau > 0$, consider the function $\hat{f}(t) = f(t-\tau)$, then:

$$\mathcal{L}\left\{\hat{f}(t)\right\} = \mathcal{L}\left\{f(t-\tau)\right\} = e^{-\tau s}F(s).$$

- **Complex-domain translation**: For any $\alpha \in \mathbb{C}$, consider the function $\hat{f}(t) = e^{\alpha t}f(t)$, then:

$$\mathcal{L}\left\{\hat{f}(t)\right\} = \mathcal{L}\left\{e^{\alpha t}f(t)\right\} = F(s-\alpha).$$

- **Complex-domain derivative**: The derivative of the function $F : s \to F(s)$ with respect to the complex variable s is equal to:

$$\frac{dF(s)}{ds} = \mathcal{L}\left\{tf(t)\right\}.$$

- **Time convolution**: The Laplace transform of the convolution integral between two time functions $f_1(t)$ and $f_2(t)$ is equal to the product of their transforms $F_1(s)$ and $F_2(s)$:

$$\mathcal{L}\left\{\int_{-\infty}^{+\infty} f_1(t-\tau)f_2(\tau)d\tau\right\} = F_1(s)F_2(s).$$

Appendix B lists several fundamental transforms useful for solving key problems in linear dynamics.

SUBSECTION 3.2.2

Inverse Laplace Transform

In mathematics, the inverse Laplace transform, also known as the Bromwich integral or the inverse Mellin formula, is given by the line integral:

$$\mathcal{L}^{-1}\left\{F(s)\right\} = f(t) = \frac{1}{2\pi i} \lim_{T\to\infty} \int_{\gamma-iT}^{\gamma+iT} e^{st} F(s) ds,$$

where the integration is done along the vertical line $\mathrm{Re}(s) = \gamma$ in the complex plane such that γ is greater than the real part of all singularities of $F(s)$ and $F(s)$ is bounded on the line.

Here we will focus on the procedures for obtaining the inverse Laplace transforms of rational functions, which are the most common in problems typically encountered in the dynamics of linear systems.

By applying the classical polynomial division algorithm, any rational function can be expressed as the sum of a polynomial and a rational function, where the degree of the denominator exceeds the degree of the numerator. Specifically, for a rational function of the form:

$$F(s) = \frac{N(s)}{D(s)} = \frac{b_m s^m + \cdots + b_1 s + b_0}{a_n s^n + \cdots + a_1 s + a_0},$$

the *relative degree* is defined as the difference $n - m$. The objective at this stage is to rewrite the ratio of polynomials as a sum of elementary terms, simplifying the computation of the inverse transform (a process known as *partial fraction decomposition*). Depending on the relative degree, the following cases arise:

- $n - m > 0$: the fraction is already strictly proper, and the ratio between $N(s)$ and $D(s)$ can be decomposed into a sum of terms that are readily inverse transformed;

- $n - m = 0$: it is necessary to first decompose the function $F(s)$ into the sum of a strictly proper fraction and a constant, before applying partial fraction decomposition;

- $n - m < 0$: the system is anti-causal, implying that the output is nonzero for $t < 0$.

This systematic procedure enables a rigorous analysis of rational functions. In particular, for the computation of the inverse Laplace transform of a complex valued rational function $F(s)$, the application of the *Residue Theorem* is often employed. The decomposition of a complex function into partial fractions is expressed as follows:

$$F(s) = \frac{N(s)}{D(s)} = \frac{N(s)}{(s-p_1)(s-p_2)\dots(s-p_n)} = \sum_{i=1}^{n} \frac{K_i}{s-p_i},$$

where p_i are the *zeros* (or *poles*) of the polynomial $D(s)$ at the denominator, and K_i are the *residues* corresponding to the various poles. These are computed as:

$$K_i = (s - p_i)\frac{N(s)}{D(s)}\bigg|_{s=p_i}.$$

Using the linearity property:

$$\mathcal{L}^{-1}\left\{\frac{1}{s-\alpha}\right\} = e^{\alpha t},$$

the inverse transform of the output is given by:

$$y(t) = \sum_{i=1}^{n} K_i e^{p_i t}.$$

Now suppose there are h distinct poles, denoted as p_j, and that each has a multiplicity $r_i \geq 1$. The partial fraction decomposition of the system's output transform can be expressed as:

$$F(s) = \frac{N(s)}{(s-p_1)^{r_1}(s-p_2)^{r_2}\dots(s-p_n)^{r_k}} = \sum_{i=1}^{h}\sum_{l=1}^{r_i}\frac{K_{il}}{(s-p_i)^{r_i-l+1}},$$

where the residues K_{il} are calculated as:

$$K_{il} = \frac{1}{(l-1)!}\frac{d^{l-1}}{ds^{l-1}}(s-p_i)^{r_i}\frac{N(s)}{D(s)}\bigg|_{s=p_i}.$$

Exploiting the linearity property of Laplace transforms and the relation:

$$\mathcal{L}\left\{t^n e^{\alpha t}\right\} = \frac{n!}{(s-\alpha)^{n+1}},$$

we finally obtain the inverse transform of $F(s)$ as:

$$y(t) = \sum_{i=1}^{h}\sum_{l=1}^{r_i}\frac{K_i}{(r_i-l)!}t^{r_i-l}e^{p_i t}.$$

SECTION 3.3

Mathematical Representations for Mechanical Systems

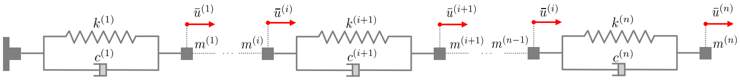

Figure 3.4. General family of linear MDoF mechanical systems.

In the study of mechanical systems, accurate mathematical representations are crucial for understanding and predicting the system's behavior. This section focuses on two fundamental representations: the state-space representation and the frequency domain representation.

The state-space representation provides a comprehensive framework for modeling Multi-Degree-of-Freedom (MDoF) mechanical systems, encapsulating the dynamics of the system through a set of first-order ODEs. We begin with the second-order ODE governing the motion of a general class of MDoF system, which incorporates mass, damping, and stiffness matrices. By reformulating this equation into state-space form, we can derive the matrices that describe the system's dynamics, including the state matrix.

Following the state-space representation, we will explore the frequency domain representation. This approach leverages the Laplace transform to convert the time-domain equations into a form that is often easier to manipulate. By applying the Laplace transform to the state-space equations, we obtain expressions that reveal the relationship between the system's input and output in the frequency domain.

Overall, this section aims to provide a clear and methodical understanding of the mathematical representations used for mechanical systems, highlighting their importance and practical differences.

Subsection 3.3.1

State-Space Representation

The following section presents the state-space formulation for a general family of linear MDoF systems as depicted in Fig. 3.4. This formulation is derived from the second-order ODE that governs the motion of the system, expressed as follows:

$$\mathbf{M}\ddot{\bar{\mathbf{u}}} + \mathbf{C}\dot{\bar{\mathbf{u}}} + \mathbf{K}\bar{\mathbf{u}} = \mathbf{p}. \tag{3.3.1}$$

In this equation, $\mathbf{M}$, $\mathbf{C}$, $\mathbf{K} \in \mathbb{R}^{n\times n}$ represent the mass, damping, and stiffness matrices, respectively. The variables

$\ddot{\bar{\mathbf{u}}}$, $\dot{\bar{\mathbf{u}}}$, $\bar{\mathbf{u}} \in \mathbb{R}^{n\times 1}$ denote the accelerations, velocities, and displacements of the system. This general setting serves as the basis for deriving the state-space representation, enabling a systematic analysis of the system's dynamics.

To obtain the representation seen in Eq. (3.1.1), the equation of motion is rewritten by defining $\mathbf{x}_1 := \bar{\mathbf{u}}$ and $\mathbf{x}_2 := \dot{\bar{\mathbf{u}}}$, obtaining the following system:

$$\begin{cases} \dot{\mathbf{x}}_1 = \mathbf{x}_2 \\ \dot{\mathbf{x}}_2 = \mathbf{M}^{-1}(\mathbf{p} - \mathbf{C}\mathbf{x}_2 - \mathbf{K}\mathbf{x}_1), \end{cases}$$

thus, the matrices $\mathbf{A} \in \mathbb{R}^{2n\times 2n}$ and $\mathbf{B} \in \mathbb{R}^{2n\times n}$, previously introduced are:

$$\mathbf{A} = \begin{bmatrix} \mathbf{0} & \mathbf{I} \\ -\mathbf{M}^{-1}\mathbf{K} & -\mathbf{M}^{-1}\mathbf{C} \end{bmatrix}, \qquad \mathbf{B} = \begin{bmatrix} \mathbf{0} \\ \mathbf{M}^{-1} \end{bmatrix}, \tag{3.3.2}$$

where $\mathbf{0} \in \mathbb{R}^{n\times n}$ is the zero matrix, and $\mathbf{I} \in \mathbb{R}^{n\times n}$ is the identity matrix. The input vector is $\mathbf{u}(t) = \mathbf{p} \in \mathbb{R}^{n\times 1}$.

Regarding the output variables that represent displacement, velocity, and acceleration, the following relationships are established:

$$\begin{cases} \mathbf{y}_1 = \mathbf{x}_1 \\ \mathbf{y}_2 = \mathbf{x}_2 \\ \mathbf{y}_3 = \mathbf{M}^{-1}(\mathbf{p} - \mathbf{C}\mathbf{x}_2 - \mathbf{K}\mathbf{x}_1). \end{cases}$$

Thus, the matrices $\mathbf{C} \in \mathbb{R}^{3n\times 2n}$ and $\mathbf{D} \in \mathbb{R}^{3n\times n}$ are:

$$\mathbf{C} = \begin{bmatrix} \mathbf{I} & \mathbf{0} \\ \mathbf{0} & \mathbf{I} \\ -\mathbf{M}^{-1}\mathbf{K} & -\mathbf{M}^{-1}\mathbf{C} \end{bmatrix}, \qquad \mathbf{D} = \begin{bmatrix} \mathbf{0} \\ \mathbf{0} \\ \mathbf{M}^{-1} \end{bmatrix}.$$

In such a way, the system represented by Eq. (3.3.1) has been reduced to the more general system of first-order ODEs described by Eq. (3.1.1).

SUBSECTION 3.3.2

Frequency Domain Representation

In this section, we derive the frequency domain representation of a MDoF system based on the previously established state-space formulation. Specifically, by applying the Laplace transform, we can facilitate the evaluation of system responses, which is particularly beneficial for various engineering applications. We begin by considering a linear system described by Eq. (3.1.1). Upon applying the Laplace transform to both equations, we obtain the following system:

$$\begin{cases} s\mathbf{X}(s) - \mathbf{X}(0) = \mathbf{A}\mathbf{X}(s) + \mathbf{B}\mathbf{U}(s) \\ \mathbf{Y}(s) = \mathbf{C}\mathbf{X}(s) + \mathbf{D}\mathbf{U}(s). \end{cases}$$

From here, using matrix properties, the first equation can be rewritten as:

$$(s\mathbf{I} - \mathbf{A})\mathbf{X}(s) = \mathbf{X}(0) + \mathbf{B}\mathbf{U}(s),$$

where the term $(s\mathbf{I} - \mathbf{A})$ represents an invertible matrix only if $s \neq \lambda_i$ for $i = 1, \ldots, n$[2]. By explicitly solving for $\mathbf{X}(s)$ and $\mathbf{Y}(s)$, the system becomes:

$$\begin{cases} \mathbf{X}(s) = (s\mathbf{I} - \mathbf{A})^{-1}\mathbf{X}(0) + (s\mathbf{I} - \mathbf{A})^{-1}\mathbf{B}\mathbf{U}(s) \\ \mathbf{Y}(s) = \mathbf{C}(s\mathbf{I} - \mathbf{A})^{-1}\mathbf{X}(0) + [\mathbf{C}(s\mathbf{I} - \mathbf{A})^{-1}\mathbf{B} + \mathbf{D}]\mathbf{U}(s). \end{cases}$$

Remark It is worth noting that the Laplace transforms of matrices previously introduced to obtain Eqs. (3.1.5)-(3.1.6) appear again here. Specifically:

- $\mathbf{\Phi}(t) := e^{\mathbf{A}t} \longrightarrow \mathcal{L}\{\mathbf{\Phi}(t)\} = \mathbf{\Phi}(s) = (s\mathbf{I} - \mathbf{A})^{-1}$
- $\mathbf{H}(t) := e^{\mathbf{A}t}\mathbf{B} \longrightarrow \mathcal{L}\{\mathbf{H}(t)\} = \mathbf{H}(s) = \mathbf{\Phi}(s)\mathbf{B}$
- $\mathbf{\Psi}(t) := \mathbf{C}e^{\mathbf{A}t} \longrightarrow \mathcal{L}\{\mathbf{\Psi}(t)\} = \mathbf{\Psi}(s) = \mathbf{C}\mathbf{\Phi}(s)$
- $\mathbf{W}(t) := \mathbf{C}e^{\mathbf{A}t}\mathbf{B} \longrightarrow \mathcal{L}\{\mathbf{W}(t)\} = \mathbf{W}(s) = \mathbf{C}\mathbf{\Phi}(s)\mathbf{B} + \mathbf{D}$.

Therefore, Eqs. (3.1.5)-(3.1.6) can be rewritten in the following form:

$$\begin{cases} \mathbf{X}(s) = \mathbf{\Phi}(s)\mathbf{X}(0) + \mathbf{H}(s)\mathbf{U}(s) = \mathbf{X}_l(s) + \mathbf{X}_f(s) \\ \mathbf{Y}(s) = \mathbf{\Psi}(s)\mathbf{X}(0) + \mathbf{W}(s)\mathbf{U}(s) = \mathbf{Y}_l(s) + \mathbf{Y}_f(s), \end{cases}$$

where the terms $\mathbf{\Phi}(s)\mathbf{X}(0)$ and $\mathbf{\Psi}(s)\mathbf{X}(0)$ correspond to the Laplace transforms of the free response of the state $\mathbf{X}_l(s)$ and the output $\mathbf{Y}_l(s)$, respectively. Similarly, the terms $\mathbf{H}(s)\mathbf{U}(s)$ and $\mathbf{W}(s)\mathbf{U}(s)$ represent the Laplace transforms of the forced responses $\mathbf{X}_f(s)$ and $\mathbf{Y}_f(s)$, respectively.

Section 3.4

Time Domain

---

[2] With λ_i representing the eigenvalues of matrix $\mathbf{A}$

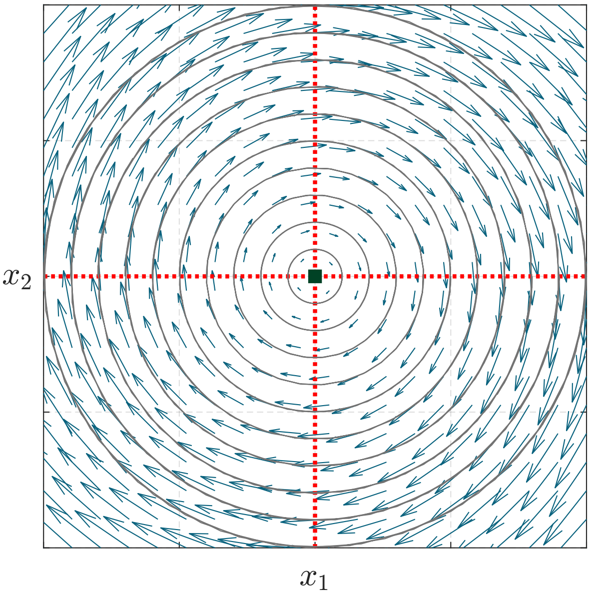

Figure 3.5. Phase portrait for undamped SDoF mechanical system.

In civil engineering, the analysis of commonly used linear dynamical systems can be effectively carried out in the time domain, using the previously introduced state-space representation. Below, we will demonstrate how this approach can be applied to the analysis of two SDoF systems, with and without viscous damping.

Subsection 3.4.1

Undamped SDoF System

Based on the formulation presented for the MDoF system (Section 3.3) we now consider a mechanical system in which there is no damping and where $n = 1$. This assumption reduces the model to a Single-Degree-of-Freedom (SDoF) system, simplifying the matrices $\mathbf{M}$, $\mathbf{K}$ to scalar quantities m and k, whereas the vectors $\ddot{\bar{\mathbf{u}}}$, $\dot{\bar{\mathbf{u}}}$, $\bar{\mathbf{u}}$ become scalar variables representing the mass's acceleration, velocity, and displacement.

Using Eq. (3.3.2), where $\omega^2 := \frac{k}{m}$ is the natural frequency of the system, we obtain:

$$\begin{bmatrix} \dot{x}_1 \\ \dot{x}_2 \end{bmatrix} = \begin{bmatrix} 0 & 1 \\ -\omega^2 & 0 \end{bmatrix} \begin{bmatrix} x_1 \\ x_2 \end{bmatrix}, \tag{3.4.1}$$

which in matrix form is:

$$\dot{\mathbf{x}} = \mathbf{A}\mathbf{x}.$$

The dynamics of this system is fully determined by Eq. (3.1.4), which is reported below for the reader convenience:

$$\mathbf{x}_l(t) = e^{\mathbf{A}(t-t_0)}\mathbf{x}_0.$$

By setting $t_0 = 0$, it is necessary to evaluate only the matrix exponential $e^{\mathbf{A}t}$ (Appendix A) to determine the system's dynamics for all possible initial conditions $\mathbf{x}_0$. To achieve this, we must evaluate the eigenvalues λ of the *state matrix* $\mathbf{A}$. In this case, we have:

$$\det(\lambda\mathbf{I} - \mathbf{A}) = \det\begin{bmatrix} \lambda & -1 \\ \omega^2 & \lambda \end{bmatrix} = \lambda^2 + \omega^2 = 0,$$

whose roots are:

$$\begin{cases} \lambda_1 = i\omega \\ \lambda_2 = -i\omega. \end{cases}$$

Thus, we obtain two complex conjugate eigenvalues, indicative of periodic solutions with a fixed-point in $[0, 0]^T$ as shown in Fig. 3.5.

To evaluate the eigenvectors, we need to solve the following system of linear equations:

$$(\lambda_1\mathbf{I} - \mathbf{A})\mathbf{u}_1 = \mathbf{0},$$

which can be rewritten as:

$$\begin{bmatrix} i\omega & -1 \\ \omega^2 & i\omega \end{bmatrix} \begin{bmatrix} u_{11} \\ u_{12} \end{bmatrix} = \begin{bmatrix} 0 \\ 0 \end{bmatrix}.$$

The two equations are linearly dependent therefore, by the Rouché-Capelli theorem, this system admits ∞^1 solutions. Assigning one of the unknowns as a fixed value, for example $u_{11} = 1$, we have:

$$\begin{cases} u_{11} = 1 \\ u_{12} = i\omega \end{cases} \rightarrow \mathbf{u}_1 = \begin{bmatrix} 1 \\ i\omega \end{bmatrix}.$$

To preserve the real form of the modal matrix containing the system's eigenvectors, we can rewrite the vector $\mathbf{u}_1$ as follows:

$$\mathbf{u}_1 = \mathbf{u}_a + i\mathbf{u}_b = \begin{bmatrix} 1 \\ 0 \end{bmatrix} + i \begin{bmatrix} 0 \\ \omega \end{bmatrix}.$$

Thus, the real modal matrix $\mathbf{U}_R$ is:

$$\mathbf{U}_R = \begin{bmatrix} \mathbf{u}_a & \mathbf{u}_b \end{bmatrix} = \begin{bmatrix} 1 & 0 \\ 0 & \omega \end{bmatrix},$$

while the real diagonal matrix of eigenvalues $\mathbf{\Lambda}_R$ is:

$$\mathbf{\Lambda}_R = \begin{bmatrix} 0 & \omega \\ -\omega & 0 \end{bmatrix} = \mathbf{U}_R^{-1}\mathbf{A}\mathbf{U}_R.$$

The inverse matrix $\mathbf{U}_R^{-1}$ is evaluated as:

$$\mathbf{U}_R^{-1} = \frac{1}{\det(\mathbf{U}_R)} \begin{pmatrix} \mathrm{Cof}(u_{11}) & \mathrm{Cof}(u_{12}) \\ \mathrm{Cof}(u_{21}) & \mathrm{Cof}(u_{22}) \end{pmatrix}^{\mathrm{T}}.$$

Hence, the inverse of the real modal matrix is:

Note that $\mathrm{Cof}(u_{ij}) = (-1)^{i+j}\det(U_{ij})$.

$$\mathbf{U}_R^{-1} = \begin{bmatrix} 1 & 0 \\ 0 & \frac{1}{\omega} \end{bmatrix}.$$

Finally, by using the properties of the matrix exponential (Appendix A), we obtain:

$$e^{\mathbf{A}t} = \mathbf{U}_R e^{\mathbf{\Lambda}_R t}\mathbf{U}_R^{-1} = \begin{bmatrix} 1 & 0 \\ 0 & \omega \end{bmatrix} \begin{bmatrix} \cos\omega t & \sin\omega t \\ -\sin\omega t & \cos\omega t \end{bmatrix} \begin{bmatrix} 1 & 0 \\ 0 & \frac{1}{\omega} \end{bmatrix},$$

which is:

$$e^{\mathbf{A}t} = \begin{bmatrix} \cos\omega t & \frac{1}{\omega}\sin\omega t \\ -\omega\sin\omega t & \cos\omega t \end{bmatrix}.$$

Given the matrix exponential, for any pair of initial conditions $\mathbf{x}_0$, the system's free response can be determined using Eq. (3.1.4) as:

$$\mathbf{x}(t) = e^{\mathbf{A}t}\mathbf{x}_0 = \begin{bmatrix} \cos\omega t & \frac{1}{\omega}\sin\omega t \\ -\omega\sin\omega t & \cos\omega t \end{bmatrix} \begin{bmatrix} x_1(0) \\ x_2(0) \end{bmatrix} =$$

$$= \begin{bmatrix} x_1(0)\cos\omega t + \frac{x_2(0)}{\omega}\sin\omega t \\ -\omega x_1(0)\sin\omega t + x_2(0)\cos\omega t \end{bmatrix}.$$

It is evident that the response in terms of displacement and velocity coincides with well-known results from the literature

[21].

Subsection 3.4.2

Damped SDoF System

Based on the formulation presented for the MDoF system (Section 3.3) we now consider a mechanical system with damping and where $n = 1$. This assumption reduces the model to a SDoF system, simplifying the matrices $\mathbf{M}$, $\mathbf{C}$, and $\mathbf{K}$ to scalar quantities m, c, and k, whereas the vectors $\ddot{\bar{\mathbf{u}}}$, $\dot{\bar{\mathbf{u}}}$, $\bar{\mathbf{u}}$ become scalar variables representing the mass's acceleration, velocity, and displacement.

Also in this case, by using Eq. (3.3.2), where $\omega^2 := \frac{k}{m}$ is the natural frequency of the system and $\zeta := \frac{c}{2m\omega}$ is the damping ratio, we obtain:

$$\begin{bmatrix} \dot{x}_1 \\ \dot{x}_2 \end{bmatrix} = \begin{bmatrix} 0 & 1 \\ -\omega^2 & -2\zeta\omega \end{bmatrix} \begin{bmatrix} x_1 \\ x_2 \end{bmatrix}, \tag{3.4.2}$$

which, in matrix form, becomes:

$$\dot{\mathbf{x}} = \mathbf{A}\mathbf{x}.$$

As in the undamped SDoF system, we evaluate the eigenvalues λ of the *state matrix* $\mathbf{A}$ for the current system by solving:

$$\det(\lambda\mathbf{I} - \mathbf{A}) = \det \begin{bmatrix} \lambda & -1 \\ \omega^2 & +2\zeta\omega + \lambda \end{bmatrix} = \lambda^2 + 2\zeta\omega\lambda + \omega^2 = 0,$$

whose roots are given by:

$$\lambda = \frac{-2\zeta\omega \pm \sqrt{4\zeta^2\omega^2 - 4\omega^2}}{2} = -\zeta\omega \pm \omega\sqrt{\zeta^2 - 1}.$$

Differently from the undamped system, here we can distinguish three cases depending on the value of the damping ratio ζ. Specifically, we have:

1. $\zeta > 1 \Rightarrow \lambda_1, \lambda_2 \in \mathbb{R}$ (overdamped system).
2. $\zeta = 1 \Rightarrow \lambda_1, \lambda_2 = \lambda \in \mathbb{R}$ (critically damped system).
3. $\zeta < 1 \Rightarrow \lambda_1, \lambda_2 \in \mathbb{C}$ (underdamped system).

We will now analyze each of these cases individually.

3.4.2.1 Overdamped System

When $\zeta > 1$, the system is referred to as *overdamped.* In this case, the eigenvalues of the system's *state matrix* $\mathbf{A}$ are:

$$\lambda_{1,2} = -\zeta\omega \pm \omega\sqrt{\zeta^2 - 1} \in \mathbb{R}.$$

The corresponding eigenvectors can be computed by solving the following systems of linear equations:

$$(\lambda_1 \mathbf{I} - \mathbf{A})\,\mathbf{u}_1 = 0 \;\rightarrow \begin{bmatrix} -\zeta\omega + \omega\sqrt{\zeta^2-1} & -1 \\ \omega & \zeta\omega + \omega\sqrt{\zeta^2-1} \end{bmatrix} \begin{bmatrix} u_{11} \\ u_{12} \end{bmatrix} = \begin{bmatrix} 0 \\ 0 \end{bmatrix}$$

$$\left(-\zeta\omega + \omega\sqrt{\zeta^2-1}\right) u_{11} = u_{12} \rightarrow \begin{cases} u_{11} = 1 \\ u_{12} = -\zeta\omega + \omega\sqrt{\zeta^2-1} \end{cases}$$

$$(\lambda_2 \mathbf{I} - \mathbf{A})\,\mathbf{u}_2 = 0 \;\rightarrow \begin{bmatrix} -\zeta\omega - \omega\sqrt{\zeta^2-1} & -1 \\ \omega & \zeta\omega - \omega\sqrt{\zeta^2-1} \end{bmatrix} \begin{bmatrix} u_{21} \\ u_{22} \end{bmatrix} = \begin{bmatrix} 0 \\ 0 \end{bmatrix}$$

$$\left(-\zeta\omega - \omega\sqrt{\zeta^2-1}\right) u_{21} = u_{22} \rightarrow \begin{cases} u_{21} = \frac{1}{-\zeta\omega + \omega\sqrt{\zeta^2-1}} \\ u_{22} = 1 \end{cases},$$

which correspond to the following eigenvectors:

$$\mathbf{u}_1 = \begin{bmatrix} 1 \\ \lambda_1 \end{bmatrix}, \quad \mathbf{u}_2 = \begin{bmatrix} \frac{1}{\lambda_2} \\ 1 \end{bmatrix}.$$

Based on these eigenvalues and eigenvectors, we can construct the diagonal eigenvalues matrix $\mathbf{\Lambda}$ and the modal matrix $\mathbf{U}$ as follows:

$$\mathbf{\Lambda} = \begin{bmatrix} \lambda_1 & 0 \\ 0 & \lambda_2 \end{bmatrix}, \qquad \mathbf{U} = [\mathbf{u}_1 \; \mathbf{u}_2] = \begin{bmatrix} 1 & \frac{1}{\lambda_2} \\ \lambda_1 & 1 \end{bmatrix}.$$

In this case, the matrix exponential can be evaluated using the following relation:

$$e^{\mathbf{A}t} = \mathbf{U} e^{\mathbf{\Lambda}t} \mathbf{U}^{-1},$$

and we will therefore need to compute the inverse matrix $\mathbf{U}^{-1}$, which is:

$$\mathbf{U}^{-1} = \frac{\lambda_2}{\lambda_2 - \lambda_1} \begin{bmatrix} 1 & -\frac{1}{\lambda_2} \\ -\lambda_1 & 1 \end{bmatrix}.$$

Finally, the matrix exponential is:

$$
\begin{aligned}
e^{\mathbf{A}t} &= \mathbf{U}e^{\mathbf{\Lambda}t}\mathbf{U}^{-1} = \\
&= \begin{bmatrix} 1 & 1/\lambda_2 \\ \lambda_1 & 1 \end{bmatrix} \begin{bmatrix} e^{\lambda_1 t} & 0 \\ 0 & e^{\lambda_2 t} \end{bmatrix} \begin{bmatrix} 1 & -1/\lambda_2 \\ -\lambda_1 & 1 \end{bmatrix} \frac{\lambda_2}{\lambda_2 - \lambda_1} = \\
&= \begin{bmatrix} \frac{\lambda_2}{\lambda_2-\lambda_1}e^{\lambda_1 t} - \frac{\lambda_1}{\lambda_2}\frac{\lambda_2}{\lambda_2-\lambda_1}e^{\lambda_2 t} & -\frac{1}{\lambda_1}\frac{\lambda_2}{\lambda_2-\lambda_1}e^{\lambda_1 t} + \frac{1}{\lambda_2}\frac{\lambda_2}{\lambda_2-\lambda_1}e^{\lambda_2 t} \\ \lambda_1\frac{\lambda_2}{\lambda_2-\lambda_1}e^{\lambda_1 t} - \lambda_1\frac{\lambda_2}{\lambda_2-\lambda_1}e^{\lambda_2 t} & -\frac{\lambda_1}{\lambda_2}\frac{\lambda_2}{\lambda_2-\lambda_1}e^{\lambda_1 t} + \frac{\lambda_2}{\lambda_2-\lambda_1}e^{\lambda_2 t} \end{bmatrix}.
\end{aligned}
$$

Once the matrix exponential is known, for any pair of initial conditions $\mathbf{x}_0$, applying Eq. (3.1.4), the free response of the system can be obtained as:

$$
\begin{aligned}
\mathbf{x}(t) &= e^{\mathbf{A}t}\mathbf{x}(0) = \\
&= \begin{bmatrix} \frac{\lambda_2}{\lambda_2-\lambda_1}e^{\lambda_1 t} - \frac{\lambda_1}{\lambda_2-\lambda_1}e^{\lambda_2 t} & -\frac{1}{\lambda_2-\lambda_1}e^{\lambda_1 t} + \frac{1}{\lambda_2-\lambda_1}e^{\lambda_2 t} \\ \frac{\lambda_1\lambda_2}{\lambda_2-\lambda_1}e^{\lambda_1 t} - \frac{\lambda_1\lambda_2}{\lambda_2-\lambda_1}e^{\lambda_2 t} & -\frac{\lambda_1}{\lambda_2-\lambda_1}e^{\lambda_1 t} + \frac{\lambda_2}{\lambda_2-\lambda_1}e^{\lambda_2 t} \end{bmatrix} \begin{bmatrix} x_1(0) \\ x_2(0) \end{bmatrix} = \\
&= \begin{bmatrix} \frac{\lambda_2 x_1(0)}{\lambda_2-\lambda_1}e^{\lambda_1 t} - \frac{\lambda_1 x_1(0)}{\lambda_2-\lambda_1}e^{\lambda_2 t} - \frac{x_2(0)}{\lambda_2-\lambda_1}e^{\lambda_1 t} + \frac{x_2(0)}{\lambda_2-\lambda_1}e^{\lambda_2 t} \\ \frac{\lambda_1\lambda_2 x_1(0)}{\lambda_2-\lambda_1}e^{\lambda_1 t} - \frac{\lambda_1\lambda_2 x_1(0)}{\lambda_2-\lambda_1}e^{\lambda_2 t} - \frac{\lambda_1 x_2(0)}{\lambda_2-\lambda_1}e^{\lambda_1 t} + \frac{\lambda_2 x_2(0)}{\lambda_2-\lambda_1}e^{\lambda_2 t} \end{bmatrix}.
\end{aligned}
$$

These expressions can be reformulated into the standard form commonly employed in the literature [21] to represent such solutions, as detailed below:

$$
\begin{aligned}
x_1(t) &= A_1 e^{\lambda_1 t} + A_2 e^{\lambda_2 t}, \\
x_2(t) &= \lambda_1 A_1 e^{\lambda_1 t} + \lambda_2 A_2 e^{\lambda_2 t},
\end{aligned}
$$

where:

$$
\begin{cases} A_1 = \frac{\lambda_2 x_1(0) - x_2(0)}{\lambda_2 - \lambda_1} \\ A_2 = \frac{x_2(0) - \lambda_1 x_1(0)}{\lambda_2 - \lambda_1}. \end{cases}
$$

3.4.2.2 Critically Damped System

When $\zeta = 1$, the system is referred to as *critically damped.* In this case, the eigenvalues of the *state matrix* $\mathbf{A}$ are:

$$
\lambda_1 = \lambda_2 = \lambda = -\omega \in \mathbb{R}.
$$

Here, we have a single eigenvalue with an algebraic multiplicity of 2. To verify whether a basis of eigenvectors can be constructed, we need to check the relationship between the algebraic and geometric multiplicities. Specifically, the geometric multiplicity is given by:

$$
m_{\mathrm{g}}(\lambda) = n - \mathrm{rk}\left(\lambda\mathbf{I} - \mathbf{A}\right),
$$

where n is the order of the *state matrix* $\mathbf{A}$. In this case, we have:

$$m_{\mathrm{g}}(\lambda) = 2 - \mathrm{rk}(\mathbf{A} - \lambda\mathbf{I}) = 2 - \mathrm{rk}\left(\begin{bmatrix} \omega & 1 \\ -\omega^2 & -\omega \end{bmatrix}\right) = 1.$$

Thus, the algebraic multiplicity $m_{\mathrm{a}}(\lambda) = 2$ differs from the geometric multiplicity $m_{\mathrm{g}}(\lambda) = 1$, indicating that the matrix $\mathbf{A}$ is not diagonalizable. Therefore, we need to work with generalized eigenvectors, through which we can construct the Jordan form of the matrix $\mathbf{A}$.

The Jordan form matrix $\mathbf{U}_J$ is an invertible matrix such that the following equality holds:

$$\mathbf{J} = \mathbf{U}_J^{-1}\mathbf{A}\mathbf{U}_J,$$

where the matrix $\mathbf{J}$ is the Jordan canonical form of the matrix $\mathbf{A}$. The Jordan canonical form of a square matrix is a triangular matrix $\mathbf{J}$, similar[3] to $\mathbf{A}$, that has a structure as close as possible to a diagonal matrix. The matrix is diagonal if and only if $\mathbf{A}$ is diagonalizable; otherwise, it is divided into Jordan blocks.

To compute the generalized eigenvectors, we evaluate the following generalized eigenspaces:

$$\begin{aligned} U_1 &= \left\{\mathbf{u} \in \mathbb{R}^2 : (\mathbf{A} - \lambda\mathbf{I})\mathbf{u} = \mathbf{0}\right\}, \\ U_1^2 &= \left\{\mathbf{u} \in \mathbb{R}^2 : (\mathbf{A} - \lambda\mathbf{I})^2\mathbf{u} = \mathbf{0}\right\}. \end{aligned}$$

From the eigenspace U_1 we obtain the following systems of equations:

$$(\mathbf{A} - \lambda\mathbf{I}) = \begin{bmatrix} 0 & 1 \\ -\omega^2 & -2\omega \end{bmatrix} + \begin{bmatrix} \omega & 0 \\ 0 & \omega \end{bmatrix} = \begin{bmatrix} \omega & 1 \\ -\omega^2 & -\omega \end{bmatrix},$$

which give the following eigenvectors:

$$\begin{bmatrix} \omega & 1 \\ -\omega^2 & -\omega \end{bmatrix} \begin{bmatrix} u_{11} \\ u_{12} \end{bmatrix} = \begin{bmatrix} 0 \\ 0 \end{bmatrix} \Rightarrow \begin{bmatrix} -\frac{1}{\omega} \\ 1 \end{bmatrix} \text{ and } \begin{bmatrix} 1 \\ -\omega \end{bmatrix}.$$

On the other hand, from the eigenspace U_1^2 we obtain:

$$(\mathbf{A} - \lambda\mathbf{I})^2 = \begin{bmatrix} \omega & 1 \\ -\omega^2 & -\omega \end{bmatrix} \begin{bmatrix} \omega & 1 \\ -\omega^2 & \omega \end{bmatrix} = \begin{bmatrix} 0 & 2\omega \\ 0 & -2\omega^2 \end{bmatrix},$$

which give the following eigenvector:

$$\begin{bmatrix} 0 & 2\omega \\ 0 & -2\omega^2 \end{bmatrix} \begin{bmatrix} u_{11} \\ u_{12} \end{bmatrix} = \begin{bmatrix} 0 \\ 0 \end{bmatrix} \Rightarrow \begin{bmatrix} 1 \\ 0 \end{bmatrix},$$

---

[3] In linear algebra, two $n \times n$ matrices $\mathbf{A}$ and $\mathbf{B}$ are called similar if there exists an invertible $n \times n$ matrix $\mathbf{P}$ such that $\mathbf{B} = \mathbf{P}^{-1}\mathbf{A}\mathbf{P}$.

from which we can construct the matrix $\mathbf{U}_J$ by identifying the Jordan chains as:

$$\begin{bmatrix} \omega & 1 \\ -\omega^2 & -\omega \end{bmatrix} \begin{bmatrix} 1 \\ 0 \end{bmatrix} = \begin{bmatrix} \omega \\ -\omega^2 \end{bmatrix}.$$

The resulting matrices are:

$$\mathbf{U}_J = \begin{bmatrix} \omega & 1 \\ -\omega^2 & 0 \end{bmatrix}, \quad \mathbf{U}_J^{-1} = \begin{bmatrix} 0 & -\frac{1}{\omega^2} \\ 1 & \frac{1}{\omega} \end{bmatrix}.$$

As a result, the Jordan canonical form of the matrix $\mathbf{A}$ is:

$$\begin{aligned} \mathbf{J} &= \mathbf{U}_J^{-1}\mathbf{A}\mathbf{U}_J = \\ &= \begin{bmatrix} 0 & -\frac{1}{\omega^2} \\ 1 & \frac{1}{\omega} \end{bmatrix} \begin{bmatrix} 0 & 1 \\ -\omega^2 & -2\omega \end{bmatrix} \begin{bmatrix} \omega & 1 \\ -\omega^2 & 0 \end{bmatrix} = \begin{bmatrix} -\omega & 1 \\ 0 & -\omega \end{bmatrix}. \end{aligned}$$

In this case, the matrix exponential is computed using the following relation:

$$\mathbf{e}^{\mathbf{A}t} = \mathbf{U}_J \mathbf{e}^{\mathbf{J}t} \mathbf{U}_J^{-1},$$

and thus we need to compute the matrix exponential of $\mathbf{J}$, that is:

$$\mathbf{e}^{\mathbf{J}t} = \begin{bmatrix} e^{-\omega t} & te^{-\omega t} \\ 0 & e^{-\omega t} \end{bmatrix}.$$

Finally, the matrix exponential of the system is:

$$\begin{aligned} \mathbf{e}^{\mathbf{A}t} &= \mathbf{U}_J \mathbf{e}^{\mathbf{J}t} \mathbf{U}_J^{-1} = \begin{bmatrix} \omega & 1 \\ -\omega^2 & 0 \end{bmatrix} \begin{bmatrix} e^{-\omega t} & te^{-\omega t} \\ 0 & e^{-\omega t} \end{bmatrix} \begin{bmatrix} 0 & -\frac{1}{\omega^2} \\ 1 & \frac{1}{\omega} \end{bmatrix} = \\ &= \begin{bmatrix} \omega te^{-\omega t} + e^{-\omega t} & -\frac{1}{\omega}e^{-\omega t} + te^{-\omega t} + \frac{1}{\omega}e^{-\omega t} \\ -\omega^2 + e^{-\omega t} & e^{-\omega t} - \omega te^{-\omega t} \end{bmatrix}. \end{aligned}$$

With the matrix exponential known, for any initial conditions $\mathbf{x}_0$, by applying Eq. (3.1.4) we obtain the free response of the system as:

$$\begin{aligned} \mathbf{x}(t) &= \mathbf{e}^{\mathbf{A}t}\mathbf{x}_0 = \\ &= \begin{bmatrix} \omega te^{-\omega t} + e^{-\omega t} & -\frac{1}{\omega}e^{-\omega t} + te^{-\omega t} + \frac{1}{\omega t}e^{\omega t} \\ -\omega^2 + e^{-\omega t} & e^{-\omega t} - \omega te^{-\omega t} \end{bmatrix} \begin{bmatrix} x_1(0) \\ x_2(0) \end{bmatrix} \\ &= \begin{bmatrix} \left\{x_1(0) + t\left[\omega x_1(0) + x_2(0)\right]\right\} e^{-\omega t} \\ \left\{x_2(0) - t\left[\omega^2 x_1(0) + x_2(0)\omega\right]\right\} e^{-\omega t} \end{bmatrix}, \end{aligned}$$

which correspond to the solutions commonly found in the literature [21].

3.4.2.3 Underdamped System

When $0 < \zeta < 1$, the system is referred to as *underdamped.* In this case, the eigenvalues of the *state matrix* $\mathbf{A}$ are complex conjugates and equal to:

$$\lambda_{1,2} = -\zeta\omega \pm i\omega\sqrt{1-\zeta^2} \in \mathbb{C}.$$

The associated eigenvectors are found, as in the case of the undamped system, by solving the following system of linear equations:

$$(\lambda_1 \mathbf{I} - \mathbf{A})\,\mathbf{u}_1 = \mathbf{0}.$$

This can be rewritten as follows:

$$\begin{bmatrix} \lambda_1 & -1 \\ \omega^2 & +2\zeta - \omega + \lambda_1 \end{bmatrix} \begin{bmatrix} u_{11} \\ u_{12} \end{bmatrix} = \begin{bmatrix} 0 \\ 0 \end{bmatrix}.$$

The two equations that make up this system are linearly dependent. Therefore, according to the Rouché-Capelli theorem, the system admits ∞^1 solutions. Assigning one of the two unknowns as a fixed parameter, for example $u_{11} = 1$, we obtain:

$$\mathbf{u}_1 = \begin{bmatrix} 1 \\ -\zeta\omega + i\omega\sqrt{1-\zeta^2} \end{bmatrix}.$$

As in the case of the undamped system, in order to preserve the real form of the modal matrix, we can rewrite the vector $\mathbf{u}_1$ as follows:

$$\mathbf{u}_1 = \mathbf{u}_a + i\mathbf{u}_b = \begin{bmatrix} 1 \\ -\zeta\omega \end{bmatrix} + i \begin{bmatrix} 0 \\ \Omega \end{bmatrix},$$

where $\Omega = \omega\sqrt{1-\zeta^2}$. In such a way, the real modal matrix $\mathbf{U}_R$ is:

$$\mathbf{U}_R = \begin{bmatrix} \mathbf{u}_a & \mathbf{u}_b \end{bmatrix} = \begin{bmatrix} 1 & 0 \\ -\zeta\omega & \Omega \end{bmatrix},$$

whereas the real diagonal eigenvalue matrix $\mathbf{\Lambda}_R$ is:

$$\mathbf{\Lambda}_R = \begin{bmatrix} -\zeta\omega & \Omega \\ -\Omega & -\zeta\omega \end{bmatrix} = \mathbf{U}_R^{-1}\mathbf{A}\mathbf{U}_R.$$

The inverse matrix $\mathbf{U}_R^{-1}$ is calculated as in the previous cases and is:

$$\mathbf{U}_R^{-1} = \begin{bmatrix} 1 & 0 \\ \frac{\zeta\omega}{\Omega} & \frac{1}{\Omega} \end{bmatrix}.$$

Once again, using the properties of the matrix exponential (Appendix A), we have:

$$
\begin{aligned}
e^{\mathbf{A}t} &= \mathbf{U}_R e^{\mathbf{\Lambda}_R t} \mathbf{U}_R^{-1} = \\
&= e^{-\zeta\omega t} \begin{bmatrix} 1 & 0 \\ -\zeta\omega & \Omega \end{bmatrix} \begin{bmatrix} \cos\Omega t & \sin\Omega t \\ -\sin\Omega t & \cos\Omega t \end{bmatrix} \begin{bmatrix} 1 & 0 \\ \frac{\zeta\omega}{\Omega} & \frac{1}{\Omega} \end{bmatrix} = \\
&= e^{-\zeta\omega t} \begin{bmatrix} \cos\Omega t + \frac{\zeta\omega}{\Omega}\sin\Omega t & \frac{1}{\Omega}\sin\Omega t \\ -\Omega\sin\Omega t - \frac{(\zeta\omega)^2}{\Omega}\sin\Omega t & -\frac{\zeta\omega}{\Omega}\sin\Omega t + \cos\Omega t \end{bmatrix}.
\end{aligned}
$$

Now, knowing the matrix exponential, for any initial condition $\mathbf{x}_0$, by applying Equation (3.1.4), it is possible to obtain the free response of the system as:

$$
\begin{aligned}
&\mathbf{x}(t) = e^{\mathbf{A}t}\mathbf{x}_0 = \\
&= \begin{bmatrix} e^{-\zeta\omega t}\left\{x_1(0)\cos\Omega t + \left[\frac{x_2(0)+x_1(0)\zeta\omega}{\Omega}\right]\sin\Omega t\right\} \\ e^{-\zeta\omega t}\left\{x_2(0)\cos\Omega t - \left[\Omega x_1(0) + \frac{(\zeta\omega)^2}{\Omega}x_1(0) + \frac{\zeta\omega}{\Omega}x_2(0)\right]\sin\Omega t\right\} \end{bmatrix}.
\end{aligned}
$$

Note how the response in terms of displacement and velocity matches the widely known results in the literature [21].

SECTION 3.5

Frequency Domain

In this section, we show how the analysis of dynamical systems commonly encountered in civil engineering is systematically conducted in the frequency domain, employing the previously introduced Laplace transforms and their inverses. The subsequent discussion illustrates how this approach simplifies the analysis of the SDoF systems examined earlier. Each step of the process is detailed to elucidate how the same results are obtained through this frequency-domain methodology.

SUBSECTION 3.5.1

Undamped SDoF System

By recalling the results presented in Section 3.4.1 and applying the methodology discussed in Section 3.3.2, we derive that for the undamped system described by Eq. (3.4.1), the matrix $\mathbf{\Phi}(s)$ is given by:

$$
\mathbf{\Phi}(s) = \frac{1}{s^2+\omega^2} \begin{bmatrix} s & 1 \\ -\omega^2 & s \end{bmatrix}.
$$

Thus, recalling that:

$$\mathbf{\Phi}(t) = e^{\mathbf{A}t} = \mathcal{L}^{-1}\left\{\mathbf{\Phi}(s)\right\},$$

and using the *Residue Theorem* seen in Section 3.2.2, we obtain the exponential matrix as:

$$e^{\mathbf{A}t} = \begin{bmatrix} \cos(\omega\, t) & \frac{\sin(\omega\, t)}{\omega} \\ -\omega\,\sin(\omega\, t) & \cos(\omega\, t) \end{bmatrix}.$$

The obtained result matches the expression found in Section 3.4.1. Additionally, recalling that $\mathbf{X}_l(s) = \mathbf{\Phi}(s)\mathbf{X}(0)$, we can easily obtain the free response of the system as:

$$\mathbf{x}(t) = \mathcal{L}^{-1}\left\{\mathbf{X}_l(s)\right\} = \begin{bmatrix} x_1(0)\,\cos(\omega\, t) + \frac{x_2(0)}{\omega}\,\sin(\omega\, t) \\ -\omega\, x_1(0)\,\sin(\omega\, t) + x_2(0)\,\cos(\omega\, t) \end{bmatrix}.$$

These solutions coincide with those obtained in the time domain but are simpler to derive, as they do not require solving differential equations directly.

Subsection 3.5.2

Damped SDoF System

By recalling the results presented in Section 3.4.2 and applying the methodology discussed in Section 3.3.2, we derive that for the damped system described by Eq. (3.4.2), the matrix $\mathbf{\Phi}(s)$ is given by:

$$\mathbf{\Phi}(s) = \frac{1}{s^2 + 2\zeta\omega s + \omega^2}\begin{bmatrix} s + 2\zeta\omega & 1 \\ -\omega^2 & s \end{bmatrix}.$$

Thus, the system's displacement response in the frequency domain is:

$$X_1(s) = \frac{X_2(0) + 2\zeta\omega X_1(0) + sX_1(0)}{s^2 + 2\zeta\omega s + \omega^2}.$$

To return to the time domain and obtain $x_1(t)$, it is necessary to perform the inverse Laplace transform of the rational complex function $X_1(s)$. Specifically, this process depend on the *poles* of $X_1(s)$, which are:

$$s = -\zeta\omega \pm \omega\sqrt{\zeta^2 - 1}.$$

Once again, we can distinguish three cases depending on the value of ζ. Specifically, we have:

1. $\zeta > 1 \Rightarrow$ real and distinct poles.
2. $\zeta = 1 \Rightarrow$ real and coincident poles.
3. $\zeta < 1 \Rightarrow$ complex conjugate poles.

3.5.2.1 Overdamped Systems

When $\zeta > 1$ we are once again dealing with an *overdamped* system. In this case, the poles of the function $X_1(s)$ are:

$$p_{1,2} = -\zeta\omega \pm \omega\sqrt{\zeta^2 - 1}.$$

By expressing the function in partial fractions, we have:

$$\begin{aligned} X_1(s) &= \frac{X_2(0) + 2\zeta\omega X_1(0) + sX_1(0)}{(s-p_1)(s-p_2)} = \\ &= \frac{A}{s-p_1} + \frac{B}{s-p_2} = \frac{A(s-p_2) + B(s-p_1)}{(s-p_1)(s-p_2)}, \end{aligned}$$

where

$$A = \frac{p_2 X_1(0) - X_2(0)}{p_2 - p_1}, \quad B = \frac{X_2(0) - p_1 X_1(0)}{p_2 - p_1}.$$

The system's response in the time domain is obtained by taking the inverse Laplace transform of the previous expression:

$$\begin{aligned} x_1(t) &= \mathcal{L}^{-1}\left\{\frac{A}{s-p_1}\right\} + \mathcal{L}^{-1}\left\{\frac{B}{s-p_2}\right\} = Ae^{p_1 t} + Be^{p_2 t} = \\ &= \frac{p_2 x_1(0) - x_2(0)}{p_2 - p_1} e^{p_1 t} + \frac{x_2(0) - p_1 x_1(0)}{p_2 - p_1} e^{p_2 t}. \end{aligned}$$

3.5.2.2 Critically Damped System

When $\zeta = 1$ we are once again dealing with a *critically damped* system. In this case, the poles of the function $X_1(s)$ are:

$$p_{1,2} = p = -\omega.$$

Expressing the function in partial fractions gives:

$$\begin{aligned} X_1(s) &= \frac{X_2(0) + 2\zeta\omega X_1(0) + sX_1(0)}{(s-p)^2} = \\ &= \frac{A_1}{(s-p)^2} + \frac{A_2}{(s-p)} = \frac{A_1 + A_2 s - A_2 p}{(s-p)^2}, \end{aligned}$$

where

$$A_1 = X_2(0) + \omega X_1(0), \quad A_2 = X_1(0).$$

The system's response in the time domain is obtained by taking the inverse Laplace transform of the previous expression as follows:

$$\begin{aligned} x_1(t) &= \mathcal{L}^{-1}\left\{\frac{A_1}{(s-p)^2}\right\} + \mathcal{L}^{-1}\left\{\frac{A_2}{(s-p)}\right\} = \\ &= A_1 e^{pt} t + A_2 e^{pt} = (A_1 t + A_2)\, e^{pt} = \\ &= [x_2(0)t + \omega t x_1(0) + x_1(0)]\, e^{-\omega t}. \end{aligned}$$

3.5.2.3 Underdamped System

Finally, when $\zeta < 1$, we are once again dealing with an *underdamped* system. In this case, the poles of the function $X_1(s)$ are:

$$p_{1,2} = -\zeta\omega \pm i\omega\sqrt{1-\zeta^2}.$$

Expressing the function in partial fractions, we have:

$$X_1(s) = \frac{sX_1(0) + X_2(0) + 2\zeta\omega X_1(0)}{s^2 + 2\zeta\omega s + \omega^2} = \frac{As + B}{[(s+\alpha)^2 + \Omega^2]}.$$

By imposing

$$s^2 + 2\zeta\omega s + \omega^2 = s^2 + 2\alpha s + \alpha^2 + \Omega^2,$$

we obtain:

$$\alpha = \zeta\omega, \quad \Omega = \omega\sqrt{1-\zeta^2},$$

and thus the expression for $X_1(s)$ becomes:

$$X_1(s) = \frac{As + B}{[(s+\zeta\omega)^2 + \Omega^2]},$$

where

$$A = X_1(0), \quad B = X_2(0) + 2\zeta\omega X_1(0).$$

The system's response in the time domain is obtained by simply taking the inverse Laplace transform of the previous expression as follows:

$$\begin{aligned} x_1(t) &= \mathcal{L}^{-1}\left\{\frac{X_1(0)(s+\zeta\omega-\zeta\omega)}{[(s+\zeta\omega)^2+\Omega^2]}\right\} + \mathcal{L}^{-1}\left\{\frac{\Omega}{\Omega}\,\frac{X_2(0)+2\zeta\omega X_1(0)}{[(s+\zeta\omega)^2+\Omega^2]}\right\} = \\ &= e^{-\zeta\omega t}\left[x_1(0)\cos(\Omega t) + \frac{x_2(0)+\zeta\omega x_1(0)}{\Omega}\sin(\Omega t)\right]. \end{aligned}$$

It is noteworthy that the same results achieved in the time domain (Section 3.4) are obtained here through a significantly simpler approach, without the need to directly solve the differential equation governing the problem.

CHAPTER

4

Nonlinear Dynamical Systems

On dira que la science n'est qu'une classification et qu'une classification ne peut être vraie, mais seulement commode. Mais il est certain qu'elle est commode, qu'elle l'est non seulement pour moi, mais pour tous les hommes; il est vrai enfin que tout cela ne peut pas être seulement par hasard.

— Jules Henri Poincaré

In linear systems, the whole is quite simply the sum of the parts. But the world is not linear. While many systems behave approximately linearly for small displacements, all systems are bounded by natural constraints (the length of a spring, the size of the system) and cannot maintain linearity to all levels of excitation. Some systems are fundamentally nonlinear, even for their smallest excursions. And when these systems have several degrees of freedom, most of the intuition and mathematical tools we use for linear systems no longer apply, and an entirely new toolbox is needed to understand these types of systems [64].

This chapter provides a comprehensive exploration of nonlinear dynamical systems, beginning with a comprehensive framework that underpins the study of such systems. It encompasses a variety of topics, including smooth nonlinear dynamics and the behavior of one-dimensional, two-dimensional, and three-dimensional flows. The discussion extends to periodic solutions and Poincaré maps, as well as bifurcation theory, which are essential for understanding the stability and transitions within these systems.

Furthermore, the chapter delves into the realm of non-smooth nonlinear dynamical systems, with a particular focus on hysteretic mechanical systems. It examines mathematical modeling techniques for hysteresis, including the Vaiana-Rosati model, and introduces Poincaré map based continuation methods to analyze system behavior. Finally, the chapter concludes with an investigation of the energy components in hysteretic systems, offering insights into their dynamic responses.

SECTION 4.1

A Framework for Nonlinear Dynamical Systems

Our objective is to delineate the logical structure that underpins the study of nonlinear dynamical systems. Specifically, we will use the theoretical framework proposed by [80] to guide our analysis, focusing on the number of variables necessary to characterize the system's state, which corresponds to the dimension of the state-space. This approach is particularly pertinent in nonlinear systems, as increasing the state-space dimension from $n = 1$ to $n \geq 3$ introduces distinct phenomena at each level: for $n = 1$, we observe fixed-points and their bifurcations; for $n = 2$, nonlinear oscillations may also arise; and for $n \geq 3$, complex behaviors such as chaos and fractals emerge. In this context, a geometric approach proves to be highly effective, offering significant insights even when explicit solutions to the differential equations are not available (see Table 4.1).

Furthermore, the proposed framework encompasses a frontier of topics that, while not entirely uncharted, delineate the limits of current understanding. Notably, research has demonstrated that *non-smooth* dynamical models exhibit a broader spectrum of possible behaviors compared to *smooth* models. Some of these behaviors arise specifically when considering discontinuous ODEs [74]. The inherent complexity of such problems, coupled with their nonlinear and *non-smooth* characteristics, will persist in presenting significant challenges for future research endeavors.

Table 4.1. Nonlinear system signatures [64].

Breakdown of linear superposition
Exponential sensitivity to initial conditions
Sudden discontinuous changes (thresholds, jumps, bifurcations, intermittency)
Amplitude-frequency coupling, frequency entrainment or phase locking (synchronization)
Hysteresis
Order within chaos (islands of stability)
Self-similarity (fractals and scaling)
Emergence (large-scale structure/order arising from local interactions among many parts)

SECTION 4.2

Smooth Nonlinear Dynamical Systems

In Chapter 2, we introduced the general system:

$$\dot{\mathbf{x}} = \mathbf{f}(\mathbf{x}), \tag{4.2.1}$$

where $\mathbf{x} \in \mathbb{R}^n$ is the state vector and $\mathbf{f} : \mathbb{R}^n \times \mathbb{R} \to \mathbb{R}^n$ is a nonlinear smooth vector field $\mathbf{f} \in C^2$. The solutions of this system can be visualized as trajectories flowing through an n-dimensional state-space with coordinates $[x_1, \ldots, x_n]^T$.

SUBSECTION 4.2.1

One-dimensional Flows

Before addressing the more complex cases, we begin with the simplest scenario for Eq. (4.2.1), where $n = 1$. This results in a single equation of the following form:

$$\dot{x} = f(x).$$

In this context, $x : t \to x(t)$ represents a real-valued function of time t, whereas f denotes a smooth, real-valued nonlinear function of x. To clarify terminology, the term "system" is used here in the context of a dynamical system, rather than in the classical sense of a collection of two or more equations. Consequently, a single equation may also be considered a "system" [80].

One-dimensional (1D) dynamical systems, although seemingly simple, exhibit behaviors that can be generalized to higher dimensions, including two-dimensions and beyond. For instance, the identification of fixed-points within a 1D system underscores the significance of linearization and the classification of these fixed-points [64]. When the function equals zero, we have:

$$\dot{x} = f(x^*) = 0,$$

indicating that the position x^* defines a fixed-point of the flow. At this point, the time rate of change of the variable is zero, suggesting that the system cannot move away from this fixed-point (Section 2.4). However, it is essential to assess the stability of the fixed-point. To address this, the system is linearized around the fixed-point using the expression:

$$f(x) = f(x^*) + (x - x^*)f^{'}(x^*) + \ldots,$$

where $f(x^*) = 0$. To the lowest order, this simplifies to:

$$f(x) \approx (x - x^*)f^{'}(x^*).$$

By introducing the change of variable $\eta = x - x^*$, the differential equation becomes:

$$\dot{\eta} \approx f^{'}\eta,$$

which has the solution:

$$\eta(t) = \eta(0)e^{\lambda t},$$

where:

$$\lambda = \left.\frac{df(x)}{dx}\right|_{x^*},$$

is referred to as the *Lyapunov exponent*. This leads to a classification based on the value of λ:

$\lambda < 0$ Stable Node (Attractor)
$\lambda > 0$ Unstable Node (Repellor).

In the case of a stable node, small perturbations are contrasted by a restoring force, similar to the behavior of a spring, whereas for an unstable node, small perturbations are amplified, leading to positive feedback.

Example

Consider a mass m immersed in a vat of highly viscous fluid, experiencing a damping force represented by $c\dot{u}$. According to Newton's law, the governing equation for this system is expressed as:

$$m\ddot{u} + c\dot{u} = p(u).$$

In scenarios where the viscous damping is significantly stronger than the inertial effect, (i.e., when $c\dot{u} \gg m\ddot{u}$), the system can be approximated by the equation:

$$c\dot{u} = p(u),$$

which can be rearranged to yield:

$$\dot{u} = \frac{p(u)}{c} = f(u).$$

In this overdamped limit, the dynamics of the mechanical system become clear. The mass tends to settle at a stable

> equilibrium point, characterized by the conditions $f(u) = 0$ and $f^{'}(u) < 0$. When the mass is slightly displaced from this equilibrium position, it is gradually returned to equilibrium by the restoring force, reflecting a slow response due to the high damping. Notably, no overshoot occurs, as the extensive damping prevents any oscillatory behavior. Consequently, undamped oscillations are not a viable possibility under these conditions.

SUBSECTION 4.2.2

Two-dimensional Flows

Two-dimensional (2D) dynamical systems present more interesting and complex behaviors than those found in 1D systems. The governing equations remain relatively simple, whereas the visual representations facilitate a more comprehensive understanding of the system's dynamics. Moreover, 2D systems are particularly important as they establish a clear contrast to the behaviors exhibited by dynamical systems in three dimensions and higher. This contrast not only deepens our understanding of dynamical behavior but also serves as a foundational framework for the exploration of more complex, higher-dimensional systems.

Consider a 2D dynamical system described by the following equations:

$$\begin{cases} \dot{x}_1 = f_1\left(x_1, x_2\right) \\ \dot{x}_2 = f_2\left(x_1, x_2\right). \end{cases}$$

Let us denote the fixed-point of this system as $\mathbf{x}^* \equiv [a, b]^T$, where we have $f_1(a, b) = f_2(a, b) = 0$ (Section 2.4). To analyze the behavior of small disturbances from the fixed-point, we define the perturbations as follows:

$$\delta x_1 = x_1 - a, \quad \delta x_2 = x_2 - b.$$

Next, we examine the time derivative of δx_1 to determine the evolution of this disturbance in time:

$$\dot{\delta x_1} = \frac{d}{dt}(\delta x_1) = \dot{x}_1,$$

where a is treated as a constant. Substituting the expression for δx_1, we obtain:

$$\dot{\delta x_1} = f_1(a + \delta x_1, b + \delta x_2).$$

By applying a Taylor series expansion around the fixed point, we derive the following expression:

$$\dot{\delta x_1} = f_1(a,b) + \left.\frac{\partial f_1}{\partial x_1}\right|_{\mathbf{x}^*} \delta x_1 + \left.\frac{\partial f_1}{\partial x_2}\right|_{\mathbf{x}^*} \delta x_2 + \dots$$

Similarly, for δx_2, we have:

$$\dot{\delta x_2} = f_2(a,b) + \left.\frac{\partial f_2}{\partial x_1}\right|_{\mathbf{x}^*} \delta x_1 + \left.\frac{\partial f_2}{\partial x_2}\right|_{\mathbf{x}^*} \delta x_2 + \dots$$

Consequently, the disturbances evolve according to the following differential system:

$$\begin{bmatrix} \dot{\delta x_1} \\ \dot{\delta x_2} \end{bmatrix} = \begin{bmatrix} \frac{\partial f_1}{\partial x_1} & \frac{\partial f_1}{\partial x_2} \\ \frac{\partial f_2}{\partial x_1} & \frac{\partial f_2}{\partial x_2} \end{bmatrix}_{\mathbf{x}^*} \begin{bmatrix} \delta x_1 \\ \delta x_2 \end{bmatrix} + \dots$$

In matrix form, this can be expressed as:

$$\dot{\boldsymbol{\delta}} = \mathbf{J}\boldsymbol{\delta} + \dots,$$

where $\mathbf{J}$ is defined as the *Jacobian matrix* at the fixed-point $\mathbf{x}^*$. By neglecting higher-order terms, we arrive at the linearized system:

$$\dot{\boldsymbol{\delta}} = \mathbf{J}\boldsymbol{\delta}. \tag{4.2.2}$$

The dynamics of the system described by Eq. (4.2.2) can be analyzed by seeking solutions of the form:

$$\boldsymbol{\delta} = e^{\lambda t}\mathbf{v}.$$

Substituting this expression into Eq. (4.2.2) yields:

$$(\mathbf{J} - \lambda\mathbf{I})\,\mathbf{v} = \mathbf{0},$$

indicating that solutions exist if $\mathbf{v}$ is an *eigenvector* of $\mathbf{J}$ corresponding to the *eigenvalue* λ. In general, the eigenvalues of the matrix $\mathbf{J}$ are determined by the characteristic equation:

$$\det(\mathbf{J} - \lambda\mathbf{I}) = 0,$$

which simplifies to:

$$\lambda^2 - \mathrm{tr}(\mathbf{J})\lambda + \det(\mathbf{J}) = 0.$$

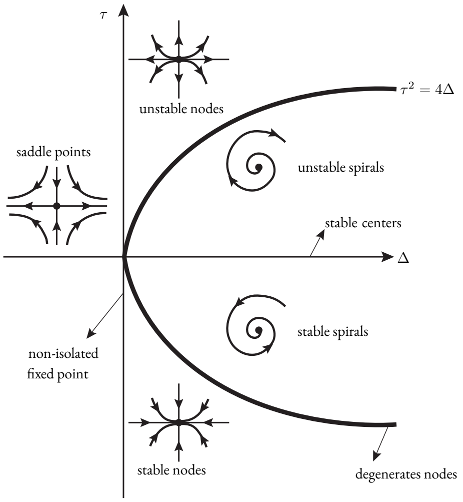

Figure 4.1. Equilibrium type as a function of the trace (τ) and determinant (Δ) of the Jacobian matrix evaluated near a fixed-point.

4.2.2.1 Classification of fixed-points

We can show the type and stability of all the different fixed-points on a single diagram (Fig. 4.1). To arrive at Fig. 4.1 we need the following formulas:

$$\lambda_{1,2} = \frac{\tau \pm \sqrt{\tau^2 - 4\Delta}}{2},$$

where $\tau = \mathrm{tr}(\mathbf{J})$ and $\Delta = \det(\mathbf{J})$. In fact, we can observe that:

- $\Delta < 0$, the eigenvalues are real and have opposite signs ($\lambda_2 < 0 < \lambda_1$); hence, the fixed-point is a *saddle node.*
- $\Delta > 0$, the eigenvalues are either real with the same sign (*node*), or complex conjugate (*spirals* and *centers*). In particular, *nodes* satisfy $\tau^2 > 4\Delta$, and *spirals* satisfy $\tau^2 < 4\Delta$.
- $\Delta = 0$, at least one of the eigenvalues is zero. Then points on the vertical line at the origin, in the (Δ, τ) plane are not isolated fixed-points.
- The points on the parabola $\tau^2 - 4\Delta = 0$ are the borderline between nodes and spirals; on this line we have the degenerate nodes.

The stability of the nodes and spirals is determined by τ:

- $\tau < 0$, both eigenvalues have negative real parts, so the fixed-point is *stable.*

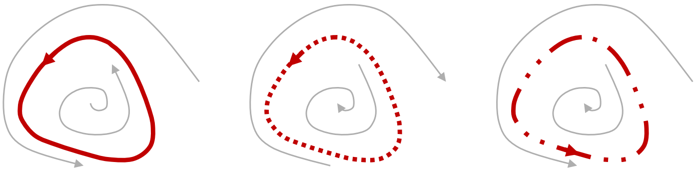
(a) (b) (c)

Figure 4.2. Limit cycles: Stable (a), unstable (b), and half-stable (c) [80].

- $\tau > 0$, the fixed-point is *unstable*.
- $\tau = 0$, here the eigenvalue are purely imaginary, and we have *stable centers*.

Centers, stars, degenerate nodes, and non-isolated fixed-points are *borderline cases* that occur along the curves in the (Δ, τ)-plane. Of these borderline cases, centers are by far the most important, since they occur very commonly in conservative mechanical systems. If $\operatorname{Re}(\lambda) \neq 0$ for both eigenvalues, the fixed-point is often called *hyperbolic*. Hyperbolic fixed-points are sturdy; their stability type is not affected by small nonlinear terms. On the other hand, *non-hyperbolic* fixed-points have brittle stability.

These ideas have also been generalized to higher-order systems.

Definition 5 A fixed-point of an n^{th} order system is *hyperbolic* if all the eigenvalues of the linearization lie off the imaginary axis, i.e., $\operatorname{Re}(\lambda_i) \neq 0$ for $i = 1, \ldots, n$.

4.2.2.2 Limit Cycles

Fixed-points are not the only possible steady-state solutions in a dynamical system. A 2D (or higher) system may also exhibit repetitive oscillations or orbits, known as *limit cycles*.

Definition 6 A limit cycle is defined as an isolated closed trajectory, where isolated means that nearby trajectories are not closed but instead spiral either toward or away from the limit cycle.

In a 2D system, limit cycles can be classified into three types, as illustrated in Fig. 4.2: *stable*, *unstable*, and *saddle limit cycles*. A stable limit cycle attracts neighboring trajectories, while an unstable limit cycle repels them. The saddle limit cycle[4], which is relatively rare, attracts trajectories on one side

[4] In some cases they are also called *half-stable* limit cycles [80]

and repels them on the other [64].

Stable limit cycles are of significant scientific importance, particularly in modeling systems that exhibit self-sustained oscillations. In structural dynamics, for example, they are associated with potentially dangerous self-excited vibrations, such as those occurring in bridges or airplane wings. In these scenarios, the system tends to oscillate with a characteristic period, waveform, and amplitude. Even when subjected to small perturbations, the system returns to its standard cycle, illustrating the robustness of the stable limit cycle.

Remark Limit cycles are inherently nonlinear phenomena. They can't occur in linear systems. Of course, a linear system $\dot{\mathbf{x}} = \mathbf{A}\mathbf{x}$ can have closed orbits, but they won't be isolated (Section 3.4.1). In fact, if $\mathbf{x}(t)$ is a periodic solution, then so is $c\mathbf{x}(t)$ $\forall c \neq 0$. Hence, $\mathbf{x}(t)$ is surrounded by a one-parameter family of closed orbits (see Fig. 3.5). Consequently, the amplitude of a linear oscillation is set entirely by its initial conditions, any slight disturbance to the amplitude will persist forever. In contrast, limit cycle oscillations are determined by structure of the system itself. Normally it's difficult to tell whether a given system has a limit cycle, or indeed any closed orbits, from the governing equations alone.

Subsection 4.2.3

Three-dimensional Flows

The behavior of nonlinear dynamical systems changes dramatically when going from 2D to 3D state-space. Dynamic systems are subjected to non-crossing theorem, which states that no trajectory can cross itself (in finite time). However, in a 3D state-space there is plenty of "room" for trajectories to move above and below and around other trajectories without intersecting. Hence, the addition of a third dimension opens the possibility for chaotic behaviors. Because the transition to chaos occurs in the transition from 2D to 3D, the most “interesting” chaotic systems tend to have low dimensionality of three or four dimensions. These systems can totter on the edge of chaos, and are tipped into or out of chaos depending on the parameters defining the dynamics. In systems of high dimension, on the other hand, chaos is more easily displayed, as for instance in the motions of a gas molecule in a gas at thermodynamic equilibrium [64].

Flow in 3D take the form:

$$\begin{cases} \dot{x}_1 = f_1\left(x_1, x_2, x_3\right) \\ \dot{x}_2 = f_2\left(x_1, x_2, x_3\right) \\ \dot{x}_3 = f_3\left(x_1, x_2, x_3\right). \end{cases}$$

The Jacobian matrix is:

$$\mathbf{J} = \begin{bmatrix} \frac{\partial f_1}{\partial x_1} & \frac{\partial f_1}{\partial x_2} & \frac{\partial f_1}{\partial x_3} \\ \frac{\partial f_2}{\partial x_1} & \frac{\partial f_2}{\partial x_2} & \frac{\partial f_2}{\partial x_3} \\ \frac{\partial f_3}{\partial x_1} & \frac{\partial f_3}{\partial x_2} & \frac{\partial f_3}{\partial x_3} \end{bmatrix},$$

with characteristic values given by:

$$\det\left(\mathbf{J} - \lambda\mathbf{I}\right) = 0,$$

which yields a cubic equation:

$$\lambda^3 + p\lambda^2 + q\lambda + r = 0,$$

which is solved for three eigenvalues and eigenvectors.

3D Fixed-Points Classification Fixed-points in 3D systems are classified according to the signs of the real and imaginary parts of the characteristic values of the Jacobian matrix. Table 4.2 shows the possible combinations of the characteristic values and the associated fixed-point classification [64].

Table 4.2. 3D fixed-point classification.

Characteristic values	**Fixed-point**
$(-,-,-)$	Attracting node
$(-,-r+ia,-r-ia)$	Stable spiral
$(+,+,+)$	Repellor
$(+,+r+ia,+r-ia)$	Unstable spiral
$(-,-,+)$	Saddle point index 1
$(-,+,+)$	Saddle point index 2
$(-r+ia,-r-ia,+)$	Spiral saddle index 1
$(-,+r+ia,+r-ia)$	Spiral saddle index 2

Subsection 4.2.4

Periodic Solutions and Poincaré Maps

4.2.4.1 Periodic Solutions

Definition 7

A solution of a continuous-time system is periodic with least period T if:

$$\mathbf{x}(t+T) = \mathbf{x}(t) \quad \text{and} \quad \mathbf{x}(t+\tau) \neq \mathbf{x}(t) \quad \text{for} \quad 0 < \tau < T.$$

Unlike equilibrium solutions, periodic solutions are characterized by time-varying states. A periodic solution is a dynamic solution that is characterized by one basic frequency. The spectrum of a periodic signal consists of a spike at zero frequency[5] and spikes at integer multiples of the basic frequency. The amplitudes of some of the frequency components may be zero.

[5] If the signal has a non-zero mean.

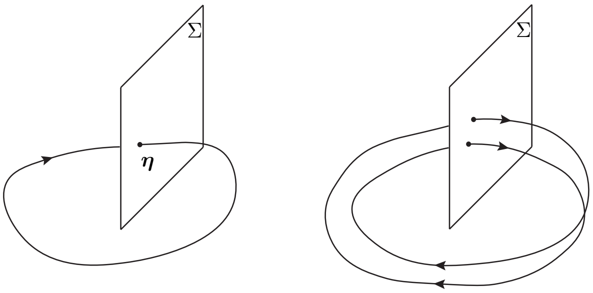

(a) (b)

Figure 4.4. Poincaré section of periodic orbits: (a) one intersection with Σ and (b) two intersections with Σ.

Remark A periodic solution is called a limit cycle if there are no other periodic solutions sufficiently close to it. In other words, a limit cycle is an isolated periodic solution and corresponds to an isolated closed orbit in the state-space.

4.2.4.2 Poincaré Map

Poincaré maps are useful for studying the flow near a periodic orbit, or the flow in some chaotic systems [80]. Consider a generic n-dimensional system described by Eq. (4.2.1), and let Σ be a $(n-1)$ dimensional *Poincaré Section* (Fig. 4.3). The surface of section Σ is required to be transverse to the flow, i.e., all trajectories starting on Σ flow through it, and not parallel to it.

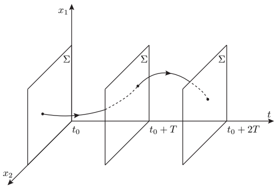

Figure 4.3. Poincaré section Σ of a 2D system with time-periodic terms.

Definition 8 The *Poincaré map* **P** is a mapping from Σ to itself, obtained by following trajectories from one intersection with Σ to the next one. If $\mathbf{x}_k \in \Sigma$ denotes the k-th intersection, then the Poincaré map is defined by:

$$\mathbf{x}_{k+1} = \mathbf{P}\left(\mathbf{x}_k\right).$$

If $\boldsymbol{\eta}$ is a fixed-point of **P** (i.e., $\mathbf{P}(\boldsymbol{\eta}) = \boldsymbol{\eta}$), a trajectory starting at $\boldsymbol{\eta}$ returns to $\boldsymbol{\eta}$ after some time T, and is therefore a closed orbit for the original system.

Moreover, by looking at the behavior of **P** near this fixed-point, we can determine the stability of the closed orbit. Thus, the Poincaré map converts problems about closed orbits (which are difficult) into problems about fixed-points of a mapping (which are easier in principle, though not always in practice). The snag is that it's typically very difficult to find an exact closed-form for **P** in nonlinear systems.

Since $\mathbf{x}_{k+1}$ uniquely specifics $\mathbf{x}_k$ and vice versa, a Poincaré map is an invertible map. Hence, we have:

$$\mathbf{x}_k = \mathbf{P}^{-1}(\mathbf{x}_{k+1}).$$

In Fig. 4.4 two periodic orbits of an autonomous system are shown in the corresponding state-space. The periodic orbit in Fig. 4.4a intersects the hypersurface Σ transversely once at the point $\boldsymbol{\eta}$, so it is a fixed-point of the associated Poincaré map $\mathbf{P}$; that is:

$$\boldsymbol{\eta} = \mathbf{P}(\boldsymbol{\eta}).$$

In the case shown in Fig. 4.4b, each point on the section Σ is a period-two point of the associated Poincaré map $\mathbf{P}$ and a fixed-point of the map $\mathbf{P}^2$. In a general setting, a periodic orbit of a continuous-time system may intersect a Poincaré section k times before closing on itself. Let one of these k-intersections be $\boldsymbol{\eta}$. Then, the corresponding Poincaré map $\mathbf{P}$ is such that:

$$\boldsymbol{\eta} = \mathbf{P}^k(\boldsymbol{\eta}),$$

implying that $\boldsymbol{\eta}$ is a period-k point of $\mathbf{P}$ or a fixed-point of $\mathbf{P}^k$. Hence, the stability of a periodic orbit of a continuous-time system may be determined by examining the stability of a fixed-point of an associated map.

4.2.4.3 Linear Stability of Periodic Solutions

In order to understand how a Poincaré map can be used to determine the stability of a closed orbit, let us consider a system as the one in Eq. (4.2.1) with a closed orbit. Equivalently, we want to determine if the correspondending fixed-point $\boldsymbol{\eta}$ of the Poincaré map is stable or unstable.

Let $\delta\boldsymbol{\eta}_0$ be an infinitesimal perturbation such that $\boldsymbol{\eta} + \delta\boldsymbol{\eta}_0$ is in Σ. Then, after the first return to Σ:

$$\boldsymbol{\eta} + \delta\boldsymbol{\eta}_1 = \mathbf{P}\left(\boldsymbol{\eta} + \delta\boldsymbol{\eta}_0\right) = \mathbf{P}\left(\boldsymbol{\eta}\right) + \left.\frac{\partial \mathbf{P}\left(\boldsymbol{\eta}\right)}{\partial \mathbf{x}}\right|_{\boldsymbol{\eta}} \delta\boldsymbol{\eta}_0 + \ldots,$$

where $\frac{\partial \mathbf{P}(\boldsymbol{\eta})}{\partial \mathbf{x}}$ is a $(n-1) \times (n-1)$ matrix called the *monodromy matrix* $\boldsymbol{\Phi}$ (Jacobian of the Poincaré map) at $\boldsymbol{\eta}$.

Being $\boldsymbol{\eta} = \mathbf{P}\left(\boldsymbol{\eta}\right)$ and assuming that we can neglect the high order terms, we get:

$$\delta\boldsymbol{\eta}_1 = \frac{\partial \mathbf{P}\left(\boldsymbol{\eta}\right)}{\partial \mathbf{x}}\, \delta\boldsymbol{\eta}_0 = \boldsymbol{\Phi}(\boldsymbol{\eta})\, \delta\boldsymbol{\eta}_0.$$

The stability criterion is expressed in terms of the eigenvalues λ_j of the monodromy matrix.

Definition 9 The closed orbit is linearly stable if and only if $|\lambda_j| < 1$ for all $j = 1, \ldots, n-1$. The λ_j are called the *characteristic* or *Floquet multipliers* of the periodic orbit.

Remark These are the nontrivial multipliers since there is always an additional trivial multiplier $\lambda = 1$ corresponding to perturbations along the periodic orbit. In general, the Floquet multipliers can only be found by numerical integration.

To understand this criterion, let us consider the generic case where there are no repeated eigenvalues. Then, there is a basis of eigenvectors $\mathbf{v}_j$ of $\mathbf{\Phi}$ and we can write:

$$\delta \boldsymbol{\eta}_0 = \sum_{j=1}^{n-1} \eta_j \mathbf{v}_j .$$

As a result,

$$\delta \boldsymbol{\eta}_1 = \frac{\partial \mathbf{P}(\boldsymbol{\eta})}{\partial \mathbf{x}} \sum_{j=1}^{n-1} \eta_j \mathbf{v}_j = \sum_{j=1}^{n-1} \eta_j \lambda_j \mathbf{v}_j .$$

Iterating the linearized map k-times gives:

$$\delta \boldsymbol{\eta}_k = \sum_{j=1}^{n-1} \eta_j \left(\lambda_j\right)^k \mathbf{v}_j .$$

Hence, if all $|\lambda_j| < 1$, then $|\delta \boldsymbol{\eta}_k| \to 0$ geometrically fast. This proves that $\boldsymbol{\eta}$ is linearly stable. Conversely, if $|\lambda_j| > 1$ for some j, then perturbations along $\mathbf{v}_j$ grow, so $\boldsymbol{\eta}$ is unstable. A borderline case occurs when the largest eigenvalue has magnitude $|\lambda_m| = 1$; this occurs at bifurcations of periodic solutions, and then a nonlinear stability analysis is required.

Example As an example, we consider the construction of a Poincaré section and of a Poincaré map, reported in [62], for a generic 3D flow:

$$\begin{bmatrix} \dot{x}_1 \\ \dot{x}_2 \\ \dot{x}_3 \end{bmatrix} = \begin{bmatrix} f_1(x_1, x_2, x_3) \\ f_2(x_1, x_2, x_3) \\ f_3(x_1, x_2, x_3) \end{bmatrix} . \tag{4.2.3}$$

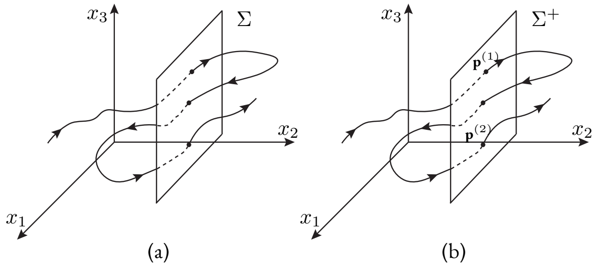

Figure 4.5. Poincaré section of a three-dimensional flow: (a) two-sided section Σ and (b) one-sided section Σ^+.

A *Poincaré section* is defined as a hypersurface in the state-space that is transverse to the flow of a given system of equations. If the trajectory evolves in an n-dimensional space, it follows that the Poincaré section is a $(n-1)$-dimensional surface and hence each point on this section is specified by $(n-1)$ coordinates.

By letting $\mathbf{n}(\mathbf{x})$ denote a unit vector normal to the Poincaré section located at $\mathbf{x}$, and $\mathbf{f}(\mathbf{x})$ the vector field describing the flow, the transversality condition is enforced by:

$$\mathbf{n}(\mathbf{x}) \cdot \mathbf{f}(\mathbf{x}) \neq 0.$$

A trajectory of the system in Eq. (4.2.3) in the (x_1, x_2, x_3)-space and a two-dimensional section Σ transverse to it are shown in Fig. 4.5. The section Σ is defined as:

$$\Sigma = \{(x_1, x_2, x_3) \in \mathbb{R} \times \mathbb{R} \times \mathbb{R} : x_2 = c\}.$$

The vector normal to Σ is given by:

$$\mathbf{n} = \begin{bmatrix} 0 \\ 1 \\ 0 \end{bmatrix}.$$

The section Σ is transverse to the trajectories of the 3D autonomous system whenever:

$$\mathbf{n} \cdot \mathbf{f} = \begin{bmatrix} 0 \\ 1 \\ 0 \end{bmatrix} \cdot \begin{bmatrix} f_1(x_1, c, x_3) \\ f_2(x_1, c, x_3) \\ f_3(x_1, c, x_3) \end{bmatrix} = f_2(x_1, c, x_3) \neq 0.$$

On the other hand, the section Σ^+ is defined similarly to the section Σ as:

$$\Sigma^+ = \{(x_1, x_2, x_3) \in \mathbb{R} \times \mathbb{R} \times \mathbb{R} : x_2 = c, f_2 > 0\}.$$

Poincaré sections, such as Σ, where $\mathbf{n} \cdot \mathbf{f}$ does not have the same sign for all intersections, are called two-sided sections (Fig. 4.5a). Whereas Poincaré sections, such as Σ^+, where $\mathbf{n} \cdot \mathbf{f}$ has the same sign for all intersections, are called one-sided sections (Fig. 4.5b). In Fig. 4.5a, there are three intersections, two of them correspond to a positive value of f_2, and one of them corresponds to a negative value of f_2. On the other hand, in Fig. 4.5b the first and second intersection of the trajectory with Σ^+ have been marked as $\mathbf{p}^{(1)}$ and $\mathbf{p}^{(2)}$. It is important to note that the time interval between two successive intersections of a trajectory with a chosen Poincaré section is not a constant in all situations.

In a general setting, let the successive intersections of a trajectory of an autonomous system with a one-sided Poincaré section be $\mathbf{p}^{(1)}$, $\mathbf{p}^{(2)}$, $\mathbf{p}^{(3)}$, and so on. The transformation or map that maps the current intersection to the subsequent intersection on a Poincaré section is called a *Poincaré map*. This map, which is $(n-1)$-dimensional, is described by:

$$\mathbf{p}^{(i+1)} = \mathbf{P}(\mathbf{p}^{(i)}).$$

Finally, it is important to specify that one can construct Poincaré sections at different locations on the periodic orbit. Consequently, one can obtain different Poincaré maps for the considered orbit. However, in most cases there exists a differentiable coordinate transformation from one Poincaré map to another, and the maps on the different sections exhibit the same qualitative dynamics; that is, the same number of fixed-points, similar stability properties of fixed-points, and so forth.

4.2.4.4 Nonautonomous Systems

In nonautonomous systems, the period associated with a periodic orbit is usually explicitly known. If the vector field $\mathbf{f}$ is periodic in time with period T, then a periodic solution of the dynamic system has a period that is either an integer multiple or integer submultiple of the period T. This period can be used to construct a Poincaré section. For an n-dimensional nonautonomous system, the Poincaré section is an n-dimensional surface and the associated map $\mathbf{P}$ is n-dimensional (Fig. 4.6).

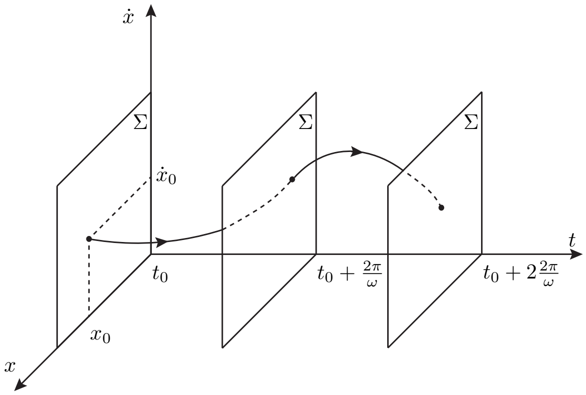

Figure 4.6. Poincaré section Σ of an orbit of a two-dimensional nonautonomous system with time-periodic terms.

The Poincaré map is also called the first-return map, because if a trajectory starts at a certain value on the line $\theta = 0 \pmod{2\pi}$, then the Poincaré map is the value when it returns to that line for the first time.

Example

Consider the case of a periodically forced linear oscillator as the one in Eq. (2.3.4). Our goal is to study the nature of the solutions in the context of the Poincaré maps, as reported in [94]. This will enable us to obtain a new point of view on something relatively familiar and to see the value of this new point of view.

Rewriting Eq. (2.3.4) as a system of first-order ODEs, we obtain:

$$\dot{\mathbf{x}} = \mathbf{F}(\mathbf{x}, t, \omega) \rightarrow \begin{cases} \dot{x}_1 = x_2 \\ \dot{x}_2 = -\omega_0^2 x_1 - 2\zeta x_2 + F\cos(\omega t)\,. \end{cases} \tag{4.2.4}$$

By rewriting Eq. (4.2.4) as an autonomous system, we get:

$$\mathbf{f}(\mathbf{x}, \omega) = \begin{cases} x_2 \\ -\omega_0^2 x_1 - 2\zeta x_2 + F\cos(x_3) \\ \omega. \end{cases} \tag{4.2.5}$$

The flow generated by Eq. (4.2.5) in the space $(x_1, x_2, x_3) \in \mathbb{R}\times\mathbb{R}\times\mathbb{S}$ is given by $(x_1(t), x_2(t), \omega t + x_3(t = 0))$. In particular, to compute the solution of the system using Eq. (3.1.2) which gives:

$$x_1(t) = e^{-\zeta t}\left[C_1\cos(\bar{\omega}t) + C_2\sin(\bar{\omega}t)\right] + A\cos(\omega t) + B\sin(\omega t)\,,$$

and:

$$\begin{aligned} x_2(t) &= e^{-\zeta t}\left\{[-\zeta C_1+\bar{\omega}C_2]\cos(\bar{\omega}t)-[\zeta C_2+\bar{\omega}C_1]\sin(\bar{\omega}t)\right\} = \\ &= -A\omega\cos(\omega t)+B\omega\sin(\omega t)\,, \end{aligned}$$

where $\bar{\omega}=\sqrt{\omega_0^2-\zeta^2}$, and:

$$A=\frac{\left(\omega_0^2-\omega^2\right)F}{\left(\omega_0^2-\omega^2\right)^2+(2\zeta\omega)^2},\qquad B=\frac{2\zeta\omega F}{\left(\omega_0^2-\omega^2\right)^2+(2\zeta\omega)^2}.$$

The constants C_1 and C_2 are obtained by requiring:

$$\begin{cases} x_1(0)=x_1(t=0) \\ x_2(0)=x_2(t=0), \end{cases}$$

which yields,

$$\begin{cases} C_1=x_1(0)-A \\ C_2=\frac{1}{\bar{\omega}}\left[\zeta\left(x_1(0)-A\right)+x_2(0)-\omega B\right]. \end{cases}$$

Next we turn to the construction of the Poincaré map. For this we will consider only the case where $\zeta<1$ since the other cases are similar.
As a first step, we construct a Poincaré section at $x_3=0$, i.e., this is why we specified the initial conditions at $t=0$, as follows:

$$\Sigma=\left\{(x_1,x_2,x_3)\in\mathbb{R}\times\mathbb{R}\times\mathbb{S}:x_3=0\in[0,2\pi)\right\}.$$

The Poincaré map is given by $\mathbf{P}:\Sigma\to\Sigma$, so we have to evaluate $x_1\left(\frac{2\pi}{\omega}\right)$ and $x_2\left(\frac{2\pi}{\omega}\right)$:

$$\begin{aligned} \begin{bmatrix} x_1 \\ x_2 \end{bmatrix} &\to e^{-\zeta\frac{2\pi}{\omega}}\begin{bmatrix} \mathcal{C}+\frac{\zeta}{\bar{\omega}}\mathcal{S} & \frac{1}{\bar{\omega}}\mathcal{S} \\ -\frac{\omega_0^2}{\bar{\omega}}\mathcal{S} & \mathcal{C}-\frac{\zeta}{\bar{\omega}}\mathcal{S} \end{bmatrix}\begin{bmatrix} x_1 \\ x_2 \end{bmatrix}+ \\ &+e^{-\zeta\frac{2\pi}{\omega}}\begin{bmatrix} -A\mathcal{C}-\left(\frac{\zeta}{\bar{\omega}}A+\frac{\omega}{\bar{\omega}}B\right)\mathcal{S} \\ -\omega B\mathcal{C}+\left(\frac{\omega_0^2}{\bar{\omega}}A+\frac{\zeta\omega}{\bar{\omega}}B\right)\mathcal{S} \end{bmatrix}+\begin{bmatrix} A \\ \omega B \end{bmatrix}, \end{aligned} \tag{4.2.6}$$

where

$$\mathcal{C}=\cos\left(2\pi\frac{\bar{\omega}}{\omega}\right),\qquad \mathcal{S}=\sin\left(2\pi\frac{\bar{\omega}}{\omega}\right).$$

This is an example of an *affine map*, i.e., it is a linear map

plus a translation. The Poincaré map has a single fixed-point given by $\boldsymbol{\eta} \equiv [A, \omega B]^T$.
A simple calculation shows that the eigenvalues of the derivative of the Poincaré map (the *monodromy matrix*) evaluated at the fixed-point $\boldsymbol{\eta}$ are given by:

$$\left.\frac{\partial \mathbf{P}}{\partial \mathbf{x}}\right|_{\boldsymbol{\eta}} = e^{-\zeta\frac{2\pi}{\omega}} \begin{bmatrix} \mathcal{C} + \frac{\zeta}{\bar{\omega}}\mathcal{S} & \frac{1}{\bar{\omega}}\mathcal{S} \\ -\frac{\omega_0^2}{\bar{\omega}}\mathcal{S} & \mathcal{C} - \frac{\zeta}{\bar{\omega}}\mathcal{S} \end{bmatrix} \rightarrow \lambda_{1,2} = e^{-\zeta\frac{2\pi}{\omega} \pm i\frac{2\pi\bar{\omega}}{\omega}}, \tag{4.2.7}$$

thus, the fixed-point is asymptotically stable with nearby orbits.
In the case of *resonance* ($\bar{\omega} = \omega$) we have that:

$$\mathcal{C} = \cos\left(2\pi\frac{\omega}{\omega}\right) = 1, \qquad \mathcal{S} = \sin\left(2\pi\frac{\omega}{\omega}\right) = 0.$$

The Poincaré map becomes:

$$\begin{bmatrix} x \\ \dot{x} \end{bmatrix} \rightarrow e^{-\zeta\frac{2\pi}{\omega}} \begin{bmatrix} 1 & 0 \\ 0 & 1 \end{bmatrix} \begin{bmatrix} x \\ \dot{x} \end{bmatrix} + \left(1 - e^{-\zeta\frac{2\pi}{\omega}}\right) \begin{bmatrix} A \\ \omega B \end{bmatrix}, \tag{4.2.8}$$

in this case the eigenvalues of $\left.\frac{\partial \mathbf{P}}{\partial \mathbf{x}}\right|_{\boldsymbol{\eta}}$ are:

$$\lambda = e^{-\zeta\frac{2\pi}{\omega}},$$

thus, the fixed-point $\boldsymbol{\eta}$ is asymptotically stable with nearby orbits appearing (Fig. 4.7). In this case orbits do not spiral near the fixed-point since the eigenvalues are purely real.

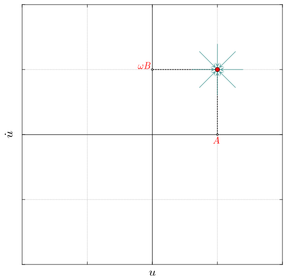

Figure 4.7. Asymptotically stable fixed-point.

In the previous example, we note that for $\zeta > 0$ in all cases the free oscillation dies out, and we are left with the forced oscillation of frequency ω which is represented as an attracting fixed-point of the Poincaré map (Fig. 4.7). On the other hand, in the case $\zeta = 0$, we see that this does not happen. In general, for $\zeta = 0$, it should be clear that the solution is a superposition of solutions of frequencies ω and ω_0.

Example Another example is provided by the autonomous system in Eq. (4.2.5), with $\zeta = 0$:

$$\mathbf{f}(\mathbf{x}, \omega) = \begin{cases} x_2 \\ -\omega_0^2 x_1 + F\cos(x_3) \\ \omega. \end{cases} \tag{4.2.9}$$

For this system we will first write down the Poincaré map and then consider each case individually. The solutions in terms of displacement and velocity for Eq. (4.2.9) are given by:

$$\begin{aligned} x_1(t) &= C_1 \cos(\omega_0 t) + C_2 \sin(\omega_0 t) + \bar{A}\cos(\omega t), \\ x_2(t) &= -\omega_0 C_1 \sin(\omega_0 t) + \omega_0 C_2 \cos(\omega_0 t) + \bar{A}\omega \sin(\omega t), \end{aligned}$$

where:

$$\bar{A} = \frac{F}{\omega_0^2 - \omega^2}, \quad C_1 = x_1(0) + \bar{A}, \quad C_2 = \frac{x_2(0)}{\omega_0},$$

from the existence condition for $\bar{A}$, it follows that $\omega \neq \omega_0$. Examining the solution $x_1(t)$, it is evident that it represents a superposition of solutions with frequencies ω and ω_0. The behavior of the system can be analyzed by considering various cases depending on the relationship between ω and ω_0.
The Poincaré map, denoted by $\mathbf{P} : \Sigma \to \Sigma$, can be derived by evaluating $x_1\left(\frac{2\pi}{\omega}\right)$ and $x_2\left(\frac{2\pi}{\omega}\right)$ as follows:

$$\begin{aligned} \begin{bmatrix} x_1 \\ x_2 \end{bmatrix} \to &\begin{bmatrix} \cos\left(2\pi\frac{\omega_0}{\omega}\right) & \frac{1}{\omega_0}\sin\left(2\pi\frac{\omega_0}{\omega}\right) \\ -\omega_0 \sin\left(2\pi\frac{\omega_0}{\omega}\right) & \cos\left(2\pi\frac{\omega_0}{\omega}\right) \end{bmatrix} \begin{bmatrix} x_1 \\ x_2 \end{bmatrix} + \\ &+ \begin{bmatrix} \bar{A}\left[1 - \cos\left(2\pi\frac{\omega_0}{\omega}\right)\right] \\ \omega_0 \bar{A} \sin\left(2\pi\frac{\omega_0}{\omega}\right) \end{bmatrix}. \end{aligned}$$

The fixed-points of the map are determined by solving:

$$\begin{aligned} &\begin{bmatrix} 1 - \cos\left(2\pi\frac{\omega_0}{\omega}\right) & -\frac{1}{\omega_0}\sin\left(2\pi\frac{\omega_0}{\omega}\right) \\ \omega_0 \sin\left(2\pi\frac{\omega_0}{\omega}\right) & 1 - \cos\left(2\pi\frac{\omega_0}{\omega}\right] \end{bmatrix} \begin{bmatrix} x_1 \\ x_2 \end{bmatrix} = \\ &\qquad = \begin{bmatrix} \bar{A}\left[1 - \cos\left(2\pi\frac{\omega_0}{\omega}\right)\right] \\ \omega_0 \bar{A} \sin\left(2\pi\frac{\omega_0}{\omega}\right) \end{bmatrix}, \end{aligned}$$

whose unique solution is the point $\left[\bar{A}, 0\right]^T$, which is a fixed-point, as starting from this point, the system returns to the same solution after a period of $T = \frac{2\pi}{\omega}$. In the other cases, as reported in [94], we have:

- Subharmonic Response: $\frac{\omega}{\omega_0} = m$ with $m > 1$;
- Ultraharmonic Response: $\frac{\omega}{\omega_0} = \frac{1}{n}$ with $n > 1$;
- Ultrasubharmonic Response: $\frac{\omega}{\omega_0} = \frac{m}{n}$ with $m,\ n > 1$;
- Quasiperiodc Response: $\frac{\omega}{\omega_0} =$ irrational number.

SUBSECTION 4.2.5

Bifurcation Theory

Bifurcation, a term derived from French and introduced into nonlinear dynamics by Henri Poincaré, denotes a qualitative change in the characteristics of a system, such as the number and type of solutions, as one or more parameters that influence the system are varied.

Definition 10 A *local bifurcation* refers to a qualitative change that occurs in the vicinity of a fixed-point or a periodic solution of a dynamical system.

Definition 11 Any qualitative change that occurs outside the neighborhood of a fixed-point or periodic solution is classified as a *global bifurcation.*

Definition 12 The *state-control space* is defined as the space formed by the state variables and control parameters of the system, which is instrumental in analyzing bifurcation problems.

Many authors classify bifurcations as *continuous* or *discontinuous*[6], based on whether the states of the system change continuously or discontinuously as the control parameter is varied gradually through its critical value [46, 62]. Discontinuous bifurcations can be further classified into *dangerous* and *explosive* bifurcations, depending on whether the system response transitions suddenly to a disconnected attractor or expands into a larger attractor, with the new attractor including the previous one as a proper subset [62].

In the case of a *dangerous bifurcation*, the current attractor suddenly vanishes from the state-space of the system. The post-bifurcation response shifts to a remote attractor, which may be either bounded or unbounded. Bounded responses can manifest as point, periodic, quasiperiodic, or chaotic attractors. Conversely, unbounded responses can result in catastrophic outcomes, such as the capsizing of ships or voltage collapses in power systems. The outcome of a dangerous bifurcation may be deterministic or indeterminate, depending on whether a single attractor exists beyond the critical control value. When multiple attractors are present, the post-bifurcation response is influenced by the rate of control sweep and the presence of noise

[6] Also referred to as catastrophic bifurcations.

[62].

In an *explosive bifurcation*, the system response does not transition to a remote attractor. The outcome of this bifurcation is deterministic, unaffected by the rate of control parameter adjustment, and insensitive to noise. Consequently, if the control sweep is reversed in a quasi-stationary manner, the new larger attractor collapses back to the original smaller attractor at the same critical bifurcation value. Explosive bifurcations can lead to intermittent transitions to chaos [62].

4.2.5.1 Local Bifurcations of Fixed-Points

Let us suppose that as one or more control parameters are varied, a fixed-point becomes nonhyperbolic at a certain location in the state-control space. Then, if the state-space portraits before and after this location are qualitatively different, this location is called a *bifurcation point* and the accompanying qualitative change is called a *bifurcation*. Furthermore, a bifurcation that requires at least m independent control parameters to occur is called a *codimension-m bifurcation*.

If we start with control parameters corresponding to a stable fixed-point of a continuous-time system, and then slowly vary one of the control parameters, this fixed-point can lose stability through one of the following bifurcations [3]:

- saddle-node bifurcation;
- pitchfork or symmetry-breaking bifurcation;
- transcritical bifurcation;
- Hopf bifurcation.

Remark

> In alignment with the classifications established by various authors [57, 58, 62], bifurcations can be further categorized as *static* or *dynamic*. Specifically, at bifurcation points associated with saddle-node, pitchfork, and transcritical bifurcations, since only branches of fixed-points or static solutions converge these three types of bifurcations are designated as *static bifurcations*. In contrast, at a Hopf bifurcation point, the intersection occurs between branches of fixed-points and periodic solutions. Thus, Hopf bifurcations are classified as *dynamic bifurcations*.

4.2.5.2 Bifurcation of Periodic Solutions

In Section 4.2.4, we analyzed the stability of periodic solutions. It was established that, in a general setting, the monodromy

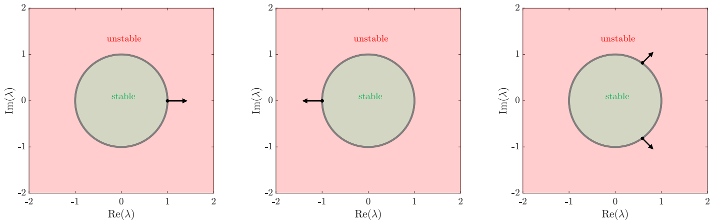

(a) (b) (c)

Figure 4.8. Scenarios depicting how the Floquet multipliers leave the unit circle for different local bifurcations: (a) transcritical, symmetry-breaking, and fold bifurcation; (b) period-doubling bifurcation; and (c) Neimark-Sacker bifurcation.

matrix and the corresponding Floquet multipliers are dependent on the control parameters. Specifically, by considering a situation in which one or more control parameters are varied, leading to a periodic solution becoming nonhyperbolic at a specific point within the state-control space, if the qualitative characteristics of the state-space portraits prior to and following this point differ, this point is referred to as a *bifurcation point.* The associated qualitative change is a *bifurcation.* Furthermore, a bifurcation that requires the variation of at least m independent control parameters is classified as a *codimension-m* bifurcation. This systematic classification enhances our understanding of the dynamics within nonlinear systems.

Specifically, if we start with control parameters corresponding to a stable periodic solution of a continuous-time nonlinear system as:

$$\dot{\mathbf{x}} = \mathbf{f}\left(\mathbf{x}, \alpha\right), \quad \mathbf{x} \in \mathbb{R}^n, \quad \alpha \in \mathbb{R}, \tag{4.2.10}$$

and then vary one of the control parameters until this periodic solution loses stability, the resulting solution depends on the manner in which the Floquet multipliers leave the unit circle. There are three possible scenarios, as depicted in Fig. 4.8:

1. A Floquet multiplier leaves the unit circle through $+1$ (Fig. 4.8a), resulting in one of the following three bifurcations:
    - Transcritical bifurcations.
    - Symmetry-breaking bifurcations.
    - Cyclic-fold bifurcations.
2. A Floquet multiplier leaves the unit circle through -1 (Fig. 4.8b), resulting in a period-doubling bifurcation.

3. Two complex conjugate Floquet multipliers leave the unit circle away from the real axis (Fig. 4.8c), resulting in a secondary Hopf or Neimark-Sacker bifurcation.

Since the Floquet multipliers correspond to the eigenvalues of the monodromy matrix, which is derived by solving a linearized system of equations around the periodic solution under investigation (Section 4.2.4), it follows that the bifurcations associated with this periodic solution are classified as *local bifurcations*. This classification emphasizes the inherent connection between the stability analysis of the periodic solution and the local behavior of the system in its vicinity.

We also note that the three scenarios in Fig. 4.8 are similar to those encountered in the context of local bifurcations of fixed-points. Specifically, if a Poincaré map:

$$\mathbf{P}\left(\boldsymbol{\eta}, \alpha\right) : \Sigma \rightarrow \Sigma,$$

associated with a periodic solution, where Σ is a local Poincaré section, can be constructed. The local bifurcation of the considered periodic solution can be studied by examining the local bifurcation of the fixed-point of the map.

As in the case of bifurcations of fixed-points, bifurcations of limit cycles can be classified into *continuous* and *discontinuous* (or catastrophic) bifurcations. In the case of continuous bifurcations, the motion of the system evolves continuously onto another motion as a control parameter is varied in a quasi-stationary manner [62]. As in the case of fixed-points, discontinuous (or catastrophic) bifurcations may be:

- *Dangerous bifurcation*: In a dangerous bifurcation, the system response jumps to a remote attractor which may be infinity, as a control parameter is varied in a quasi-stationary manner. The outcome of these bifurcations may be determinate or indeterminate, depending on whether the system has a single attractor past the bifurcation value or not [62].

- *Explosive bifurcation*: In an explosive bifurcation, the old attractor explodes into a larger attractor, with the old attractor being a proper subset of the new attractor. Again, the new attractor may or may not be chaotic [62].

4.2.5.3 Symmetry-Breaking Bifurcation

When a Floquet multiplier leaves the unit circle through $+1$, as shown in Fig. 4.8a, the associated bifurcation depends on the

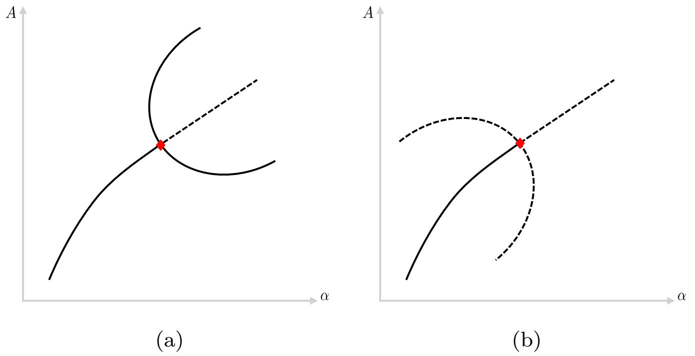

(a) (b)

Figure 4.9. Local scenarios: (a) supercritical symmetry-breaking bifurcation and (b) subcritical symmetry-breaking bifurcation (continuous line: stable behavior; dashed line: unstable behavior).

nature of the periodic solution prior to the bifurcation. Let us suppose that the periodic solution prior to the bifurcation is a symmetric solution; that is, it possesses a symmetry property. Then, if the bifurcation breaks the symmetry of the periodic solution, it is called a symmetry-breaking bifurcation [62].

In some continuous-time systems with odd nonlinearities[7] a solution possesses the symmetry:

$$\mathbf{x}(t) = -\mathbf{x}\left(t + \frac{T}{2}\right),$$

where T is the period of the solution. This symmetry property is called *inversion symmetry.* The spectra of the scalar components of $\mathbf{x}$ contain only odd harmonics of the frequency $\frac{2\pi}{T}$. However, this symmetry is broken when a bifurcation introduces a zero frequency component and/or an even harmonic of the frequency $\frac{2\pi}{T}$. Both the phase portrait and power spectrum[8] are indicative of the inversion symmetry of the periodic solution.

The behavior near *supercritical* and *subcritical* symmetry-breaking bifurcation points is illustrated in Figs. 4.9a and 4.9b, respectively. In these diagrams, the amplitude A of the periodic solution is plotted against the scalar control parameter α. Solid lines represent branches of stable periodic solutions, whereas dashed lines indicate unstable ones.

At the bifurcation points, the branches corresponding to symmetric and asymmetric periodic solutions intersect. In both Figs. 4.9a and 4.9b, the stable branch of symmetric periodic solutions, which exists before the bifurcation, transitions into an unstable branch of symmetric periodic solutions beyond the bifurcation point. Further, in the case of:

---

[7] Odd function: It is a function for which $f(-x) = -f(x)$ and therefore which is symmetrical with respect to the origin. Even function: It is a function for which $f(-x) = f(x)$ and therefore which is symmetrical with respect to the y-axis.

[8] A power spectrum provides a measure of the energy of a system at different frequencies

- *Supercritical bifurcation*, locally stable asymmetric periodic solutions coexist with unstable symmetric periodic solutions on one side of the bifurcation point (Fig. 4.9a).
- *Subcritical bifurcation*, locally unstable asymmetric periodic solutions coexist with stable symmetric periodic solutions on one side of the bifurcation point (Fig. 4.9b).

We note that supercritical and subcritical symmetry-breaking bifurcations are examples of continuous and discontinuous bifurcations, respectively [62].

4.2.5.4 Cyclic-Fold Bifurcation

The scenario near a cyclic-fold bifurcation point is as follow, a branch of stable periodic solutions and a branch of unstable periodic solutions, which exist for $\alpha < \alpha_c$, coalesce and obliterate each other at the bifurcation point α_c. Typically, the unstable periodic solutions are of the saddle type (Fig. 4.10).

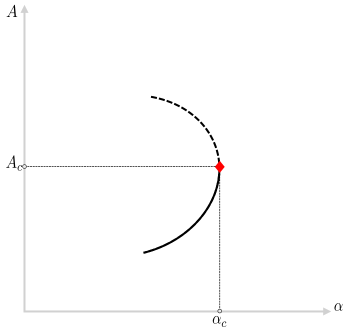

Figure 4.10. Scenario near to a cyclic-fold bifurcation (continuous line: stable behavior; dashed line: unstable behavior).

Remark

> Note that locally there are no other solutions in the vicinity of the bifurcation point on one side (i.e., $\alpha > \alpha_c$). Therefore, cyclic-fold bifurcations are discontinuous or catastrophic bifurcations.

When a dynamical system undergoes a cyclic-fold bifurcation, the system will be in a state corresponding to an attracting limit cycle for $\alpha < \alpha_c$. On the other hand, for $\alpha > \alpha_c$, the system behavior cannot be determined from local considerations alone and global considerations are necessary. The post-bifurcation state is usually determined through numerical simulations and there are two possibilities:

1. The system evolution may be attracted to a distant solution, which is either bounded or unbounded. The bounded solution may be a point attractor, or a periodic attractor, or an aperiodic attractor. The bifurcation is dangerous and its outcome may be determinate or indeterminate.
2. The old attractor may explode into a new larger attractor with the old attractor being a proper subset of the new attractor. Such a bifurcation is an example of an explosive bifurcation. An orbit on this attractor spends long stretches of time near the destroyed limit cycle (ghost or phantom limit cycle), with interruptions in the form of excursions or outbreaks away from the ghost limit cycle. When the attractor is chaotic or strange, the stretches of

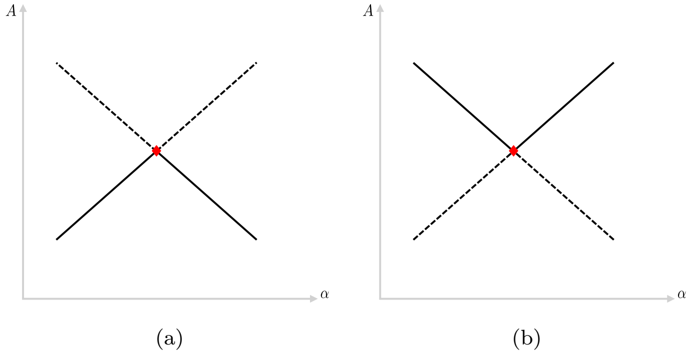

Figure 4.11. Two examples of local scenarios for a transcritical bifurcation (continuous line: stable behavior; dashed line: unstable behavior).

time spent near the ghost limit cycle are called laminar phases, and the excursions away from the ghost limit cycle are called turbulent or chaotic bursts.

Remark Note that a cyclic-fold bifurcation of a periodic solution of a dynamical system may lead to a chaotic solution of the considered dynamical system [62].

4.2.5.5 Transcritical Bifurcation

A transcritical bifurcation of a periodic solution may occur when a Floquet multiplier leaves the unit circle through $+1$, as shown in Fig. 4.8a. The branches of stable and unstable periodic solutions that exist before the transcritical bifurcation continue as branches of unstable and stable periodic solutions, respectively, after the bifurcation. Hence, a transcritical bifurcation leads to an exchange of stability (Fig. 4.11).

4.2.5.6 Period-Doubling Bifurcation

When a Floquet multiplier crosses the unit circle through -1 (Fig. 4.8b), a period-doubling bifurcation occurs. The branch of stable periodic solutions that exists prior to the bifurcation (i.e., for $\alpha < \alpha_c$) becomes an unstable branch of periodic solutions at the bifurcation point $\alpha = \alpha_c$. If the bifurcation is *supercritical*, a stable branch of period-doubled solutions emerges, whereas in the case of a *subcritical* bifurcation, the unstable branch of period-doubled solutions is annihilated (Fig. 4.12). In the power spectrum of a period-doubled solution, a peak at $\frac{T}{2}$ appears, indicating that the fundamental frequency of the system is halved relative to the excitation frequency.

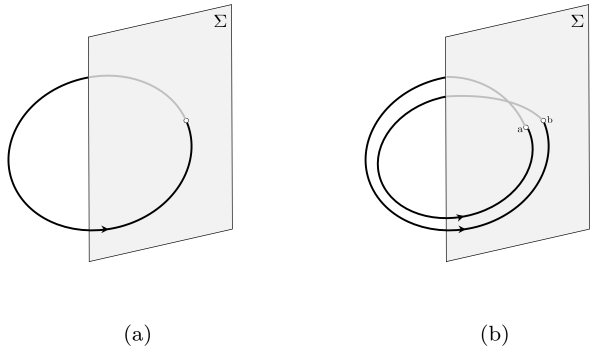

(a) (b)

Figure 4.12. Periodic orbit (a) before and (b) after period-doubling bifurcation.

Remark Period-doubling bifurcations can occur successively as a single control parameter is varied, leading to an infinite sequence of such bifurcations, which ultimately results in a chaotic solution [62].

4.2.5.7 Secondary Hopf or Neimark-Sacker Bifurcation

A Hopf bifurcation of a fixed-point of a continuous-time system leads to a periodic solution of this system. So, essentially, a Hopf bifurcation introduces a new frequency (possibly incommensurate) with the first one in the bifurcating solution. Similarly, a Hopf bifurcation of a periodic solution[9] occurs when two complex conjugate eigenvalues exit the unit circle away from the real axis, as shown in Fig. 4.8c. The bifurcating solution may be periodic or two-period quasiperiodic, depending on the relationship between the newly introduced frequency and the frequency of the periodic solution that exists prior to the bifurcation.

Similar to *subcritical* and *supercritical* Hopf bifurcations of fixed-points, there are subcritical and supercritical Neimark-Sacker bifurcations of periodic solutions. In both bifurcations, the branch of stable periodic solutions that exists prior to the Neimark-Sacker bifurcation continues as a branch of unstable periodic solutions after the bifurcation. A branch of stable quasiperiodic solutions is created if the bifurcation is *supercritical.* This bifurcation is an example of a continuous bifurcation. On the other hand, a branch of unstable quasiperiodic solutions is destroyed if the bifurcation is *subcritical* [62].

SUBSECTION 4.2.6

Nonlinear Resonance and Frequency Response

[9] Called a secondary Hopf or Neimark-Sacker bifurcation

Nonlinear resonance occurs when the oscillations of a nonlinear system are amplified due to a correspondence between the frequency of an external forcing and a natural frequency of the system. Unlike linear resonance, where the behavior is predictable, nonlinear resonance can lead to complex and unpredictable outcomes. This phenomenon is particularly intriguing in the context of chaos theory and the stability of dynamical systems.

Henri Poincaré, one of the founders of chaos theory, significantly contributed to the understanding of resonance in nonlinear systems. Poincaré maps associated with second-order ODEs in resonance can demonstrate that the qualitative structure of solutions may change significantly due to nonlinearity.

Nonlinear resonance plays a fundamental role in various scientific and engineering fields, with relevant applications in acoustics, structural engineering, and biology.

- In acoustics, nonlinear resonance is crucial for understanding the generation of higher harmonics during the propagation of sound waves. This phenomenon is particularly important in ultrasound applications, where the distortion of ultrasonic waves can enhance the quality of diagnostic images. This improvement is attributed to the ability of harmonic waves to provide superior details compared to traditional linear sound waves.

- In structural engineering, nonlinear resonance is carefully considered in the design of buildings and infrastructures. It is essential to anticipate the emergence of nonlinear vibrations that could cause structural damage. To mitigate such effects, vibration control techniques are implemented, such as damping devices or seismic isolators, which reduce the risk of critical resonance.

- In biology, nonlinear resonance is observed in various complex systems, influencing processes such as the synchronization of neural activities and the dynamics of cellular populations. Such synchronization processes are vital for the proper functioning of biological networks, such as the central nervous system.

In recent years, nonlinear resonance has been the subject of intensive studies, with new applications particularly in the fields of imaging and materials analysis.

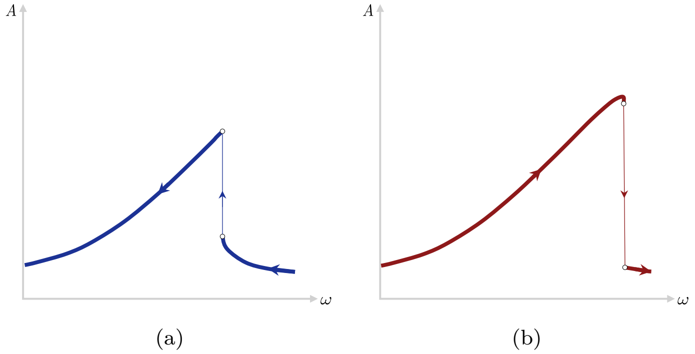

(a) (b)

Figure 4.13. Nonlinear resonance hysteresis: Arrows indicate the direction of progression along the resonance curve when the excitation frequency undergoes gradual variation.

4.2.6.1 Duffing Model

A linear oscillator always responds at the driving frequency, once transients are damped out. The oscillator response grows very large when the driving frequency approaches the natural frequency of the oscillator[10] [37]. In contrast, if a small nonlinearity is present, periodic solutions still occur and resonant instabilities are now possible for rational frequency ratios between the driving frequency and the natural oscillator response[11].

One of the most extensively studied models in the field of nonlinear dynamics is the Duffing oscillator [61]. This system is characterized as a nonlinear SDoF oscillator, which may also include a small linear damping component, that is subjected to an external periodic force. The equation of motion governing this system is expressed as follows:

$$\ddot{u} + 2\zeta\dot{u} + u + \varepsilon u^3 = f\cos(\omega t)\,, \tag{4.2.11}$$

where f and ω are considered to be parameters, fixed at any given time, but variable in order to study the oscillator's response to this time-dependent driving force.

The introduction of the nonlinear term introduces at least three distinct physical effects associated with its presence:

- When the driving frequency is progressively decreased from above the resonance frequency, the system's amplitude exhibits a sudden transition to a higher value at a specific frequency threshold (Fig. 4.13a). In contrast, when the driving frequency is gradually increased from a lower frequency range, the amplitude remains stable until it reaches a significantly higher frequency threshold, at

[10] This is the resonance.

[11] This phenomenon plays a key role in the route to chaos for Hamiltonian systems.

which point it experiences an abrupt decrease (Fig. 4.13b). This directional dependence, whereby the oscillator retains a form of "memory" about whether the driving frequency ω is being adjusted upwards or downwards, is known as *hysteresis* within the framework of nonlinear dynamics. In the subsequent section, we will formally define hysteresis as it pertains specifically to mechanical systems.

- Under specific conditions, subharmonic frequencies (such as $\frac{\omega}{n}$, where n represents an integer) can be generated. The existence of subharmonics indicates that the system can exhibit a significant response even when driven at n times the natural resonant frequency. However, stable solutions will only arise for particular driving amplitudes.
- A nonlinear system can function as a mixer. When excited by two distinct frequencies, the output of the system generates oscillations at both the sum and the difference of the original exciting frequencies. While there are numerous practical applications for this effect, it is particularly noteworthy that most radio receivers utilize nonlinear mixer devices within their circuitry. For the purposes of this discussion, we will acknowledge this effect without delving into further details.

4.2.6.2 Introduction to the Analysis of Nonlinear Oscillator Dynamics

In this section, we investigate the behavior of a nonlinear oscillator modeled by the Duffing equation, given by Eq. (4.2.11) where ε represents the nonlinearity, ζ indicates damping, f is the amplitude of the driving force, and ω is the driving frequency.

We begin by selecting specific parameters: $\varepsilon = \frac{1}{10}$, $f = 1$, and $\zeta = 0.05$. The oscillator is driven precisely at its resonant frequency of the linear part, $\omega = 1$. The phase plane plot $(u, \dot{u})$ of the solution, obtained through numerical integration, is presented in Fig. 4.14.

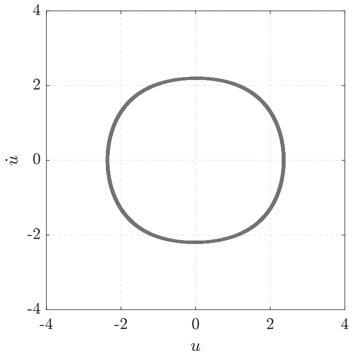

Figure 4.14. Duffing oscillator with $\varepsilon = 0.1$, $\zeta = 0.05$, and $f = 1$ when $\omega = 1$.

In the absence of the nonlinear term, the expected trajectory in the phase plane would yield a perfect circle, represented by the equation:

$$u(t) = \frac{f}{1-\omega^2} \cos(\omega t) .$$

However, as we observed in Fig. 4.14, the presence of nonlinearity leads to a distorted trajectory of finite amplitude[12].

[12] Even in the absence of damping.

For such a reason, we assume that the solution is periodic, allowing us to express it in terms of a Fourier series. By using the symmetries[13] inherent in Eq. (4.2.11), we can simplify our analysis. The time-reversal symmetry indicates that the Fourier series consist solely of cosine terms. Additionally, through the transformation invariance of the equation, we can deduce that only odd harmonics appear in the series expansion:

$$u(t) = \sum_{n=1,3,5,\dots} A_n(\omega)\cos(n\omega t)\,.$$

By substituting this expression into Eq. (4.2.11), without the dumping term, we obtain:

$$\begin{aligned}&(1-\omega^2)A_1\cos(\omega t) + (1-9\omega^2)A_3\cos(3\omega t) + \dots\\ &+\varepsilon\left[\frac{3}{4}A_1^3\cos(\omega t) + \frac{1}{4}A_1^3\cos(3\omega t) + \dots\right] = f\cos(\omega t)\,,\end{aligned} \tag{4.2.12}$$

where we used the trigonometric identity reported in Appendix C. The coefficients of each harmonic, $\cos(n\omega t)$, must vanish, since we can isolate each one of them by Fourier analysis. Thus, Eq. (4.2.12) implies that, to this level of approximation:

$$\begin{cases}(1-\omega^2)A_1 + \frac{3}{4}\varepsilon A_1^3 = f\\ (1-9\omega^2)A_3 + \frac{1}{4}\varepsilon A_1^3 = 0,\end{cases}$$

where, given ω and f we can solve the first equation for A_1, and then we can solve the second one for A_3[14].

At this point we assume $\zeta \neq 0$. Let's assume a solution of the type:

$$\begin{aligned}u(t) &= a\cos(\omega t) + b\sin(\omega t)\,,\\ \dot{u}(t) &= -\omega a\sin(\omega t) + \omega b\cos(\omega t)\,,\\ \ddot{u}(t) &= -\omega^2 a\cos(\omega t) - \omega^2 b\sin(\omega t)\,.\end{aligned}$$

By substituting these expressions into Eq. (4.2.11) we obtain:

$$\begin{aligned}\left[-\omega^2 a + 2\zeta\omega\ b + a\right]\cos(\omega t) + \left[-\omega^2 b - 2\zeta\omega\ a + b\right]\sin(\omega t) +\\ +\varepsilon\left[a\cos(\omega t) + b\sin(\omega t)\right]^3 = f\cos(\omega t)\,.\end{aligned}$$

In this expression, remembering the trigonometric relations in the Appendix C, and neglecting the terms of the higher har-

[13] Eq. (4.2.11) is invariant with respect to the transformations:

$$\begin{aligned}t &\to t+\pi,\\ u &\to -u.\end{aligned}$$

[14] The method we have used here is called *harmonic analysis.*

monics:

$$\left[-\omega^2 a + 2\zeta\omega\ b + a\right]\cos(\omega t) + \left[-\omega^2 b - 2\zeta\omega\ a + b\right]\sin(\omega t) + \\ + \frac{3}{4}\varepsilon\left[a^3\cos(\omega t) + b^3\sin(\omega t) + a^2 b\sin(\omega t) + ab^2\cos(\omega t)\right] = \\ = f\cos(\omega t)\,.$$

Thus,

$$\begin{cases} -\omega^2 a + 2\zeta\omega\ b + a + \frac{3}{4}\varepsilon a\left(a^2+b^2\right) = f \\ -\omega^2 b - 2\zeta\omega\ a + b + \frac{3}{4}\varepsilon b\left(a^2+b^2\right) = 0, \end{cases}$$

But $A_1 = a^2 + b^2$ therefore, by squaring both equations and adding them up, we have that:

$$A_1 = \frac{f}{\sqrt{\left(1-\omega^2+\frac{3}{4}\varepsilon A_1^2\right)^2 + (2\zeta\omega)^2}}. \tag{4.2.13}$$

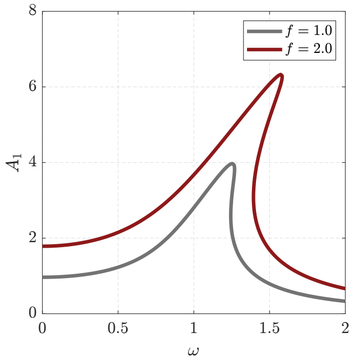

Figure 4.15. Frequency response curves for different values of f obtained using Eq. (4.2.13) with $\varepsilon = 0.05$ and $\zeta = 0.1$.

This equation highlights the relationship between the amplitude A_1, the driving force f, the frequency ω, the damping coefficient ζ, and the nonlinearity parameter ε.

Figure 4.15 presents two curves obtained by applying Eq. (4.2.13) under various operational conditions. These plots provide valuable insights into the amplitude response of the oscillator as a function of the driving frequency, highlighting the effects of nonlinearity and damping on the system's dynamics. This framework allow us to derive the coefficients of the Fourier series and analyze the Duffing oscillator response under the specified driving conditions, leading to insights regarding the system's dynamic behavior in the presence of nonlinearity and damping.

Section 4.3

Non-smooth Nonlinear Dynamical Systems

So far, we have considered nonlinear systems where the vector field $\mathbf{f}(\mathbf{x})$ is a continuous function. Therefore, the solution is a continuously differentiable curve, whose time derivative always (i.e., $\forall t \geq t_0$) follows the direction of the vector field. However, the requirement of the vector field to be continuous in many cases is too much restrictive.

Example Consider friction phenomena in mechanical systems, mechanical impacts, power electronics (switching in gates), genetic circuits, optimal control problems, sliding model control, relay feedback control, and many others. In non-smooth mechanics, the evolution of rigid bodies is subject to velocity jumps and force discontinuities as a result of friction and impacts [24].

Since the vector field is discontinuous, continuously differentiable curves that satisfy the associated dynamical system do not exist in general, and we must face the issue of identifying a suitable notion of solution. A look into the literature reveals that there is not a unique answer to this question. Depending on the specific problem at hand, authors have used different notions [23].

Caratheodory solutions are the most natural generalization of the classical notion of solution. Roughly speaking, one proceeds by allowing classical solutions not to follow the direction of the vector field at a few time instants. However, Caratheodory solutions do not exist in many applications. The reason is that their focus on the value of the vector field at each specific point makes them too rigid to cope with the discontinuities [23].

On the other hand, *Filippov solutions* utilize the concept of differential inclusion. To define a differential inclusion, one employs set-valued maps. Similar to a standard map, which associates a point in one space to a point in another, we can define a set-valued map as follows:

Definition 13 A set-valued map assigns a point in some space to a set of points in another space.

It is important to note that a standard map can be viewed as a set-valued map that maps points to singletons, which are sets containing a single point.

Definition 14 A differential inclusion is an equation that stipulates that the derivative of the state must belong to a set of permissible directions, rather than being confined to a specific direction determined by the vector field.

This added flexibility is crucial for establishing general conditions under which Filippov solutions exist. Such notions of solutions are particularly significant in a variety of applications, including mechanics involving friction and sliding mode control

[23].

The continuity of the vector field in ODEs does not necessarily ensure uniqueness of solutions, and this remains true for non-smooth vector fields regardless of the chosen solution concept. When uniqueness is absent, additional analysis is required, particularly when studying properties of dynamical systems. The potential for multiple solutions from the same initial condition introduces the need to differentiate between "weak" and "strong" properties. "Weak" properties are satisfied if at least one solution from each initial condition holds the property, while "strong" properties are satisfied if all solutions from each initial condition meet the criterion [23].

SUBSECTION 4.3.1

Hysteretic Mechanical Systems

As discussed in Chapter 2, a dynamical system can be formally defined as a combination of a state-space $\mathcal{X}$, a set of times $\mathcal{T}$, and a rule $\mathcal{R}$ that specifies how the system's state evolves over time. Hysteretic mechanical systems subjected to time-periodic inputs fit within this general framework. Specifically, these systems are governed by a set of first-order nonautonomous ODEs of the form:

$$\dot{\mathbf{x}} = \mathbf{F}\left(\mathbf{x}, t, \Omega\right), \tag{4.3.1}$$

where t represents time, $\mathbf{x}$ denotes the state vector containing the system's state variables, $\mathbf{F}$ represents a typically non-differentiable vector field associated with the problem, and Ω is the control parameter, referred to as the *continuation parameter*[15].

To analyze the behavior of Eq. (4.3.1), the governing ODEs can be reformulated, as outlined in Section 2.3.2. This is achieved by employing the transformation described in Eq. (2.3.3), resulting in a system of first-order autonomous ODEs expressed as follows:

$$\dot{\mathbf{x}} = \mathbf{f}\left(\mathbf{x}, \Omega\right). \tag{4.3.2}$$

It is important to note that in Eqs. (4.3.1) and (4.3.2), there is a slight abuse of notation, as the same symbol $\mathbf{x}$ is used to denote vectors of different dimensions, as well as the vector fields $\mathbf{F}$ and $\mathbf{f}$.

SUBSECTION 4.3.2

Mathematical Modeling of Hysteresis Phenomena

[15] Typically the driving frequency.

The analytical modeling and response prediction of hysteretic systems is an area of growing interest. Certain systems subjected to severe loading conditions, such as earthquakes and pressure shock waves, exhibit nonlinear hysteretic behavior. Additionally, some systems inherently possess nonlinear hysteretic characteristics [50].

Hysteresis is present in a variety of phenomena across disciplines including physics, chemistry, biology, and engineering. For example, in physics, hysteresis is observed in processes such as plasticity, friction, ferromagnetism, ferroelectricity, superconductivity, and in the adsorption and desorption processes, as well as in materials with shape memory. More broadly, hysteresis manifests in phase transitions [88].

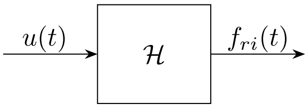

Figure 4.16. Hysteretic dynamical system.

Rate-dependent hysteresis has been recognized by mathematicians for many years, with Volterra's pioneering studies tracing back to the early 20^{th} century [89]. Conversely, the study of rate-independent hysteresis has a relatively short history, as mathematical developments in this area have lagged behind those in physics and engineering. While mathematics has been applied in the work of applied scientists on rate-independent hysteresis, it has often been utilized in a more calculus-oriented framework rather than through functional analysis. It was not until 1966 that a functional approach to rate-independent hysteresis was first introduced, pioneered by engineering student R. Bouc, who modeled various hysteresis phenomena by treating hysteresis as a mapping between function spaces [8, 9].

To illustrate these concepts, let us consider a simple system characterized by two scalar variables, u and f_{ri}, which depend continuously on time t. In the context of system theory, u is referred to as the input, while f_{ri} is designated as the output. This discussion adopts a purely *phenomenological* perspective.

Definition 15 In a phenomenological approach, the system is treated as a deterministic black box, disregarding its internal structure. It is assumed that the evolution of the output variable f_{ri} is determined only by the evolution of the input variable u (see Fig. 4.16).

4.3.2.1 Duhem Model

In this section, we introduce a rate-independent hysteresis model commonly attributed to the 19^{th} century physicist Pierre Duhem. This model offers a notable straightforward analytical representation; however, it presents certain limitations that restrict its applicability. Specifically, for some materials, the state cannot be fully characterized by the pair (u, f_{ri}), necessitating that the model also accounts for the evolution of one or more internal parameters [88].

In the Duhem model, for every differentiable input function $u(t)$ and for any initial value of the output function $f_{ri}(u_P) = f_P$, the output function $f_{ri}(t)$ is defined as the solution to the following Cauchy problem:

$$\begin{cases} \dot{f}_{ri} = k_1(u, f_{ri})\dot{u}^+ - k_2(u, f_{ri})\dot{u}^- \\ f_{ri}(u_P) = f_P \end{cases} \quad \text{in} \quad]0, T[, \tag{4.3.3}$$

where we define:

$$u^+ := \frac{|u| + u}{2}, \quad u^- := \frac{|u| - u}{2} \quad \forall u \in \mathbb{R},$$

whereas the functions k_1 and k_2 are non-negative and sufficiently regular to guarantee a unique solution to the previously defined Cauchy problem[16]. Assuming that Eq. (4.3.3) holds exclusively for $t > 0$ and imposing $dt > 0$, we obtain:

$$\frac{df_{ri}}{du} = \begin{cases} k_1(u, f_{ri}) & du > 0 \\ k_2(u, f_{ri}) & du < 0 \end{cases} \quad \text{in} \quad]0, T[\tag{4.3.4}$$

In such a way, by integrating the fields k_1 and k_2, two families of curves in the plane (u, f_{ri}) are obtained, which describe the evolutionary paths for increasing and decreasing u. These curves cover the entire plane $\mathbb{R}^2$ or a subset of it. By imposing:

$$\operatorname{sgn}(x) := \begin{cases} -1 & x < 0 \\ 0 & x = 0 \\ +1 & x > 0 \end{cases}$$

and

$$\begin{cases} k(u, f_{ri}, -1) := k_1(u, f_{ri}) \\ k(u, f_{ri}, 0) := 0 \\ k(u, f_{ri}, +1) := k_2(u, f_{ri}) \end{cases} \quad \forall (u, f_{ri}) \in \mathbb{R}^2,$$

we can rewrite Eq. (4.3.4) as:

$$\frac{df_{ri}}{du} = k\left(u, f_{ri}, \operatorname{sgn}(\dot{u})\right) \quad \text{in} \quad]0, T[\quad (dt > 0),$$

[16] They are Lipschitz in f_{ri} and continuous in t, thus for some $\varepsilon > 0$, there exists a unique solution $f_{ri}(t)$ to the initial value problem on the interval $[t_0 - \varepsilon, t_0 + \varepsilon]$.

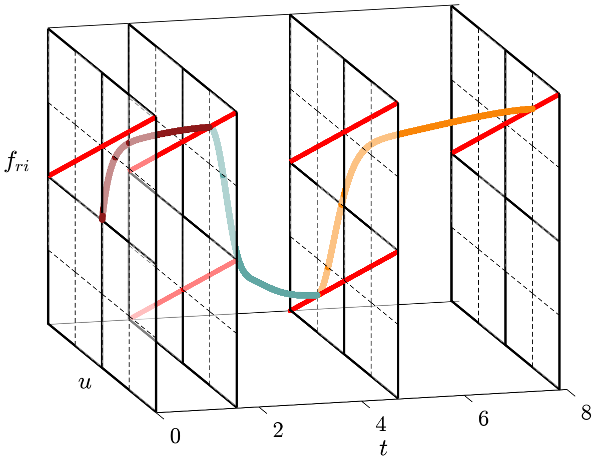

Figure 4.17. State-Space for the VRM+D.

or equivalently:

$$\frac{df_{ri}}{dt} = h\left(u, f_{ri}, \dot{u}\right) \quad \text{in} \quad]0, T[\quad (dt > 0),$$

where the function h is positively homogeneous of degree one with respect to $\dot{u}$. Hence, Duhem models are expressed by non-smooth differential equations of the form:

$$\dot{f}_{ri} = k\left(u, f_{ri}, \operatorname{sgn}(\dot{u})\right)\dot{u}. \tag{4.3.5}$$

4.3.2.2 Differential Vaiana-Rosati Model

Vaiana and Rosati introduced a new phenomenological model to simulate the rate-independent hysteretic behavior exhibited by mechanical systems [84]. This model, denominated, for simplicity, VRM, uses closed-form expressions for the evaluation of the output variable. Specifically, it enables an uncoupled modeling of the loading and unloading phases and permits an easy identification of the involved parameters thanks to their clear mechanical and/or graphical interpretation.

Recently, Vaiana and Rosati proposed an enhanced equivalent differential formulation of the model (VRM+D) to allow for its use in the field of nonlinear dynamics [83]. Both the original and reformulated models effectively address the challenges associated with the simulation of complex hysteresis phenomena and, thanks to the extension provided by VRM+D, offer a practical solution for the analysis of hysteretic mechanical systems.

According to the VRM+D [83], the generalized rate-independent hysteretic force f_{ri} is governed by the following ODE:

$$\dot{f}_{ri} = \left\{k_e\left(u\right) + k_b + \alpha f_0 + s\alpha\left[f_e\left(u\right) + k_b u - f_{ri}\right]\right\}\dot{u},$$

where the generalized function k_e is expressed as:

$$k_e\left(u\right) = \beta_1\beta_2 e^{\beta_2 u} + 4\gamma_1\gamma_2\frac{e^{-\gamma_2(u-\gamma_3)}}{\left[1+e^{-\gamma_2(u-\gamma_3)}\right]^2},$$

whereas f_e is given by:

$$f_e\left(u\right) = \beta_1\left(e^{\beta_2 u} - 1\right) + 2\gamma_1\frac{1-e^{-\gamma_2(u-\gamma_3)}}{1+e^{-\gamma_2(u-\gamma_3)}}.$$

An example of hysteresis loop obtaied using the VRM+D is shown in Fig. 4.17.

Furthermore, the model parameters need to be updated depending on the sign of the velocity $\dot{u}$, namely $s := \operatorname{sgn}\left(\dot{u}\right)$. In particular, $k_b = k_b^+\left(k_b^-\right)$, $f_0 = f_0^+\left(f_0^-\right)$, $\alpha = \alpha^+\left(\alpha^-\right)$, $\beta_1 = \beta_1^+\left(\beta_1^-\right)$, $\beta_2 = \beta_2^+\left(\beta_2^-\right)$, $\gamma_1 = \gamma_1^+\left(\gamma_1^-\right)$, $\gamma_2 = \gamma_2^+\left(\gamma_2^-\right)$, $\gamma_3 = \gamma_3^+\left(\gamma_3^-\right)$ if $s > 0$ $(s < 0)$. The mechanical/graphical interpretation of the above-mentioned model parameters is reported below for the reader convenience:

- k_b is the slope of the limiting straight lines when $\beta_1 = \beta_2 = \gamma_1 = \gamma_2 = \gamma_3 = 0$;
- f_0 represents the ordinate of the intersection point between the limiting curve and the vertical axis;
- α represents the grow rate of the hysteretic tangent stiffness;
- β_1, β_2, γ_1 and γ_2 allow us to transform the limiting straight lines into limiting curves with different number of inflecting points;
- γ_3 allow us to modify the position of the inflection point.

More details on the mechanical/graphical interpretation of the above model parameters can be found in [83, 84].

Subsection 4.3.3

Poincaré Map Based Continuation

The problem of constructing periodic solutions of general nonlinear dynamical systems and assessing their stability is a common problem in applied mechanics as well as in various fields of applied sciences [50].

When dealing with strong nonlinearities and with a global dynamic behavior, recourse to numerical technique is nearly unavoidable[17]. The Poincaré map based continuation method is a numerical algorithm to compute variation of periodic solutions and their codimension-one bifurcations. It is particularly useful in the case of non-smooth systems[18] since some components of the vector field are non-differentiable.

This section presents a brief overview of the Poincaré map-based continuation procedure, in the form originally introduced in [50], to facilitate the efficient numerical calculation of periodic solutions for hysteretic dynamical systems subjected to a time-periodic input. This method also enables the determination of stability and bifurcations through the use of Floquet's Theory. Our objective is to provide a comprehensive framework with particular emphasis on implementation details able to ensure the reproducibility of the procedure.

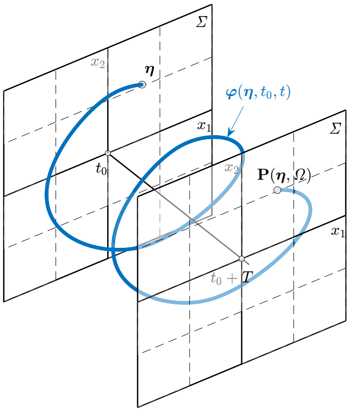

Figure 4.18. Graphical representation of the first return map for a 2D nonautonomous system periodic in time with period T.

4.3.3.1 How to find periodic solutions

Computing periodic solutions for hysteretic mechanical systems under time-periodic inputs is a highly challenging task. However, in the case of the n-dimensional hysteretic mechanical systems described by Eq. (4.3.2), the period associated with a periodic orbit can be explicitly determined. This is due to the fact that the vector field $\mathbf{f}$ exhibits periodicity with a period $T = \frac{2\pi}{\Omega}$. As a result, a periodic solution of Eq. (4.3.2) will have a period that is either an integer multiple or an integer submultiple of T. The knowledge of this period can be used, as shown in the sequel, to construct a Poincaré section, enabling the mapping of intersecting points after a specific return period $T^{\mathrm{j}} = \mathrm{j}T$ [47, 62].

A *Poincaré section* is a hypersurface in the state-space defined as:

$$\Sigma := \left\{ \mathbf{x} \in \mathbb{R}^{\mathrm{n}-1} \times \mathbb{S} : x_n = \mathrm{j}\frac{2\pi}{T}(t - t_0) \right\},$$

where $x_n = \Omega t \pmod{2\pi}$ is the additional state variable introduced to deal with time dependence. Moreover, the space which

---

[17] This is the case with hysteretic systems.

[18] Specifically, in the case of hysteretic systems.

the state variables belong to is a cylindrical space written as $\mathbb{R}^{\mathrm{n}-1} \times \mathbb{S}$ [62].

The hypersurface Σ of dimension $(n-1)$ must be chosen so as to ensure that the flow defined by Eq. (4.3.2) is everywhere transversal to Σ [36], that is:

$$\mathbf{n}\left(\mathbf{x}\right) \cdot \mathbf{f}\left(\mathbf{x}, \Omega\right) \neq 0 \quad \forall \mathbf{x} \in \Sigma,$$

where $\mathbf{n}\left(\mathbf{x}\right)$ represents the unit vector normal to the Poincaré section Σ at point $\mathbf{x}$.

To obtain a global section[19] the $(n \times 1)$ normal vector $\mathbf{n}(\mathbf{x})$ is defined as:

$$\mathbf{n}(\mathbf{x}) \coloneqq \begin{bmatrix} 0 \\ \vdots \\ 0 \\ 1 \end{bmatrix} \quad \forall \mathbf{x} \in \mathbb{R}^{\mathrm{n}-1} \times \mathbb{S}.$$

It is now possible to introduce a *Poincaré map* based on the return time T^{j} as the value that the trajectory having $\tilde{\mathbf{x}} \in \Sigma$ as its initial point at time t_0 takes on when $t = t_0 + T^{\mathrm{j}}$. In other words, we can express the Poincaré map as:

$$\mathbf{P}^{\mathrm{j}}\left(\mathbf{x}, \Omega\right) : \Sigma \to \Sigma \quad \mathbf{P}^{\mathrm{j}}\left(\tilde{\mathbf{x}}, \Omega\right) = \boldsymbol{\varphi}\left(\tilde{\mathbf{x}}, t_0, t_0 + T^{\mathrm{j}}\right).$$

Hence, assuming that a specific point $\boldsymbol{\eta} \in \Sigma$ is a fixed-point of the first return map $\mathbf{P}\left(\boldsymbol{\eta}, \Omega\right)$, then all trajectories starting from $\boldsymbol{\eta}$ return to the same point after a period T, which is equal to the period of the input (Fig. 4.18). This condition, called fixed-point condition, can then be written as follows:

$$\mathbf{P}\left(\boldsymbol{\eta}, \Omega\right) = \boldsymbol{\eta},$$

and a periodic solution can be found as a solution of the fixed-point equation:

$$\mathbf{P}\left(\boldsymbol{\eta}, \Omega\right) - \boldsymbol{\eta} = \mathbf{0}. \tag{4.3.6}$$

This is conceptually simpler than searching for periodic solution, but it requires refined numerical tools to solve the problem. Moreover, since most of the problems of interest do not have a closed-form expression for the Poincaré map, it is necessary to rely on approximate methods or simulations instead of analytical solutions.

[19] Transverse to the flow everywhere in the state-space.

4.3.3.2 How to solve the fixed-point equation

When strong nonlinearities are involved, numerical techniques such as continuation become necessary to solve the fixed-point equation. This is especially true in the case of hysteretic mechanical systems since a time-periodic input can cause different behavior depending on the frequency of the applied loading.

Basically a continuation scheme is a numerical algorithm that:

- compute solution branches through both regular points and singular points;
- detect and diagnose bifurcation points;
- switch branches at bifurcation points.

In practice, it is rare that an analytical solution to Eq. (4.3.6) can be found, although it is commonly assumed that at least one solution point $(\boldsymbol{\eta}_0, \Omega_0)$ is known a priori. Due to the difficulty in finding analytical solution, a great deal of work in the technical literature has been directed towards developing efficient and accurate numerical continuation schemes to compute approximate solutions. Hence, the two basic steps of a continuation scheme are:

1. A predictor step to generate an initial guess of a new solution point $(\boldsymbol{\eta}^{(1)}, \Omega^{(1)})$ near the last converged solution point.
2. An iterative correction algorithm designed to successively update and improve the initial guess until some convergence criterion is met.

Perhaps the most popular solution algorithm with these capabilities is the *pseudo-arclength* continuation scheme [47, 73, 95].

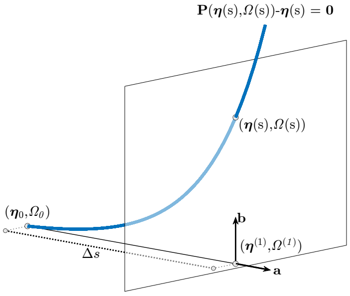

Figure 4.19. Graphical representation of the pseudo-arclength scheme in the case of 3D $(\boldsymbol{\eta}, \Omega)$-space.

4.3.3.3 Pseudo-arclength continuation method

The pseudo-arclength method describes the solution path defined by Eq. (4.3.6) incrementally, using a sequence of arclength increments Δs. The main idea is to extrapolate a distance of Δs in the $(\boldsymbol{\eta}, \Omega)$-space from the known solution point $(\boldsymbol{\eta}_0, \Omega_0)$ along the tangent vector $\mathbf{a}$ at the known solution point. This serves as a prediction, but then a numerical method is performed to get back onto the solution branch, as shown in [33], individuated by its intersection with the plane perpendicular to $\mathbf{a}$ at a distance of

Δs. Figure 4.19 shows a representation of the pseudo-arclength continuation method where s denotes the arclength along the solution curve.

Expressing both the periodic solution $\boldsymbol{\eta}$ and the continuation parameter Ω as functions of the coordinate s, the number of unknowns is increased by one and the fixed-point equation (4.3.6) is reparameterized as:

$$\mathbf{p}\left(\boldsymbol{\eta}(s), \Omega(s)\right) = \mathbf{P}\left(\boldsymbol{\eta}(s), \Omega(s)\right) - \boldsymbol{\eta}(s) = \mathbf{0}. \tag{4.3.7}$$

The initial prediction is evaluated by means of a linear extrapolation along the unit tangent direction $\mathbf{a}$ defined as:

$$\mathbf{a} = \left[\frac{\partial \boldsymbol{\eta}_0}{\partial s}, \frac{\partial \Omega_0}{\partial s}\right]^{\mathrm{T}}.$$

Since $(\boldsymbol{\eta}(s), \Omega(s))$ satisfies Eq. (4.3.7) $\forall s$, at $s_0 + \Delta s$, the new solution point must satisfy the Taylor expansion of Eq. (4.3.7) at $s_0 + \Delta s$, given by:

$$\begin{aligned}&\mathbf{p}(\boldsymbol{\eta}(s_0 + \Delta s), \Omega(s_0 + \Delta s)) = \\ &\quad = \left[\mathbf{p}_{\boldsymbol{\eta}}(\boldsymbol{\eta}(s_0), \Omega(s_0)) \cdot \boldsymbol{\eta}_s + \mathbf{p}_{\Omega}(\boldsymbol{\eta}(s_0), \Omega(s_0))\Omega_s\right] \Delta s + \ldots,\end{aligned} \tag{4.3.8}$$

where the subscript denotes differentiation with respect to the subscript. By neglecting higher-order terms, one can cast in matrix form Eq. (4.3.8) as:

$$\left[\mathbf{p}_{\boldsymbol{\eta}}(\boldsymbol{\eta}(s_0), \Omega(s_0)), \mathbf{p}_{\Omega}(\boldsymbol{\eta}(s_0), \Omega(s_0))\right] \cdot \mathbf{a} = \mathbf{0},$$

where $\left[\mathbf{p}_{\boldsymbol{\eta}}, \mathbf{p}_{\Omega}\right]$ is the $(n+1) \times (n+1)$ matrix, and $\mathbf{a}$ the $(n+1)$ tangent vector, evaluated in the point with abscissa s_0 (Fig. 4.19). At this point, we assume that the tangent vector $\mathbf{a}$ has unit length by imposing $\mathbf{a} \cdot \mathbf{a} = 1$, which gives:

$$\boldsymbol{\eta}_s \cdot \boldsymbol{\eta}_s + \Omega_s^2 = 1. \tag{4.3.9}$$

The matrix $\mathbf{p}_{\boldsymbol{\eta}}$ is assumed to be nonsingular together with $\mathbf{p}_{\Omega} \neq \mathbf{0}$ [47]. Therefore, Eq. (4.3.8) can be rewritten as:

$$\mathbf{p}_{\boldsymbol{\eta}}(\boldsymbol{\eta}(s_0), \Omega(s_0)) \cdot \boldsymbol{\eta}_s = -\mathbf{p}_{\Omega}(\boldsymbol{\eta}(s_0), \Omega(s_0))\Omega_s,$$

since $\boldsymbol{\eta}_s$ is proportional to Ω_s, the unknown vector $\boldsymbol{\eta}_s$ is expressed as:

$$\boldsymbol{\eta}_s = \Omega_s \mathbf{c},$$

while the normalization condition (Eq. (4.3.9)) solved for Ω_s, gives:

$$\Omega_s = \pm\frac{1}{\sqrt{\mathbf{c}\cdot\mathbf{c}+1}}.$$

The sign in the previous equation is chosen such that the orientation of $\mathbf{a}$ is close to that of the tangent vector $\mathbf{a}_{\text{previous}}$ at the previous value of s, i.e. we require $\mathbf{a}\mathbf{a}^T_{\text{previous}} > 0$ [72]. The initial guess for the updated solution at $s_0 + \Delta s$ can be obtained as:

$$\begin{bmatrix}\boldsymbol{\eta}^{(1)}\\ \Omega^{(1)}\end{bmatrix} = \begin{bmatrix}\boldsymbol{\eta}_0\\ \Omega_0\end{bmatrix} + \mathbf{a}\Delta s,$$

The updated equilibrium solution is sought as the intersection between the plane perpendicular to the unit tangent vector $\mathbf{a}$ passing through $\left[\boldsymbol{\eta}^{(1)}, \Omega^{(1)}\right]^T$ and the solution curve (Fig. 4.19).

Denoting by $\mathbf{b}$ the vector normal to the tangent vector $\mathbf{a}$ passing through $(\boldsymbol{\eta}^{(1)}, \Omega^{(1)})$:

$$\mathbf{b} = \begin{bmatrix}\boldsymbol{\eta}(s) - \boldsymbol{\eta}^{(1)}\\ \Omega(s) - \Omega^{(1)}\end{bmatrix},$$

the updated state of the system $(\boldsymbol{\eta}(s), \Omega(s))$ is sought as the solution of the fixed-point equation, e.g., Eq. (4.3.7), subjected to the orthogonality condition $\mathbf{b}\cdot\mathbf{a} = 0$. Hence, one has to solve the following nonlinear equation:

$$g\left(\boldsymbol{\eta}(s), \Omega(s)\right) = \left[\boldsymbol{\eta}(s) - \boldsymbol{\eta}_0\right]\cdot\frac{\partial\boldsymbol{\eta}_0}{\partial s} + \left[\Omega(s) - \Omega_0\right]\frac{\partial\Omega_0}{\partial s} - \Delta s = 0.$$

Based on the known solution point $(\boldsymbol{\eta}_0, \Omega_0)$, and given the Δs increment, the solution of the augmented system is sought as a solution of the following system:

$$\begin{cases}\mathbf{p}\left(\boldsymbol{\eta}(s), \Omega(s)\right) = \mathbf{0}\\ g\left(\boldsymbol{\eta}(s), \Omega(s)\right) = 0.\end{cases} \tag{4.3.10}$$

To solve the system of nonlinear equations obtained in Eq. (4.3.10), several methods can be used, as shown in [31–33]. The most classical one, used for example in [48–50], is the Newton-Raphson method.

4.3.3.4 Newton-Raphson method

According to the Newton-Raphson method, at the k-th iteration, one sets:

$$\begin{aligned}\boldsymbol{\eta}^{(\text{k})} &= \boldsymbol{\eta}^{(\text{k-1})} + \Delta\boldsymbol{\eta}^{(\text{k})},\\ \Omega^{(\text{k})} &= \Omega^{(\text{k-1})} + \Delta\Omega^{(\text{k})},\end{aligned}$$

into Eq. (4.3.10) so that a Taylor expansion about $(\boldsymbol{\eta}^{(\text{k-1})}, \Omega^{(\text{k-1})})$ yields the incremental linearized equations in matrix form:

$$\mathbf{J}^{(\text{k-1})}\Delta\mathbf{z}^{(\text{k})} = -\mathbf{r}^{(\text{k-1})}, \tag{4.3.11}$$

where the notation (k-1) indicates that the scalar and matrix-valued functions are evaluated at $(\boldsymbol{\eta}^{(\text{k-1})}, \Omega^{(\text{k-1})})$. In particular, the augmented unknown vector and the augmented residual vector are given, respectively, by:

$$\begin{aligned}\Delta\mathbf{z}^{(\text{k})} &= \begin{bmatrix}\Delta\boldsymbol{\eta}^{(\text{k})}\\ \Delta\Omega^{(\text{k})}\end{bmatrix},\\ \mathbf{r}^{(\text{k-1})} &= \begin{bmatrix}\mathbf{P}\left(\boldsymbol{\eta}^{(\text{k-1})}, \Omega^{(\text{k-1})}\right) - \boldsymbol{\eta}^{(\text{k-1})}\\ g\left(\boldsymbol{\eta}^{(\text{k-1})}, \Omega^{(\text{k-1})}\right)\end{bmatrix},\end{aligned}$$

while the augmented $(n+1)\times(n+1)$ Jacobian matrix is:

$$\mathbf{J}^{(\text{k-1})} = \begin{bmatrix}\left(\frac{\partial\mathbf{P}}{\partial\boldsymbol{\eta}} - \mathbf{I}\right)^{(\text{k-1})} & \left(\frac{\partial\mathbf{P}}{\partial\Omega}\right)^{(\text{k-1})}\\ \left(\frac{\partial\boldsymbol{\eta}_0}{\partial s}\right)^{\text{T}} & \frac{\partial\Omega_0}{\partial s}\end{bmatrix}.$$

The Jacobian matrix of the Poincaré map with respect to the periodic solution $\boldsymbol{\eta}$ and the control parameter Ω is computed via a central finite-difference scheme, according to the following expressions:

$$\begin{aligned}\frac{\partial\mathbf{P}}{\partial\boldsymbol{\eta}}\cdot\mathbf{e}_{\text{m}} &\approx \frac{\mathbf{P}(\boldsymbol{\eta}+\delta_1\mathbf{e}_{\text{m}},\Omega) - \mathbf{P}(\boldsymbol{\eta}-\delta_1\mathbf{e}_{\text{m}},\Omega)}{2\delta_1},\\ \frac{\partial\mathbf{P}}{\partial\Omega} &\approx \frac{\mathbf{P}(\boldsymbol{\eta},\Omega+\delta_2) - \mathbf{P}(\boldsymbol{\eta},\Omega-\delta_2)}{2\delta_2},\end{aligned} \tag{4.3.12}$$

where δ_1 and δ_2 are the finite differences in the two gradients computations, respectively, and $\mathbf{e}_{\text{m}}$ is the m-th column of the $(n\times n)$ identity matrix $\mathbf{I}$.

Since the Jacobian $\mathbf{J}$ is generally nonsingular [47], the solution can be determined as:

$$\Delta\mathbf{z}^{(\mathrm{k})} = -\left[\mathbf{J}^{(\mathrm{k\text{-}1})}\right]^{-1}\mathbf{r}^{(\mathrm{k\text{-}1})}.$$

The iterations are continued until a suitable convergence condition is satisfied.

When the convergence is achieved, the new periodic solution on the solution curve at $s + \Delta s$ is assumed as the new known solution $(\boldsymbol{\eta}_0, \Omega_0)$.

Remark Since the matrix $\mathbf{p}_{\boldsymbol{\eta}}^{(\mathrm{k\text{-}1})} = \left(\frac{\partial\mathbf{P}}{\partial\boldsymbol{\eta}} - \mathbf{I}\right)^{(\mathrm{k\text{-}1})}$ is almost everywhere nonsingular [47], a bordering algorithm may be employed as follows:

$$\mathbf{p}_{\boldsymbol{\eta}}^{(\mathrm{k\text{-}1})} \cdot \Delta\boldsymbol{\eta}^{(\mathrm{k})} = -\mathbf{p}^{(\mathrm{k\text{-}1})} - \mathbf{p}_{\Omega}^{(\mathrm{k\text{-}1})}\Delta\Omega^{(\mathrm{k})}.$$

By virtue of the principle of superposition, the incremental vector $\Delta\boldsymbol{\eta}^{(\mathrm{k})}$ is expressed as a linear combination of two vectors according to:

$$\Delta\boldsymbol{\eta}^{(\mathrm{k})} = \mathbf{z}_1 + \Delta\Omega^{(\mathrm{k})}\mathbf{z}_2, \tag{4.3.13}$$

where $\mathbf{z}_1$ and $\mathbf{z}_2$ are found by solving the following linear equations:

$$\begin{aligned}\mathbf{p}_{\boldsymbol{\eta}}^{(\mathrm{k\text{-}1})} \cdot \mathbf{z}_1 &= -\mathbf{p}^{(\mathrm{k\text{-}1})},\\ \mathbf{p}_{\boldsymbol{\eta}}^{(\mathrm{k\text{-}1})} \cdot \mathbf{z}_2 &= -\mathbf{p}_{\Omega}^{(\mathrm{k\text{-}1})}.\end{aligned}$$

If the matrix $\mathbf{p}_{\boldsymbol{\eta}}^{(\mathrm{k\text{-}1})}$ does not happen to become singular at any of the iterative steps, the unknown vectors can be determined as:

$$\begin{aligned}\mathbf{z}_1 &= -\left[\mathbf{p}_{\boldsymbol{\eta}}^{(\mathrm{k\text{-}1})}\right]^{-1} \cdot \mathbf{p}^{(\mathrm{k\text{-}1})},\\ \mathbf{z}_2 &= -\left[\mathbf{p}_{\boldsymbol{\eta}}^{(\mathrm{k\text{-}1})}\right]^{-1} \cdot \mathbf{p}_{\Omega}^{(\mathrm{k\text{-}1})}.\end{aligned}$$

The incremental load multiplier $\Delta\Omega^{(\mathrm{k})}$ is obtained through the $(n+1)$-th equations, given by the second equation in Eqs. (4.3.11), which, by substitution of Eq. (4.3.13), the increment is obtained as:

$$\Delta\Omega^{(\mathrm{k})} = -\frac{\boldsymbol{\eta}_s \cdot \mathbf{z}_1 + g^{(\mathrm{k\text{-}1})}}{\boldsymbol{\eta}_s \cdot \mathbf{z}_2 + \Omega_s}.$$

Initial conditions

```
Start with $(\boldsymbol{\eta}_0, \Omega_0)$ and $\Delta s$
set stepcut $= 0$, contflag $= 0$, PA iter $= 1$
```

Computations at each Pseudo-Arclength (PA) step

```
while (contflag == 0)
    Compute initial prediction $\left(\boldsymbol{\eta}^{(1)}, \Omega^{(1)}\right)$
    set corrflag $= 0$
    while (corrflag == 0)
        Correct the initial prediction$^{\star}$
        Check corrector stopping criteria$^{\dagger}$
    if (corrflag == 1)
        Study Stability and Bifurcation
        PA iter $= +1$, stepcut $= 0$, adjust $\Delta s$ and $(\boldsymbol{\eta}_0, \Omega_0)$
    else
        $\Delta s = \frac{\Delta s}{2}$, stepcut $= +1$
        Check continuation stopping criteria$^{\ddagger}$
end
```

* Newton-Raphson
Modified Newton-Raphson
Krylov accelerated Newton-Raphson

† (corrflag $= 1$) convergence attained
(corrflag $= 2$) divergence detected
(corrflag $= 3$) maximum number of iterations exceeded

‡ (contflag $= 1$) exceeded maximum number of steps
(contflag $= 2$) $\Omega_0 < \Omega_{\text{min}}$
(contflag $= 3$) $\Omega_0 > \Omega_{\text{max}}$

Table 4.3. Pseudo Code of the Pseudo-Arclength continuation method.

4.3.3.5 Pseudocode description

In this section, we present a detailed description of the pseudocode outlined in Table 4.3. A step-by-step analysis is provided to explain the logic and methodology behind each line of the pseudocode, aiming to clarify its computational processes and algorithmic structure.

The arclength parameter s is used for continuation and, to compute the solution at $s + \Delta s$, a Newton-Raphson scheme is employed with a tangent predictor, in conjunction with the bordering algorithm. The iterations proceed until the convergence criterion is met within the Newton-Raphson process.

Initial Conditions The initial stage of the analysis involves defining the parameters of the hysteretic mechanical system under consideration. Specifically, the excitation frequency Ω is designated as the control parameter governing the system's dynamic behavior. This methodological approach enables the investigation of the system's response over a range of frequencies, providing a comprehensive understanding of its complex behavior under external excitation across varying amplitude levels.

The parameters employed in the pseudo-arclength path following procedure are summarized in Table 4.4. The selection of these parameters is grounded in a robust foundation of previous studies, particularly those conducted by Lacarbonara and collaborators, which have consistently demonstrated the algorithm's reliable convergence characteristics [50].

In earlier investigations by Lacarbonara and Vestroni [49], a central finite-difference scheme was used to compute the Jacobian of the Poincaré map for Masing and Bouc–Wen oscillators. In these studies, the tolerances for the convergence test ($tol = 10^{-6}$) and the finite difference increment ($\delta_i = 10^{-3}$) were determined as optimal. The normalized time step ($T/\Delta t = 2048$) was also carefully chosen, with the study revealing that the bifurcation results were not sensitive to the specific numerical integration method used, whether it was the fourth-order Runge–Kutta or the Fehlberg-Dormand-Prince schemes.

Subsequent research [48] continued this approach, confirming that the use of central-difference schemes for Jacobian computation and the previously prescribed tolerances and time steps ($T/\Delta t = 2048$) yielded consistent and reliable results. The robustness of the algorithm was further verified, with no significant sensitivity to the choice of numerical integration scheme affecting the bifurcation outcomes.

In more recent work [32], the authors adopted a fourth-order Runge–Kutta procedure with a fixed time step. Again, the tolerances for the convergence test ($tol = 10^{-6}$) and finite difference increments ($\delta_i = 10^{-3}$) remained consistent. The number of time steps per excitation period ($T/\Delta t = 2048$) was maintained, further corroborating the stability and insensitivity of these parameters to the specific numerical method used for bifurcation analysis.

This well-established parameter set, detailed in Table 4.4, ensures the stability of the numerical procedures, with minimal

Table 4.4. Parameters used for the pseudo-archlength path following procedure.

$T/\Delta t$	δ_1	δ_2	*tol*	$\Delta s_{\min}$	$\Delta s_{\max}$	$\bar{k}$	k^{m}
2048	10^{-3}	10^{-3}	10^{-6}	10^{-10}	10^{-3}	10	100

impact on the accuracy of the bifurcation results.

To obtain an initial equilibrium point $(\boldsymbol{\eta}_0, \Omega_0)$, we solve the equation of motion for the hysteretic mechanical system with zero initial conditions, for a time of integration $t_{\max} = 100\,T$. In such a way, the steady-state response can be obtained for the first value of Ω analyzed.

At this point we can enforce the following quantities: stepcut = 0, contflag = 0, PA iter = 1.

Computations at each Pseudo-Arclength step

1. **Compute initial prediction:** While we are still within the Pseudo-Arclength (PA) algorithm, we start by computing the following matrix associated with the equilibrium point $(\boldsymbol{\eta}_0, \Omega_0)$:

$$\mathbf{J}^0 = \begin{bmatrix} \left(\frac{\partial \mathbf{P}}{\partial \boldsymbol{\eta}} - \mathbf{I}\right)_0 & \left(\frac{\partial \mathbf{P}}{\partial \Omega}\right)_0 \\ \left(\frac{\partial \boldsymbol{\eta}_0}{\partial s}\right)^{\mathrm{T}} & \frac{\partial \Omega_0}{\partial s} \end{bmatrix}.$$

The components of the Jacobian matrix of the map, and those of the derivative of the map with respect to the control parameter are computed numerically via a finite-difference scheme, with a central-difference technique. The following quantities are evaluated to compute numerically the elements on the first row of $\mathbf{J}^0$:

$$\frac{\partial \mathbf{P}}{\partial \boldsymbol{\eta}} \cdot \mathbf{e}_{\mathrm{m}} \approx \frac{\mathbf{P}(\boldsymbol{\eta}_0 + \delta_1 \mathbf{e}_{\mathrm{m}}, \Omega_0) - \mathbf{P}(\boldsymbol{\eta}_0 - \delta_1 \mathbf{e}_{\mathrm{m}}, \Omega_0)}{2\delta_1},$$

$$\frac{\partial \mathbf{P}}{\partial \Omega} \approx \frac{\mathbf{P}(\boldsymbol{\eta}_0, \Omega_0 + \delta_2) - \mathbf{P}(\boldsymbol{\eta}_0, \Omega_0 - \delta_2)}{2\delta_2}.$$

where $\mathbf{e}_{\mathrm{m}}$ is the m-th column of the $(n \times n)$ identity matrix, δ_1 and δ_2 are the central-difference parameters (10^{-3}). In order to compute the Poincaré map, we use a fourth-order Runge-Kutta scheme (ode45) to integrate Eq. (4.3.1) from t_0 to $t_0 + T_n$ subject to the initial condition $\boldsymbol{\eta}_0$.

The matrix $\frac{\partial \mathbf{P}}{\partial \boldsymbol{\eta}}$ for the system under consideration will have dimensions $n \times n$, given that $\mathbf{P}(\boldsymbol{\eta}, \Omega)$ is a $(n \times 1)$

vector, as is the vector $\boldsymbol{\eta}_0$ with respect to which it is derived. Whereas, $\frac{\partial \mathbf{P}}{\partial \Omega}$ is a $(n \times 1)$ vector. In particular, the components of the matrices $\frac{\partial \mathbf{P}}{\partial \boldsymbol{\eta}}$ and $\frac{\partial \mathbf{P}}{\partial \Omega}$ are expressed as follows:

$$\frac{\partial \mathbf{P}}{\partial \boldsymbol{\eta}} \cdot \begin{bmatrix} 1 \\ \vdots \\ 0 \end{bmatrix} = \frac{\mathbf{P}\left(\boldsymbol{\eta}_0 + \delta_1 \begin{bmatrix} 1 \\ \vdots \\ 0 \end{bmatrix}, \Omega_0\right) - \mathbf{P}\left(\boldsymbol{\eta}_0 - \delta_1 \begin{bmatrix} 1 \\ \vdots \\ 0 \end{bmatrix}, \Omega_0\right)}{2\delta_1},$$

$$\frac{\partial \mathbf{P}}{\partial \boldsymbol{\eta}} \cdot \begin{bmatrix} 0 \\ \vdots \\ 1 \end{bmatrix} = \frac{\mathbf{P}\left(\boldsymbol{\eta}_0 + \delta_1 \begin{bmatrix} 0 \\ \vdots \\ 1 \end{bmatrix}, \Omega_0\right) - \mathbf{P}\left(\boldsymbol{\eta}_0 - \delta_1 \begin{bmatrix} 0 \\ \vdots \\ 1 \end{bmatrix}, \Omega_0\right)}{2\delta_1},$$

$$\frac{\partial \mathbf{P}}{\partial \Omega} = \frac{\mathbf{P}\left(\boldsymbol{\eta}_0, \Omega_0 + \delta_2\right) - \mathbf{P}\left(\boldsymbol{\eta}_0, \Omega_0 - \delta_2\right)}{2\delta_2}.$$

Now recalling the Taylor series expansion made for the initial problem $\mathbf{P}\left(\boldsymbol{\eta}(s), \Omega(s)\right) - \boldsymbol{\eta}(s) = \mathbf{0}$ we have that:

$$\left(\frac{\partial \mathbf{P}}{\partial \boldsymbol{\eta}} - \mathbf{I}\right)_0 \cdot \frac{\partial \boldsymbol{\eta}_0}{\partial s} = -\left(\frac{\partial \mathbf{P}}{\partial \Omega}\right)_0 \frac{\partial \Omega_0}{\partial s}.$$

Since $\frac{\partial \boldsymbol{\eta}_0}{\partial s}$ and $\frac{\partial \Omega_0}{\partial s}$ are proportional, the unknown vector $\frac{\partial \boldsymbol{\eta}_0}{\partial s}$ can be expressed as:

$$\frac{\partial \boldsymbol{\eta}_0}{\partial s} = \frac{\partial \Omega_0}{\partial s} \mathbf{z}, \tag{4.3.14}$$

through which we can write:

$$\left(\frac{\partial \mathbf{P}}{\partial \boldsymbol{\eta}} - \mathbf{I}\right)_0 \cdot \mathbf{z} = -\left(\frac{\partial \mathbf{P}}{\partial \Omega}\right)_0.$$

In this expression the only unknown quantity is the $\mathbf{z}$ vector which can be computed as:

$$\mathbf{z} = -\left(\frac{\partial \mathbf{P}}{\partial \boldsymbol{\eta}} - \mathbf{I}\right)_0^{-1} \left(\frac{\partial \mathbf{P}}{\partial \Omega}\right)_0.$$

On the other hand, the requirement for the tangent vector

a to have unit norm enables us to compute $\frac{\partial \Omega_0}{\partial s}$ as:

$$\frac{\partial \boldsymbol{\eta}_0}{\partial s} \cdot \frac{\partial \boldsymbol{\eta}_0}{\partial s} + \left(\frac{\partial \Omega_0}{\partial s}\right)^2 = 1 \rightarrow \frac{\partial \Omega_0}{\partial s} = \pm \frac{1}{\sqrt{\mathbf{c} \cdot \mathbf{c} + 1}}.$$

Specifically, the sign in this expression is chosen such that the orientation of **a** is close to that of the preceding vector **a** (indicated as $\mathbf{a}^{\text{pre}}$). This implies checking whether $\mathbf{a} \cdot \mathbf{a}^{\text{pre}} > 0$ (or < 0). In this case, the sign will be set to + (-).

At this point, by invoking Eq. (4.3.14) we can compute $\frac{\partial \boldsymbol{\eta}_0}{\partial s}$ and complete the evaluation of the Jacobian matrix $\mathbf{J}^0$, and also proceed to evaluate the initial prediction as:

$$\begin{bmatrix} \boldsymbol{\eta}^{(1)} \\ \Omega^{(1)} \end{bmatrix} = \begin{bmatrix} \boldsymbol{\eta}_0 \\ \Omega_0 \end{bmatrix} + \mathbf{a}\Delta s.$$

2. **Correct the initial prediction:** To correct the initial prediction, several methods can be used, such as the Newton-Raphson method, the Modified Newton-Raphson method, and the Krylov-accelerated Newton-Raphson method, as shown in [31–33].

   The most classical method, used for example in [48–50], is the Newton-Raphson method, for which we begin with the evaluation of the residual:

$$\mathbf{r}^{(\text{k-1})} = \begin{bmatrix} \mathbf{P}\left(\boldsymbol{\eta}^{(\text{k-1})}, \Omega^{(\text{k-1})}\right) - \boldsymbol{\eta}^{(\text{k-1})} \\ g\left(\boldsymbol{\eta}^{(\text{k-1})}, \Omega^{(\text{k-1})}\right) \end{bmatrix}.$$

   Specifically, if $|\mathbf{r}^{(\text{k-1})}| < tol$, the iterations are ended. Otherwise, since $\left(\frac{\partial \mathbf{P}}{\partial \boldsymbol{\eta}} - \mathbf{I}\right)^{(\text{k-1})}$ is nonsingular almost everywhere [47], a bordering algorithm can be employed to obtain a new estimation of the solution point. Based on the bordering algorithm, and invoking the superposition principle, we can set:

$$\Delta \boldsymbol{\eta}^{(\text{k})} = \mathbf{z}_1 + \Delta \Omega^{(\text{k})} \mathbf{z}_2,$$

the two unknown vectors $\mathbf{z}_1$ and $\mathbf{z}_2$ can be computed as:

$$\mathbf{z}_1 = -\left[\left(\frac{\partial \mathbf{P}}{\partial \boldsymbol{\eta}} - \mathbf{I}\right)^{\text{(k-1)}}\right]^{-1} \cdot \left[\mathbf{P}\left(\boldsymbol{\eta}^{\text{(k-1)}}, \Omega^{\text{(k-1)}}\right) - \boldsymbol{\eta}^{\text{(k-1)}}\right],$$

$$\mathbf{z}_2 = -\left[\left(\frac{\partial \mathbf{P}}{\partial \boldsymbol{\eta}} - \mathbf{I}\right)^{\text{(k-1)}}\right]^{-1} \cdot \left(\frac{\partial \mathbf{P}}{\partial \Omega}\right)^{\text{(k-1)}}.$$

On the other hand, the increment $\Delta\Omega^{\text{(k)}}$ can be obtained as:

$$\Delta\Omega^{\text{(k)}} = -\frac{\frac{\partial \boldsymbol{\eta}_0}{\partial s} \cdot \mathbf{z}_1 + g^{\text{(k-1)}}}{\frac{\partial \boldsymbol{\eta}_0}{\partial s} \cdot \mathbf{z}_2 + \frac{\partial \Omega_0}{\partial s}}.$$

3. **Study stability and bifurcations:** An additional advantage of the described procedure is the possibility of using Poincaré maps to determine the stability and bifurcation of a periodic solution by analyzing its behavior near a fixed-point (Floquet's Theory) [47, 62]. After achieving convergence, the procedure furnishes the Jacobian matrix evaluated at the periodic solution (i.e., the so-called monodromy matrix $\boldsymbol{\Phi}$):

$$\boldsymbol{\Phi} = \frac{\partial \mathbf{P}}{\partial \boldsymbol{\eta}}.$$

   The eigenvalues of the monodromy matrix $\boldsymbol{\Phi}$, known as *Floquet multipliers*, allow us to ascertain the stability of the calculated orbit and its bifurcations using the concepts introduced in Section 4.2.5.

4. **Adjust Δs:** As indicated by many authors in the literature [73, 95], the basic issue of the procedure is controlling the size of the step length Δs. In fact, the convergence characteristics of the correction procedure vary along different parts of a solution curve. For this reason, it is important to have an adaptive step length control strategy to ensure a reasonable performance of the continuation procedure.

   A common design goal for developing step length control procedures is to choose Δs to maintain a certain user-defined target iteration count [95]. By prescribing an initial Δs and a desired number $\bar{k}$ of loops to achieve convergence at the solution point, the increment $\Delta s^{\text{(k+1)}}$ at the (k+1)-th solution step is set based on the number of iterations $k^\star$ actually needed for the convergence at the k-th solution step, according to the general formula:

$$\Delta s^{(\mathrm{k+1})} = \rho^{(\mathrm{k})} \Delta s^{(\mathrm{k})}, \qquad \Delta s^{(\mathrm{k+1})} \in [\Delta s_{\mathrm{min}}, \Delta s_{\mathrm{max}}] \,, \tag{4.3.15}$$

where $\rho^{(\mathrm{k})}$ is a coefficient that corrects the step Δs depending on the assigned law. For example, Riks in [73] proposed:

$$\rho^{(\mathrm{k})} := \left(\frac{\bar{k}}{k^{\star}} \right)^{0.5} .$$

This value provides good results, although it tends to maintain an excessively small step in some portions of the solution curve. More recently, Formica et al. in [33] proposed the following expression for the coefficient $\rho^{(\mathrm{k})}$:

$$\rho^{(\mathrm{k})} := \left(1 + \frac{\bar{k} - k^{\star}}{\bar{k} + k^{\mathrm{m}}} \right) , \tag{4.3.16}$$

where k^{m} is the maximum number of admissible iteration loops. Such an expression, as shown in [33], provides excellent computational times.

Subsection 4.3.4

Energy Components in Hysteretic Systems

In applications where devices with a strongly nonlinear response are required, a fundamental piece of information is the time evolution of the energy components of the SDoF systems [68]. In particular, the damping ratio for the viscoelastic system is defined by equating the energy dissipated in a cycle by the rate-independent hysteretic force with the energy dissipated by the equivalent viscoelastic system in the steady-state response at resonance [40]. Furthermore, the response of many mechanical systems and materials is strongly influenced by degradation phenomena often quantified based on energy components [34, 98].

For this reason, over the years, many researchers have derived expressions of the energy components starting from the nonlinear equilibrium equation of a SDoF hysteretic mechanical system [10, 38, 81]. In these papers, the amount of mechanical energy lost by the system is denominated *dissipated energy*, without specifying whether it refers to rate-dependent or rate-independent phenomena. In addition, the work done by the generalized rate-independent forces is typically referred to in the literature with different, sometimes misleading, denominations such as *absorbed energy* or *strain energy*, and its closed-form

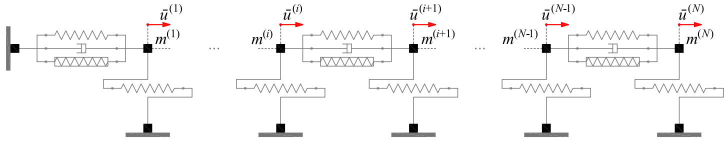

Figure 4.20. Structural model of the selected family of MDoF hysteretic mechanical systems.

expressions are provided only for some models, such as the symmetric bilinear one, while for some phenomenological models, it is derived in incremental form.

Such an issue has been the object of a recent paper by Vaiana, Capuano and Rosati [82], in which the Modified Work-Energy (MWE) theorem has been generalized and applied to MDoF hysteretic systems in order to properly account for the definition and evaluation of path-dependent work and internal energy change associated with non-conservative internal forces. The general findings contributed in [82] are here shown and then specialized to the case of a SDoF subjected to both conservative and non-conservative forces, to understand the energy and work evolution in hysteretic mechanical systems.

4.3.4.1 MDoF Hysteretic Mechanical Systems

The selected family of MDoF hysteretic mechanical systems can be analyzed by employing the structural model illustrated in Figure 4.20.

Such a structural model is made up of N masses, N external elements, and $3N$ internal elements; the former (latter) are referred to as external (internal) elements since they do not (do) allow for interaction among masses.

The motion of mass $m^{(i)}$ is described by the generalized displacement $\overline{u}^{(i)}$, the generalized velocity $\dot{\overline{u}}^{(i)}$, and the generalized acceleration $\ddot{\overline{u}}^{(i)}$ evaluated with respect to the mass equilibrium position. Such a mass is subjected to the generalized external force $p_e^{(i)}$, exhibited by the i^{th} external elastic element, and to the generalized external force $p^{(i)}$. The former is a function of the generalized displacement $\overline{u}^{(i)}$, that is, $p_e^{(i)}(\overline{u}^{(i)})$, whereas the latter is a function of time t, namely $p^{(i)}(t)$.

In addition, the i^{th} and $(i+1)^{th}$ masses are connected by means of three different types of internal elements:

- an elastic element exhibiting a generalized internal elastic force $f_e^{(i+1)}$ that is a function of the relative generalized displacement $u^{(i+1)}$ between the two masses, that is, $f_e^{(i+1)}(u^{(i+1)})$, with $u^{(i+1)} = \overline{u}^{(i+1)} - \overline{u}^{(i)}$;

- a rate-dependent hysteretic element that displays a generalized internal rate-dependent hysteretic force $f_{rd}^{(i+1)}$ that is a function of the relative generalized velocity $\dot{u}^{(i+1)}$ between the two masses, namely $f_{rd}^{(i+1)}(\dot{u}^{(i+1)})$, where $\dot{u}^{(i+1)} = \dot{\bar{u}}^{(i+1)} - \dot{\bar{u}}^{(i)}$;
- a rate-independent hysteretic element exhibiting a generalized internal rate-independent hysteretic force $f_{ri}^{(i+1)}$ that is a function of the relative generalized displacement $u^{(i+1)}$ between the two masses, that is, $f_{ri}^{(i+1)}(u^{(i+1)})$.

To derive the nonlinear equilibrium equations of the above-described structural model at the generic time t, we invoke Newton's second law:

$$\bar{\mathbf{f}}(t) = \overline{\mathbf{M}}\ddot{\bar{\mathbf{u}}}(t), \tag{4.3.17}$$

where $\bar{\mathbf{f}}(t)$ represents the generalized force vector, $\overline{\mathbf{M}}$ the constant mass matrix, and $\ddot{\bar{\mathbf{u}}}(t)$ the generalized acceleration vector.

The generalized force vector $\bar{\mathbf{f}}(t)$ can be expressed as the sum of two components:

$$\bar{\mathbf{f}}(t) = \bar{\mathbf{f}}_c(t) + \bar{\mathbf{f}}_{nc}(t), \tag{4.3.18}$$

in which $\bar{\mathbf{f}}_c(t)$ is the generalized conservative force vector, namely a force vector whose integral is path-independent, whereas $\bar{\mathbf{f}}_{nc}(t)$ represents the generalized non-conservative force vector, that is, a force vector whose integral is path-dependent. In particular, such vectors can be written as:

$$\bar{\mathbf{f}}_c(t) = -\bar{\mathbf{f}}_e(t) - \bar{\mathbf{p}}_e(t), \tag{4.3.19}$$

$$\bar{\mathbf{f}}_{nc}(t) = -\bar{\mathbf{f}}_{rd}(t) - \bar{\mathbf{f}}_{ri}(t) + \bar{\mathbf{p}}(t), \tag{4.3.20}$$

where $\bar{\mathbf{f}}_e(t)$, $\bar{\mathbf{f}}_{rd}(t)$, $\bar{\mathbf{f}}_{ri}(t)$ are, respectively, the generalized internal elastic force vector, the generalized internal rate-dependent hysteretic force vector, and the generalized internal rate-independent hysteretic force vector, whereas $\bar{\mathbf{p}}_e(t)$ and $\bar{\mathbf{p}}(t)$ represent, respectively, the generalized conservative and non-conservative external force vectors. It is important to note that the minus signs appearing into Eqs. (4.3.19) and (4.3.20) are adopted to take into account that the generalized internal forces as well as the generalized conservative external ones act in an opposite direction with respect to the motion.

Making use of Eqs. (4.3.17)-(4.3.20), it is possible to obtain the set of N nonlinear equilibrium equations:

$$\overline{\mathbf{M}}\ddot{\overline{\mathbf{u}}}(t)+\bar{\mathbf{f}}_e(t)+\bar{\mathbf{f}}_{rd}(t)+\bar{\mathbf{f}}_{ri}(t)=-\overline{\mathbf{p}}_e(t)+\overline{\mathbf{p}}(t), \tag{4.3.21}$$

whose extended form is available in Appendix D.

The i^{th} equation of (4.3.21) represents the equilibrium condition of the i^{th} mass isolated from the other ones:

$$\begin{aligned}m^{(i)}\ddot{\bar{u}}^{(i)}(t)+f_e^{(i)}(t)-f_e^{(i+1)}(t)+\\+f_{rd}^{(i)}(t)-f_{rd}^{(i+1)}(t)+f_{ri}^{(i)}(t)-f_{ri}^{(i+1)}(t)=\\=-p_e^{(i)}(t)+p^{(i)}(t).\end{aligned}$$

It can be easily observed that the i^{th} component of the generalized internal force vectors $\bar{\mathbf{f}}_e(t)$, $\bar{\mathbf{f}}_{rd}(t)$, $\bar{\mathbf{f}}_{ri}(t)$ represents the difference between the two forces exerted by the i^{th} and $(i+1)^{th}$ elements, respectively, on the i^{th} mass.

In order to simplify the evaluation of the work done by generalized conservative and non-conservative internal forces, it is convenient to rewrite the set of N nonlinear equilibrium equations by assuming as unknowns the relative generalized displacement, velocity, and acceleration between two consecutive masses. To this end, we first express the generalized displacement, velocity, and acceleration vectors as:

$$\overline{\mathbf{u}}=\mathbf{T}\,\mathbf{u}, \tag{4.3.22a}$$

$$\dot{\overline{\mathbf{u}}}=\mathbf{T}\,\dot{\mathbf{u}}, \tag{4.3.22b}$$

$$\ddot{\overline{\mathbf{u}}}=\mathbf{T}\,\ddot{\mathbf{u}}, \tag{4.3.22c}$$

where $\mathbf{T}$ represents the coordinate transformation matrix, whose expression is given in Appendix D, whereas $\mathbf{u}$, $\dot{\mathbf{u}}$, and $\ddot{\mathbf{u}}$ are the relative generalized displacement, velocity, and acceleration vectors. Accordingly, the nonlinear equilibrium equations in the new reference frame ruled by $\mathbf{T}$ read:

$$\mathbf{M}\ddot{\mathbf{u}}(t)+\mathbf{f}_e(t)+\mathbf{f}_{rd}(t)+\mathbf{f}_{ri}(t)=-\mathbf{p}_e(t)+\mathbf{p}(t), \tag{4.3.23}$$

where:

$$\mathbf{M}=\mathbf{T}^T\overline{\mathbf{M}}\mathbf{T}, \tag{4.3.24a}$$

$$\mathbf{f}_e(t)=\mathbf{T}^T\bar{\mathbf{f}}_e(t),\quad \mathbf{f}_{rd}(t)=\mathbf{T}^T\bar{\mathbf{f}}_{rd}(t),\quad \mathbf{f}_{ri}(t)=\mathbf{T}^T\bar{\mathbf{f}}_{ri}(t), \tag{4.3.24b}$$

$$\mathbf{p}_e(t)=\mathbf{T}^T\overline{\mathbf{p}}_e(t),\quad \mathbf{p}(t)=\mathbf{T}^T\overline{\mathbf{p}}(t). \tag{4.3.24c}$$

As done for Eq. (4.3.21), the extended form of Eq. (4.3.23) is illustrated in Appendix D.

The i^{th} equation in (4.3.23) represents the equilibrium condition of a system made up by the last $(N+1-i)$ masses, that is, masses from the i^{th} to the N-th ones:

$$\begin{aligned} m^{(i)}\ddot{\bar{u}}^{(i)}(t) + \cdots + m^{(N)}\ddot{\bar{u}}^{(N)}(t) + f_e^{(i)}(t) + f_{rd}^{(i)}(t) + f_{ri}^{(i)}(t) = \\ = -p_e^{(i)}(t) + p^{(i)}(t) + \cdots - p_e^{(N)}(t) + p^{(N)}(t). \end{aligned}$$

In particular, the i^{th} component of the generalized internal force vectors $\mathbf{f}_e(t)$, $\mathbf{f}_{rd}(t)$, $\mathbf{f}_{ri}(t)$ represents the force applied by the i^{th} element on the i^{th} mass. As it will be shown in the sequel, such a coordinate transformation will simplify the evaluation of the work done by generalized conservative and non-conservative internal forces.

Modified Work-Energy Theorem Let us invoke the Work-Energy (WE) theorem stating that the change in the generalized kinetic energy $\widetilde{E}_K$ of the system is equal to the work $\widetilde{W}$ done by all the generalized forces acting on it [43]. Thus, it is possible to write:

$$\Delta\widetilde{E}_K = \widetilde{W}, \tag{4.3.25}$$

that represents the integral form of the WE theorem. Note that the symbol "$\widetilde{\ }$" is employed to emphasize that such scalar quantities are computed with reference to generalized forces acting on masses.

As done for the generalized force vector $\bar{\mathbf{f}}(t)$, the generalized work $\widetilde{W}$ can be expressed as the sum of two components:

$$\widetilde{W} = \widetilde{W}_c + \widetilde{W}_{nc}, \tag{4.3.26}$$

in which $\widetilde{W}_c$ is the work related to generalized conservative forces, whereas $\widetilde{W}_{nc}$ represents the work performed by the generalized non-conservative ones. In particular, such work components can be written as:

$$\widetilde{W}_c = -\Delta\widetilde{E}_P^i - \Delta\widetilde{E}_P^e, \tag{4.3.27}$$

$$\widetilde{W}_{nc} = \widetilde{W}_{nc}^i + \widetilde{W}_{nc}^e, \tag{4.3.28}$$

where $\widetilde{E}_P^i$ ($\widetilde{E}_P^e$) is the generalized internal (external) potential energy of the system, whereas $\widetilde{W}_{nc}^i$ ($\widetilde{W}_{nc}^e$) is the work done by generalized non-conservative internal (external) forces.

By combining Eqs. (4.3.25)-(4.3.28), it is possible to obtain the expression of the MWE theorem stating that the change in the generalized mechanical energy $\widetilde{E}_M = \widetilde{E}_K + \widetilde{E}_P^i + \widetilde{E}_P^e$ of the system is equal to the work $\widetilde{W}_{nc}$ done by all the generalized non-conservative forces acting on it:

$$\Delta\widetilde{E}_M = \Delta\widetilde{E}_K + \Delta\widetilde{E}_P^i + \Delta\widetilde{E}_P^e = \widetilde{W}_{nc}^i + \widetilde{W}_{nc}^e. \tag{4.3.29}$$

Specifically, the change in the kinetic energy and in the internal and external potential energies can be computed as:

$$\Delta\widetilde{E}_K = \frac{1}{2}\mathbf{M}\dot{\mathbf{u}}_f \cdot \dot{\mathbf{u}}_f - \frac{1}{2}\mathbf{M}\dot{\mathbf{u}}_i \cdot \dot{\mathbf{u}}_i, \tag{4.3.30}$$

$$\Delta\widetilde{E}_P^i = -\widetilde{W}_e, \tag{4.3.31}$$

$$\Delta\widetilde{E}_P^e = -\widetilde{W}_{pe}, \tag{4.3.32}$$

whereas the work done by generalized non-conservative internal and external forces can be evaluated as:

$$\widetilde{W}_{nc}^i = \widetilde{W}_{rd} + \widetilde{W}_{ri}, \tag{4.3.33}$$

$$\widetilde{W}_{nc}^e = \widetilde{W}_p. \tag{4.3.34}$$

In the previous equations, $\dot{\mathbf{u}}_i$ ($\dot{\mathbf{u}}_f$) represents the relative generalized velocity vector computed at the initial (final) time t_i (t_f) of a generic time interval, $\widetilde{W}_e$ and $\widetilde{W}_{pe}$ are the amounts of work done by generalized internal and external elastic forces, respectively, whereas $\widetilde{W}_{rd}$, $\widetilde{W}_{ri}$, $\widetilde{W}_p$ represent the amounts of work performed by generalized internal rate-dependent and rate-independent hysteretic forces and by generalized external forces, respectively. In particular, they can be computed as follows:

$$\widetilde{W}_e = -\int_{\mathbf{u}_i}^{\mathbf{u}_f} \mathbf{f}_e \cdot \mathrm{d}\mathbf{u}, \tag{4.3.35a}$$

$$\widetilde{W}_{pe} = -\int_{\mathbf{T}\mathbf{u}_i}^{\mathbf{T}\mathbf{u}_f} \left[\left(\mathbf{T}^T\right)^{-1} \mathbf{p}_e\right] \cdot \mathrm{d}\left(\mathbf{T}\mathbf{u}\right), \tag{4.3.35b}$$

$$\widetilde{W}_{rd} = -\int_{\mathbf{u}_i}^{\mathbf{u}_f} \mathbf{f}_{rd} \cdot \mathrm{d}\mathbf{u}, \tag{4.3.35c}$$

$$\widetilde{W}_{ri} = -\int_{\mathbf{u}_i}^{\mathbf{u}_f} \mathbf{f}_{ri} \cdot \mathrm{d}\mathbf{u}, \tag{4.3.35d}$$

$$\widetilde{W}_p = +\int_{\mathbf{T}\mathbf{u}_i}^{\mathbf{T}\mathbf{u}_f} \left[\left(\mathbf{T}^T\right)^{-1} \mathbf{p}\right] \cdot \mathrm{d}\left(\mathbf{T}\mathbf{u}\right), \tag{4.3.35e}$$

where $\mathbf{u}_i$ ($\mathbf{u}_f$) is the relative generalized displacement vector evaluated at the initial (final) time t_i (t_f) of a generic time interval.

For the reader's convenience, in Appendix D, we have rewritten Eqs. (4.3.35a)-(4.3.35d) to express the different work components of the system, namely $\widetilde{W}_e$, $\widetilde{W}_{pe}$, $\widetilde{W}_{rd}$, $\widetilde{W}_{ri}$, as the sum of contributions respectively computed with reference to the generalized force acting on the i^{th} element, that is, $W_e^{(i)}$, $W_{pe}^{(i)}$, $W_{rd}^{(i)}$, $W_{ri}^{(i)}$.

Remark It is important to note that the work done by generalized external (internal) force vectors needs to be evaluated by considering the (relative) generalized displacement vector $\bar{\mathbf{u}} = \mathbf{T}\,\mathbf{u}$ ($\mathbf{u}$). In addition, we can also observe that the work computed by using Eqs. (4.3.35a)-(4.3.35d) is negative since the generalized internal forces and the generalized conservative external ones act in a direction opposite to the one of the motion. Conversely, the work evaluated by Eq. (4.3.35e) may be positive or negative.

Finally, taking into account that the generalized mechanical energy of the system is converted (*dissipated*) into the generalized internal energy $\widetilde{E}_I$ due to the work done by all the generalized non-conservative internal forces, it is possible to write:

$$\widetilde{W}_{nc}^i = -\Delta\widetilde{E}_I = -\Delta(\widetilde{E}_I)_{rd} - \Delta(\widetilde{E}_I)_{ri}, \tag{4.3.36}$$

and, consequently, Eq. (4.3.29) can be rewritten as:

$$\Delta\widetilde{E}_M + \Delta\widetilde{E}_I = \widetilde{W}_{nc}^e. \tag{4.3.37}$$

4.3.4.2 SDoF Hysteretic Mechanical Systems

The results previously shown are now specialized for SDoF hysteretic mechanical systems. Specifically, the selected general family of SDoF hysteretic mechanical systems is illustrated in Fig. 4.21. Such a model consists of a mass m connected with three different types of elements in parallel:

- an elastic spring;
- a rate-dependent hysteretic element;
- a rate-independent hysteretic spring.

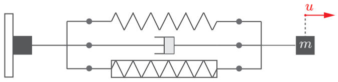

Figure 4.21. SDoF hysteretic mechanical system.

Denoting by u, $\dot{u}$ and $\ddot{u}$ the generalized displacement, velocity and acceleration, respectively, the nonlinear equilibrium equation of the system having mass m can be derived from the general form of the Newton's second law:

$$f_R = \frac{dq}{dt}, \tag{4.3.38}$$

where f_R denotes the resulting force acting on the mass and q the momentum. Considering the mass as a constant quantity over time, we can obtain the well known equation of motion:

$$f_R = m\ddot{u}. \tag{4.3.39}$$

The resulting force f_R, introduced in Eq. (4.3.38), can be evaluated considering the free body diagram in Fig. 4.22, where all forces acting on the mass are illustrated; therefore,

$$f_R = -f_e(u) - f_{rd}(\dot{u}) - f_{ri}(u) + p(t) = -f(u, \dot{u}) + p(t), \tag{4.3.40}$$

where f_e (f_{ri}) is the generalized elastic (rate-independent hysteretic) force exerted on the elastic (rate-independent hysteretic) element, assumed to be a function of the generalized displacement u. Furthermore, f_{rd} is the generalized rate-dependent hysteretic force exerted on the rate-dependent hysteretic element, expressed as a function of the generalized velocity $\dot{u}$; finally, p is the generalized external force acting on the mass and depending on time t.

The forces exerted by the three elements on the mass have a negative sign since they tend to bring the system back to its equilibrium position; on the contrary, the generalized external force $p(t)$ is assumed to be positive if having the same direction of the generalized displacement u.

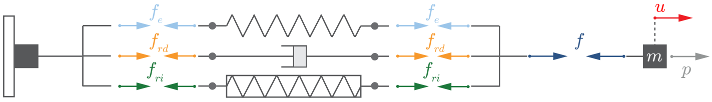

Figure 4.22. Free body diagram of the SDoF hysteretic mechanical system.

The equation of motion for the general family of SDoF hysteretic mechanical systems illustrated in Fig. 4.21, can be easily obtained combining Eqs. (4.3.39) and (4.3.40):

$$m\ddot{u} + f_{rd}(\dot{u}) + f_{ri}(u) + f_e(u) = p(t). \tag{4.3.41}$$

The numerical solution of Eq. (4.3.41), performed by employing a suitable time integration method [86], requires the following two initial conditions:

$$u(0) = u_0,$$
$$\dot{u}(0) = \dot{u}_0,$$

where u_0 and $\dot{u}_0$ are, respectively, the generalized displacement and velocity of the SDoF hysteretic mechanical system at the beginning of the analysis.

Modified Work-Energy Theorem We now proceed to specialize the MWE theorem previously outlined to SDoF hysteretic mechanical systems. Although the theorem is well known in standard textbooks of physics [43], it is instructive to briefly recall the basic assumptions underlying its derivation mainly to introduce the relevant notation adopted in the sequel.

By integrating Eq. (4.3.39) in a generalized displacement interval $[u_i, u_f]$, where u_i and u_f denote the initial and the final generalized displacements respectively, one obtains:

$$W = \int_{u_i}^{u_f} f_R \, du = \int_{u_i}^{u_f} m\ddot{u} \, du, \tag{4.3.42}$$

where W represents the generalized work performed on the mass by the resulting force f_R.

Denoting by $\dot{u}_i$ ($\dot{u}_f$) the velocity of the mass at the beginning (end) of the interval of interest, the right-hand side of Eq. (4.3.42) can be further elaborated upon by writing:

$$\int_{u_i}^{u_f} m\ddot{u} \, du = \int_{\dot{u}_i}^{\dot{u}_f} m\dot{u} \, d\dot{u} = \frac{1}{2} m(\dot{u}_f^2 - \dot{u}_i^2) = \Delta E_K,$$

where ΔE_K is defined as the variation of generalized kinetic energy E_K.

In conclusion, Eq. (4.3.42) can be rewritten as:

$$W = \Delta E_K, \tag{4.3.43}$$

stating that the variation in generalized kinetic energy of a system is equal to the generalized work done by all the generalized forces acting on it. This classical result is known in physics as the WE theorem [43].

In turn, the generalized work W can be expressed as the sum of two contributions:

$$W = W_c + W_{nc}, \tag{4.3.44}$$

in which W_c (W_{nc}) is the generalized work related to the generalized conservative (non-conservative) forces. In this respect, we recall that the former (latter) represent forces for which the integral along a closed displacement path is equal to (different from) zero.

Denoting by E_P the generalized potential energy, defined as:

$$\Delta E_P = -W_c, \tag{4.3.45}$$

one obtains the general expression of the MWE theorem by combining Eqs. (4.3.43)-(4.3.45):

$$\Delta E_K + \Delta E_P = \Delta E_M = W_{nc}. \tag{4.3.46}$$

The previous equation states that the sum of the variation of generalized kinetic and potential energy, usually called generalized mechanical energy E_M, is equal to the generalized work done by all the non-conservative forces acting on the mass. In particular, if the generalized work related to the non-conservative forces is zero, the generalized mechanical energy E_M of the system is constant.

To be specific let us make reference to the hysteretic mechanical system shown in Fig. 4.21. The only generalized conservative force is the one exerted by the elastic spring f_e (Fig. 4.22), and the related generalized work provides:

$$W_c = W_e = -\int_{u_i}^{u_f} f_e(u)\, du. \tag{4.3.47}$$

On the other hand, the generalized work done on the mass

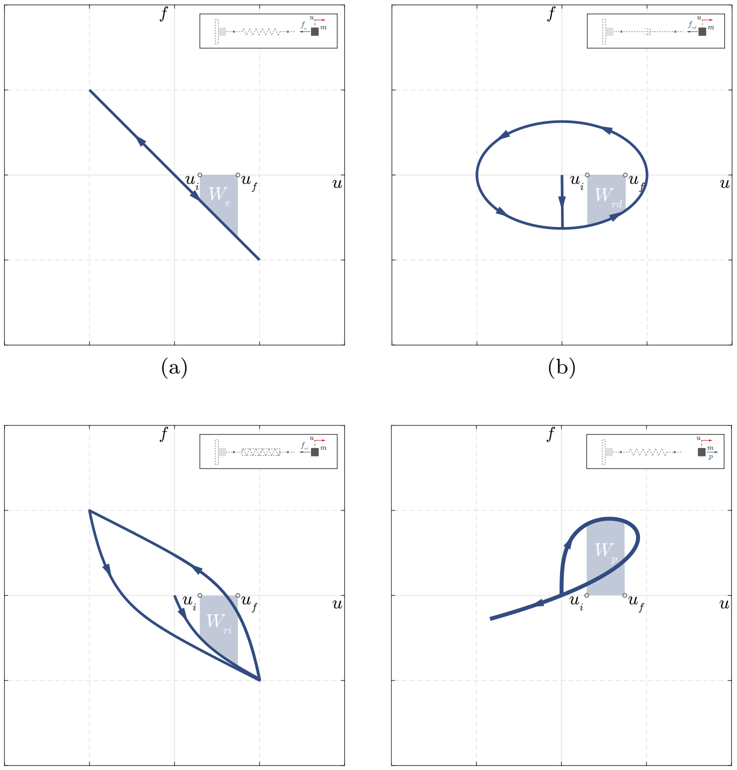

(a) (b) (c) (d)

Figure 4.23. Graph of the generalized restoring: (a) linear elastic force-displacement $-f_e(u)$ and elastic work W_e; (b) hysteretic rate-dependent force-displacement $-f_{rd}(\dot{u})$ and rate-dependent work W_{rd}; (c) hysteretic rate-independent force-displacement $-f_{ri}(u)$ and rate-independent work W_{ri}; (d) generalized external force-displacement $p(t)$ and external work W_p.

by the generalized non-conservative forces, can be expressed as the sum of two contributions:

$$W_{nc} = W_{nc}^{int} + W_{nc}^{ext}, \tag{4.3.48}$$

where W_{nc}^{int} (W_{nc}^{ext}) represents the work done by the generalized non-conservative internal (external) forces. Specifically, the former is associated with the generalized non-conservative internal forces, namely the generalized forces exhibited by the hysteretic elements (Fig. 4.22), and can be evaluated as:

$$W_{nc}^{int} = W_{rd} + W_{ri} = -\int_{u_i}^{u_f} f_{rd}(\dot{u})\, du - \int_{u_i}^{u_f} f_{ri}(u)\, du, \tag{4.3.49}$$

where W_{rd} (W_{ri}) is the generalized work done by the generalized rate-dependent (rate-independent) hysteretic force on the mass m.

Furthermore, the work W_{nc}^{ext} done by the generalized non-conservative external force is given by:

$$W_{nc}^{ext} = W_p = \int_{u_i}^{u_f} p(t)\, du. \tag{4.3.50}$$

It is clear from Eqs. (4.3.49)-(4.3.50) that, W_{rd} and W_{ri} are resisting works ($W < 0$), whereas W_p can be both resisting or motor work ($W > 0$), depending on the relationship between the sign of the generalized external force $p(t)$ and the generalized displacement $u(t)$ at a specific time.

Figure 4.23a graphically shows the generalized restoring force $-f_e(u)$ (the force acting on the mass) versus the generalized displacement for the elastic force and also the associated work that can be calculated by means of Eq. (4.3.47).

Similarly, Fig. 4.23b (Fig. 4.23c) shows the generalized restoring force versus the generalized displacement for the rate-dependent $-f_{rd}(\dot{u})$ (rate-independent $-f_{ri}(u)$) hysteretic force and the related work that can be evaluated by using Eq. (4.3.49).

Finally, in Fig. 4.23d, it is shown a generic generalized external force $p(t)$ versus the generalized displacement and the work associated with the external force that can be computed by means of Eq. (4.3.50).

Eq. (4.3.46) can be further elaborated upon by using Eq. (4.3.48) as:

$$\Delta E_M = W_{nc}^{int} + W_{nc}^{ext}.$$

At this point, due to the work of the non-conservative internal forces W_{nc}^{int}, one naturally wonders which kind of energy the variation of generalized mechanical energy ΔE_M is associated with.

The answer to this question is provided by the generalized *internal energy* E_I of the system, a concept mainly related to the energy at a molecular level and/or thermal energy of the system, which the generalized mechanical energy is converted to. In particular, it is possible to write that:

$$W_{nc}^{int} = -\Delta E_I = -\Delta(E_I)_{rd} - \Delta(E_I)_{ri}.$$

According to this interpretation, the total amount of energy of an hysteretic mechanical system is equal to the work done by all the generalized non-conservative external forces acting on it; consequently, the single contribution of the total energy can change over time, as a result of the transformations of one type of energy into the other, but leaving constant the sum of the separate contributions. In other words, the sum of the variation between generalized mechanical and internal energy of the system is equal to the work done by the external force:

$$\Delta E_M + \Delta E_I = W_p.$$

CHAPTER

5

Applications

This chapter offers a thorough examination of various aspects of hysteretic mechanical systems and their dynamic responses. The initial section focuses on complex hysteretic mechanical responses, discussing dimensional systems and the process of nondimensionalization, followed by an analysis of frequency response characteristics.

Subsequent sections investigate the influence of asymmetry in hysteretic systems, providing detailed insights into the mathematical models utilized, the properties of the analyzed systems, and the numerical results obtained. A discussion on the frequency response of negative stiffness metamaterials is included, encompassing both mathematical modeling and specific system analyses.

The chapter further explores hysteretic rocking systems, addressing their dimensional characteristics, the influence of shape types, and the responses achieved through the combination of different shapes. It concludes with an investigation into the dynamic response of MDoF hysteretic mechanical systems, emphasizing the application of the Krylov algorithm and the key phenomena encountered in these systems. Finally, the chapter examines the work and energy components within hysteretic systems, providing a comprehensive understanding of their behavior and implications.

Through this organized approach, the chapter aims to provide a comprehensive understanding of hysteretic mechanical systems and their behaviors.

Hic sunt leones.

Section 5.1

Frequency-Response Curves for Rate-Independent Hysteretic Mechanical Responses of Complex Shape

The analytical modeling and prediction of the response of hysteretic systems is an area of growing interest in physics, engineering, and material science since hysteresis is an almost ubiquitous nonlinear phenomenon.

For instance, electrical systems often exhibit nonlinear hysteretic behavior, a peculiar feature common to magnetic ones as well [92]. Analogously, the cardiovascular system, along with other biological systems, also exhibits a nonlinear response, having a hysteretic nature, to changes in blood pressure [101]. Mechanical systems such as engines and machines, may exhibit nonlinear hysteretic behavior as a result of the nonlinear behavior of the materials used in their construction [11, 78, 82]. Finally, civil engineering structures exhibit nonlinear hysteretic behavior when exposed to large amplitude vibrations due, e.g., to wind loads or earthquakes. Moreover, hysteresis is often deliberately incorporated into the system to influence its behavior in a controlled manner [22, 25, 67].

The occurrence of hysteresis in such a wide range of materials and systems used in different fields underscores the importance of understanding the influence of hysteresis in the design and analysis of structures subjected to cyclic loading. An accurate modeling of hysteresis is crucial for researchers and designers to better grasp and predict the behavior of systems under different conditions, since this can significantly impact the design and optimization of different devices and processes.

Over the years, many mathematical models have been developed to accurately reproduce experimentally measured hysteretic behaviors. Focusing on mechanical hysteresis only, some of the well-known phenomenological models include the models by Bouc and Wen [9, 93], by Baber and Noori [5, 13], by Preisach [69], by Vaiana et al [85, 87] and by Graesser and Cozzarelli [35]. However, one of the main limitations of these models is their inability to capture different types of hysteretic behavior in a unified manner. In fact, each model is most effective at modeling systems with specific hysteretic behavior and may not be accurate for other complex loop shapes. Additionally, the parameters of such models do not always have a clear mechanical interpretation, making it challenging to determine their values only on the basis of physical experiments. Consequently, it is often necessary to use a combination of experimental testing and numerical optimization techniques to accurately estimate the parameters of the adopted model. This makes it difficult to apply these models to real-world systems without significant computational resources and experimental data.

To overcome these difficulties, Vaiana and Rosati [84] introduced a new approach for modeling rate-independent hysteretic behavior in mechanical systems and materials (Section 4.3.2). Upon classifying complex hysteresis loops, ranging from asymmetric to flag-shaped, they proposed a novel rate-independent hysteretic model, denominated VRM, having an exponential nature and allowing for closed-form expressions in the evaluation of the output variable. As discussed in Section 4.3.2, the VRM enables uncoupled modeling of the loading and unloading phases and allows for a straightforward identification procedure due to the clear interpretation of the involved parameters. More recently Vaiana and Rosati [83], improved their original model by formulating the VRM+A, and proposed in addition a differential formulation, namely VRM+D, in order to allow for its use in the field of nonlinear dynamics. To sum up both the original and the improved model formulated by Vaiana and Rosati address the difficulties associated with modeling hysteretic behavior quite efficiently and offer a practical solution for analyzing hysteretic mechanical systems subjected to time-periodic inputs.

Hence, it is natural to evaluate the adequacy of the VRM+D in addressing the search for periodic solutions of hysteretic mechanical systems and evaluating their stability and bifurcation. In the literature both analytical and numerical techniques have been used to study this phenomenon; to the first class belongs the method of slowly varying parameters [41] and the harmonic balance method [96, 97]. They have been used to obtain the steady-state dynamics of SDoF hysteretic mechanical systems subjected to time-periodic forcing input. Interestingly, it has been found that the response of these systems can be multivalued and include jumps, this contradicts a widely-held belief in the early sixties according to which all hysteretic systems should have had stable and single-valued frequency response curves [19, 39].

On the other hand, when dealing with strong nonlinearities, such as those found in hysteretic mechanical systems, and in situations where global dynamic behaviors are involved, numerical techniques are often necessary. Some of these techniques

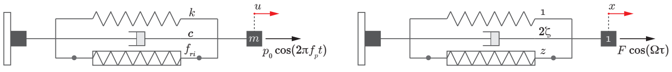

(a) (b)

Figure 5.1. Dimensional (a) and non-dimensional (b) SDoF hysteretic mechanical systems.

include frequency-domain, time-domain, and frequency/time-domain methods. A well-established and powerful numerical strategy to find periodic solutions and determine their stability and bifurcations is the Poincaré map-based method developed in [50], often used in conjunction with Floquet theory (described in Section 4.3.3). Specifically, this method was applied to investigate the response and stability of elastoplastic oscillators. Additionally, in a later work by Lacarbonara and Vestroni [49], the responses and stability of SDoF hysteretic mechanical systems endowed with Bouc-Wen and Masing hysteretic models were examined using the Poincaré map-based method in the time-domain.

In this section, we show how the unifying modeling features of the VRM+D [83] are carried over to an accurate prediction of periodic solutions for mechanical systems characterized by hysteretic response of complex shape. The result is obtained by combining the VRM+D (Section 4.3.2) with the Poincaré map continuation method (Section 4.3.3) and systematically constructing a series of frequency-response curves. By means of such curves the steady-state response, stability, and bifurcation of the systems are illustrated and discussed for each shape of the assumed hysteretic behavior.

Subsection 5.1.1

Dimensional Equations of Motion

This section focuses on formulating the nonlinear equations of motion for a general class of SDoF hysteretic mechanical systems. Specifically, we derive these equations in their dimensional form.

The dimensional SDoF hysteretic mechanical system (shown in Fig. 5.1a) consists of a mass m connected in parallel to three distinct types of elements:

- a linear elastic spring;
- a linear rate-dependent hysteretic element;
- a rate-independent hysteretic spring.

Denoting by u, $\dot{u}$ and $\ddot{u}$ the generalized displacement, velocity and acceleration, respectively, the dimensional equations of motion of the SDoF hysteretic mechanical system (Fig. 5.1a) can be derived from the general form of the Newton's second law as:

$$m\ddot{u} + c\dot{u} + ku + f_{ri} = p_0 \cos\left(2\pi f_p t\right), \tag{5.1.1}$$

where c is the viscous damping coefficient, k is the stiffness of the elastic spring, f_{ri} is the generalized rate-independent hysteretic force exerted on the hysteretic element, whereas p_0 (f_p) is the amplitude (frequency) of the input force.

According to the VRM+D (Section 4.3.2) the generalized rate-independent hysteretic force f_{ri} in Eq. (5.1.1) is governed by the following ODE:

$$\dot{f}_{ri} = \left\{k_e\left(u\right) + k_b + \alpha f_0 + s\alpha\left[f_e\left(u\right) + k_b u - f_{ri}\right]\right\}\dot{u}, \tag{5.1.2}$$

where $s \coloneqq \operatorname{sgn}\left(\dot{u}\right)$, and the generalized function k_e is given by:

$$k_e\left(u\right) = \beta_1\beta_2 e^{\beta_2 u} + 4\gamma_1\gamma_2\frac{e^{-\gamma_2(u-\gamma_3)}}{\left[1+e^{-\gamma_2(u-\gamma_3)}\right]^2}.$$

Similarly, the generalized function f_e is given by:

$$f_e\left(u\right) = \beta_1\left(e^{\beta_2 u} - 1\right) + 2\gamma_1\frac{1-e^{-\gamma_2(u-\gamma_3)}}{1+e^{-\gamma_2(u-\gamma_3)}}.$$

As seen in Section 4.3.2, the model parameters in Eq. (5.1.2) can be updated depending on the sign of the velocity $\dot{u}$. In particular, $k_b = k_b^+\left(k_b^-\right)$, $f_0 = f_0^+\left(f_0^-\right)$, $\alpha = \alpha^+\left(\alpha^-\right)$, $\beta_1 = \beta_1^+\left(\beta_1^-\right)$, $\beta_2 = \beta_2^+\left(\beta_2^-\right)$, $\gamma_1 = \gamma_1^+\left(\gamma_1^-\right)$, $\gamma_2 = \gamma_2^+\left(\gamma_2^-\right)$, $\gamma_3 = \gamma_3^+\left(\gamma_3^-\right)$ if $s > 0$ ($s < 0$).

SUBSECTION 5.1.2

Non-dimensionalization Procedure

In this section, we follow a systematic procedure consisting of five steps (Section 2.5) to obtain the non-dimensional form for the system of interest and a non-dimensional version of the VRM+D for the evaluation of the hysteretic variable.

Non-dimensionalization, as we have seen in Section 2.5, is a fundamental technique employed in the analysis of systems governed by ODEs. There are many reasons for using such a technique. Firstly, this approach simplifies the problem by reducing the number of the involved parameters. This simplification makes it easier to analyze and grasp the relationship between the parameters of the system. Secondly, non-dimensionalization allows for the comparison of different systems with varying physical parameters on the same scale, facilitating the identification of common trends and properties across different systems. Moreover, it helps to eliminate the units of measurement, making the problem more general and independent of specific units [80].

Although there are several approaches to non-dimensionalize an equation, see, e.g., [80], the non-dimensionalization procedure can be systematically divided into five distinct steps. These sequential steps include; i) identifying all independent and dependent variables; ii) replacing all variables with non-dimensional quantities based on characteristic units; iii) dividing the obtained equation by the coefficient of the highest-order derivative; iv) selecting the characteristic unit for each variable so that potential auxiliary conditions become as simple as possible; v) rewriting the equation in terms of new dimensionless quantities.

By applying these steps to the system of differential equations represented by Eqs. (5.1.1) and (5.1.2) we have that:

i) The independent variable is the time t whereas the generalized displacement u, and the generalized rate-independent hysteretic force f_{ri} are the dependent variables.

ii) We introduce as non-dimensional variables:

$$\tau := \frac{t - t_r}{t_s}, \quad x := \frac{u - u_r}{u_s}, \quad z := \frac{f_{ri} - f_r}{f_s}.$$

These quantities are defined as the difference between the dimensional variable and a reference value, (i.e., t_r, u_r and f_r), scaled by a dimensional scaling factor (i.e., t_s, u_s and f_s). Based on these definitions, the dimensional variables can be expressed as follows:

$$t = t_s \tau + t_r, \quad u = u_s x + u_r, \quad f_{ri} = f_s z + f_r. \tag{5.1.3}$$

Now it is possible to replace the dimensional variables in Eqs. (5.1.1) and (5.1.2) with the non-dimensional ones, by using Eqs. (5.1.3). In particular, we obtain for Eq. (5.1.1):

$$\begin{aligned} \frac{m u_s}{t_s^2} \frac{d^2 x}{d\tau^2} + \frac{c u_s}{t_s} \frac{dx}{d\tau} + k\left(u_s x + u_r\right) + \left(f_s z + f_r\right) = \\ = p_0 \cos\left[2\pi f_p \left(t_s \tau + t_r\right)\right]. \end{aligned} \tag{5.1.4}$$

On the other hand, if we plug Eqs. (5.1.3) into Eq. (5.1.2), we obtain:

$$\begin{aligned}\frac{f_s}{t_s}\frac{dz}{d\tau} = \{ & k_e\left(u_s x + u_r\right) + k_b + \alpha f_0 + \\ & \operatorname{sgn}\left(\frac{u_s}{t_s}\frac{dx}{d\tau}\right)\alpha\left[f_e\left(u_s x + u_r\right) + k_b\left(u_s x + u_r\right) + \right. \\ & \left. -\left(f_s z + f_r\right)\right]\} \frac{u_s}{t_s}\frac{dx}{d\tau}. \qquad (5.1.5)\end{aligned}$$

iii) The coefficients of the highest-order term in Eq. (5.1.4) and (5.1.5) are $\frac{mu_s}{t_s^2}$ and $\frac{f_s}{t_s}$, respectively. Hence, upon dividing Eq. (5.1.4) by $\frac{mu_s}{t_s^2}$ and Eq. (5.1.5) by $\frac{f_s}{t_s}$ one obtains:

$$\begin{aligned}\ddot{x} + \frac{ct_s}{m}\dot{x} + \frac{kt_s^2}{m}x + \frac{f_s t_s^2}{mu_s}z + \frac{t_s^2}{mu_s}\left(ku_r + f_r\right) &= \\ = \frac{p_0 t_s^2}{mu_s}\cos\left[2\pi f_p\left(t_s\tau + t_r\right)\right],\end{aligned}$$

and

$$\begin{aligned}\dot{z} = \frac{u_s}{f_s}\{ & k_e\left(u_s x + u_r\right) + k_b + \alpha f_0 + \\ & + \operatorname{sgn}\left(\frac{u_s}{t_s}\dot{x}\right)\alpha\left[f_e\left(u_s x + u_r\right) + k_b\left(u_s x + u_r\right) + \right. \\ & \left. -\left(f_s z + f_r\right)\right]\}\dot{x}.\end{aligned}$$

where the superimposed dot now represents the derivative with respect to the non-dimensional time τ.

iv) To simplify the final dimensionless expressions as much as possible, we impose that the reference values t_r, u_r, f_r are equal to zero. In such a way we obtain:

$$\ddot{x} + \frac{ct_s}{m}\dot{x} + \frac{kt_s^2}{m}x + \frac{f_s t_s^2}{mu_s}z = \frac{p_0 t_s^2}{mu_s}\cos\left(2\pi f_p t_s\tau\right), \qquad (5.1.6)$$

and

$$\begin{aligned}\dot{z} = \frac{u_s}{f_s}\{ & k_e\left(u_s x\right) + k_b + \alpha f_0 + \operatorname{sgn}\left(\frac{u_s}{t_s}\dot{x}\right) \\ & \alpha\left[f_e\left(u_s x\right) + k_b u_s x - f_s z\right]\}\dot{x}. \qquad (5.1.7)\end{aligned}$$

Thus, it is only necessary to determine the scaling factors t_s, u_s and f_s so that Eqs. (5.1.6) and (5.1.7), and potential auxiliary conditions, become as simple as possible. One possible choice is to set the coefficients in front of x and z in Eq. (5.1.6) equal to one:

$$\begin{aligned} \frac{kt_s^2}{m} &= 1 \rightarrow t_s = \sqrt{\frac{m}{k}}, \\ \frac{f_s t_s^2}{mu_s} &= 1 \rightarrow k = \frac{f_s}{u_s}. \end{aligned}$$

A further assumption concerning Eq. (5.1.7) can be made by requiring that:

$$\operatorname{sgn}\left(\frac{u_s}{t_s}\dot{x}\right) = \operatorname{sgn}(\dot{u}) \Rightarrow \frac{u_s}{t_s} > 0.$$

Let $\alpha^+ = \alpha^- = \alpha$ and $f_0^+ = f_0^- = f_0$. Knowing, from the general formulation of the model by Vaiana and Rosati [83, 84], that $\alpha > 0$, and imposing that $f_0 > 0$, we can define the scaling factors as:

$$u_s \coloneqq \frac{1}{\alpha}, \quad f_s \coloneqq f_0,$$

so as to obtain:

$$\frac{u_s}{t_s} = \sqrt{\frac{f_0}{\alpha m}} > 0.$$

As a result, the other non-dimensional coefficients are defined as follows:

$$\begin{aligned} 2\zeta &\coloneqq \frac{ct_s}{m} = \frac{c}{\sqrt{mk}}, \\ F &\coloneqq \frac{p_0 t_s^2}{mu_s} = \frac{p_0}{f_0}, \\ \Omega &\coloneqq 2\pi f_p t_s = 2\pi f_p \sqrt{\frac{m}{k}}. \end{aligned}$$

v) The final non-dimensional SDoF hysteretic mechanical system (see Fig. 5.1b) is ruled by the following ODEs:

$$\ddot{x} + 2\zeta\dot{x} + x + z = F\cos(\Omega\tau), \tag{5.1.8}$$

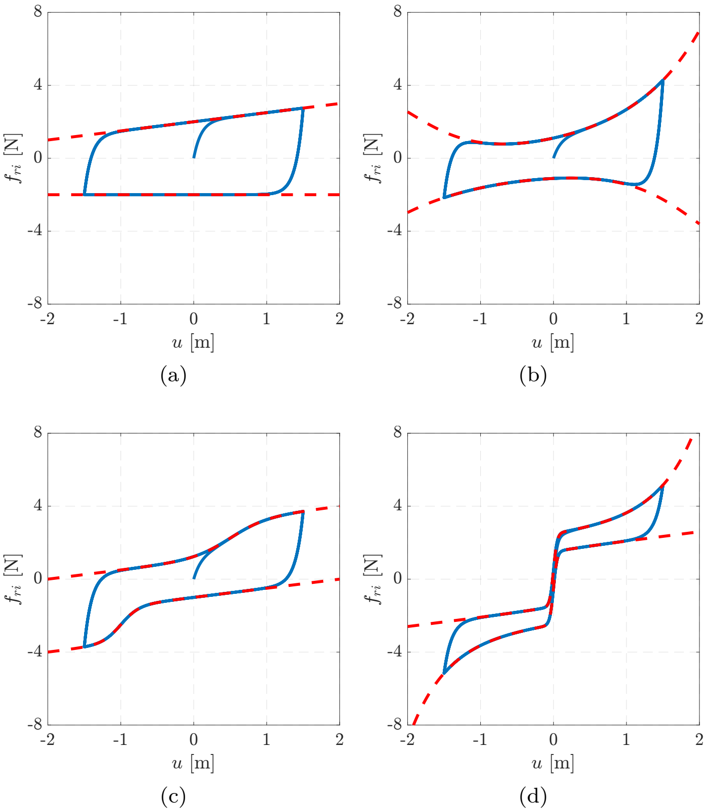

(a)

(b)

(c)

(d)

Figure 5.2. Dimensional hysteresis loops simulated by using the VRM+D parameters in Table 5.1.

and

$$\dot{z} = \left\{ \frac{k_e\left(\frac{x}{\alpha}\right)}{f_0\alpha} + \frac{k_b}{f_0\alpha} + 1 + s\left[\frac{f_e\left(\frac{x}{\alpha}\right)}{f_0} + \frac{k_b}{f_0\alpha}x - z\right]\right\}\dot{x}. \tag{5.1.9}$$

5.1.2.1 Non-dimensional VRM+D

The non-dimensional form of the VRM+D in Eq. (5.1.9) can be further simplified if we define two new non-dimensional functions:

$$\kappa_e(x) := \frac{k_e\left(\frac{x}{\alpha}\right)}{f_0\alpha} \quad \text{and} \quad \phi_e(x) := \frac{f_e\left(\frac{x}{\alpha}\right)}{f_0}.$$

Figure	sgn($\dot{u}$)	k_b	f_0	α	β_1	β_2	γ_1	γ_2	γ_3
5.2a	+	0.5	2.0	10	0.0	0.0	0.0	0.0	0.0
	−	0.0	2.0	10	0.0	0.0	0.0	0.0	0.0
5.2b	+	0.5	4.0	10	0.5	1.2	1.5	-2.0	-2.0
	−	0.0	4.0	10	-0.5	-0.8	1.5	-2.0	2.0
5.2c	+	0.5	2.0	10	0.0	0.0	0.5	4.0	0.5
	−	0.5	2.0	10	0.0	0.0	0.5	8.0	-1.0
5.2d	+	0.5	0.5	10	0.1	2.0	1.0	40	0.0
	−	0.5	0.5	10	-0.1	-2.0	1.0	40	0.0

Table 5.1. Dimensional VRM+D parameters adopted to simulate the hysteresis loops in Figure 5.2.

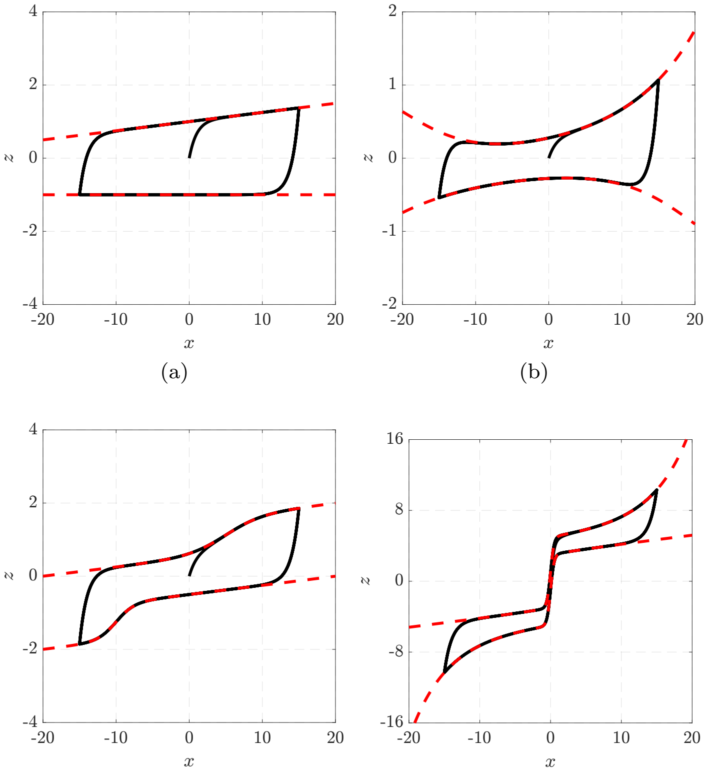

(c) (d)

Figure 5.3. Non-dimensional hysteresis loops simulated by using the VRM+D parameters in Table 5.2.

Figure	sgn($\dot{x}$)	χ_1	χ_2	χ_3	χ_4	χ_5	χ_6
5.3a	$+$	0.0	0.0	0.0	0.0	0.0	0.025
	$-$	0.0	0.0	0.0	0.0	0.0	0.0
5.3b	$+$	0.125	0.12	0.75	-0.2	-20.0	0.0125
	$-$	-0.125	-0.08	0.75	-0.2	20.0	0.0
5.3c	$+$	0.0	0.0	0.5	0.4	5.0	0.025
	$-$	0.0	0.0	0.5	0.8	-10.0	0.025
5.3d	$+$	0.2	0.2	4.0	4.0	0.0	0.1
	$-$	-0.2	-0.2	4.0	4.0	0.0	0.1

Table 5.2. Non-dimensional VRM+D parameters adopted to simulate the hysteresis loops in Figure 5.3.

Along with these non-dimensional functions, we can define six non-dimensional model parameters such as:

$$\begin{aligned} &\chi_1 \coloneqq \frac{\beta_1}{f_0}, \quad \chi_2 \coloneqq \frac{\beta_2}{\alpha}, \quad \chi_3 \coloneqq \frac{2\gamma_1}{f_0}, \\ &\chi_4 \coloneqq \frac{\gamma_2}{\alpha}, \quad \chi_5 \coloneqq \alpha\gamma_3, \quad \chi_6 \coloneqq \frac{k_b}{f_0\alpha}. \end{aligned} \tag{5.1.10}$$

Some of these quantities appear in the non-dimensional function $\kappa_e\left(x\right)$:

$$\kappa_e\left(x\right) = \chi_1\chi_2 e^{\chi_2 x} + 2\chi_3\chi_4 \frac{e^{-\chi_4(x-\chi_5)}}{\left[1+e^{-\chi_4(x-\chi_5)}\right]^2},$$

and in the non-dimensional function $\phi_e\left(x\right)$:

$$\phi_e\left(x\right) = \chi_1\left(e^{\chi_2 x}-1\right) + \chi_3 \frac{1-e^{-\chi_4(x-\chi_5)}}{1+e^{-\chi_4(x-\chi_5)}}.$$

Finally, the general form of the non-dimensional VRM+D can be expressed as follows:

$$\dot{z} = \left\{\kappa_e\left(x\right) + \chi_6 + 1 + s\left[\phi_e\left(x\right) + \chi_6 x - z\right]\right\}\dot{x}. \tag{5.1.11}$$

Remark It is worth noting that the non-dimensionalization led to a reduction in the number of parameters upon which the hysteretic mechanical system is dependent, from 21 in the model depicted in Fig. 5.1a to 15 in the one illustrated in Fig. 5.1b.

On account of the reduced number of parameters in the non-dimensional model, it is natural to ask if some information has been lost in the description of the system behavior, an issue that, to the best of our knowledge, has not been addressed in the specialized literature. For this reason, we have decided to compare the loop shapes predicted by the dimensional and non-dimensional form of the VRM+D. Specifically, by using the dimensional parameters given in Table 5.1 and imposing a sinusoidal generalized displacement having an amplitude of 1.5 m and a frequency of 1 Hz, we obtained the dimensional hysteresis loops in Fig. 5.2. On the other hand, for the non-dimensional model, it is easy to derive the non-dimensional parameters listed in Table 5.2 by applying Eqs. (5.1.10). These parameters are used in Eq. (5.1.11) to derive the non-dimensional hysteresis loops in Fig. 5.3.

Remark It is important to note that for both dimensional and non-dimensional loops, the classification proposed in [84] does apply. In fact, according to their proposal hysteresis loops can be classified into four main categories:

- Shape type $S1$: Characterized by hysteresis loops limited by two straight lines (Figs. 5.2a and 5.3a).
- Shape type $S2$: Characterized by hysteresis loops limited by two curves with no inflection point (Figs. 5.2b and 5.3b).
- Shape type $S3$: Characterized by hysteresis loops limited by two curves with one inflection point (Figs. 5.2c and 5.3c).
- Shape type $S4$: Characterized by hysteresis loops limited by two curves with two inflection points (Figs. 5.2d and 5.3d).

In the sequel we shall derive the Frequency-Response Curves (FRCs) for the four categories of loop shapes.

Subsection 5.1.3

Description of the Analyzed Systems

The four SDoF hysteretic mechanical systems under analysis are:

1. System $S1$: In the first system, both upper and lower limiting curves (red dashed lines in Figs. 5.2 and 5.3) are

represented by straight lines (shape type $S1$). This system exhibits asymmetric behavior due to the different values of χ_6^+ and χ_6^- while no other parameters contribute to the hysteretic behavior.

2. System $S2$: The second system has a more complex hysteretic behavior, since all parameters are different from zero. Both upper and lower limiting curves has a pronounced curvature due to the contributions of χ_1, χ_2, χ_3, χ_4, and χ_5 but no inflection points (shape type $S2$). The asymmetry between the loading and unloading phases arises from distinct values of χ_1, χ_2, and χ_6 during each phase.

3. System $S3$: For the third system, both upper and lower limiting curves are characterized by one inflection point (shape type $S3$). Furthermore, this system exhibits asymmetry between upper and lower limiting curves, with different values of χ_4 and χ_5 causing the hysteresis loop to be wider in one direction than in the other.

4. System $S4$: The fourth system has a symmetric hysteresis loop shape, with both upper and lower limiting curves exhibiting two inflection points (shape type $S4$) and significant stiffening effects. The non-zero values of χ_1, χ_2, χ_3, and χ_4 all contribute to the complex flag-shaped behavior of this system. On the other hand, the high value of χ_6 contribute to the stiffening behavior.

5.1.3.1 Methods

We analyze the four SDoF hysteretic mechanical systems and obtain their FRCs using the procedure described in Section 4.3.3 (the pseudo-code can be found in Table 4.3). The continuation parameter is Ω, while the non-dimensional amplitude of the input force F remains constant. Furthermore, the parameters used in the procedure are listed in Table 4.4.

In particular, $T/\Delta\tau$ is the number of steps that are numerically used to evaluate the Poincaré map using the MATLAB function ode45. The parameters δ_1 and δ_2 are introduced in Eq. (4.3.12) for the evaluation of the Jacobian matrix of the Poincaré map, and *tol* is the value of the tolerance imposed for the stopping criterion of the Newton-Raphson method ($|\mathbf{r}^{(k)}| < tol$). The last four parameters in Table 4.4 are used for the step length control using Eqs. (4.3.15) and (4.3.16).

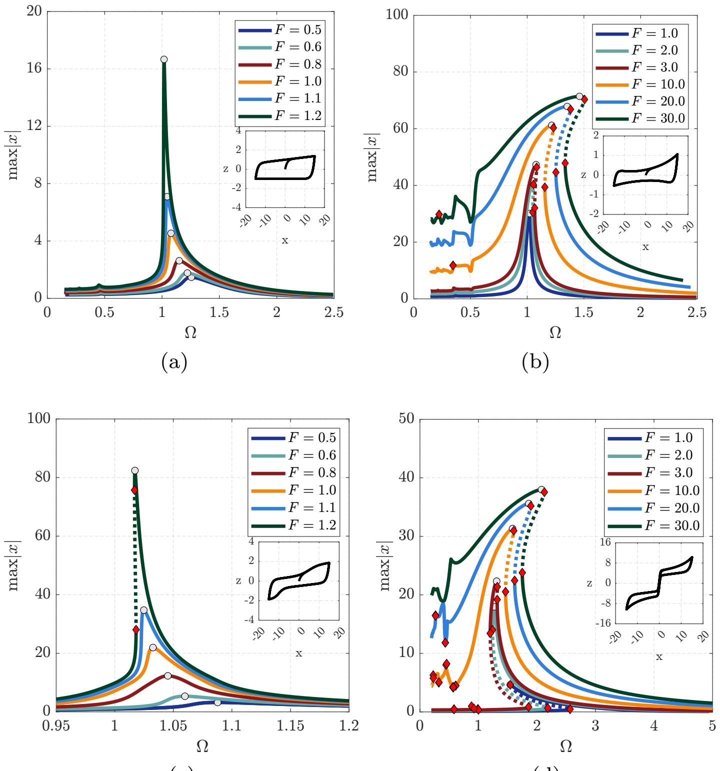

(a) (b)

(c) (d)

Figure 5.4. FRCs for SDoF hysteretic mechanical systems having S1 (a), S2 (b), S3 (c), S4 (d) hysteresis loops and different amplitudes F of the input force.

The procedure provides a fixed-point of the Poincaré map, which is used as the initial condition to integrate Eqs. (5.1.8) and (5.1.11) again in order to obtain the FRCs shown in Fig. 5.4, where max$|x|$ is plotted against Ω, and those in Fig. 5.12, expressing the maximum displacement, velocity, transmitted force, and normalized transmitted force. In Figs. 5.4 and 5.12 the gray dot markers represents the maximum value for the FRC.

To determine the stability of the solutions and their bifurcations in the 3D state-space, the evolution of the three *Floquet multipliers* associated with the 3×3 monodromy matrix is examined. The solid lines in Figs. 5.4 and 5.12 indicate stable periodic solutions, where the magnitude of their complex-valued *Floquet multipliers* is less than 1. Conversely, dashed lines correspond to unstable responses for which the magnitude of at least one of the multipliers exceeds 1. In Fig. 5.4 red diamond markers represent the bifurcation points.

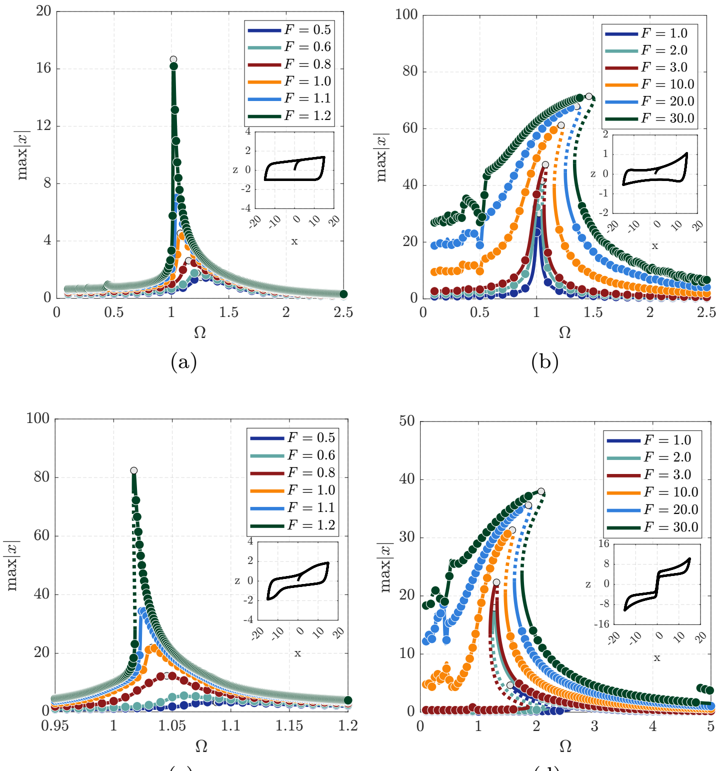

(a) (b)

(c) (d)

Figure 5.5. Validation of the results in Fig. 5.4 through NLTHAs (dot markers) for different amplitudes F of the input force.

Finally, the accuracy of the periodic solutions estimated by the continuation algorithm is verified by performing Nonlinear Time History Analyses (NLTHAs), that is, directly integrating Eqs. (5.1.8) and (5.1.11), and analyzing the stable solution indicated by the dot marker in Fig. 5.5. In Appendix E additional details can be found on the number of maximum, minimum and average iterations required by the Newton-Raphson method to achieve convergence for all numerical experiments.

Subsection 5.1.4

Frequency-Response Curves: Stability and Bifurcation

In this section, we discuss a comprehensive examination of the FRCs of the four SDoF hysteretic mechanical systems subjected to time-periodic input. The assumed hysteretic behaviors are the

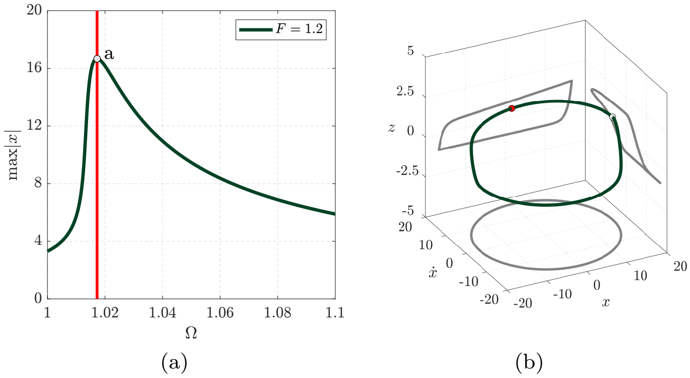

(a) (b)

Figure 5.6. System $S1$: FRC assuming as amplitude of the input force $F = 1.2$ (a) and periodic orbit in the state-space at $\Omega = 1.01725$ (b).

ones previously described and depicted in Fig. 5.3. This comprehensive analysis provides valuable insights into the stability and bifurcation characteristics of the analyzed systems.

We analyze the hysteretic mechanical system depicted in Figure 5.1b with four different hysteretic laws, namely those whose loop shapes are obtained by applying the parameters listed in Table 5.2. Each system is defined by Eqs. (5.1.8) and (5.1.11), with the additional condition $\zeta = 0$.

The results are organized in order to improve readability. In particular, they are grouped according to loop shape typology, and for each shape, a detailed description of the FRCs obtained for different amplitudes of the input is provided, along with stability and bifurcation indications. Finally, for each system, significant points of the FRCs are represented in state-space in order to comment on specific results for particular amplitudes and angular frequencies.

Furthermore, for the hysteresis loop $S4$ in Fig. 5.3d, four additional FRCs are provided. These additional curves are expressed in terms of maximum velocity, acceleration, transmitted force and normalized transmitted force, which can be useful in various engineering applications.

5.1.4.1 System S1

In the following we present the outcomes of the investigation conducted on System $S1$, as described in Section 5.1.3, using different amplitudes of the input force F. The amplitudes of interest are $0.5,\ 0.6,\ 0.8,\ 1.0,\ 1.1,\ 1.2$.

Frequency-response curves For all tested levels of F, it can be observed in Fig. 5.4a that the FRCs are bent to the left (indicating a softening nonlinearity) and globally stable within the investigated range of F and Ω. Specifically:

- $F = 0.5$
  Three resonance peaks are observed at angular frequencies of 0.282694, 0.460423, and 1.25527.

- $F = 0.6$
  Similarly to the previous case, three resonance peaks are observed at angular frequencies of 0.282297, 0.466413, and 1.22085.

- $F = 0.8$
  The observed resonance peaks increase to four, occurring at angular frequencies of 0.200937, 0.282297, 0.461909, and 1.14957.

- $F = 1.0$
  As in the previous case, four resonance peaks are observed at angular frequencies of 0.200095, 0.279511, 0.455687, and 1.07779.

- $F = 1.1$
  Four resonance peaks are still present, but they occur within an angular frequencies range of $(0.15,\ 1.05)$, specifically at 0.155183, 0.278341, 0.452139, and 1.04455.

- $F = 1.2$
  The four resonance peaks are located within the previous range, occurring at angular frequencies of 0.199027, 0.277747, 0.449525, and 1.01725. Hence, the first and last two values become closer with respect to the case $F = 1.1$, with the initial value of the first (second) pair increasing (decreasing).

Orbits in the state-space It is of interest to examine the state-space of the system at specific values of Ω and F. When $F = 1.2$ and $\Omega = 1.01725$, corresponding to the fourth resonance peak, there is only one intersection with the FRC in Fig. 5.6a. This intersection indicates the existence of a unique stable periodic solution for the system, with a maximum displacement ($\max |x|$) equal to 16.6649.

Figure 5.6b shows the shape of the periodic orbit in the state-space, as well as its projections onto the planes $(x,\ \dot{x})$, $(x,\ z)$, and $(\dot{x},\ z)$. The figure also includes the fixed-point provided by the procedure (red dot) and the point corresponding to the maximum displacement reported in the FRC (gray dot).

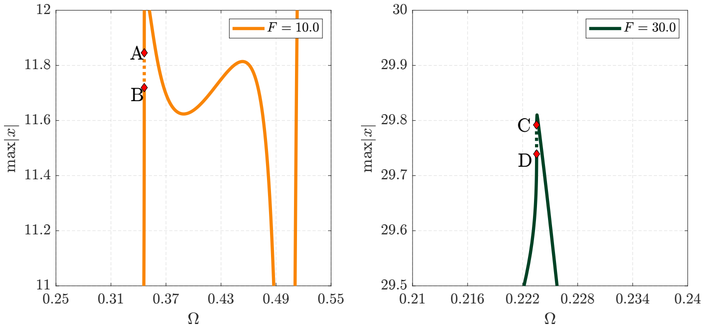

(a) (b)

Figure 5.7. Enlarged views of the FRCs in Fig. 5.4b (system $S2$) assuming as amplitude of the input force $F = 10.0$ (a) and $F = 30.0$ (b).

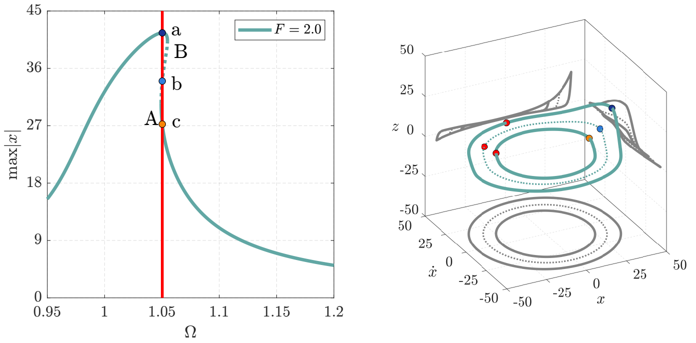

(a) (b)

Figure 5.8. System $S2$: FRC assuming as amplitude of the input force $F = 2.0$ (a) and periodic orbits in the state-space at $\Omega = 1.05$ (b).

5.1.4.2 System S2

In the sequel we present the results obtained from the analysis of the System $S2$, as described in Section 5.1.3, under different values of amplitudes for the input force F, that are 1.0, 2.0, 3.0, 10.0, 20.0, 30.0.

Frequency-response curves Making reference to the FRCs in Fig. 5.4b one has:

- $F = 1.0$
  At this level of load amplitude, it can be observed that the FRC is slightly bent to the right (indicating an hardening nonlinearity) and globally stable within the investigated range of Ω.

- $F = 2.0$
  By increasing the load value, the hardening behavior of the FRC is accentuated. Furthermore, at points

$(1.04927,\ 30.5508)$ and $(1.05482,\ 40.2793)$ the system exhibits two *fold bifurcations*.

- $F = 3.0$
  In this case, the behavior exhibited by the curve is of the same type as the previous level of amplitude. Indeed, there is a further increase in the hardening behavior of the FRC, while the two *fold bifurcations* at points $(1.06602,\ 32.0483)$ and $(1.08362,\ 46.3749)$ move slightly away.

- $F = 10.0$
  In this case, there is a further increase in the hardening behavior of the FRC. The two *fold bifurcations* at points $(1.15556,\ 39.3649)$ and $(1.23174,\ 60.3052)$ move further away. Furthermore, as shown in Fig. 5.7a, the FRC loses its stability at A $\equiv$ $(0.3463,\ 11.8456)$ and B $\equiv$ $(0.346303,\ 11.7194)$ due to two *fold bifurcations*.

- $F = 20.0$
  A further increase in the amplitude modifies the bifurcation scenario, as the system exhibits two *fold bifurcations* at points $(1.25333,\ 44.6038)$ and $(1.38267,\ 66.8305)$. In addition, the unstable portion in the region of small Ω is lost.

- $F = 30.0$
  In this last case, there is a further increase in the hardening behavior of the FRC. In particular, the two *fold bifurcations* at points $(1.33497,\ 47.8529)$ and $(1.50612,\ 70.3138)$ move further away. Moreover, as shown in Fig. 5.7b, the FRC loses its stability again at points C $\equiv$ $(0.223514,\ 29.792)$ and D $\equiv$ $(0.223526,\ 29.7392)$ due to two *fold bifurcations*.

Referring to the FRCs with an amplitude of $1.0,\ 2.0,\ 3.0$, a series of resonance peaks were observed in the range $\Omega \in (0.1,\ 0.4)$. These peaks become less sharp when the force amplitude is increased.

Orbits in the state-space The investigation of the state-space at specific values of Ω and F is a matter of interest. In particular, by observing the FRC obtained for the analyzed system for $F = 2.0$ (Fig. 5.8a), it can be seen that there are three intersections with the FRC at $\Omega = 1.05$.

This indicates the existence of three periodic solutions for the system of interest. Specifically, two stable orbits (labeled as

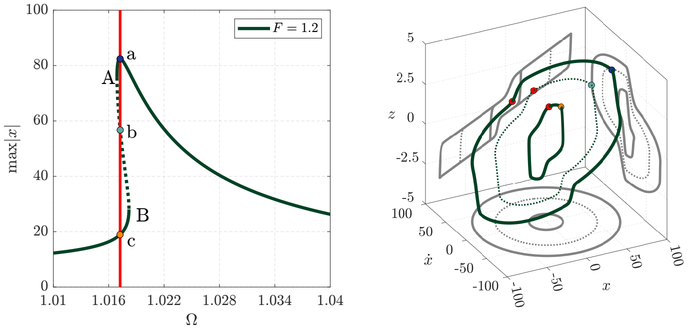

(a) (b)

Figure 5.9. System $S3$: FRC assuming as amplitude of the input force $F = 1.2$ (a) and periodic orbits in the state-space at $\Omega = 1.01724$ (b).

a and c in Fig. 5.8a), and one unstable solution (labeled as b in Fig. 5.8a).

The shape of the periodic orbits in the state-space is illustrated in Fig. 5.8b that also depicts the projections of the periodic orbits onto the planes $(x,\ \dot{x})$, $(x,\ z)$ and $(\dot{x},\ z)$ in the state-space. Additionally, the orbits in Fig. 5.8b also include the fixed-points provided by the procedure (red dots) and the points corresponding to the maximum displacement reported in the FRC (colored dots).

5.1.4.3 System S3

The following results are obtained by analyzing System $S3$, described in Section 5.1.3, subjected to amplitudes of the input force F equal to $0.5,\ 0.6,\ 0.8,\ 1.0,\ 1.1,\ 1.2$.

Frequency-response curves The FRCs reported in Fig. 5.4c show that:

- $F = 0.5,\ 0.6,\ 0.8,\ 1.0,\ 1.1$
  For these amplitude of the input force it can be observed that the FRCs are softening and globally stable within the investigated range of Ω.
- $F = 1.2$
  The FRC shows an accentuated softening behavior, and two *fold bifurcations* are experienced at points $(1.01689,\ 75.7157)$ and $(1.01819,\ 28.0416)$.

Orbits in the state-space Of particular interest is the exploration of the state-space at specific Ω and F values. In particular, by observing the FRC obtained for the system under

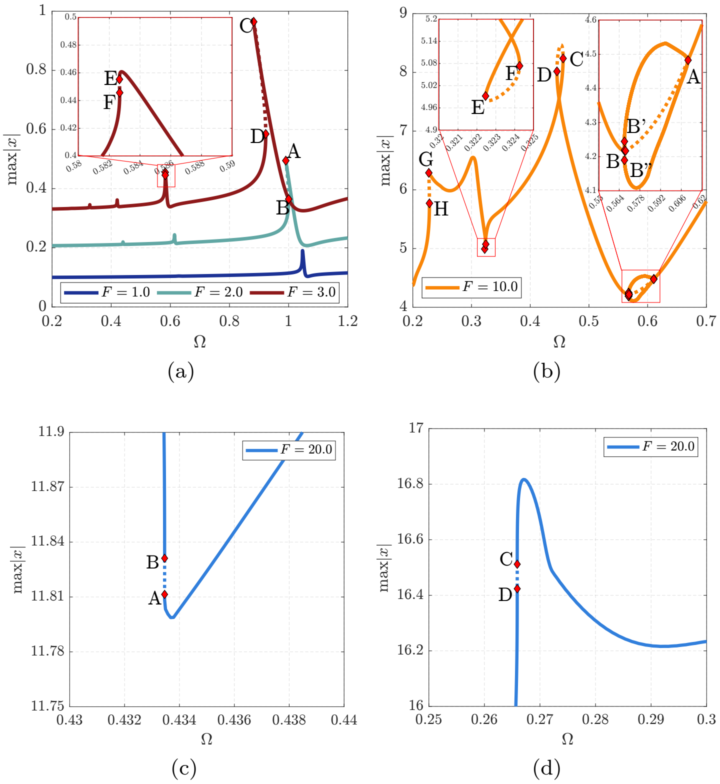

(a) (b)

(c) (d)

Figure 5.10. Enlarged views of the FRCs in Fig. 5.4d (system $S4$) assuming as amplitude of the input force $F = 1.0,\ 2.0,\ 3.0$ (a), $F = 10.0$ (b) and $F = 20.0$ (c)-(d).

consideration for $F = 1.2$ (Fig. 5.9a), it can be seen that there are three intersections with the FRC at $\Omega = 1.01724$.

This indicates the existence of three periodic solutions for the system, specifically, two stable orbits (labeled as a and c in Fig. 5.9a) and a unique unstable periodic solution (labeled as b in Fig. 5.9a).

The shapes of the periodic orbits in state-space are illustrated in Fig. 5.9b, in which their projections onto the planes $(x,\ \dot{x})$, $(x,\ z)$, and $(\dot{x},\ z)$ are also shown. Additionally, the orbits in Fig. 5.9b include the fixed-points provided by the procedure (red dots) and the points corresponding to the maximum displacement reported in the FRC (colored dots).

5.1.4.4 System S4

Let us now illustrate the results obtained by analyzing System $S4$, as described in Section 5.1.3, under different amplitudes of the input force F equal to 1.0, 2.0, 3.0, 10.0, 20.0, 30.0.

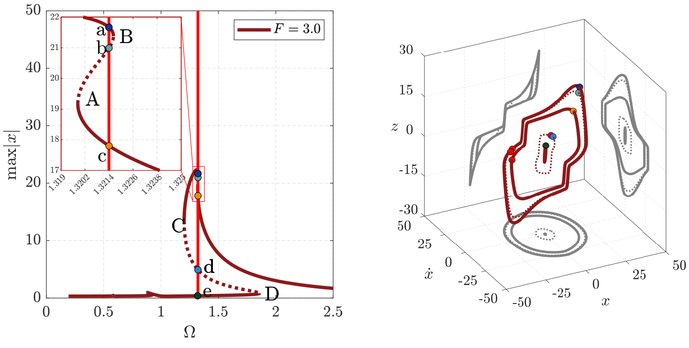

(a) (b)

Figure 5.11. System $S4$: FRC assuming as amplitude of the input force $F = 3.0$ (a) and periodic orbits in the state-space at $\Omega = 1.3214$ (b).

Frequency-response curves From the FRCs in Fig. 5.4d one infers:

- $F = 1.0$
  At this level of amplitude, the FRC exhibits a softening behavior. Additionally, the system undergoes two *fold bifurcations* at points (1.54293, 4.61446) and (2.56595, 0.457121). Moreover, a resonance peak is observed at an angular frequency of 1.04696 (shown in Fig. 5.10a).

- $F = 2.0$
  For this level of amplitude, the FRC exhibits an intermediate behavior between hardening and softening. The system undergoes two *fold bifurcations* at points (1.23972, 14.0108) and (2.18536, 0.6483). Furthermore, as shown in Fig. 5.10a, the FRC loses stability at points A ≡ (0.990398, 0.494804) and B ≡ (1.00008, 0.364599) due to two *fold bifurcations*, as shown in Fig. 5.10a. Three resonance peaks are also present at the angular frequencies of 0.439879, 0.614078, and 0.990398 (shown in Fig. 5.10a).

- $F = 3.0$
  The system exhibits an intermediate behavior between hardening and softening of the FRC. Additionally, the system undergoes a series of eight *fold bifurcations* (shown at points A ≡ (1.31984, 19.1817), B ≡ (1.32162, 21.378), C ≡ (1.20139, 13.4231), D ≡ (1.85713, 0.837714) in Fig. 5.11a, while, in Fig. 5.10a, at C ≡ (0.881828, 0.964232), D ≡ (0.922575, 0.584871), E ≡ (0.582661, 0.455316), F ≡ (0.582676, 0.445658)). Finally, there are four resonance

Figure	$F = 1$	$F = 2$	$F = 3$
5.4d	(1.5449, 4.64)	(1.2727, 17.96)	(1.3108, 22.33)
5.12a	(1.5463, 7.81)	(1.2748, 23.24)	(1.3151, 28.84)
5.12b	(1.5512, 10.47)	(1.2753, 31.87)	(1.3142, 46.81)
5.12c	(1.5449, 10.41)	(1.2727, 31.83)	(1.3108, 46.79)
5.12d	(1.5449, 10.41)	(1.2727, 15.91)	(1.3108, 15.59)

Table 5.3. Coordinates of the peaks of the FRCs associated with the system $S4$ for different amplitudes F of the input force (Figs. 5.4d and 5.12).

peaks corresponding to angular frequencies of 0.32768, 0.420242, 0.58274 and 0.881875 (shown in Fig. 5.10a).

- $F = 10.0$
  For such an amplitude level the system exhibits a fully hardening behavior of the FRC. The bifurcation scenario of the system includes two *fold bifurcations* at points (1.46291, 20.5305) and (1.6029, 30.9474). Additionally, the system undergoes two *pitchfork bifurcations* at points A ≡ (0.610606, 4.48271) (supercritical) and B ≡ (0.567639, 4.21748) (subcritical) (shown in Fig. 5.10b). The equilibrium paths that arise from these bifurcations are stable until points B' ≡ (0.567554, 4.24512) and B" ≡ (0.567562, 4.18991) where they lose stability through two *fold bifurcations* (shown in Fig. 5.10b). Moreover, there are six *fold bifurcations* at points C ≡ (0.45597, 8.23794), D ≡ (0.445504, 8.01708), E ≡ (0.322458, 4.99206), F ≡ (0.324257, 5.07358), G ≡ (0.227272, 6.2892) and H ≡ (0.22834, 5.7705) in Fig. 5.10b.

- $F = 20.0$
  At this level of amplitude, there is a further increase in the hardening behavior of the FRC. Specifically, at points (1.61803, 22.4509) and (1.89484, 35.1896), the two *fold bifurcations* move further apart. Additionally, as shown in Figs. 5.10c and 5.10d, the stability of the FRC is lost at points A ≡ (0.433459, 11.8114), B ≡ (0.43346, 11.8312), C ≡ (0.265907, 16.5118) and D ≡ (0.265908, 16.4237), due to four *fold bifurcations*.

- $F = 30.0$
  Finally, for this amplitude level the FRC shows a hardening behavior with only two *fold bifurcations* at (1.74896, 23.782) and (2.12659, 37.5445).

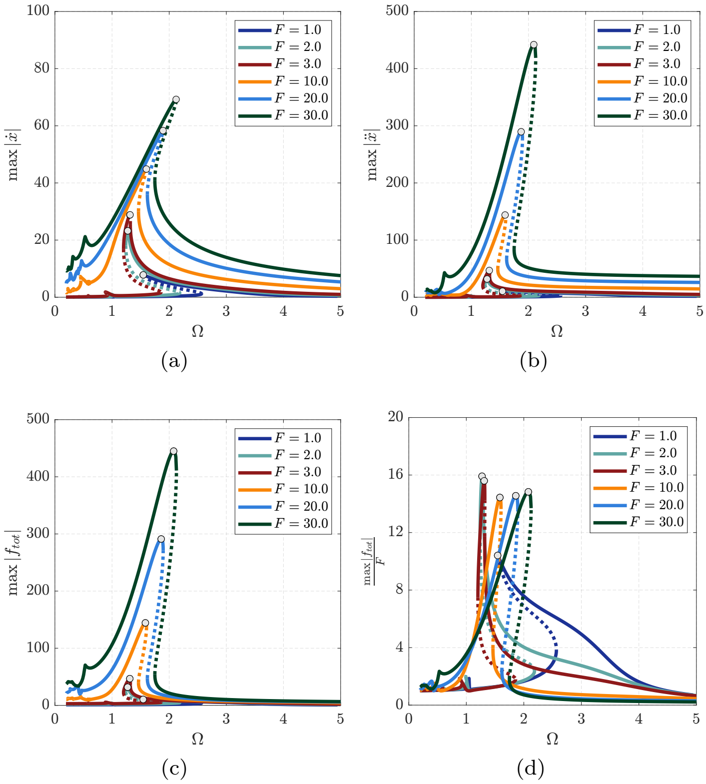

(a) (b) (c) (d)

Figure 5.12. System $S4$: FRCs in terms of maximum velocity (a), acceleration (b), transmitted force (c), and normalized transmitted force (d) for different amplitudes F of the input force.

Table 5.4. Coordinates of the peaks of the FRCs associated with the system $S4$ for different amplitudes F of the input force (Figs. 5.4d and 5.12).

Figure	$F = 10$	$F = 20$	$F = 30$
5.4d	(1.5831, 31.32)	(1.8597, 35.60)	(2.0785, 37.98)
5.12a	(1.5463, 7.81)	(1.8920, 58.32)	(2.1212, 69.24)
5.12b	(1.5908, 143.91)	(1.8717, 289.6)	(2.0931, 442.0)
5.12c	(1.5834, 144.37)	(1.8601, 291.2)	(2.0780, 444.9)
5.12d	(1.5834, 14.44)	(1.8601, 14.56)	(2.0780, 14.83)

In addition to the FRCs in Fig. 5.4d, which represent the variation of the maximum displacement as a function of the angular frequency Ω for the $S4$ system, we have also obtained the additional FRCs shown in Fig. 5.12. We have not explicitly reported the analogous FRCs related to the systems $S1$, $S2$, and $S3$ due to space limitations and also because the $S4$ system, due to its peculiar features, has been considered to be worth deserving a greater attention.

In particular, once the fixed-point of the Poincaré map is obtained by further integrating the equations of motion using the fixed-point as the initial condition, a series of significant quantities can be obtained for the periodic orbit, such as:

- the maximum velocity of the obtained response (Fig. 5.12a);
- the maximum acceleration of the obtained response (Fig. 5.12b);
- the maximum transmitted force $f_{tot} = x + z$ (Fig. 5.12c);
- the maximum normalized transmitted force $\frac{f_{tot}}{F}$ (Fig. 5.12d).

The stability and bifurcation behavior of the curves in Fig. 5.12 remain the same as previously described. However, it is noted in Table 5.3-5.4 that, for different amplitude levels of the input force F, the value of the angular frequency for which the maximum value is obtained in the equivalent FRC does modify.

The observation that the FRCs for other quantities such as maximum velocity, acceleration, and transmitted force are affected by the amplitude level of the input force in a different way than the maximum displacement is crucial for many engineering applications.

Example

As an example, in the design of mechanical systems, it is important to consider not only the maximum displacement but also the maximum velocity and acceleration to ensure that the system does not exceed its safe operating limits. Similarly, in the analysis of civil and mechanical structures such as bridges and motors, it is important to consider the maximum transmitted force to ensure that the considered structure can withstand the loads imposed on it.

Therefore, understanding how the amplitude of the input force affects the value of the angular frequencies at which different significant quantities reach their maximum value is critical for the design and analysis of many physical systems.

Orbits in the state-space Examining the state-space for specific values of Ω and F is an intriguing prospect. In particular, by observing the FRC obtained for the system under consideration for $F = 3.0$ (Fig. 5.11a), it can be seen that there are five intersections with the FRC at $\Omega = 1.3214$.

This indicates the existence of five periodic solutions for the system, specifically, three stable orbits (labeled as a, c, and e in Fig. 5.11a) and two unstable periodic solutions (labeled as b and d in Fig. 5.11a).

The shape of the periodic orbits in the state-space are illustrated in Fig. 5.11b in which the projections of the periodic orbits onto the planes $(x,\ \dot{x})$, $(x,\ z)$, and $(\dot{x},\ z)$ are reported. Additionally, the orbits in Fig. 5.11b also include the fixed-points provided by the procedure (red dots) and the points corresponding to the maximum displacement reported in the FRC in Fig. 5.11a (colored dots).

SUBSECTION 5.1.5

Conclusions

We analyzed the behavior of SDoF hysteretic mechanical systems subjected to time-periodic input by combining the VRM+D hysteretic model with a continuation procedure based on Poincaré maps. By applying this approach to different types of hysteresis loop shapes, we have shown its effectiveness in accurately predicting the behavior of complex mechanical systems, including their steady-state response, stability and bifurcation. In particular, the bifurcation analysis provides valuable information on the dynamics of the system under different loading conditions and can help in the design of control strategies to mitigate unwanted effects related to hysteresis.

For these reasons further studies will be conducted to explore the full potential of the proposed approach. In particular, we will integrate the proposed procedure with algorithms able to perform branch-switching and compute the bifurcation points of codimension-one.

SECTION 5.2

Influence of asymmetric behavior on the frequency response and stability of rate-independent hysteretic mechanical systems

We address the modeling of mechanical systems exhibiting a rate-independent hysteretic behavior, i.e. a nonlinear phenomenon in which the output variable depends upon the past history of the input, beside its current value, but not upon its rate of change [77]. Behaviors of this kind are typically caused by plastic deformation and/or low-velocity friction mechanisms [11, 12]. The onset and evolution of hysteretic behaviors are characterized by loops, associated with loading and unloading curves relating input and output variables, having different shapes and analytical properties. Mechanical hysteresis phenomena can be broadly categorized as either symmetric or asymmetric, depending on whether they exhibit or not, in the input-output plane, the same shape during the loading and unloading phase. Specifically, we focus on asymmetric loops, i.e. those that commonly characterize materials like metals, polymers, and shape memory alloys, as well as in structural elements such as reinforced concrete and steel beam-column connections [56, 77].

The complex asymmetric rate-independent hysteretic behavior observed in mechanical systems has been mainly modeled by means of algebraic [70], transcendental [45, 85], differential [66], and integral models [69], this classification referring to the analytical approach used to compute the output variable [13].

Asymmetric hysteresis phenomena are mostly simulated by differential models that basically stand as modified versions of the celebrated Bouc-Wen Model (BWM) [9, 93] belonging to the wider class of Duhem models (Section 4.3.2). Basically, all of these evaluate the generalized force as the sum of a linear elastic component, depending on a generalized displacement, and a rate-independent hysteretic component. The latter is a function of a generalized hysteretic variable, derived through the solution of a nonlinear first-order ODE usually formulated on a *ad-hoc* basis. Such models can be further grouped in:

1. models that deviate from the BWM by incorporating in the generalized hysteretic force a modulating function to scale the hysteretic component [27, 63];

2. models that differ from the BWM because the expression of the ODE, used to compute the hysteretic variable, is properly modified [79, 90].

Although significant advancements have been achieved, such models fail to encompass different types of complex hysteretic behavior within a unifying framework. Typically, each model is optimized to reproduce specific hysteretic responses and may not perform well for loops having differing shapes. Furthermore, the model parameters often lack a clear mechanical meaning thus complicating the calibration process. As a result, numerical optimization methods are frequently required to estimate these parameters accurately.

To overcome such drawbacks, Vaiana and Rosati introduced a new phenomenological model to simulate the rate-independent hysteretic behavior exhibited by mechanical systems [84]. More recently, Vaiana and Rosati proposed an enhanced analytical version of the model (VRM+A) and presented its equivalent differential formulation (VRM+D) [83]. This advancement aims to facilitate the application of the model in nonlinear dynamics by simplifying and providing a more comprehensive analysis of systems that have been explored in the existing literature [4, 6, 65]. In summary, both the original and reformulated model effectively address the challenges associated with the simulation of complex hysteresis phenomena and, thanks to the extension provided by VRM+D, provide an effective approach for examining hysteretic mechanical systems subjected to periodic inputs [82]. In this regard, Capuano et al. [14] have recently shown the ability of VRM+D to analyze SDoF hysteretic mechanical systems under the action of periodic forces, employing a well-established numerical method based on Poincaré maps [50]. This methodology, generally integrated with Floquet theory, has been employed to study the response and stability of various types of SDoF systems, utilizing different hysteretic models, including elasto-plastic, Masing, and Bouc-Wen models [50].

In this section, we perform an accurate frequency response analysis of asymmetric hysteretic systems modeled by means of the VRM+D. In particular, we begin with a detailed formulation of the equilibrium equations, followed by the derivation of the associated non-dimensional form. Next, after a brief summary of the typical shapes of hysteresis loop generally observed in rate-independent hysteretic mechanical systems, we illustrate the asymmetric responses characterizing the selected non-dimensional hysteretic systems. Finally, we present the re-

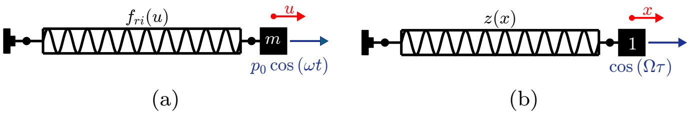

Figure 5.13. Dimensional (a) and non-dimensional (b) classes of SDoF hysteretic mechanical systems.

sults of the analyses performed on them, with a focus on the influence of asymmetry on their frequency response and stability.

Subsection 5.2.1

Mathematical Model

In this section, we outline the equations of motion for the class of hysteretic mechanical systems under investigation. After a detailed formulation of the dimensional governing equations, we derive the associated non-dimensional ones thus reducing the number of parameters and facilitating a more general analysis of the systems' dynamics.

5.2.1.1 Equations of Motion

The dimensional equation of motion for the class of SDoF hysteretic mechanical systems shown in Fig. 5.13a is derived from Newton's second law in its general form as:

$$m\ddot{u} + f_{ri}(u) = p_0 \cos(\omega t)\,. \tag{5.2.1}$$

In this context, u, $\dot{u}$, and $\ddot{u}$ represent the generalized displacement, velocity, and acceleration of mass m, respectively. Furthermore, $f_{ri}(u)$ denotes the generalized rate-independent hysteretic force acting on the hysteretic element, whereas p_0 (ω) is the amplitude (angular frequency) of the external generalized force.

According to the VRM+D, as seen in Section 4.3.2, the generalized rate-independent hysteretic force f_{ri}, appearing in Eq. (5.2.1), is governed by the following ODE:

$$\dot{f}_{ri} = \{k_e(u) + k_b + \alpha f_0 + s\alpha\,[f_e(u) + k_b u - f_{ri}]\}\,\dot{u}, \tag{5.2.2}$$

where the generalized function k_e is expressed as:

$$k_e(u) = \beta_1\beta_2 e^{\beta_2 u} + 4\gamma_1\gamma_2 \frac{e^{-\gamma_2(u-\gamma_3)}}{\left[1+e^{-\gamma_2(u-\gamma_3)}\right]^2},$$

whereas f_e is given by:

$$f_e\left(u\right)=\beta_1\left(e^{\beta_2 u}-1\right)+2\gamma_1\frac{1-e^{-\gamma_2\left(u-\gamma_3\right)}}{1+e^{-\gamma_2\left(u-\gamma_3\right)}}.$$

In Eq. (5.2.2), the model parameters need to be updated depending on the sign of the velocity $\dot{u}$, namely $s:=\operatorname{sgn}\left(\dot{u}\right)$. In particular, $k_b=k_b^+\left(k_b^-\right)$, $f_0=f_0^+\left(f_0^-\right)$, $\alpha=\alpha^+\left(\alpha^-\right)$, $\beta_1=\beta_1^+\left(\beta_1^-\right)$, $\beta_2=\beta_2^+\left(\beta_2^-\right)$, $\gamma_1=\gamma_1^+\left(\gamma_1^-\right)$, $\gamma_2=\gamma_2^+\left(\gamma_2^-\right)$, $\gamma_3=\gamma_3^+\left(\gamma_3^-\right)$ if $s>0$ $(s<0)$.

5.2.1.2 Non-dimensionalization Procedure

To ensure a more general analysis of the asymmetric behavior of the systems under consideration and minimize the number of involved parameters, we perform a non-dimensionalization of the governing equilibrium equations (see Section 2.5). This approach eliminates the system's reliance on specific units of measurement, enabling a more abstract and general treatment. The non-dimensionalization procedure involves five steps, as detailed in [14], and is performed on Eqs. (5.2.1) and (5.2.2). For the reader's convenience, these five steps are presented below:

i) We observe that time t is the independent variable whereas the generalized displacement u and the generalized rate-independent hysteretic force f_{ri} represent the dependent ones.

ii) We introduce the following non-dimensional variables:

$$\tau:=\frac{t}{t_s},\quad x:=\frac{u}{u_s},\quad z:=\frac{f_{ri}}{f_s}.$$

Each of them is defined as the associated dimensional variable scaled by a dimensional scaling factor (i.e., t_s, u_s, and f_s). Based on these definitions, the dimensional variables can be expressed as follows:

$$t=t_s\tau,\quad u=u_s x,\quad f_{ri}=f_s z. \tag{5.2.3}$$

Consequently, by using Eqs. (5.2.3), it is possible to replace the dimensional variables in Eqs. (5.2.1) and (5.2.2) with the non-dimensional ones. In particular, for Eq. (5.2.1), we obtain:

$$\frac{m u_s}{t_s^2}\frac{d^2 x}{d\tau^2}+f_s z=p_0\cos\left(\omega t_s\tau\right), \tag{5.2.4}$$

whereas for Eq. (5.2.2) we have:

$$\frac{f_s}{t_s}\frac{dz}{d\tau} = \{k_e\left(u_s x\right) + k_b + \alpha f_0 + \\ + \operatorname{sgn}\left(\frac{u_s}{t_s}\frac{dx}{d\tau}\right)\alpha\left[f_e\left(u_s x\right) + k_b u_s x - f_s z\right]\}\frac{u_s}{t_s}\frac{dx}{d\tau}. \tag{5.2.5}$$

iii) The coefficients of the highest-order term in Eqs. (5.2.4) and (5.2.5) are $\frac{mu_s}{t_s^2}$ and $\frac{f_s}{t_s}$, respectively. Hence, upon dividing Eq. (5.2.4) by $\frac{mu_s}{t_s^2}$ and Eq. (5.2.5) by $\frac{f_s}{t_s}$, one obtains:

$$\ddot{x} + \frac{f_s t_s^2}{mu_s} z = \frac{p_0 t_s^2}{mu_s}\cos\left(\omega t_s \tau\right), \tag{5.2.6}$$

and

$$\dot{z} = \frac{u_s}{f_s}\{k_e\left(u_s x\right) + k_b + \alpha f_0 + \\ + \operatorname{sgn}\left(\frac{u_s}{t_s}\dot{x}\right)\alpha\left[f_e\left(u_s x\right) + k_b u_s x - f_s z\right]\}\dot{x}. \tag{5.2.7}$$

We note that, with a slight abuse of notation, the overdot now represents the derivative with respect to the non-dimensional time τ.

iv) To simplify the final non-dimensional expressions as much as possible, we suitably select the scaling factors t_s, u_s, and f_s and impose auxiliary conditions. A possible approach is to set the amplitude of the harmonic forcing in Eq. (5.2.6) equal to one:

$$\frac{p_0 t_s^2}{mu_s} = 1 \Rightarrow t_s := \sqrt{\frac{mu_s}{p_0}}.$$

This implies that the coefficient in front of z becomes $\frac{f_s}{p_0}$. To further simplify Eq. (5.2.6), we make an additional assumption by setting:

$$f_s := p_0.$$

Consequently, the non-dimensional angular frequency is defined as:

$$\Omega := \omega t_s = \omega\sqrt{\frac{mu_s}{p_0}}.$$

Lastly, we set $u_s := 1$ to achieve the condition:

$$\operatorname{sgn}\left(\frac{u_s}{t_s}\dot{x}\right) = \operatorname{sgn}\left(\dot{u}\right) \Rightarrow \sqrt{\frac{u_s p_0}{m}} > 0.$$

v) The ODEs governing the behavior of the non-dimensional class of SDoF hysteretic mechanical systems, illustrated in Fig. 5.13b, become:

$$\ddot{x} + z = \cos\left(\Omega\tau\right), \tag{5.2.8}$$

and

$$\dot{z} = \left\{k_e\left(u_s x\right)\frac{u_s}{f_s} + \frac{k_b u_s}{f_s} + \alpha u_s \frac{f_0}{f_s} + s\alpha u_s\left[\frac{f_e\left(u_s x\right)}{f_s} + \frac{k_b u_s}{f_s}x - z\right]\right\}\dot{x}.$$

The latter can be further simplified by defining the following non-dimensional functions:

$$\kappa_e\left(x\right) := k_e\left(u_s x\right)\frac{u_s}{f_s} \quad \text{and} \quad \phi_e\left(x\right) := \frac{f_e\left(u_s x\right)}{f_s},$$

as well as the following eight non-dimensional model parameters:

$$\chi_1 := \frac{\beta_1}{f_s}, \quad \chi_2 := \beta_2 u_s, \quad \chi_3 := \frac{2\gamma_1}{f_s}, \quad \chi_4 := \gamma_2 u_s,$$
$$\chi_5 := \frac{\gamma_3}{u_s}, \quad \chi_6 := \frac{k_b u_s}{f_s}, \quad \chi_7 := \alpha u_s, \quad \chi_8 := \frac{f_0}{f_s},$$

which appear in $\kappa_e\left(x\right)$ and $\phi_e\left(x\right)$:

$$\kappa_e\left(x\right) = \chi_1\chi_2 e^{\chi_2 x} + 2\chi_3\chi_4\frac{e^{-\chi_4\left(x-\chi_5\right)}}{\left[1+e^{-\chi_4\left(x-\chi_5\right)}\right]^2},$$
$$\phi_e\left(x\right) = \chi_1\left(e^{\chi_2 x}-1\right) + \chi_3\frac{1-e^{-\chi_4\left(x-\chi_5\right)}}{1+e^{-\chi_4\left(x-\chi_5\right)}}.$$

Thus, the Non-Dimensional VRM+D (NDVRM+D) can be written as:

$$\dot{z} = \left\{\kappa_e\left(x\right) + \chi_6 + \chi_7\chi_8 + s\chi_7\left[\phi_e\left(x\right) + \chi_6 x - z\right]\right\}\dot{x}. \tag{5.2.9}$$

We may note that Eqs. (5.2.8) and (5.2.9) represent the non-dimensional form of the initial equilibrium equations.

Subsection 5.2.2

Analyzed Hysteretic Mechanical Systems

In the sequel, for the reader's convenience, we briefly summarize the four types of hysteresis loop shape that are generally observed in hysteretic mechanical systems. Subsequently, we describe the asymmetric responses characterizing the four types of selected hysteretic mechanical systems that will be numerically analyzed.

5.2.2.1 Hysteresis Loops Classification

According to the classification proposed in [84], hysteresis loops can be classified into four main categories:

- Shape type $S1$: the hysteresis loops are limited by two straight lines (Fig. 5.14).
- Shape type $S2$: the hysteresis loops are bounded by two curves with no inflection point (Fig. 5.15).
- Shape type $S3$: the hysteresis loops are limited by two curves with one inflection point (Fig. 5.16).
- Shape type $S4$: the hysteresis loops are bounded by two curves with two inflection points (Fig. 5.17).

Given their central role in the above-described classification, it is essential to formally define the terms upper and lower limiting curves within the NDVRM+D. According to the definitions provided in [83], the closed-form expression of the rate-independent hysteretic force described by Eq. (5.2.9) is given by:

$$z(x) = \begin{cases} z^+(x) = \phi_e^+(x) + \chi_6^+ x + \chi_8^+ + C^+(x_P, z_P) e^{-\chi_7^+ x} & \text{for} \quad s > 0 \\ z^-(x) = \phi_e^-(x) + \chi_6^- x - \chi_8^- + C^-(x_P, z_P) e^{+\chi_7^- x} & \text{for} \quad s < 0, \end{cases}$$

where $P \equiv (x_P, z_P)$ is a generic point in the generalized force-displacement plane whereas $C^{\pm}(x_P, z_P)$ are functions defined as:

$$\begin{cases} C^+(x_P, z_P) = -\left[\phi_e^+(x_P) + \chi_6^+ x_P + \chi_8^+ - z_P\right] e^{+\chi_7^+ x_P} & \text{for} \quad s > 0 \\ C^-(x_P, z_P) = -\left[\phi_e^-(x_P) + \chi_6^- x_P - \chi_8^- - z_P\right] e^{-\chi_7^- x_P} & \text{for} \quad s < 0. \end{cases}$$

It can be easily demonstrated, adopting the previous equations, that the upper (lower) limiting curve c_u (c_l) represents an asymptote of the generic loading curve z^+ (z^-) and that its expression is:

$$
\begin{aligned}
c_u &= \phi_e^+(x) + \chi_6^+ x + \chi_8^+ \,, \\
c_l &= \phi_e^-(x) + \chi_6^- x - \chi_8^- \,.
\end{aligned}
$$

SUBSECTION 5.2.3

Properties of the Selected Systems

The analyzed SDoF hysteretic mechanical systems, referred to as Systems $S1$, $S2$, $S3$, and $S4$, in the sequel, are respectively characterized by the non-dimensional hysteresis loops illustrated in Figs. 5.14-5.17. The latter have been obtained by imposing a non-dimensional sinusoidal generalized displacement, with 1.5 amplitude and unitary frequency, and by adopting the non-dimensional parameters listed in Tables 5.5-5.8.

5.2.3.1 Systems S1

In Systems $S1$, both upper and lower limiting curves are represented by straight lines. The three selected systems are:

- System $S1a$ (Fig. 5.14a): asymmetry arises from the different values of χ_6^+ and χ_6^-, resulting in limiting straight lines with different slopes.

- System $S1b$ (Fig. 5.14b): asymmetry is due to the different values of χ_7^+ and χ_7^- , leading to a hysteresis loop with identical limiting straight lines but generic loading and unloading curves with different curvature.

- System $S1c$ (Fig. 5.14c): asymmetry arises from the different values of χ_8^+ and χ_8^- , producing limiting straight lines with the same slope but asymmetric with respect to the x-axis.

5.2.3.2 Systems S2

Systems $S2$ are characterized by more intricate hysteretic behavior because of the significant curvature of both upper and lower limiting curves, although neither curve exhibits inflection points. Specifically, the three selected systems are:

- System $S2a$ (Fig. 5.15a): asymmetry arises from differing values of χ_7^+ and χ_7^-, leading to a hysteresis loop with identical limiting curves but loading and unloading curves with different curvature.

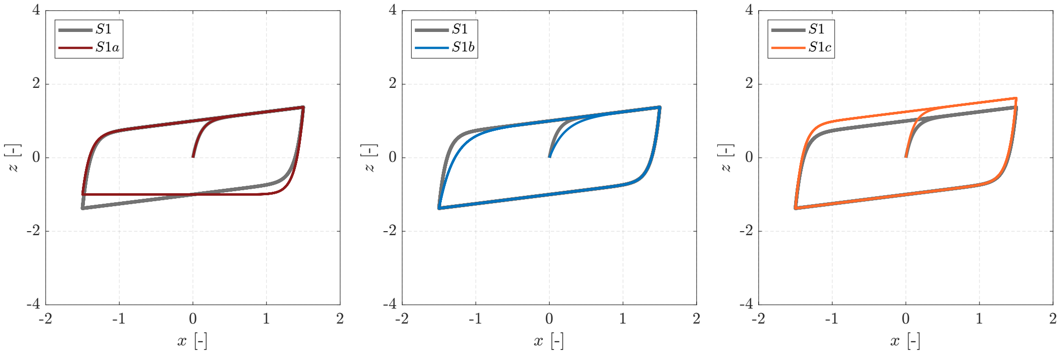

(a) (b) (c)

Figure 5.14. Asymmetric hysteresis loops, belonging to shape type $S1$, that describe the behavior of (a) System $S1a$, (b) System $S1b$ and (c) System $S1c$.

	sgn($\dot{x}$)	χ_1	χ_2	χ_3	χ_4	χ_5	χ_6	χ_7	χ_8
$S1$	+	0.00	0.00	0.00	0.00	0.00	0.25	10.00	1.00
	−	0.00	0.00	0.00	0.00	0.00	0.25	10.00	1.00
$S1a$	+	0.00	0.00	0.00	0.00	0.00	0.25	10.00	1.00
	−	0.00	0.00	0.00	0.00	0.00	0.00	10.00	1.00
$S1b$	+	0.00	0.00	0.00	0.00	0.00	0.25	5.00	1.00
	−	0.00	0.00	0.00	0.00	0.00	0.25	10.00	1.00
$S1c$	+	0.00	0.00	0.00	0.00	0.00	0.25	10.00	1.25
	−	0.00	0.00	0.00	0.00	0.00	0.25	10.00	1.00

Table 5.5. NDVRM+D parameters adopted to simulate the hysteresis loops in Figure 5.14.

- System $S2b$ (Fig. 5.15b): asymmetry is caused by variations in χ_1^+, χ_1^-, χ_2^+, and χ_2^-. Specifically, increasing χ_1^+ while decreasing χ_2^+ reduces the curvature of the upper limiting curve.

- System $S2c$ (Fig. 5.15c): asymmetry also results from different values of χ_1^+, χ_1^-, χ_2^+, and χ_2^-. In this case, decreasing χ_1^+ while increasing χ_2^+ increases the curvature of the upper limiting curve.

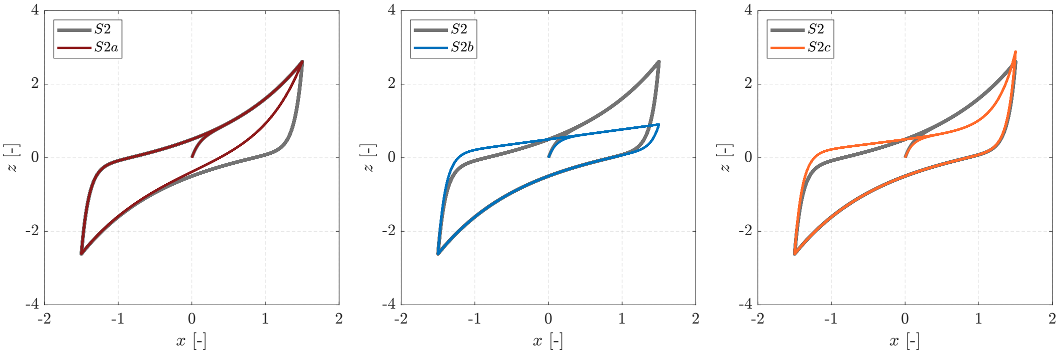

(a) (b) (c)

Figure 5.15. Asymmetric hysteresis loops, belonging to shape type $S2$, that describe the behavior of (a) System $S2a$, (b) System $S2b$ and (c) System $S2c$.

Table 5.6. NDVRM+D parameters adopted to simulate the hysteresis loops in Figure 5.15.

	sgn($\dot{x}$)	χ_1	χ_2	χ_3	χ_4	χ_5	χ_6	χ_7	χ_8
$S2$	+	0.50	1.00	0.0	0.0	0.0	0.25	10.0	0.5
	−	-0.50	-1.00	0.0	0.0	0.0	0.25	10.0	0.5
$S2a$	+	0.50	1.00	0.0	0.0	0.0	0.25	10.0	0.5
	−	-0.50	-1.00	0.0	0.0	0.0	0.25	2.0	0.5
$S2b$	+	2.00	0.01	0.0	0.0	0.0	0.25	10.0	0.5
	−	-0.50	-1.00	0.0	0.0	0.0	0.25	10.0	0.5
$S2c$	+	0.005	4.00	0.0	0.0	0.0	0.25	10.0	0.5
	−	-0.50	-1.00	0.0	0.0	0.0	0.25	10.0	0.5

5.2.3.3 Systems S3

Systems $S3$ exhibit complex hysteretic responses due to a significant curvature and the inflection point characterizing both the upper and lower limiting curves. In particular, the three selected systems are:

- System $S3a$ (Fig. 5.16a): asymmetry is due to differing values of χ_3^+ and χ_3^-. This results in an hysteresis loop with asymmetric limiting curves, leading to a larger area in the negative x-direction where the limiting curves are more widely spaced.
- System $S3b$ (Fig. 5.16b): asymmetry arise from variations in χ_4^+ and χ_4^-. This induces a change in the curvature of the upper limiting curve, creating an hysteresis loop with

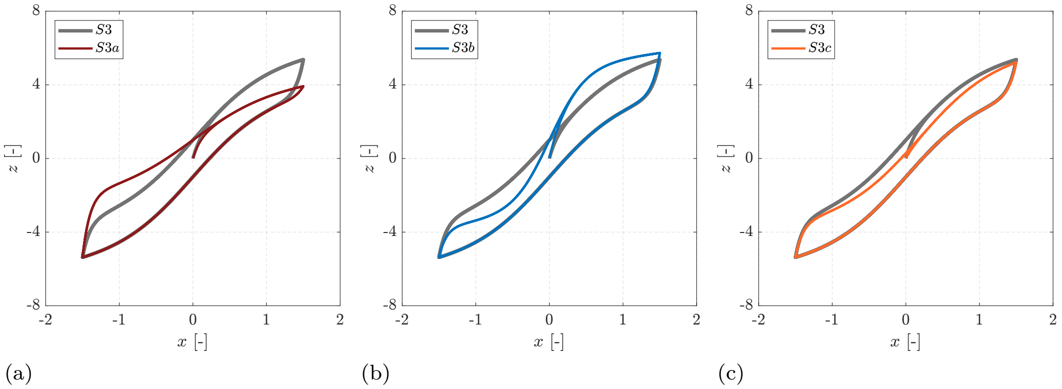

(a) (b) (c)

Figure 5.16. Asymmetric hysteresis loops, belonging to shape type $S3$, that describe the behavior of (a) System $S3a$, (b) System $S3b$ and (c) System $S3c$.

a larger area in the positive x-direction, where the limiting curves are more separated.

- System $S3c$ (Fig. 5.16c): asymmetry results from different values of χ_5^+ and χ_5^-. This causes a shift in the inflection point of the upper limiting curve, thus reducing the hysteresis loop area.

	sgn($\dot{x}$)	χ_1	χ_2	χ_3	χ_4	χ_5	χ_6	χ_7	χ_8
$S3$	+	0.00	0.00	4.00	2.00	0.00	0.50	10.00	1.00
	−	0.00	0.00	4.00	2.00	0.00	0.50	10.00	1.00
$S3a$	+	0.00	0.00	2.40	2.00	0.00	0.50	10.00	1.00
	−	0.00	0.00	4.00	2.00	0.00	0.50	10.00	1.00
$S3b$	+	0.00	0.00	4.00	4.00	0.00	0.50	10.00	1.00
	−	0.00	0.00	4.00	2.00	0.00	0.50	10.00	1.00
$S3c$	+	0.00	0.00	4.00	2.00	0.18	0.50	10.00	1.00
	−	0.00	0.00	4.00	2.00	0.00	0.50	10.00	1.00

Table 5.7. NDVRM+D parameters adopted to simulate the hysteresis loops in Figure 5.16.

5.2.3.4 Systems S4

Finally, Systems $S4$ display a quite complex behavior since both upper and lower limiting curves, having two inflection points,

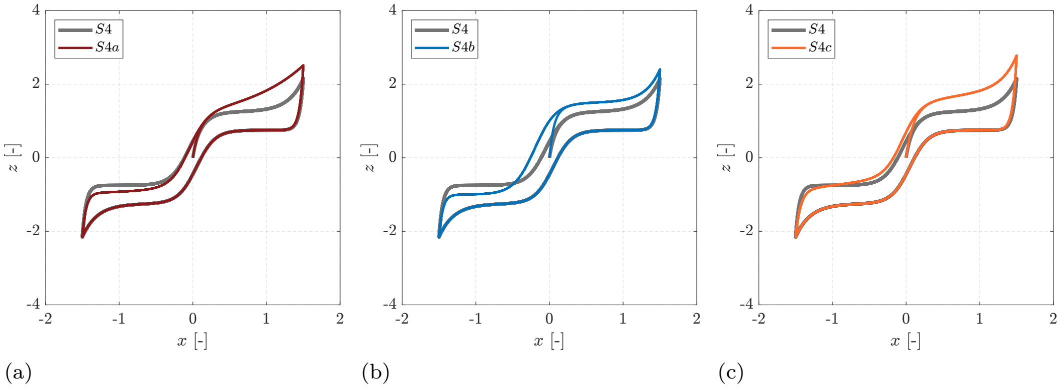

(a) (b) (c)

Figure 5.17. Asymmetric hysteresis loops, belonging to shape type $S4$, that describe the behavior of (a) System $S4a$, (b) System $S4b$ and (c) System $S4c$.

show significant stiffening effects thanks to the non-zero parameters χ_1, χ_2, χ_3, and χ_4. The three selected systems are:

- System $S4a$ (Fig. 5.17a): asymmetry arises from the differing values of χ_1^+, χ_1^-, χ_2^+, and χ_2^-. Specifically, increasing χ_1^+ while decreasing χ_2^+ results in a reduction of the curvature of the upper limiting curve.

- System $S4b$ (Fig. 5.17b): asymmetry is due to variations in χ_3^+, χ_3^-, χ_4^+, χ_4^-, χ_5^+, and χ_5^-. The combined effect of these parameters leads to an upper limiting curve with a different inflection point, being $\chi_5^+ \neq 0$, and a greater curvature at that point due to the values assumed by χ_3^+, χ_4^+, and χ_5^+.

- System $S4c$ (Fig. 5.17c): asymmetry results from different values of χ_6^+, χ_6^-, χ_7^+, χ_7^-, χ_8^+, and χ_8^-. These differences create a hysteresis loop having limiting curves with different curvatures due to variations in χ_6^+ and χ_6^-. Additionally, the intercept of the upper limiting curve is not symmetrical with respect to the lower limiting curve due to different values of χ_8^+ and χ_8^-. Furthermore, the generic loading curve has a different curvature with respect to the unloading one because of the differing values of χ_7^+ and χ_7^-.

SUBSECTION 5.2.4

Numerical Results

	$\mathrm{sgn}(\dot{x})$	χ_1	χ_2	χ_3	χ_4	χ_5	χ_6	χ_7	χ_8
$S4$	$+$	0.0005	5.0	1.00	8.0	-0.05	0.00	20	0.25
	$-$	-0.0005	-5.0	1.00	8.0	0.05	0.00	20	0.25
$S4a$	$+$	0.2500	1.2	1.00	8.0	-0.05	0.00	20	0.25
	$-$	-0.0005	-5.0	1.00	8.0	0.05	0.00	20	0.25
$S4b$	$+$	0.0005	5.0	1.25	7.0	-0.20	0.00	20	0.25
	$-$	-0.0005	-5.0	1.00	8.0	0.05	0.00	20	0.25
$S4c$	$+$	0.0005	5.0	1.00	8.0	-0.05	0.25	15	0.50
	$-$	-0.0005	-5.0	1.00	8.0	0.05	0.00	20	0.25

Table 5.8. NDVRM+D parameters adopted to simulate the hysteresis loops in Figure 5.17.

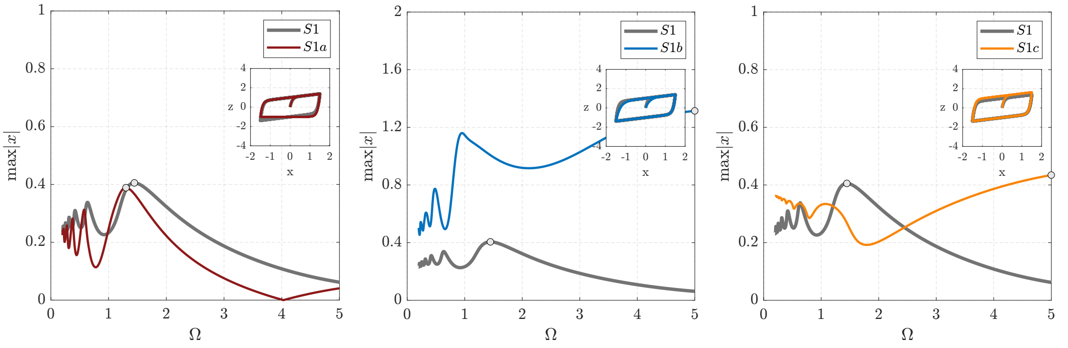

(a) (b) (c)

Figure 5.18. Effects of asymmetries on FRCs of Systems $S1$: (a) System $S1a$, (b) System $S1b$, and (c) System $S1c$.

In this section, we present the results of the analyses conducted on the non-dimensional hysteretic systems detailed in the previous sections. We analyze the systems FRCs obtained by using the procedure described in Section 4.3.3 (the pseudo-code can be found in Table 4.3), where the continuation parameter is Ω. Furthermore, the parameters used in the procedure are listed in Table 4.4. These analyses emphasize the effects of asymmetries on the FRCs and on related resonance peaks and bifurcation shifts.

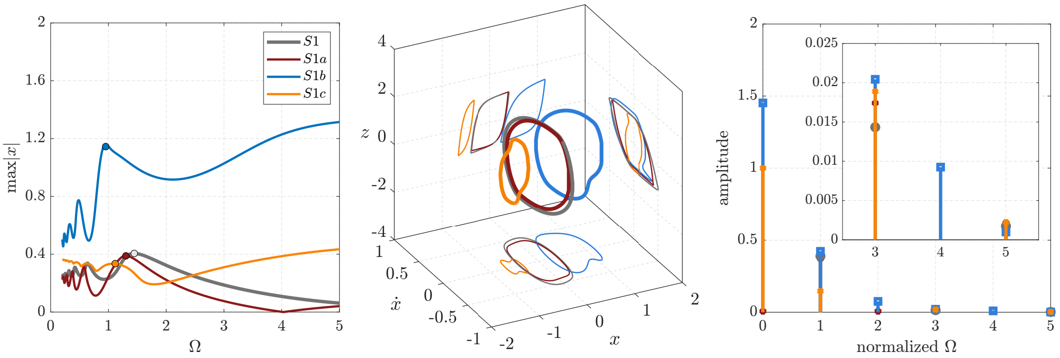

(a) (b) (c)

Figure 5.19. Systems $S1$: (a) FRCs with highlighted points, (b) corresponding state-space representation of the periodic orbits, and (c) Fourier transform of the signals $x(\tau)$.

5.2.4.1 Systems S1

In the following, we present the results of the analyses carried out on Systems $S1$ previously described. The adopted ND-VRM+D parameters are listed in Table 5.5 whereas the corresponding hysteresis loop shapes are illustrated in Fig. 5.14.

Figure 5.18 shows that the FRCs exhibit a leftward bend, indicative of a softening nonlinearity, and are globally stable within the analyzed range of Ω. Notably, the asymmetric behavior affects the resonance peak values. Indeed, while the symmetric System $S1$ has a resonance peak at $(1.4467, 0.405457)$, the asymmetric ones exhibit resonance peaks at:

- $S1a$: $(1.30146, 0.388739)$ (Fig. 5.18a);
- $S1b$: $(4.99873, 1.31446)$ (Fig. 5.18b);
- $S1c$: $(4.99913, 0.434436)$ (Fig. 5.18c).

Furthermore, in the low-frequency range, the asymmetric systems exhibit multiple resonance peaks that differ from those observed in the symmetric case. Specifically, while the symmetric system shows five resonance peaks within the frequency range $\Omega \in [0.635434, 0.212975]$, System $S1a$ displays four peaks in the range $\Omega \in [0.575991, 0.22099]$, System $S1b$ has four peaks for $\Omega \in [0.950858, 0.236365]$, and System $S1c$ shows seven peaks in the range $\Omega \in [1.07329, 0.214785]$.

Finally, Fig. 5.19 illustrates that for the points highlighted in Fig. 5.19a, both the state-space representation of the peri-

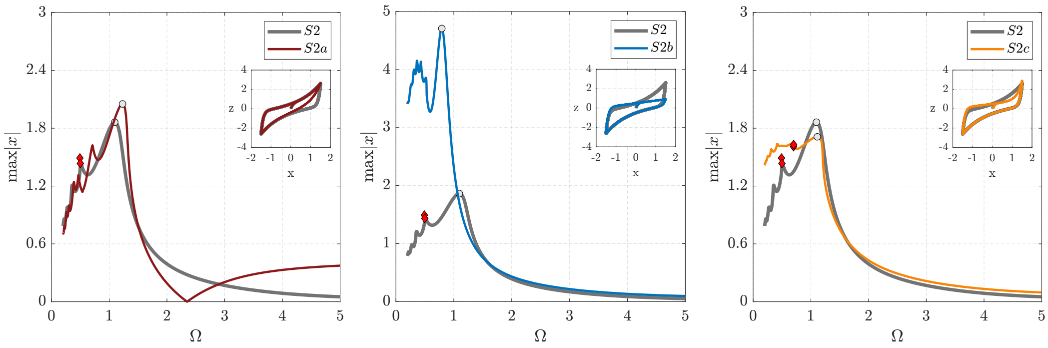

(a) (b) (c)

Figure 5.20. Effects of asymmetries on FRCs of Systems $S2$: (a) System $S2a$, (b) System $S2b$, and (c) System $S2c$.

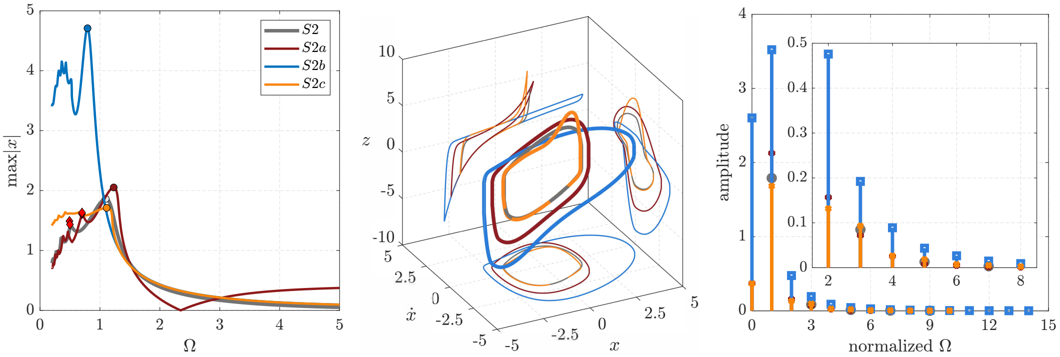

(a) (b) (c)

Figure 5.21. Systems $S2$: (a) FRCs with highlighted points, (b) corresponding state-space representation of the periodic orbits, and (c) Fourier transform of the signals $x(\tau)$.

odic orbits (Fig. 5.19b) and the Fourier transform of the corresponding $x(\tau)$ signals (Fig. 5.19c) reveal symmetry changes in the periodic solution when asymmetry is introduced into the hysteresis loop. This leads to the formation of stable asymmetric solutions. Specifically, for Systems $S1a$, $S1b$, and $S1c$, the appearance of even harmonics and a zero-frequency component can be observed, indicating a loss of symmetry due to the odd nonlinearities and the presence of a non-zero mean in the signals.

5.2.4.2 Systems S2

In this section, we illustrate the results of the analyses performed on Systems $S2$ previously introduced. The adopted model parameters are provided by Table 5.6 whereas the associated hysteresis loop shapes are presented in Fig. 5.15.

Figure 5.20 shows that the FRCs exhibit a rightward bend, indicating a hardening nonlinearity. As in the previous case, the asymmetric behavior affects the resonance peak values. Specifically, while the symmetric System $S2$ shows a resonance peak at $(1.0959, 1.86253)$, the asymmetric ones yield different peak values, which are:

- $S2a$: $(1.23028, 2.05198)$ (Fig. 5.20a);
- $S2b$: $(0.792923, 4.70872)$ (Fig. 5.20b);
- $S2c$: $(1.11139, 1.71099)$ (Fig. 5.20c).

Furthermore, the FRC for the symmetric Systems $S2$ does not exhibit global stability across the entire range of Ω, as shown in Fig. 5.20. Specifically, the system experiences a series of *fold bifurcations* at the points $(0.491811, 1.49016)$ and $(0.499025, 1.43468)$. The introduction of asymmetries alters these bifurcation scenarios. Indeed, for Systems $S2a$ and $S2b$ the unstable regions are eliminated, resulting in globally stable responses. In contrast, for System $S2c$, the *fold bifurcations* shift to the points $(0.699439, 1.60923)$ and $(0.701636, 1.62981)$.

In the low-frequency range, the asymmetric systems exhibit multiple resonance peaks that differ from those observed in the symmetric case. Specifically, while the symmetric system displays three resonance peaks at angular frequencies of 0.359254, 0.273955, and 0.21778, the asymmetric System $S2a$ exhibits six peaks within the range $\Omega \in [0.709812, 0.21953]$. In addition, System $S2b$ shows five peaks in the frequency range $\Omega \in [0.518018, 0.263544]$ and System $S2c$ reveals five peaks within $\Omega \in [0.689203, 0.226802]$.

Moreover, Fig. 5.21 demonstrates that for the resonance peaks highlighted in Fig. 5.21a, both the state-space representation of the periodic orbits (Fig. 5.21b) and the Fourier transform of the corresponding $x(\tau)$ signals (Fig. 5.21c) suggest significant changes when asymmetry is introduced into the hysteresis loop. This results in the emergence of stable asymmetric solutions for Systems $S2a$, $S2b$, and $S2c$. Finally, we may note that the appearance of even harmonics and a zero-frequency component indicate a loss of symmetry and the presence of a non-zero mean in the signals.

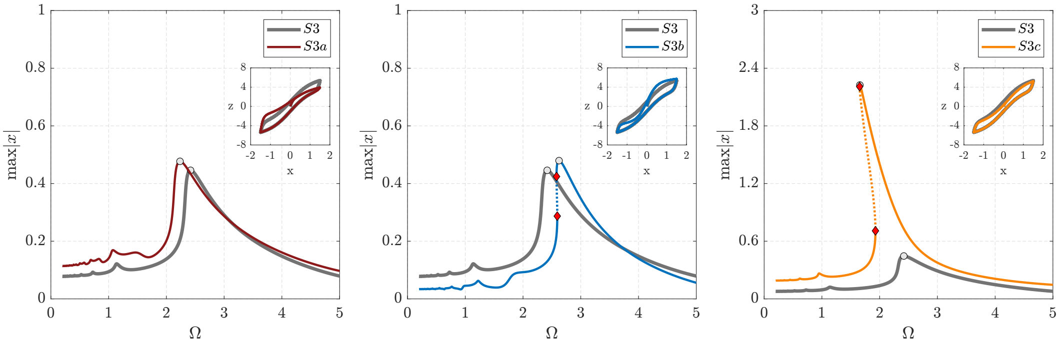

(a) (b) (c)

Figure 5.22. Effects of asymmetries on FRCs of Systems $S3$: (a) System $S3a$, (b) System $S3b$, and (c) System $S3c$.

5.2.4.3 Systems S3

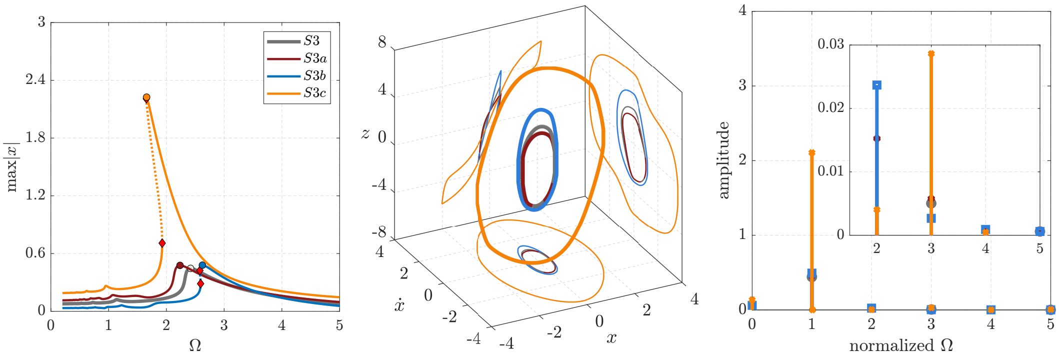

(a) (b) (c)

Figure 5.23. Systems $S3$: (a) FRCs with highlighted points, (b) corresponding state-space representation of the periodic orbits, and (c) Fourier transform of the signals $x(\tau)$.

In the sequel, we present the results of the analyses carried out on Systems $S3$ previously described. The adopted ND-VRM+D parameters are listed in Table 5.7 whereas the corresponding hysteresis loop shapes are illustrated in Fig. 5.16.

As shown in Fig. 5.22, the FRCs exhibit a slight leftward bend, indicating a softening nonlinearity. Once again, the asymmetric behavior affects the location of the resonance peak. Specifically, while the symmetric System $S3$ exhibits a resonance peak at $(2.41869, 0.445915)$, the asymmetric ones yield different results:

- $S3a$: the peak occurs at $(2.23587, 0.477059)$ (Fig. 5.22a);
- $S3b$: the peak is found at $(2.6237, 0.47944)$ (Fig. 5.22b);
- $S3c$: the peak is located at $(1.65751, 2.22496)$ (Fig. 5.22c).

Furthermore, the FRCs for both the symmetric System $S3$ and the asymmetric System $S3a$ are globally stable across the examined range of Ω, as shown in Fig. 5.22a. On the contrary, the introduction of asymmetries modifies the stability scenarios for the other two asymmetric systems. Indeed, Systems $S3b$ and $S3c$ exhibit two *fold bifurcations*, occurring at the points $(2.58044, 0.42432)$ and $(2.59294, 0.286992)$, and at $(1.65259, 2.20899)$ and $(1.92751, 0.708143)$, respectively.

In the low-frequency range, the asymmetric systems display multiple resonance peaks that differ from those observed in the symmetric case. Specifically, while the symmetric system exhibits eight resonance peaks within the frequency range $\Omega \in [1.13931, 0.21758]$, the asymmetric System $S3a$ shows sixteen peaks in the range $\Omega \in [1.48551, 0.208533]$. Furthermore, System $S3b$ presents a series of peaks within $\Omega \in [1.90118, 0.20]$ (Fig. 5.25a), whereas System $S3c$ displays seven peaks within $\Omega \in [0.94955, 0.210044]$.

Figure 5.23 reveals that the resonance peaks, indicated in Fig. 5.23a, exhibit clear symmetry changes in the state-space trajectories (Fig. 5.23b) and in the Fourier transform of the corresponding signals $x(\tau)$ (Fig. 5.23c). The introduction of hysteresis loop asymmetry in Systems $S3a$, $S3b$ and $S3c$ induces stable asymmetric periodic solutions that show the appearance of even harmonics and a zero-frequency component, confirming the loss of symmetry and the generation of a non-zero mean value in the signals.

5.2.4.4 Systems S4

Let us now present the results of the analyses performed on Systems $S4$ previously introduced. The adopted model parameters are provided by Table 5.8 whereas the associated hysteresis loop shapes are shown in Fig. 5.17.

As illustrated in Fig. 5.24, the FRCs initially display a softening behavior, followed by a slight rightward bend, indicating the presence of hardening nonlinearity. Once again, the asymmetric behavior affects the location of the resonance peak.

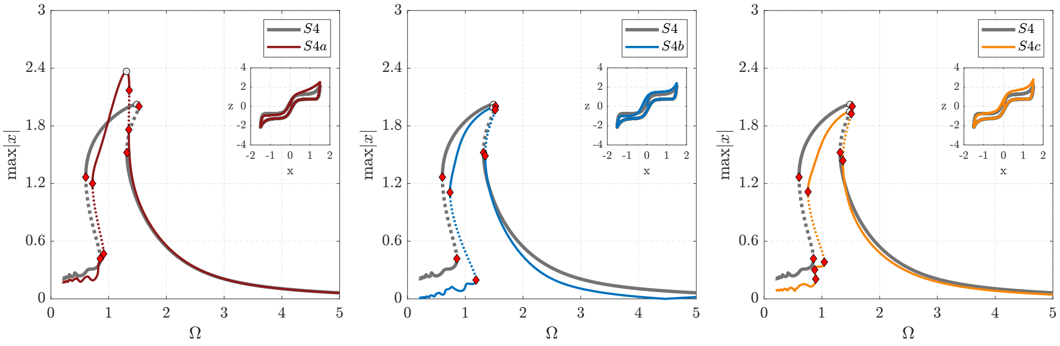

(a) (b) (c)

Figure 5.24. Effects of asymmetries on FRCs of Systems $S4$: (a) System $S4a$, (b) System $S4b$, and (c) System $S4c$.

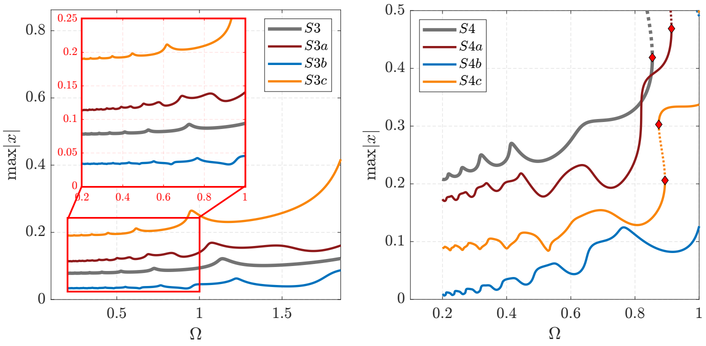

(a) (b)

Figure 5.25. Detailed view of the FRCs in the low-frequency range for Systems (a) $S3$ and (b) $S4$.

Specifically, while the symmetric System $S4$ shows a resonance peak at $(1.48753, 2.02269)$, the asymmetric ones present the following resonance peaks:

- $S4a$: $(1.30871, 2.36697)$ (Fig. 5.24a);
- $S4b$: $(1.48427, 1.98867)$ (Fig. 5.24b);
- $S4c$: $(1.4803, 1.94743)$ (Fig. 5.24c).

Additionally, the symmetric system undergoes a series of four *fold bifurcations* at $(0.603965, 1.2666)$, $(0.854123, 0.418801)$, $(1.3158, 1.52252)$, and $(1.52581, 2.00313)$. The presence of asymmetries modifies the bifurcation scenarios as follows:

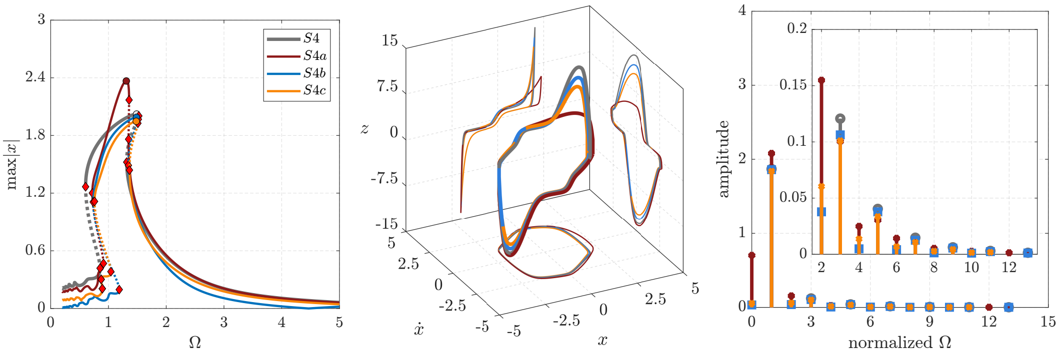

(a) (b) (c)

Figure 5.26. Systems $S4$: (a) FRCs with highlighted points, (b) corresponding state-space representation of the periodic orbits, and (c) Fourier transform of the signals $x(\tau)$.

- for System $S4a$, the four *fold bifurcations* shift to $(0.720801, 1.20065)$, $(0.913773, 0.468821)$, $(1.34854, 1.7609)$, and $(1.35695, 2.16914)$ (Fig. 5.24a);
- for System $S4b$, the *fold bifurcations* move to $(0.736037, 1.10803)$, $(1.18676, 0.19649)$, $(1.34491, 1.48896)$, and $(1.51782, 1.9683)$ (Fig. 5.24b);
- for System $S4c$, they shift to $(0.759006, 1.11382)$, $(1.04232, 0.383246)$, $(1.36337, 1.43941)$, and $(1.50922, 1.92684)$. Additionally, two more *fold bifurcations* occur at $(0.874157, 0.302852)$ and $(0.89352, 0.206033)$ (Fig. 5.24c).

In the low-frequency range, the asymmetric systems display multiple resonance peaks that differ from those observed in the symmetric case. Specifically, as shown in Fig. 5.25b, while the symmetric system exhibits five resonance peaks within the frequency range $\Omega \in [0.648081, 0.219302]$, the asymmetric System $S4a$ shows several peaks within $\Omega \in [0.837753, 0.228199]$. Additionally, System $S4b$ displays peaks in the range $\Omega \in [1.02588, 0.212699]$ whereas System $S4c$ shows peaks within the range $\Omega \in [0.891506, 0.207391]$.

In conclusion, Fig. 5.26 provides a detailed examination of the resonance peaks identified in Fig.5.26a. The accompanying state-space representation of the periodic orbits, shown in Fig. 5.26b, along with the Fourier transform of the corresponding $x(\tau)$ signals, depicted in Fig. 5.26c, clearly demonstrate how the introduction of asymmetry into the hysteresis loop alters the symmetry of the periodic solutions. This alteration results in the emergence of stable asymmetric solutions for Systems $S4a$, $S4b$, and $S4c$. In these cases, the presence of even harmonics and a zero-frequency component indicates a significant shift in symmetry, as typically expected in systems with odd nonlinearities, along with the generation of signals exhibiting a non-zero mean.

Subsection 5.2.5

Conclusions

In this study, we have performed a frequency response analysis of asymmetric hysteretic systems modeled using the VRM+D [83]. Starting from the dimensional governing equations, we derived the associated non-dimensional ones thus reducing the number of involved parameters.

By employing the Poincaré map based continuation method described in Section 4.3.3, we investigated the periodic solutions of various mechanical hysteretic systems having different asymmetric responses. In particular, the findings revealed that variations in the degree of asymmetry of the hysteresis loop significantly impact both frequency responses and stability of the analyzed systems when subjected to periodic excitations. This clarifies the intricate relationship between the asymmetry of the hysteresis loop and the dynamic behavior of such systems.

This research contributes to the ongoing efforts to better understand and model the behavior of asymmetric hysteretic mechanical systems, offering a benchmark for future studies and practical implementations. Further work may expand on the current findings by exploring other types of asymmetries and their effects on more complex, real-world systems.

Section 5.3

Frequency Response Curves of Negative Stiffness Metamaterials

Mechanical metamaterials have revolutionized material science with their ability to exhibit properties unattainable in conventional materials. These engineered structures have found applications in different fields, including vibration isolation [55], and seismic wave manipulation [20]. Among the various types of mechanical metamaterials, those with negative moduli, such as negative bulk modulus or negative elastic modulus, have garnered significant attention due to their unique deformation capabilities.

Negative metamaterials represent a significant deviation from traditional mechanical behavior. As reported in [99], historically, it has been assumed that the elasticity tensor must be positive definite, implying that both the bulk modulus and the shear modulus should be positive. This assumption has long been considered a necessary condition for the thermodynamic admissibility of elasticity tensors in continuum mechanics. The logic is that negative compressibility or stiffness leads to instability of the material; nevertheless, materials with negative compressibility or stiffness have been observed under various experimental conditions, and if their stability can be assured, such materials can have numerous practical applications [99]. Specifically, many applications of negative stiffness materials can be found in the literature, including vibration protection systems for vehicles [55], seismic protection of structures [75], and vibration isolation of railroads [54]. In spite of their promising potential, a complete understanding of the complex mechanical response of negative stiffness metamaterials is far from being achieved, mainly due to lack of mathematical modeling and experimental testing.

To bridge this gap, we present a comprehensive analysis of the FRCs for a specific Negative Stiffness Device (NSD) introduced in [75] and briefly described in Section 5.3.1. Our approach involves simulating the response of a SDoF hysteretic mechanical system with the characteristic hysteresis loop shape of the NSD. To simulate the complex hysteretic behavior of the metamaterial, we employ the VRM+D, a novel hysteresis model designed to simulate complex hysteretic behaviors (Section 4.3.2). This uniaxial phenomenological model offers several

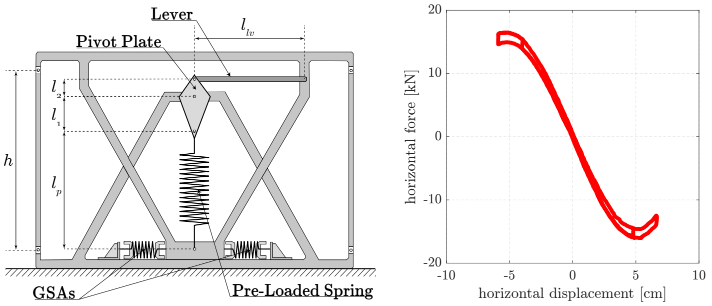

(a) (b)

Figure 5.27. Undeformed Negative Stiffness Device (a) and experimental force-displacement hysteresis loop without GSA (b) [75].

advantages over existing models [13, 85, 87] since it can describe complex shapes of hysteresis loops in a unified way; moreover, it employs differential or equivalent analytical closed-form expressions to evaluate the generalized rate-independent hysteretic force [11, 82]. Finally, we analyze the FRCs for the NSD obtained using the continuation technique based on Poincaré maps, as described in Section 4.3.3.

Subsection 5.3.1

Negative Stiffness Metamaterials

In this section, we explore the properties and applications of metamaterials with negative stiffness, with a focus on the NSD proposed in [75]. Specifically, we start by discussing the fundamental characteristics of a negative stiffness metamaterial, and then delve into the specific design and experimental observations of the NSD.

5.3.1.1 Properties of Negative Stiffness Metamaterials

Metamaterials with negative stiffness deform in the direction opposite to the applied force, creating an assisting force that facilitates further deformation. This behavior is in contrast with what happens in traditional materials with positive stiffness which deform in the direction of the applied force and generate a restoring force to resist deformation, aiming to return the material to its original shape [99].

As a consequence, negative stiffness metamaterials experience larger deformations compared to positive stiffness materials when subjected to comparable loading conditions. A number of studies [51, 53] have demonstrated that combining positive and negative stiffness elements can achieve exceptional properties, such as simultaneously high damping and stiffness, with extremely high stiffness values possible through specific arrangements of these elements [52, 91].

5.3.1.2 Negative Stiffness Device

The NSD proposed by Sarlis et al. [75] exemplifies the principles previously discussed. As illustrated in Fig. 5.27a, the device features a precompressed spring and two Gap Spring Assemblies (GSAs) at the bottom. The GSAs provide positive stiffness up to a certain displacement, resulting in an overall effective stiffness that is nearly zero within this range. Additionally, the precompressed spring connects to a mechanism with a lever and pivot plate, which transfers horizontal loads to the frame.

The device achieves negative stiffness through the rotation of the precompressed spring when the device deforms. Experimental force-displacement relations for the tested prototype under harmonic motion of 0.1 Hz frequency and 6.4 cm amplitude are shown in Fig. 5.27b [75]. The observed S-shaped, pinched hysteresis loop, caused by joint friction not accounted for in Sarlis et al.'s models [75], necessitates the use of a more elaborate model to accurately simulate the device's complex hysteretic behavior.

SUBSECTION 5.3.2

Mathematical Model

In this section, we outline the mathematical model used to analyze the NSD discussed earlier. In particular, we introduce the general class of SDoF hysteretic mechanical systems, with a focus on the hysteresis model and the non-dimensionalization procedure.

5.3.2.1 Hysteretic Mechanical System

The general class of dimensional SDoF hysteretic mechanical system, considered in [14] and shown in Fig. 5.28a, comprises a mass m connected in parallel to three different types of elements:

- a linear elastic spring with stiffness k;
- a linear rate-dependent hysteretic element with viscous damping coefficient c;
- a rate-independent hysteretic spring.

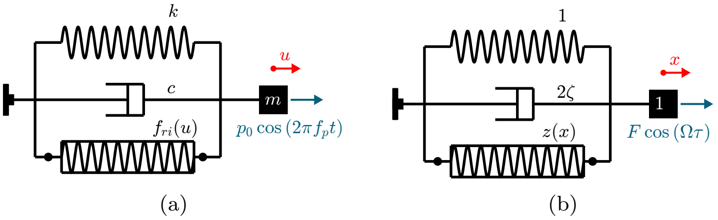

Figure 5.28. Dimensional (a) and non-dimensional (b) SDoF hysteretic mechanical systems.

For this system, the dimensional equation of motion can be derived from Newton's second law in its general form as:

$$m\ddot{u} + c\dot{u} + ku + f_{ri}(u) = p_0 \cos(2\pi f_p t), \tag{5.3.1}$$

where u, $\dot{u}$, and $\ddot{u}$ denote the generalized displacement, velocity, and acceleration of the mass m, respectively. In this equation, f_{ri} is the generalized rate-independent hysteretic force exerted on the hysteretic element, whereas p_0 (f_p) is the amplitude (frequency) of the input force.

5.3.2.2 VRM+D

To describe the rate-independent hysteretic force f_{ri} in Eq. (5.3.1) we use the VRM+D described in Section 4.3.2. According to its original formulation, the generalized rate-independent hysteretic force $f_{ri}(u)$ is governed by the following ODE:

$$\dot{f}_{ri} = \{k_e(u) + k_b + \alpha f_0 + s\alpha [f_e(u) + k_b u - f_{ri}]\}\, \dot{u}, \tag{5.3.2}$$

where $s := \operatorname{sgn}(\dot{u})$, and the generalized function k_e is given by:

$$k_e(u) = \beta_1\beta_2 e^{\beta_2 u} + 4\gamma_1\gamma_2 \frac{e^{-\gamma_2(u-\gamma_3)}}{\left[1 + e^{-\gamma_2(u-\gamma_3)}\right]^2}.$$

Similarly, the generalized function f_e is given by:

$$f_e(u) = \beta_1\left(e^{\beta_2 u} - 1\right) + 2\gamma_1 \frac{1 - e^{-\gamma_2(u-\gamma_3)}}{1 + e^{-\gamma_2(u-\gamma_3)}}.$$

In Eq. (5.3.2), the model parameters can be updated based on the sign of the velocity $\dot{u}$.

5.3.2.3 Non-dimensionalization procedure.

Non-dimensionalization is a useful technique in the analysis of systems governed by ODEs since it reduces the number of parameters involved, simplifying the analysis and aiding in understanding the relationships between system parameters. This process also allows for the comparison of different systems on a common scale by removing specific units, identifying common trends and properties, and thus generalizing the problem (Section 2.5).

The non-dimensionalization process comprises five steps [14], briefly outlined below for the reader's convenience:

i) identify all independent and dependent variables;

ii) replace all variables with non-dimensional quantities defined by relationships between dimensional variables and newly introduced dimensional coefficients;

iii) divide the resulting equation by the coefficient of the higher order derivative;

iv) select the dimensional coefficients previously introduced based on the characteristic units of the system in order to simplify any auxiliary conditions;

v) rewrite the equation in terms of new non-dimensional quantities.

By applying these five steps to the equation of motion represented by Eqs. (5.3.1) and (5.3.2) we have that a suitable non-dimensionalization of the governing equations is obtained by setting:

$$t = \sqrt{\frac{m}{k}}\tau, \quad u = \frac{x}{\alpha}, \quad f_{ri} = f_0 z.$$

In such a way, the final non-dimensional SDoF hysteretic mechanical system (see Fig. 5.28b) is ruled by the following ODEs:

$$\ddot{x} + 2\zeta\dot{x} + x + z = F\cos\left(\Omega\tau\right), \tag{5.3.3}$$

and

$$\dot{z} = \left\{\kappa_e\left(x\right) + \chi_6 + 1 + s\left[\phi_e\left(x\right) + \chi_6 x - z\right]\right\}\dot{x}, \tag{5.3.4}$$

where, with slight a abuse of notation, an overdot now represents differentiation with respect to the non-dimensional time τ and $s := \mathrm{sgn}\left(\dot{x}\right)$. Furthermore:

$$2\zeta := \frac{c}{\sqrt{mk}}, \quad F := \frac{p_0}{f_0}, \quad \Omega := 2\pi f_p\sqrt{\frac{m}{k}}.$$

sgn($\dot{x}$)	χ_1	χ_2	χ_3	χ_4	χ_5	χ_6
$+$	1.0	0.008	16.0	-0.02	0.0	0.01
$-$	-1.0	-0.008	16.0	-0.02	0.0	0.01

Table 5.9. Non-dimensional VRM+D parameters adopted to simulate the hysteresis loops in Figure 5.29.

Finally, notice that the non-dimensional form of the VRM+D in Eq. (5.3.4) depends upon the following six non-dimensional model parameters:

$$\chi_1 := \frac{\beta_1}{f_0}, \quad \chi_2 := \frac{\beta_2}{\alpha}, \quad \chi_3 := \frac{2\gamma_1}{f_0},$$
$$\chi_4 := \frac{\gamma_2}{\alpha}, \quad \chi_5 := \alpha\gamma_3, \quad \chi_6 := \frac{k_b}{f_0\alpha},$$

some of which appear in the non-dimensional function $\kappa_e\left(x\right)$:

$$\kappa_e\left(x\right) = \chi_1\chi_2 e^{\chi_2 x} + 2\chi_3\chi_4\frac{e^{-\chi_4(x-\chi_5)}}{\left[1+e^{-\chi_4(x-\chi_5)}\right]^2},$$

and $\phi_e\left(x\right)$:

$$\phi_e\left(x\right) = \chi_1\left(e^{\chi_2 x}-1\right) + \chi_3\frac{1-e^{-\chi_4(x-\chi_5)}}{1+e^{-\chi_4(x-\chi_5)}}.$$

Note that Eqs. (5.3.3) and (5.3.4) represent the non-dimensional form of the initial equilibrium equations.

Subsection 5.3.3

Description of the Analyzed System

The main advantage of the mathematical model previously described lies in its ability to analyze the behavior of a hysteretic system with loop shapes similar to those experimentally obtained for the NSD in Fig. 5.27b. Specifically, we study the SDoF hysteretic mechanical system obtained using the non-dimensional VRM+D parameters listed in Table 5.9 with $\zeta = 0$. The continuation parameter is Ω, whereas the non-dimensional amplitude of the input force F remains constant.

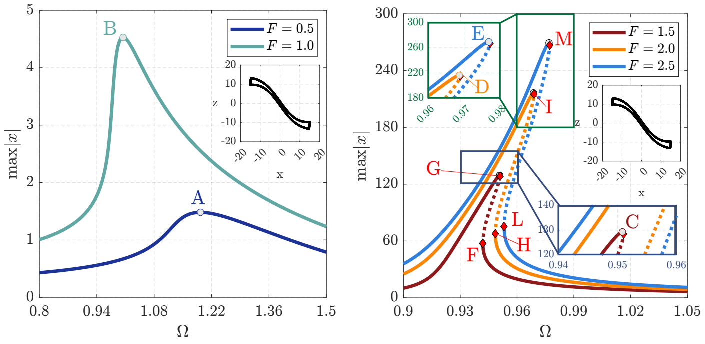

(a) (b)

Figure 5.29. FRCs for SDoF hysteretic mechanical system having hysteresis loop as in Fig. 5.27b when $F = [0.5,\ 1.0]$ (a) and when $F = [1.5,\ 2.0,\ 2.5]$ (b).

Subsection 5.3.4

Frequency-Response Curves: Stability and Bifurcation

Referring to the FRCs shown in Fig. 5.29, obtained using the procedure outlined in Section 4.3.3 imposing the parameters listed in Table 4.4 (the pseudo-code can be found in Table 4.3), we have:

- $F = 0.5$: At this level of amplitude, as shown in Fig. 5.29a, the FRC is globally stable within the investigated range of Ω and exhibits a softening behavior with a resonance peak at $\mathrm{A} \equiv (1.193,\ 1.481)$.
- $F = 1.0$: Also for this level of load amplitude, it can be observed in Fig. 5.29a that the FRC is slightly bent to the left (indicating a softening nonlinearity) and globally stable within the investigated range of Ω with a resonance peak at $\mathrm{B} \equiv (1.003,\ 4.527)$.
- $F = 1.5$: By increasing the load value, we observe in Fig. 5.29b that the FRC is bent to the right (indicating an hardening nonlinearity) with a resonance peak at $\mathrm{C} \equiv (0.951,\ 129.276)$. Furthermore, at points $\mathrm{F} \equiv (0.942,\ 57.461)$ and $\mathrm{G} \equiv (0.950,\ 128.377)$, the system exhibits two *fold bifurcations*.
- $F = 2.0$: In this case, the behavior exhibited by the FRC is of the same type as the previous level of amplitude. Indeed, there is a further increase in the hardening behavior of the curve with a resonance peak at

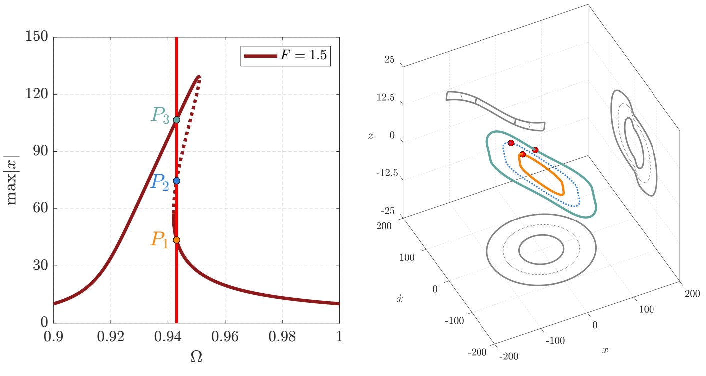

(a)

(b)

Figure 5.30. FRC for $F = 1.5$ (a) and periodic orbits in the state-space at $\Omega = 0.943$ (b).

D ≡ (0.9686, 216.494), whereas the two *fold bifurcations* at points H ≡ (0.947, 67.696) and I ≡ (0.9689, 215.182) move away.

- $F = 2.5$: In this last case, there is a further increase in the hardening behavior of the FRC with a resonance peak at E ≡ (0.977, 269.368). In particular, the two *fold bifurcations* at points L ≡ (0.952, 75.313) and M ≡ (0.977, 266.794) move further away.

5.3.4.1 Orbits in the State-Space

Of particular interest is the exploration of the state-space at specific values of Ω and F. For instance, the FRC shown in Fig. 5.30a, obtained at $F = 1.5$, reveals three intersections at $\Omega = 0.943$. This finding indicates the presence of three periodic solutions: two stable orbits (denoted P_1 and P_3 in Fig. 5.30a) and one unstable periodic solution (denoted P_2 in Fig. 5.30a).

Each of the three intersection points with the FRC corresponds to a periodic orbit in the state-space, as illustrated in Fig. 5.30b. This figure also shows the projections of these periodic orbits onto the $(x, \dot{x})$, (x, z), and $(\dot{x}, z)$ planes. In Fig. 5.30b, the red points on the orbits represent the fixed-points identified using the Poincaré map-bases continuation procedure, whereas the points on the FRC denote the maximum displacement associated with each orbit.

Subsection 5.3.5

Conclusions

The analysis confirms that the mathematical model effectively captures the behavior of hysteretic systems with loop shapes similar to experimental observations for the NSD. The frequency response curves reveal that, at lower forcing amplitude levels, the system exhibits stable and softening behavior. As the forcing amplitude increases, the system shifts to a hardening nonlinearity and shows *fold bifurcations*, highlighting complex changes in stability and dynamic behavior. Overall, these findings enhance our understanding of the system's response and demonstrate the model's ability to accurately represent hysteretic behavior and stability.

Section 5.4

Rate-Independent Hysteretic Rocking Systems

The rocking phenomenon, which refers to the rotation at the base of structural or non-structural elements under dynamic excitations, has been extensively studied in the literature to protect the involved components [26, 28, 60, 100]. In recent decades, however, the idea of exploiting the rocking mechanism between assembled elements has emerged as a potential solution to vibration control, with particular emphasis on the integration of energy dissipation devices.

Caterino et al. (2018) [17] specifically explored the possibility of actively controlling rocking through a semi-active system based on magnetorheological devices, capable of modulating the stiffness at the base of precast RC columns, allowing real-time energy dissipation during an earthquake.

Another crucial application of controlled rocking is the protection of tall wind turbine towers which are subject not only to wind-induced dynamic loads but also to wave-induced loads in offshore environments [18]. The interaction between aerodynamic and hydrodynamic forces can lead to excessive vibrations, posing a risk to the mechanical systems of the turbine and contributing to structural fatigue. To reduce top displacements and base stresses, Di Paolo et al. (2021) [30] proposed the use of a rotational friction damper in parallel with a rotational spring adopted as re-centering device.

Research has also focused on passive nonlinear control systems to optimize structural performance under dynamic loads [1, 2, 12, 27, 84, 85, 87]. Notably, Carpineto et al. (2014) [16] introduced the concept of hysteretic Tuned Mass Damper (TMD) to mitigate earthquake-induced oscillations by avoiding the limitations of traditional linear TMDs, such as detuning during operational conditions; in addition, hysteretic TMDs do not need for external power or complex control systems, as it happens with active and semi-active systems.

In this context, hysteretic rocking systems represent a promising approach for efficiently dissipating energy [1, 2, 11, 27, 82], reducing peak displacements, velocities, and accelerations, and minimizing structural stresses. These systems enhance resilience during seismic events or wind-induced vibrations. By leveraging nonlinear behavior and controlled rocking mechanisms for energy dissipation, they offer substantial potential to improve the performance of both existing and newly designed structures, making them safer and more cost-effective.

To achieve this outcome, it is essential to extend the model proposed by Di Paolo et al. (2021) [30] in order to simulate more complex hysteretic behaviors in the involved base elements. This can be accomplished through the use of the Vaiana-Rosati model of hysteresis (Section 4.3.2) since it enables a unified representation of different types of hysteresis loop shape [83, 84]. Additionally, the dynamic behavior of a hysteretic rocking system can be analyzed under periodic forcing using the continuation method based on Poincaré maps, as described in Section 4.3.3. This numerical method, similarly to analytical approaches proposed in the literature [29, 56, 59], enables the identification of the system's stability and bifurcations.

In this section, we present the mathematical model applicable to a class of rocking systems characterized by rate-independent hysteretic behavior. We begin by formulating the dimensional equations of motion for these systems. Next, we transform these equations into a non-dimensional form, which facilitates analysis by reducing the number of parameters and highlighting the key non-dimensional quantities that dictate the system's behavior. Following this transformation, we present the results of our numerical analyses. Specifically, we provide a concise explanation of the parameters utilized in the continuation method. We then investigate how the shape of the hysteresis loop affects the frequency response of four distinct hysteretic rocking systems. Furthermore, we extend our analysis to examine the effects of combining hysteretic elements with varying loop shapes, thereby offering insights into how these combinations influence the overall behavior and stability of the system.

SUBSECTION 5.4.1

Dimensional Equations of Motion

In this section, the equations of motion for a class of hysteretic rocking systems are introduced, starting with their dimensional form. The dimensional equation of motion for the class of hysteretic rocking systems shown in Fig. 5.31a is derived from Newton's second law in its general form as:

$$I\ddot{\theta} + f_{ri}^{(1)}\left(d_1\theta\right)d_1 + f_{ri}^{(2)}\left(d_2\theta\right)d_2 = \mathrm{m}_0\cos\left(\omega t\right). \tag{5.4.1}$$

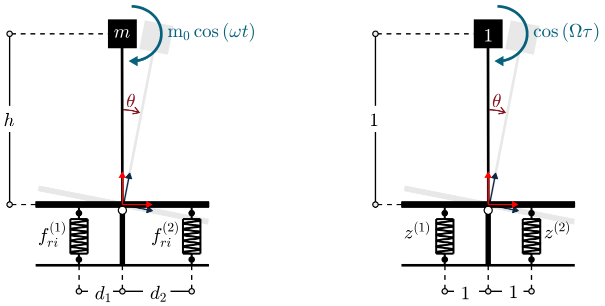

(a) (b)

Figure 5.31. Dimensional (a) and non-dimensional (b) classes of hysteretic rocking systems.

In this context, θ, $\dot{\theta}$, and $\ddot{\theta}$ represent the angular displacement, velocity, and acceleration of the rocking rigid block, respectively [71]. The block has a mass m and a moment of inertia about the axis of rotation given by $I = mh^2$. Furthermore, $f_{ri}^{(1)}$ and $f_{ri}^{(2)}$ represent the generalized rate-independent hysteretic forces acting on the left and right hysteretic elements, respectively, positioned at distances d_1 ($d_1 < 0$) and d_2 ($d_2 > 0$); in addition, m_0 and ω denote the amplitude and the angular frequency of the periodic input forcing.

According to the differential formulation of the VRM+D (Section 4.3.2), the generalized rate-independent hysteretic forces in Eq. (5.4.1) are governed by the following ODEs:

$$\begin{aligned} \dot{f}_{ri}^{(i)} = \Big[& k_e^{(i)}\left(d_i\theta\right) + k_b^{(i)} + \alpha^{(i)} f_0^{(i)} + \\ & + \mathrm{sgn}\left(d_i\dot{\theta}\right) \alpha^{(i)} \left(f_e^{(i)}\left(d_i\theta\right) + k_b^{(i)} d_i\theta - f_{ri}^{(i)}\right)\Big] d_i\dot{\theta}, \quad \text{for} \quad i = 1, 2, \end{aligned} \tag{5.4.2}$$

in which the model parameters are properly updated based on the sign of the velocity. In the previous equation, the generalized function $k_e^{(i)}$ is defined as:

$$k_e^{(i)}\left(d_i\theta\right) = \beta_1^{(i)} \beta_2^{(i)} e^{\beta_2^{(i)} d_i\theta} + 4\gamma_1^{(i)} \gamma_2^{(i)} \frac{e^{-\gamma_2^{(i)}\left(d_i\theta - \gamma_3^{(i)}\right)}}{\left[1 + e^{-\gamma_2^{(i)}\left(d_i\theta - \gamma_3^{(i)}\right)}\right]^2},$$

whereas $f_e^{(i)}$ is given by:

$$f_e^{(i)}\left(d_i\theta\right) = \beta_1^{(i)}\left(e^{\beta_2^{(i)} d_i\theta} - 1\right) + 2\gamma_1^{(i)}\frac{1 - e^{-\gamma_2^{(i)}\left(d_i\theta - \gamma_3^{(i)}\right)}}{1 + e^{-\gamma_2^{(i)}\left(d_i\theta - \gamma_3^{(i)}\right)}}.$$

SUBSECTION 5.4.2

Non-dimensionalization Procedure

To simplify the analysis and reduce the number of involved parameters, a non-dimensionalization process is carried out. This approach rescales variables and identifies essential non-dimensional parameters, leading to a set of simplified equations that more clearly reveal the behavior of the analyzed system. In addition, it offers a more general framework for examining the dynamics of the system, emphasizing the influence of the hysteretic elements and forcing frequency, and enabling the exploration of various dynamic phenomena (Section 2.5).

The analysis of the behavior of a hysteretic rocking system involves examining the above differential equations, which includes a considerable number of parameters. Specifically, 3 parameters are associated with the system's geometric and inertial properties (I, d_1, d_2), whereas 32 parameters are related to the hysteretic elements; indeed, two sets of 8 parameters, corresponding to the loading and unloading phases, are associated with each of the two rate-independent hysteretic elements. Additionally, there are 2 parameters related to the external force (m_0, ω), resulting in a total of 37 parameters.

To simplify the analysis and reduce the number of parameters, a non-dimensionalization procedure is applied to the equation of motion. This approach facilitates the understanding of the relationships between the parameters and frees the system from specific units of measurement, allowing for a more abstract and general analysis.

The non-dimensionalization procedure consists of five steps. First, all independent and dependent dimensional variables are identified and then these variables are replaced with non-dimensional quantities. The next step involves dividing the resulting equation, after the substitution of non-dimensional quantities, by the coefficient of the highest-order derivative term. Subsequently, characteristic units are selected to simplify the auxiliary conditions as much as possible. Finally, the equation is rewritten using only non-dimensional quantities [14].

By applying the above-described procedure to Eqs. (5.4.1) and (5.4.2), a more concise and manageable form of the equations is obtained. Specifically:

i) The independent variable is the time t whereas the generalized rate-independent hysteretic forces $f_{ri}^{(1)}$ and $f_{ri}^{(2)}$ represent the dependent ones. Note that θ is already a non-dimensional quantity and therefore is not included in the non-dimensionalization process.

ii) We introduce as non-dimensional variables:

$$\tau := \frac{t}{t_s}, \quad z^{(1)} := \frac{f_{ri}^{(1)}}{f_s^{(1)}}, \quad z^{(2)} := \frac{f_{ri}^{(2)}}{f_s^{(2)}}.$$

These quantities are defined as the dimensional variables scaled by specific dimensional scaling factors (i.e., t_s, $f_s^{(1)}$, and $f_s^{(2)}$) whose expressions may be chosen in order to simplify the final non-dimensional equations as much as possible. Based on these definitions, the dimensional variables can be expressed as follows:

$$t = t_s\tau, \quad f_{ri}^{(1)} = f_s^{(1)} z^{(1)}, \quad f_{ri}^{(2)} = f_s^{(2)} z^{(2)}. \tag{5.4.3}$$

By using Eq. (5.4.3), it is possible to replace the dimensional variables in Eqs. (5.4.1) and (5.4.2) with the non-dimensional ones. In particular, we obtain for Eq. (5.4.1):

$$\frac{I}{t_s^2}\frac{d^2\theta}{d\tau^2} + f_s^{(1)} d_1 z^{(1)} + f_s^{(2)} d_2 z^{(2)} = \mathrm{m}_0 \cos\left(\omega t_s \tau\right), \tag{5.4.4}$$

and for Eq. (5.4.2):

$$\frac{f_s^{(i)}}{t_s}\frac{dz^{(i)}}{d\tau} = \Big\{k_e^{(i)}\left(d_i\theta\right) + k_b^{(i)} + \alpha^{(i)} f_0^{(i)} + \\ + \mathrm{sgn}\left(\frac{d_i}{t_s}\frac{d\theta}{d\tau}\right)\alpha^{(i)}\left[f_e^{(i)}\left(d_i\theta\right) + k_b^{(i)} d_i\theta - f_s^{(i)} z^{(i)}\right]\Big\}\frac{d_i}{t_s}\frac{d\theta}{d\tau}. \tag{5.4.5}$$

iii) The highest-order terms in Eqs. (5.4.4) and (5.4.5) are $\frac{I}{t_s^2}$

and $\frac{f_s^{(i)}}{t_s}$, respectively. Dividing Eq. (5.4.4) by $\frac{I}{t_s^2}$ gives:

$$\frac{d^2\theta}{d\tau^2}+\frac{f_s^{(1)}t_s^2}{I}d_1z^{(1)}+\frac{f_s^{(2)}t_s^2}{I}d_2z^{(2)}=\frac{\mathrm{m}_0t_s^2}{I}\cos\left(\omega t_s\tau\right), \tag{5.4.6}$$

whereas, dividing Eq. (5.4.5) by $\frac{f_s^{(i)}}{t_s}$ yields:

$$\frac{dz^{(i)}}{d\tau}=\frac{d_i}{f_s^{(i)}}\Big\{k_e^{(i)}\left(d_i\theta\right)+k_b^{(i)}+\alpha^{(i)}f_{0^{(i)}}+$$
$$+\operatorname{sgn}\left(\frac{d_i}{t_s}\frac{d\theta}{d\tau}\right)\alpha^{(i)}\left[f_e^{(i)}\left(d_i\theta\right)+k_b^{(i)}d_i\theta-f_s^{(i)}z^{(i)}\right]\Big\}\frac{d\theta}{d\tau}. \tag{5.4.7}$$

iv) To determine the scaling factors t_s, $f_s^{(1)}$, and $f_s^{(2)}$ that simplify Eqs. (5.4.6) and (5.4.7) as much as possible, we need to introduce three equations. A possible approach is to set the coefficients in Eq. (5.4.6) equal to one. This results in:

$$\frac{\mathrm{m}_0t_s^2}{I}=1\rightarrow t_s:=\sqrt{\frac{I}{\mathrm{m}_0}},$$
$$\frac{f_s^{(i)}t_s^2}{I}d_i=1\rightarrow f_s^{(i)}:=\frac{\mathrm{m}_0}{d_i}\quad\text{for}\quad i=1,2.$$

As a result, the non-dimensional angular frequency in Eq. (5.4.6) is defined as follows:

$$\Omega:=\omega\sqrt{\frac{I}{\mathrm{m}_0}}.$$

On the other hand, the non-dimensional form of the VRM in Eq. (5.4.7) (which will be referred to as NDVRM in the following) can be further simplified by defining two new non-dimensional functions:

$$\kappa_e^{(i)}\left(\theta\right):=k_e^{(i)}\left(d_i\theta\right)\frac{d_i}{f_s^{(i)}}\quad\text{and}\quad\phi_e^{(i)}\left(\theta\right):=\frac{f_e^{(i)}\left(d_i\theta\right)}{f_s^{(i)}},$$

along with the non-dimensional model parameters:

$$\chi_1^{(i)} := \frac{\beta_1^{(i)}}{f_s^{(i)}}, \quad \chi_2^{(i)} := \beta_2^{(i)} d_i, \quad \chi_3^{(i)} := \frac{2\gamma_1^{(i)}}{f_s^{(i)}}, \quad \chi_4^{(i)} := \gamma_2^{(i)} d_i,$$
$$\chi_5^{(i)} := \frac{\gamma_3^{(i)}}{d_i}, \quad \chi_6^{(i)} := \frac{k_b^{(i)} d_i}{f_s^{(i)}}, \quad \chi_7^{(i)} := \alpha^{(i)} d_i, \quad \chi_8^{(i)} := \frac{f_0^{(i)}}{f_s^{(i)}}.$$

We may note that some of such quantities appear in the non-dimensional function $\kappa_e^{(i)}(\theta)$:

$$\kappa_e^{(i)}(\theta) = \chi_1^{(i)} \chi_2^{(i)} e^{\chi_2^{(i)}\theta} + 2\chi_3^{(i)} \chi_4^{(i)} \frac{e^{-\chi_4^{(i)}\left(\theta - \chi_5^{(i)}\right)}}{\left[1 + e^{-\chi_4^{(i)}\left(\theta - \chi_5^{(i)}\right)}\right]^2},$$

and in the non-dimensional function $\phi_e^{(i)}(x)$:

$$\phi_e^{(i)}(\theta) = \chi_1^{(i)} \left(e^{\chi_2^{(i)}\theta} - 1\right) + \chi_3^{(i)} \frac{1 - e^{-\chi_4^{(i)}\left(\theta - \chi_5^{(i)}\right)}}{1 + e^{-\chi_4^{(i)}\left(\theta - \chi_5^{(i)}\right)}}.$$

v) The final non-dimensional form of the equation of motion, associated with the class of hysteretic rocking systems illustrated in Fig. 5.31b, is described by a set of ODEs that depend only on the parameters of the hysteretic elements and the forcing frequency Ω. These equations are:

$$\frac{d^2\theta}{d\tau^2} + z^{(1)} + z^{(2)} = \cos(\Omega\tau), \tag{5.4.8}$$

and

$$\frac{dz^{(i)}}{d\tau} = \left\{\kappa_e^{(i)}(\theta) + \chi_6^{(i)} + \chi_7^{(i)} \chi_8^{(i)} + \right.$$
$$\left. + s^{(i)} \chi_7^{(i)} \left[\phi_e^{(i)}(\theta) + \chi_6^{(i)} \theta - z^{(i)}\right]\right\} \frac{d\theta}{d\tau} \quad \text{for} \quad i = 1, 2, \tag{5.4.9}$$

with $s^{(i)} := \operatorname{sgn}\left(d_i \sqrt{\frac{\mathrm{m}_0}{I}} \frac{d\theta}{d\tau}\right)$.

Such a non-dimensional form provides a powerful framework for analyzing the system's behavior under different conditions. As a matter of fact, by varying the parameters associated with the hysteretic elements, a wide range of dynamic phenomena can be explored.

SUBSECTION 5.4.3

Analyzed Hysteretic Rocking Systems

The non-dimensional model introduced in the previous section offers a robust tool for conducting parametric studies, enabling a detailed exploration of the system's dynamic behavior under different conditions. Specifically, the impact of varying the value of the hysteresis model parameters on the system's frequency-response behavior is crucial, and systematically altering the hysteresis loop shape characterizing the rate-independent hysteretic elements allows for a comprehensive analysis of the system's response.

The NDVRM facilitates a detailed exploration of hysteresis loop shapes which are categorized into four distinct types, each exhibiting specific characteristics according to the analytical properties of the upper and lower limiting curves (Table 5.10).

It is worth noting that by selecting Ω as the control parameter, the hysteresis parameters are considered constant during the computation of periodic solutions. To further reduce the number of involved parameters, systems with symmetric hysteresis loop shapes are analyzed. This implies the following relationships for the NDVRM parameters:

$$\begin{aligned} &\chi_1^+ = -\chi_1^-, \quad \chi_2^+ = -\chi_2^-, \quad \chi_3^+ = +\chi_3^-, \quad \chi_4^+ = +\chi_4^-, \\ &\chi_5^+ = -\chi_5^-, \quad \chi_6^+ = +\chi_6^-, \quad \chi_7^+ = +\chi_7^-, \quad \chi_8^+ = +\chi_8^-. \end{aligned}$$

The proposed approach enables the analysis of geometric asymmetries (i.e., $|d_1| \neq |d_2|$) and cases where $f_{ri}^{(1)}$ and $f_{ri}^{(2)}$ are characterized by different sets of parameters.

5.4.3.1 Shape Type S1

Shape type $S1$ is characterized by hysteresis loops bounded by two straight lines. This occurs when all parameters related to curvature and inflection points of the limiting curves are zero. This simple shape is commonly found in smooth steel reinforcing bars, steel dampers, and steel beam-column connections.

5.4.3.2 Shape Type S2

Shape type $S2$ is characterized by limiting curves with no inflection points, resulting in a more complex hysteresis loop shape compared to $S1$. This category is divided into three

Shape Type	Subtype	Parameters Conditions			
$S1$	–	$\chi_1^+ = 0$ $\chi_1^- = 0$	$\chi_2^+ = 0$ $\chi_2^- = 0$	$\chi_3^+ = 0$ $\chi_3^- = 0$	$\chi_4^+ = 0$ $\chi_4^- = 0$
$S2$	$S2.1$	$\chi_1^+ > 0$ $\chi_1^- > 0$	$\chi_2^+ > 0$ $\chi_2^- > 0$	$\chi_3^+ = 0$ $\chi_3^- = 0$	$\chi_4^+ = 0$ $\chi_4^- = 0$
	$S2.2$	$\chi_1^+ > 0$ $\chi_1^- < 0$	$\chi_2^+ > 0$ $\chi_2^- < 0$	$\chi_3^+ = 0$ $\chi_3^- = 0$	$\chi_4^+ = 0$ $\chi_4^- = 0$
	$S2.3$	$\chi_1^+ > 0$ $\chi_1^- < 0$	$\chi_2^+ > 0$ $\chi_2^- < 0$	$\chi_3^+ > 0$ $\chi_3^- > 0$	$\chi_4^+ < 0$ $\chi_4^- < 0$
$S3$	$S3.1$	$\chi_1^+ = 0$ $\chi_1^- = 0$	$\chi_2^+ = 0$ $\chi_2^- = 0$	$\chi_3^+ > 0$ $\chi_3^- > 0$	$\chi_4^+ > 0$ $\chi_4^- > 0$
	$S3.2$	$\chi_1^+ = 0$ $\chi_1^- = 0$	$\chi_2^+ = 0$ $\chi_2^- = 0$	$\chi_3^+ > 0$ $\chi_3^- > 0$	$\chi_4^+ > 0$ $\chi_4^- < 0$
	$S3.3$	$\chi_1^+ > 0$ $\chi_1^- < 0$	$\chi_2^+ > 0$ $\chi_2^- < 0$	$\chi_3^+ > 0$ $\chi_3^- > 0$	$\chi_4^+ < 0$ $\chi_4^- < 0$
$S4$	–	$\chi_1^+ > 0$ $\chi_1^- < 0$	$\chi_2^+ > 0$ $\chi_2^- < 0$	$\chi_3^+ > 0$ $\chi_3^- > 0$	$\chi_4^+ > 0$ $\chi_4^- > 0$

Table 5.10. NDVRM parameters conditions to simulate different types of hysteresis loop shape.

subcategories depending on the values of the parameters $\chi_1^\pm$, $\chi_2^\pm$, $\chi_3^\pm$, and $\chi_4^\pm$. Specifically:

- $S2.1$: The hysteresis loop takes this shape when the parameters for the upper (lower) limiting curve are $\chi_1^+ > 0$ ($\chi_1^- > 0$), $\chi_2^+ > 0$ ($\chi_2^- > 0$), and $\chi_3^+ = 0$ ($\chi_3^- = 0$), $\chi_4^+ = 0$ ($\chi_4^- = 0$). It is commonly observed in magnesium alloy bars, spring connectors, and wire rope isolators.

- $S2.2$: The hysteresis loop assumes this shape when the parameters for the upper (lower) limiting curve are $\chi_1^+ > 0$ ($\chi_1^- < 0$), $\chi_2^+ > 0$ ($\chi_2^- < 0$), $\chi_3^+ = 0$ ($\chi_3^- = 0$), and $\chi_4^+ = 0$ ($\chi_4^- = 0$). This type of loop is typical of expansion anchors and steel-concrete composite beam-column connections.

- $S2.3$: The hysteresis loop takes this shape when the parameters for the upper (lower) limiting curve are $\chi_1^+ > 0$ ($\chi_1^- < 0$), $\chi_2^+ > 0$ ($\chi_2^- < 0$), $\chi_3^+ > 0$ ($\chi_3^- > 0$), and $\chi_4^+ < 0$

$(\chi_4^- < 0)$. It generally characterizes the behavior of steel dampers.

5.4.3.3 Shape Type S3

Shape type $S3$ is defined by limiting curves with a single inflection point, adding a layer of complexity compared to the previous shape types. This category of hysteresis loops, as the previous one, is divided into three subcategories based on the values of the parameters $\chi_1^\pm$, $\chi_2^\pm$, $\chi_3^\pm$, and $\chi_4^\pm$. Specifically:

- $S3.1$: The hysteresis loop assumes this shape when the parameters for the upper (lower) limiting curve are $\chi_1^+ = 0$ $(\chi_1^- = 0)$, $\chi_2^+ = 0$ $(\chi_2^- = 0)$, $\chi_3^+ > 0$ $(\chi_3^- > 0)$, and $\chi_4^+ > 0$ $(\chi_4^- > 0)$. It is typically found in brick masonry walls, reinforced high-strength concrete columns, wood element connections, and SMA helical springs.

- $S3.2$: The hysteresis loop takes this shape when the parameters for the upper (lower) limiting curve are $\chi_1^+ = 0$ $(\chi_1^- = 0)$, $\chi_2^+ = 0$ $(\chi_2^- = 0)$, $\chi_3^+ > 0$ $(\chi_3^- > 0)$, and $\chi_4^+ > 0$ $(\chi_4^- < 0)$. This loop shape is typical of buckling steel braces, steel bar members, and steel reinforcing bars.

- $S3.3$: The hysteresis loop assumes this shape when the parameters for the upper (lower) limiting curve are $\chi_1^+ > 0$ $(\chi_1^- < 0)$, $\chi_2^+ > 0$ $(\chi_2^- < 0)$, $\chi_3^+ > 0$ $(\chi_3^- > 0)$, and $\chi_4^+ < 0$ $(\chi_4^- < 0)$. It is typically observed in negative stiffness devices.

5.4.3.4 Shape Type S4

Shape type $S4$ is characterized by limiting curves with two inflection points, making it the most complex among the four shape types. It occurs when the parameters for the upper limiting curve are $\chi_1^+ > 0$, $\chi_2^+ > 0$, $\chi_3^+ > 0$, $\chi_4^+ > 0$, whereas those for the lower limiting curve are $\chi_1^- < 0$, $\chi_2^- < 0$, $\chi_3^- > 0$, $\chi_4^- > 0$. This complex shape is commonly observed in steel framing walls, unbounded fiber-reinforced elastomeric bearings, reinforced concrete walls, pre-strained SMA wires, and steel-timber hybrid shear walls.

5.4.3.5 Continuation Procedure Parameters

The parameters employed for deriving the FRCs are essential to ensuring the accuracy and convergence of the adopted continuation procedure [14]. Specifically, the parameter $T/\Delta\tau$, governing

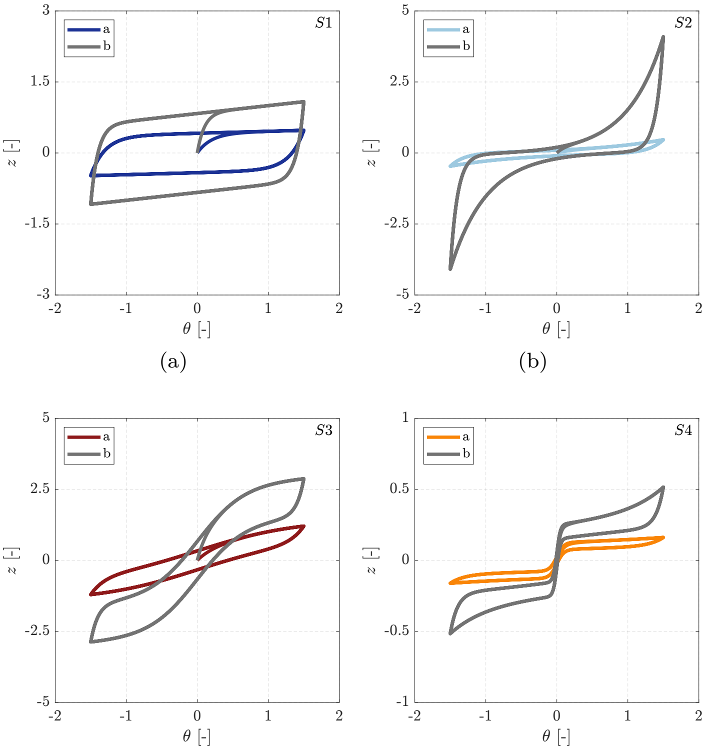

(a) (b)

(c) (d)

Figure 5.32. Non-dimensional hysteresis loops simulated by using the NDVRM parameters in Table 5.11.

the number of numerical steps in the evaluation of the Poincaré map, is set to 2048. Both δ_1 and δ_2, which represent the finite-difference increments for the numerical computation of the Jacobian matrix, are set equal to 10^{-3}, thus achieving a balance between precision and computational efficiency. To guarantee a high level of accuracy in the Newton-Raphson iterative solution process, the tolerance *tol* of the stopping criterion is set to 10^{-6}. An essential aspect of the continuation procedure is the control of the step length Δs since the convergence characteristics may significantly vary along different sections of the solution curve. To address such an aspect and optimize the algorithm performance, an adaptive step length control strategy is implemented. Specifically, the minimum (maximum) step size $\Delta s_{\min}$ ($\Delta s_{\max}$) is set to 10^{-10} (10^{-3}), ensuring the stability of the continuation procedure (see Section 4.3.3).

	Set	χ_1	χ_2	χ_3	χ_4	χ_5	χ_6	χ_7	χ_8
$S1$	a	0.0	0.0	0.0	0.0	0.0	0.0417	-5.0	-0.4167
	b	0.0	0.0	0.0	0.0	0.0	0.1667	10.0	0.8333
$S2$	a	-0.1	-1.0	0.0	0.0	0.0	0.0125	-5.0	-0.1
	b	0.2	2.0	0.0	0.0	0.0	0.0500	10.0	0.2
$S3$	a	0.0	0.0	-1.0	-1.5	0.0	0.0417	-5.0	-0.3333
	b	0.0	0.0	2.0	3.0	0.0	0.1667	10.0	0.6667
$S4$	a	-0.005	-1.0	-0.1	-20.0	0.0	0.0125	-5.0	-0.025
	b	0.010	2.0	0.2	40.0	0.0	0.0500	10.0	0.050

Table 5.11. NDVRM parameters adopted to simulate the hysteresis loops in Figure 5.32.

Subsection 5.4.4

Influence of the Shape Type

To analyze the effect of different hysteresis loop shapes on the dynamic behavior of hysteretic rocking systems, we present three different FRCs for each hysteresis loop shape detailed in the previous section. In particular, in each of them, we analyze two different configurations:

1. Symmetric Configuration (gray line): it is obtained by using the parameters from "set b" listed in Table 5.11 for both $z^{(1)}$ and $z^{(2)}$. Note that, in this symmetric setup, parameters from "set b" that are directly dependent on the sign of d_1 change sign when applied to simulate $z^{(1)}$.

2. Asymmetric Configuration (colored line): it is obtained by adopting parameters from "set a" for $z^{(1)}$ and from "set b" for $z^{(2)}$, as detailed in Table 5.11.

The symmetric configuration is reported as a reference to show the impact of having different loops for the two rate-independent elements.

The FRCs illustrate how key aspects of the periodic orbits, such as maximum angular displacement, velocity, and acceleration, vary with the angular frequency Ω. These curves are generated by first determining the fixed-point of the Poincaré map, which is then used as the initial condition for further integration to extract these important quantities. Moreover, to better

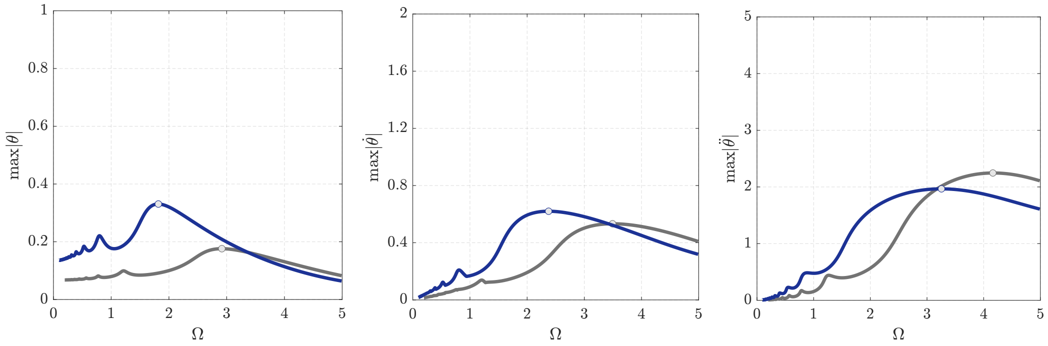

(a) (b) (c)

Figure 5.33. FRCs for Systems $S1$ where the gray (colored) line indicates the symmetric (asymmetric) configuration: maximum angular displacement (a), maximum angular velocity (b), and maximum angular acceleration (c).

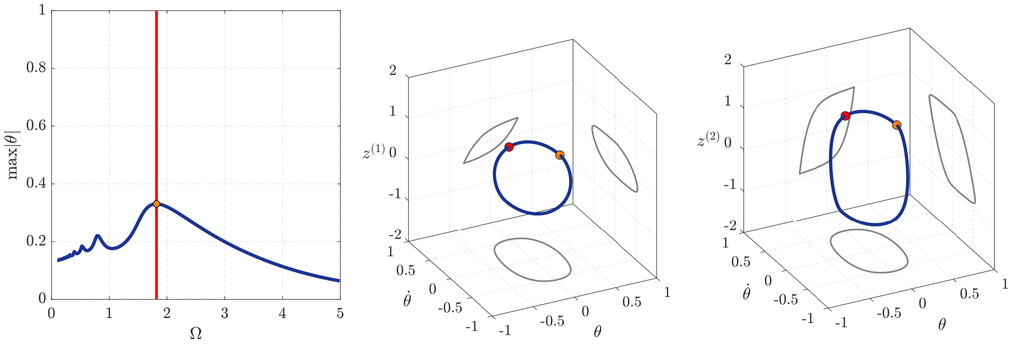

(a) (b) (c)

Figure 5.34. System $S1$: maximum angular displacement FRC (a), and periodic orbit in the state-space at $\Omega = 1.81688$ (b) and (c).

understand the system's state-space dynamics, key points along the FRCs are plotted in state-space. Being the state-space of this non-autonomous system four-dimensional, the trajectory is projected onto $(\theta, \dot{\theta}, z^{(1)})$ and $(\theta, \dot{\theta}, z^{(2)})$ to visualize the periodic orbits. This approach allows us to assess the structure and stability of the periodic orbits for specific values of Ω.

5.4.4.1 Shape Type S1

In the following, we present the results of the analysis performed on a non-dimensional hysteretic rocking system in which the rate-independent hysteretic elements are characterized by the hysteresis loops illustrated in Fig. 5.32a and are modeled by using the NDVRM parameters listed in Table 5.11.

Frequency Response Curves: Figure 5.33 shows that the FRCs for the system $S1$ bend to the left, indicating a softening nonlinearity, and are globally stable within the examined range of Ω. Notably, with a specific focus on the asymmetric configuration, the resonance peak for the three different FRCs occurs at:

- $(1.81688, 0.330704)$ for the maximum angular displacement (Fig. 5.33a);
- $(2.37554, 0.620298)$ for maximum angular velocity (Fig. 5.33b);
- $(3.25509, 1.966050)$ for maximum angular acceleration (Fig. 5.33c).

Furthermore, the system exhibits a series of resonance peaks across different frequency ranges provided by the odd superharmonics of the excitation frequency:

- for the maximum angular displacement in the range $\Omega \in [0.101374 - 0.79504]$ (Fig. 5.33a);
- for the maximum angular velocity in the range $\Omega \in [0.101374 - 0.807052]$ (Fig. 5.33b);
- for the maximum angular acceleration in the range $\Omega \in [0.101374 - 0.840424]$ (Fig. 5.33c).

Orbits in the State-Space: At the resonance frequency $\Omega = 1.81688$, corresponding to the maximum angular displacement for the asymmetric configuration, the system exhibits a unique stable periodic orbit. This is depicted in Fig. 5.34, where the projections onto $(\theta, \dot{\theta}, z^{(1)})$ (Fig. 5.34b) and $(\theta, \dot{\theta}, z^{(2)})$ (Fig. 5.34c) highlight the distinct hysteresis loop shapes inherent to shape type $S1$. The figures also show the fixed-point (red dots in Figs. 5.34a and 5.34b) and corresponding point on the FRC (orange dot), illustrating the stable periodic solution.

5.4.4.2 Shape Type S2

Below, we present the results of the analysis on a non-dimensional hysteretic rocking system, with the NDVRM parameters for the rate-independent hysteretic elements simulating the shape type shown in Fig. 5.32b, listed in Table 5.11.

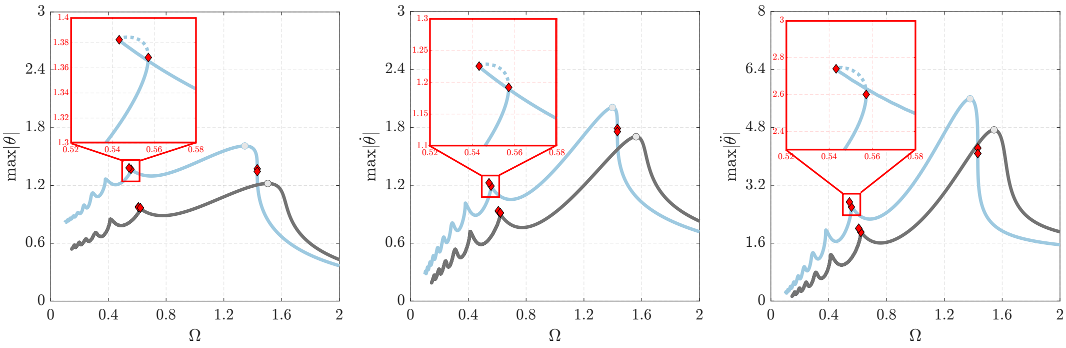

(a) (b) (c)

Figure 5.35. FRC for System $S2$ where the gray (colored) line indicates the symmetric (asymmetric) configuration: maximum angular displacement (a), maximum angular velocity (b), and maximum angular acceleration (c).

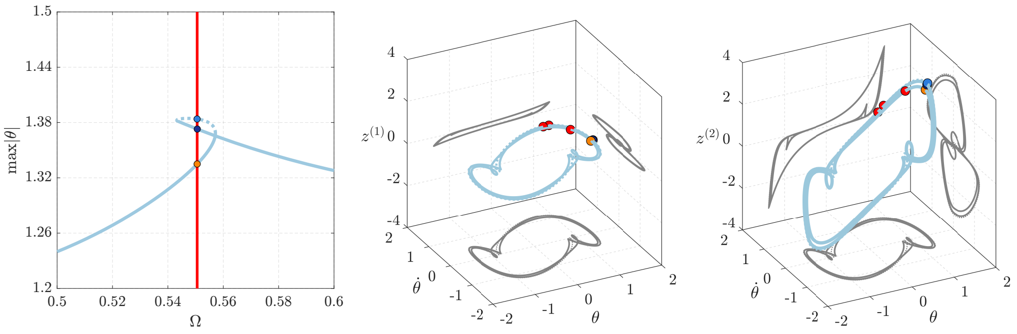

(a) (b) (c)

Figure 5.36. System $S2$: maximum angular displacement FRC (a), and periodic orbit in the state-space at $\Omega = 0.550548$ (b) and (c).

Frequency Response Curves: As shown in Fig. 5.35, the FRCs exhibit a rightward bend, indicative of hardening nonlinearity. The resonance peaks for the three FRCs in the asymmetric configuration occur at the following points:

- $(1.34534, 1.61015)$ for the maximum angular displacement (Fig. 5.35a);
- $(1.39720, 2.00636)$ for the maximum angular velocity (Fig. 5.35b);

- $(1.37807, 5.59221)$ for the maximum angular acceleration (Fig. 5.35c).

Additionally, across different ranges of Ω, the system exhibits a series of resonance peaks for each FRC due to the odd superharmonics of the excitation frequency:

- for maximum angular displacement, within the range $\Omega \in [0.100323 - 0.379318]$ (Fig. 5.35a);
- for maximum angular velocity, within the range $\Omega \in [0.100323 - 0.381185]$ (Fig. 5.35b);
- for maximum angular acceleration, within the range $\Omega \in [0.100323 - 0.208048]$ (Fig. 5.35c).

Furthermore, the FRCs are not globally stable throughout the examined range of Ω, as demonstrated in Fig. 5.35. Specifically, the asymmetric system undergoes a series of *fold bifurcations* at angular frequencies of 0.543208, 0.557175, 1.43128, and 1.43129. On the other hand, in the symmetric case, only two *fold bifurcations* occur at the values 0.607582 and 0.621976.

Orbits in the State-Space: At the angular frequency $\Omega = 0.550548$, associated with loss of stability due to *fold bifurcations*, three intersections with the FRC are observed in the asymmetric case, as depicted in Fig. 5.36a. These correspond to two stable periodic orbits with maximum angular displacements of 1.33500 and 1.37292, and an unstable orbit with a maximum angular displacement of 1.38382. The projections in the state-space, shown in Figs. 5.36b and 5.36c, further illustrate the two different structures of the periodic orbit for the shape type $S2$.

5.4.4.3 Shape Type S3

In the following, we present the results of the analysis conducted on a non-dimensional hysteretic rocking system, with the ND-VRM parameters for the rate-independent hysteretic elements simulating shape type $S3$ listed in Table 5.11, and the corresponding loop shapes illustrated in Fig. 5.32c.

Frequency Response Curves: As illustrated in Fig. 5.37, the FRCs exhibit a slight leftward bend, indicating a softening nonlinearity. Resonance peaks for the three FRCs in the asymmetric configuration occur at:

- $(2.1349, 0.60016)$ for the maximum angular displacement (Fig. 5.37a);

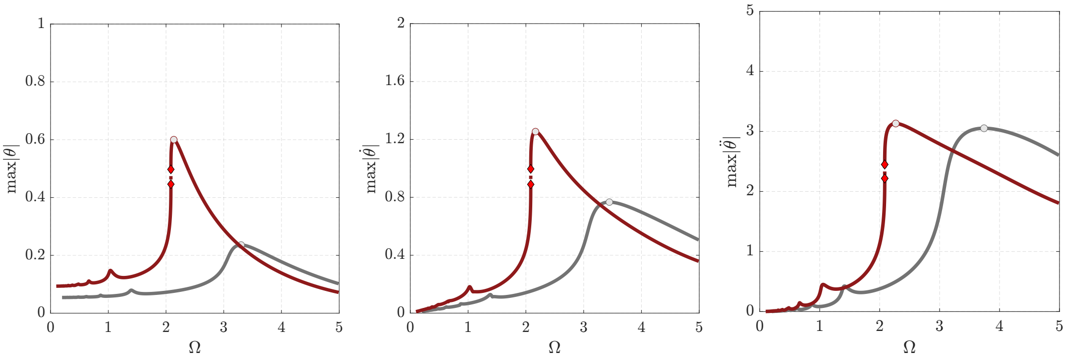

(a) (b) (c)

Figure 5.37. FRC for Systems $S3$ where the gray (colored) line indicates the symmetric (asymmetric) configuration: maximum angular displacement (a), maximum angular velocity (b), and maximum angular acceleration (c).

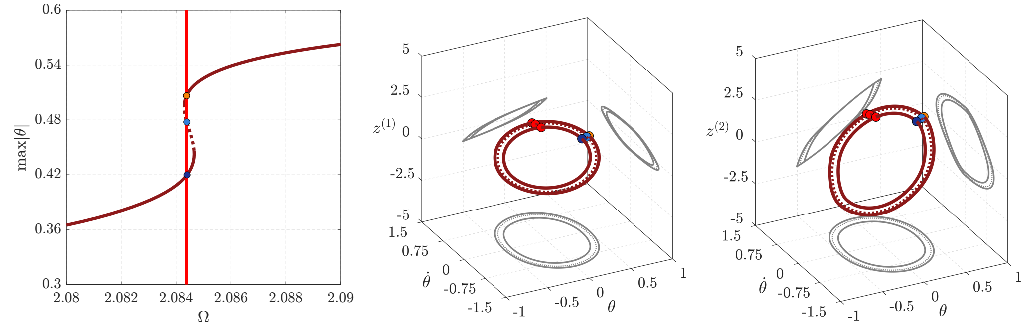

(a) (b) (c)

Figure 5.38. System $S3$: maximum angular displacement FRC (a), and periodic orbit in the state-space at $\Omega = 2.08439$ (b) and (c).

- $(2.16624, 1.25418)$ for the maximum angular velocity (Fig. 5.37b);
- $(2.2684, 3.13212)$ for the maximum angular acceleration (Fig. 5.37c).

Moreover, within different ranges of Ω, the system exhibits multiple resonance peaks across the three FRCs also in this case provided by the odd superharmonics of the driving frequency:

- for maximum angular displacement within the range $\Omega \in [0.109748 - 1.04093]$ (Fig. 5.37a);

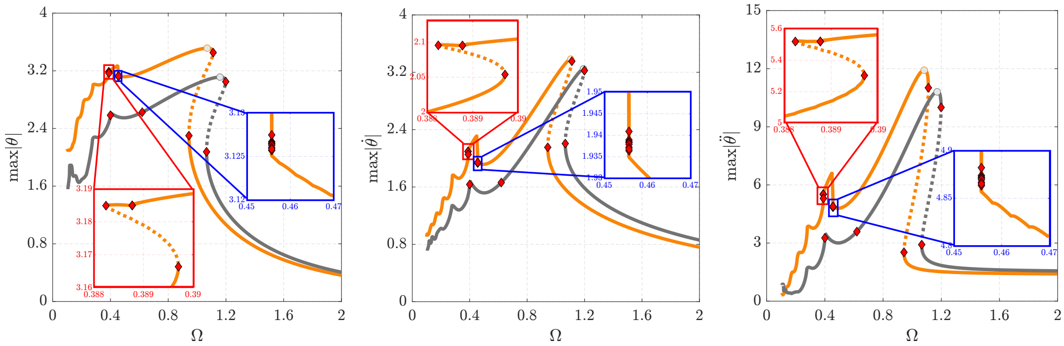

(a) (b) (c)

Figure 5.39. FRC for Systems $S4$ where the gray (colored) line indicates the symmetric (asymmetric) configuration: maximum angular displacement (a), maximum angular velocity (b), and maximum angular acceleration (c).

- for maximum angular velocity within the range $\Omega \in [0.109748 - 1.02533]$ (Fig. 5.37b);
- for maximum angular acceleration within the range $\Omega \in [0.109748 - 1.05406]$ (Fig. 5.37c).

Finally, differently from the symmetric case, the asymmetric one shows that the FRCs are not globally stable across the entire range of Ω under investigation, as illustrated in Fig. 5.37. In particular, the asymmetric system undergoes two *fold bifurcations* at angular frequencies of 2.0843 and 2.08466.

Orbits in the State-Space: At the angular frequency $\Omega = 2.08439$, the asymmetric system experiences a loss of stability, resulting in three intersections with the FRC, as shown in Fig. 5.38a. The corresponding stable periodic orbits are characterized by maximum angular displacements of 0.419855 and 0.506595, whereas the unstable orbit has a displacement of 0.477754. The state-space projections in Figs. 5.38b and 5.38c display the distinct hysteresis loop shapes of the two hysteretic elements.

5.4.4.4 Shape Type S4

In this section, we present the results of the analysis on the non-dimensional hysteretic rocking system, with the NDVRM parameters for the rate-independent hysteretic elements simulating shape type $S4$ listed in Table 5.11 and the corresponding loop shapes shown in Fig. 5.32d.

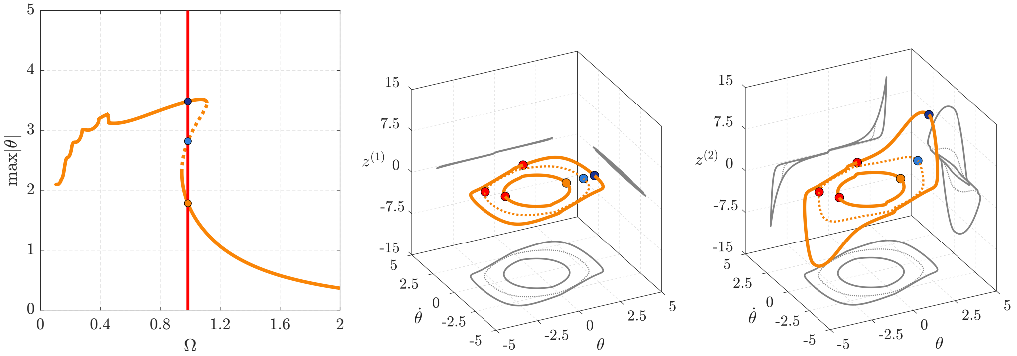

(a) (b) (c)

Figure 5.40. System $S4$: maximum angular displacement FRC (a), and periodic orbit in the state-space at $\Omega = 0.984231$ (b) and (c).

Frequency Response Curves: As depicted in Fig. 5.39, the FRCs display a rightward bend, indicating a hardening nonlinearity. The resonance peaks for the three FRCs, associated with the asymmetric configuration, are located at:

- $(1.06986, 3.51442)$ for the maximum angular displacement (Fig. 5.39a);
- $(1.10357, 3.38342)$ for the maximum angular velocity (Fig. 5.39b);
- $(1.08299, 11.9223)$ for the maximum angular acceleration (Fig. 5.39c).

Across different ranges of Ω, the system exhibits multiple resonance peaks within the three FRCs influenced by the odd superharmonics of the driving frequency:

- for maximum angular displacement within the range $\Omega \in [0.099987 - 0.282193]$ (Fig. 5.39a);
- for maximum angular velocity within the range $\Omega \in [0.099987 - 0.282795]$ (Fig. 5.39b);
- for maximum angular acceleration within the range $\Omega \in [0.099987 - 0.284134]$ (Fig. 5.39c).

The FRCs are not globally stable across the entire investigated range of Ω, as illustrated in Fig. 5.39. Notably, even the FRC for the symmetric configuration displays three regions of instability, which contrasts with the previously analyzed cases ($S1$

and $S3$). In addition, the asymmetric system undergoes multiple stability losses over different frequency ranges. Two significant regions of instability are observed between the angular frequencies 0.388241–0.389705 and 0.943656–1.11138. Further, smaller stability losses occur in the narrower frequency ranges of $\Omega \in [0.38877 - 0.388772]$ and $\Omega \in [0.455738 - 0.455742]$.

Orbits in the State-Space: At the frequency $\Omega = 0.984107$, the asymmetric system shows three intersections with the FRC, as depicted in Fig. 5.40a. The selected angular frequency lies within a region where the system experiences a loss of stability. Specifically, the two stable periodic orbits correspond to maximum angular displacements of 1.78102 and 3.48121, whereas the unstable orbit shows a maximum angular displacement of 2.81901. The distinct hysteresis loop shapes associated with shape type $S4$ are illustrated in the state-space projections shown in Figs. 5.40b and 5.40c, where we can also notice the different structures of the periodic orbit.

Subsection 5.4.5

Influence of the Combination of Different Shape Types

Based on the analyses performed for four different shape types, we examine an additional hysteretic rocking system using two different hysteresis loop shapes for the hysteretic rate-independent elements $z^{(1)}$ and $z^{(2)}$. In particular, in the following, we present the results of the analysis, focusing on the non-dimensional hysteretic system in which the element with restoring force $z^{(1)}$ uses the loop shape $S2$, whereas the element with restoring force $z^{(2)}$ employs the loop shape $S4$. The NDVRM parameters adopted for these simulations are detailed in Table 5.12.

		χ_1	χ_2	χ_3	χ_4	χ_5	χ_6	χ_7	χ_8
$S2$	$z^{(1)}$	-0.2	-2.0	0.0	0.0	0.0	0.0500	-10.0	-0.2
$S4$	$z^{(2)}$	0.01	2.0	0.2	40.0	0.0	0.0500	10.0	0.050

Table 5.12. NDVRM parameters used for evaluating the different loop shapes.

5.4.5.1 Frequency Response Curve

As shown in Fig. 5.41, the FRCs exhibit a rightward bend, indicative of hardening nonlinearity, in agreement with the behavior observed for systems $S2$ and $S4$ (see Section 5.4.4). The resonance peaks for the three FRCs occur at the following points:

- $(1.41457, 1.66524)$ for the maximum angular displacement (Fig. 5.41a);
- $(1.46133, 2.18186)$ for the maximum angular velocity (Fig. 5.41b);
- $(1.44205, 6.2510)$ for the maximum angular acceleration (Fig. 5.41c).

In this case, it is noteworthy that the results obtained by combining the two shape types are very close to those obtained for shape type $S2$ in terms of maximum angular displacement, velocity, and acceleration. However, the effect of shape type $S4$ is evident in the frequencies at which these maxima occur, as they are higher compared to the case of shape type $S2$.

Additionally, across different ranges of Ω, the system exhibits a series of resonance peaks for each FRC:

- for maximum angular displacement, within the range $\Omega \in [0.0999928 - 0.372626]$ (Fig. 5.41a);
- for maximum angular velocity, within the range $\Omega \in [0.0999928 - 0.375637]$ (Fig. 5.41b);
- for maximum angular acceleration, within the range $\Omega \in [0.0999928 - 0.373599]$ (Fig. 5.41c).

Furthermore, the FRCs are not globally stable throughout the entire range of Ω examined, as shown in Fig. 5.41, and this range is larger than that obtained for systems with $S2$ and $S4$ shape types. Specifically, the system undergoes a series of *fold bifurcations* at angular frequencies of 0.54774, 0.555669, 1.48515, and 1.48838. Finally, it is noteworthy that the instability regions have decreased compared to the behavior observed in the $S4$ system, with the instabilities previously seen in the narrower ranges now being eliminated (see Section 5.4.4).

5.4.5.2 Orbits in the State Space

For the hysteretic rocking system with the combined loop shapes $S2$ and $S4$, we consider the angular frequency $\Omega = 1.48681$, since

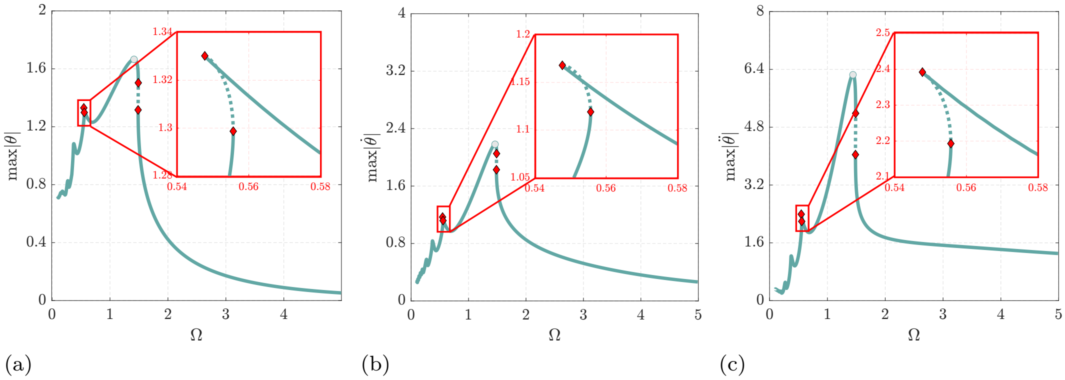

(a) (b) (c)

Figure 5.41. FRC for combined system $S2-S4$: maximum angular displacement (a), maximum angular velocity (b), and maximum angular acceleration (c).

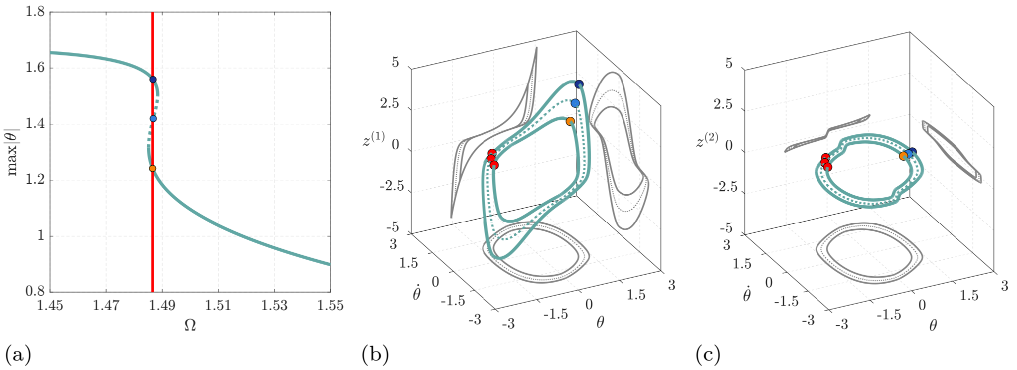

(a) (b) (c)

Figure 5.42. Combined system $S2 - S4$: maximum angular displacement FRC (a), and periodic orbit in the state-space at $\Omega = 1.48681$ (b) and (c).

this value corresponds to a region where the system undergoes a loss of stability. Specifically, at this angular frequency, there are three intersections with the FRC, as shown in Fig. 5.42a. The two stable orbits correspond to maximum angular displacements of 1.24152 and 1.55886, respectively, whereas the single unstable periodic orbit has a maximum angular displacement of 1.41969.

Figures 5.42b and 5.42c show the projections of the periodic orbit onto the $(\theta,\ \dot{\theta}, z^{(1)})$ and $(\theta,\ \dot{\theta}, z^{(2)})$ spaces, respectively. These figures also include projections onto the planes $(\theta,\ \dot{\theta})$, $(\theta,\ z^{(1)})$, $(\theta,\ z^{(2)})$, and $(\dot{\theta},\ z^{(1)})$, $(\dot{\theta},\ z^{(2)})$. The projections onto the $(\theta,\ z^{(1)})$ and $(\theta,\ z^{(2)})$ planes are particularly significant as they clearly highlight the distinct hysteresis loop shapes characterizing the hysteretic rate-independent elements. Additionally, the state-space projections shown in Figs. 5.42b and 5.42c further elucidate the different structures of the periodic orbits. These figures also mark the fixed-point determined by the procedure (red dot) and the corresponding points identified on the FRC (colored dots).

SUBSECTION 5.4.6

Conclusions

In this study, we have developed a comprehensive mathematical framework for analyzing hysteretic rocking systems, with a focus on their frequency response characteristics. Starting from the equations of motion, we have transformed them into a non-dimensional form, which has enabled a more general analysis by reducing the number of governing parameters. This simplification was essential in allowing us to focus on the primary non-dimensional quantities that influence the system's behavior.

A key part of the analysis involved classifying different hysteresis loop shapes and applying a continuation method to explore their impact on system dynamics. Through this, we were able to assess how variations in the loop shape influence the frequency response. In particular, we found that different loop shapes can lead to significant differences in system performance, especially with respect to stability.

Additionally, the study examined the combined effects of two loop shapes, providing deeper insights into how these combinations can modify system behavior. The results demonstrated that a careful selection of hysteresis loop shapes can be used to tune the dynamic response of hysteretic rocking systems, offering valuable guidance for designing resilient structures in engineering applications.

These findings contribute to a better understanding of hysteretic rocking systems and their potential for improving structural performance, particularly in environments subject to dynamic loads such as earthquakes or wind-induced vibrations. Further research could explore the practical implementation of these concepts and their applicability to specific structural systems.

SECTION 5.5

Dynamic Response of MDoF Systems with Complex Rate-Independent Hysteretic Behavior

Hysteresis, a highly nonlinear phenomenon present in various mechanical systems and materials, presents significant challenges in the dynamic analysis of rate-independent hysteretic systems, particularly under periodic excitations [12]. While previous research extensively examined Single-Degree-of-Freedom (SDoF) systems using models like Bouc-Wen [50] and Vaiana-Rosati [14], recent advancements have expanded the focus to MDoF systems. These systems exhibit more complex dynamics due to modal interactions, bifurcations, and potential chaotic responses.

Formica et al. [32] made a significant contribution by providing a robust framework for analyzing MDoF hysteretic systems by combining an exponential hysteretic model and advanced numerical techniques, to identify periodic solutions and characterize bifurcation phenomena. However, the inability of the adopted hysteretic model to capture more complex hysteresis loop shapes [85], limited its applicability to real-world scenarios.

This study overcomes these limitations by incorporating the Vaiana-Rosati model since it can accurately reproduce complex hysteresis behaviors of quite arbitrary nature. The generalized framework investigates the influence of system dimensionality on the dynamic behavior of hysteretic systems using advanced numerical methodologies. In particular, we systematically presents the governing equations of motion and the integration of the Vaiana-Rosati model (Section 5.5.1), the continuation procedures for numerical analysis (Section 5.5.3), and the influence of dimensionality on the dynamic behavior of systems with complex hysteresis loop shapes, analyzing how response patterns evolve with increasing degrees of freedom and highlighting key phenomena (Section 5.5.5).

SUBSECTION 5.5.1

Mathematical Model

In this section, we introduce the equations of motion for a class of MDoF rate-independent hysteretic mechanical systems, starting from their dimensional formulation. To facilitate the

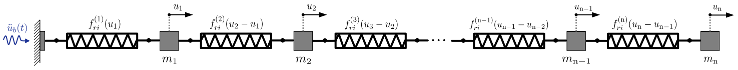

Figure 5.43. General family of MDoF hysteretic mechanical systems.

analysis and reduce the number of parameters, we present the non-dimensional form of these equations, emphasizing key non-dimensional parameters. This approach results in simplified equations that generalize the behavior of the system under investigation.

5.5.1.1 Dimensional System

The general class of dimensional MDoF hysteretic mechanical systems, considered in [32] and shown in Fig. 5.43, comprises n masses connected in series; each mass is denoted as m_j (where $j = 1, 2, \ldots, n$). These masses are interconnected by rate-independent hysteretic elements. For this system, the dimensional equation of motion can be derived from Newton's second law in its general form as:

$$\begin{cases} m_1\ddot{u}_1 + f_{ri}^{(1)}(u_1) + f_{ri}^{(2)}(u_2-u_1) = -m_1\ddot{u}_b\cos(\omega t), \\ \qquad\qquad\qquad\qquad\vdots \\ m_j\ddot{u}_j + f_{ri}^{(j)}(u_j-u_{j-1}) + f_{ri}^{(j+1)}(u_{j+1}-u_j) = -m_j\ddot{u}_b\cos(\omega t), \\ \qquad\qquad\qquad\qquad\vdots \\ m_n\ddot{u}_n + f_{ri}^{(n)}(u_n-u_{n-1}) = -m_n\ddot{u}_b\cos(\omega t), \end{cases} \tag{5.5.1}$$

where the hysteretic forces $f_{ri}^{(j)}$ are governed by the Vaiana-Rosati model, denoted as VRM+D and formulated in Section 4.3.2, that will be detailed in the following.

5.5.1.2 Non-dimensional System

Non-dimensionalization is a valuable technique in the analysis of systems governed by ODEs, as it simplifies complex systems by reducing the number of involved parameters. This method facilitates a clearer understanding of the relationships between system parameters and enables the comparison of different systems on a common scale by eliminating specific units. The non-dimensionalization process consists of five steps (Section 2.5):

1. Identify all independent and dependent variables within the system.

2. Replace all variables with non-dimensional quantities defined by relationships between the dimensional variables and newly introduced dimensional coefficients.
3. Divide the resulting equation by the coefficient of the highest-order derivative.
4. Choose the dimensional coefficients based on the characteristic units of the system, simplifying any auxiliary conditions that may arise.
5. Rewrite the equation in terms of the newly defined non-dimensional quantities.

By applying these five steps to the equations of motion in Eq. (5.5.1), a suitable non-dimensionalization of the governing equations can be effectively achieved by setting:

$$t = t_s\tau, \quad u_j = u_s x_j, \quad f_{ri}^{(j)} = f_s^{(j)} z^{(j)}, \quad \text{for } j = 1, 2, \dots, n. \tag{5.5.2}$$

The final non-dimensional MDoF hysteretic mechanical system is governed by the following ODEs:

$$\begin{cases} \ddot{x}_1 + z^{(1)}(x_1) + \psi_2 z^{(2)}(x_2 - x_1) = -A\cos(\Omega\tau), \\ \qquad\qquad\qquad\vdots \\ \ddot{x}_j + \psi_j\mu_j z^{(j)}(x_j - x_{j-1}) + \psi_{j+1}\mu_j z^{(j+1)}(x_{j+1} - x_j) = -A\cos(\Omega\tau), \\ \qquad\qquad\qquad\vdots \\ \ddot{x}_n + \psi_n\mu_n z^{(n)}(x_n - x_{n-1}) = -A\cos(\Omega\tau), \end{cases} \tag{5.5.3}$$

where:

$$\begin{aligned} & t_s := \sqrt{\frac{m_1 u_s}{f_s^{(1)}}}, \quad A := \frac{\ddot{u}_b m_1}{f_s^{(1)}}, \quad \Omega := \omega\sqrt{\frac{m_1 u_s}{f_s^{(1)}}}, \\ & \mu_j := \frac{m_1}{m_j}, \quad \psi_j := \frac{f_s^{(j)}}{f_s^{(1)}}, \quad \text{for } j = 1, 2, \dots, n. \end{aligned} \tag{5.5.4}$$

In these equations, the non-dimensional hysteretic variables $z^{(j)}$ are governed by a non-dimensional version of the VRM+D, which will be elaborated upon in the following.

SUBSECTION 5.5.2

Vaiana-Rosati Model

Vaiana and Rosati first developed a novel phenomenological model to simulate rate-independent hysteretic behavior in mechanical systems, utilizing closed-form expressions for output evaluation [84]. They later introduced an enhanced equivalent differential formulation, known as VRM+D [83]. as shown in previous sections, both models effectively address the challenges of simulating complex hysteresis phenomena, offering practical solutions for the analysis of hysteretic mechanical systems.

5.5.2.1 Dimensional Vaiana-Rosati Model

According to the VRM+D formulation [83], the generalized rate-independent hysteretic force f_{ri} is governed by the following first-order ODE:

$$\dot{f}_{ri} = \left\{k_e\left(u\right) + k_b + \alpha f_0 + s\alpha\left[f_e\left(u\right) + k_b u - f_{ri}\right]\right\}\dot{u}, \tag{5.5.5}$$

where u represents the elongation of the hysteretic element, $k_e(u)$ is the function expressed as:

$$k_e\left(u\right) = \beta_1\beta_2 e^{\beta_2 u} + 4\gamma_1\gamma_2\frac{e^{-\gamma_2\left(u-\gamma_3\right)}}{\left[1 + e^{-\gamma_2\left(u-\gamma_3\right)}\right]^2}, \tag{5.5.6}$$

whereas $f_e(u)$ is given by:

$$f_e\left(u\right) = \beta_1\left(e^{\beta_2 u} - 1\right) + 2\gamma_1\frac{1 - e^{-\gamma_2\left(u-\gamma_3\right)}}{1 + e^{-\gamma_2\left(u-\gamma_3\right)}}. \tag{5.5.7}$$

Specifically, the VRM+D enables an uncoupled modeling of the loading and unloading phases, as in Eqs. (5.5.5)-(5.5.7), the model parameters can be updated depending on the sign of the velocity $\dot{u}$ ($s := \operatorname{sgn}\left(\dot{u}\right)$). Furthermore, it facilitates the identification of the involved parameters due to their clear mechanical and/or graphical interpretation.

5.5.2.2 Non-Dimensional Vaiana-Rosati Model

Following the non-dimensionalization procedure detailed in Section 5.5.1.2, the resulting NDVRM+D is governed by the following first-order ODE:

$$\dot{z} = \left\{\kappa_e\left(x\right) + \chi_6 + \chi_7\chi_8 + s\chi_7\left[\phi_e\left(x\right) + \chi_6 x - z\right]\right\}\dot{x}, \tag{5.5.8}$$

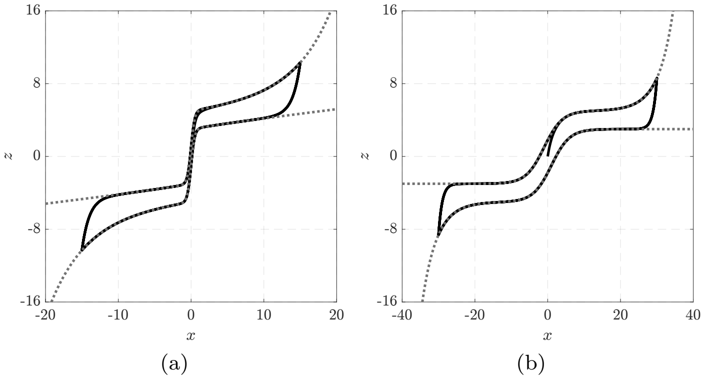

Figure 5.44. Two complex hysteresis loop shapes simulated using the NDVRM+D parameters in Table 5.13.

Table 5.13. NDVRM+D parameters used for the hysteretic elements.

Figure	sgn($\dot{x}$)	χ_1	χ_2	χ_3	χ_4	χ_5	χ_6	χ_7	χ_8
5.44a	+	0.2	0.2	4.0	4.0	0.0	0.1	1.0	1.0
	−	-0.2	-0.2	4.0	4.0	0.0	0.1	1.0	1.0
5.44b	+	0.002	0.25	4.0	0.4	-1.0	0.0	1.0	1.0
	−	-0.002	-0.25	4.0	0.4	1.0	0.0	1.0	1.0

where the functions $\kappa_e(x)$ and $\phi_e(x)$ are defined as:

$$\kappa_e\left(x\right) = \chi_1\chi_2 e^{\chi_2 x} + 2\chi_3\chi_4 \frac{e^{-\chi_4(x-\chi_5)}}{\left[1+e^{-\chi_4(x-\chi_5)}\right]^2},$$

$$\phi_e\left(x\right) = \chi_1\left(e^{\chi_2 x}-1\right) + \chi_3 \frac{1-e^{-\chi_4(x-\chi_5)}}{1+e^{-\chi_4(x-\chi_5)}}.$$

The model involves eight non-dimensional parameters, which are expressed in terms of the original dimensional parameters as follows:

$$\chi_1 := \frac{\beta_1}{f_s}, \quad \chi_2 := \beta_2 u_s, \quad \chi_3 := \frac{2\gamma_1}{f_s}, \quad \chi_4 := \gamma_2 u_s,$$

$$\chi_5 := \frac{\gamma_3}{u_s}, \quad \chi_6 := \frac{k_b u_s}{f_s}, \quad \chi_7 := \alpha u_s, \quad \chi_8 := \frac{f_0}{f_s}.$$

Finally, an illustrative example of complex hysteresis loop shapes generated by using the NDVRM+D is presented in Fig. 5.44 in which the parameters in Table 5.13 have been adopted. This highlights the effectiveness of the non-dimensional model in capturing the intricate characteristics of hysteretic behaviors.

Subsection 5.5.3
Poincaré-map Based Continuation

As discussed in Section 4.3.3, the pseudo-arclength continuation method leverages the Poincaré map, combined with arclength parameterization, to compute periodic solutions of strongly nonlinear systems as the selected control parameter varies. Specifically, when the class of systems under analysis is subjected to a T-periodic external excitation, the Poincaré map is defined as $\mathbf{P}(\boldsymbol{\eta}, \Omega) : \boldsymbol{\eta} \mapsto \mathbf{x}(\tau_0 + T, \boldsymbol{\eta}, \Omega)$, where T represents the return time. Periodic solutions are then identified as fixed-points of this map, satisfying the following equation:

$$\mathbf{P}(\boldsymbol{\eta}, \Omega) - \boldsymbol{\eta} = \mathbf{0}. \tag{5.5.9}$$

5.5.3.1 Continuation procedure

To solve Eq. (5.5.9) both the periodic solution $\boldsymbol{\eta}$ and the continuation parameter Ω are parameterized by s, resulting in a redefined fixed-point equation $\mathbf{p}\left(\boldsymbol{\eta}(s), \Omega(s)\right)$. An initial prediction is made using linear extrapolation along the unit tangent direction $\mathbf{a}$. At the new solution point $s_0 + \Delta s$, the Taylor expansion of $\mathbf{p}$ must hold and, by neglecting higher-order terms [33], we can express the unknown vector $\boldsymbol{\eta}_s$ in terms of Ω_s. The tangent vector $\mathbf{a}$ is then normalized, leading to an updated guess for the solution at $s_0 + \Delta s$. The updated state of the system $(\boldsymbol{\eta}(s), \Omega(s))$ is then obtained by solving the fixed-point equation subject to an orthogonality condition $g\left(\boldsymbol{\eta}(s), \Omega(s)\right)$, leading to the augmented system:

$$\begin{cases} \mathbf{p}\left(\boldsymbol{\eta}(s), \Omega(s)\right) = \mathbf{0} \\ g\left(\boldsymbol{\eta}(s), \Omega(s)\right) = 0. \end{cases} \tag{5.5.10}$$

The augmented system in Eq. (5.5.10) is solved using iterative procedures such as Newton-Raphson [14, 49, 50] or, for improved efficiency in high-dimensional problems, the Krylov subspace method [33].

Subsection 5.5.4
Krylov Subspace Acceleration Algorithm

Krylov subspaces represent the basis of numerous iterative algorithms in numerical linear algebra, including those for solving eigenvalue problems and linear systems of equations [76]. A Krylov subspace of dimension m, denoted as $\mathcal{K}_m$, is defined as the span of vectors generated by repeated multiplication of an initial vector $\mathbf{b}$ by a matrix $\mathbf{A}$ (e.g., the updated iteration matrix), such that:

$$\mathcal{K}_m = \text{span}\left\{\mathbf{b}, \mathbf{A}\mathbf{b}, \mathbf{A}^2\mathbf{b}, \dots, \mathbf{A}^{m-1}\mathbf{b}\right\}.$$

An essential advantage of Krylov subspace methods lies in their computational efficiency, as the matrix $\mathbf{A}$ is never explicitly formed. Instead, its action is computed through successive vector operations, avoiding the costly construction of $\mathbf{A}$. This efficiency is particularly relevant for large-scale systems where direct computation of $\mathbf{A}$ would be excessively demanding. In the context of the modified Newton–Raphson scheme and its Krylov-accelerated version, the matrix $\mathbf{A}$ is purely formal and simplifies to the identity matrix [33].

5.5.4.1 Description of the Pseudocode

The following pseudocode implements a Krylov acceleration algorithm for the iterative solution of a system of nonlinear equations.

1. Initialization: The solution vector $(\boldsymbol{\eta}, \Omega)$ is initialized with an initial value $(\boldsymbol{\eta}_0, \Omega_0)$, and the corresponding residual $\mathbf{r}_0$ is calculated. The maximum dimension of the Krylov subspace is defined as $m_{\max} + 1$, where $m_{\max}$ represents the maximum number of stored vectors, typically chosen within the range of three to six [76].

2. Main Loop: The algorithm enters an iterative loop, continuing until $\|\mathbf{r}_\mathrm{k}\| < tol$, indicating that the iterative solution has achieved satisfactory convergence.

    (a) If the dimension of the subspace m exceeds the maximum value $m_{\max}$, the tangent matrix (i.e., the system's Jacobian) is updated, and the Krylov subspace is reinitialized.

    (b) The residual vector $\mathbf{r}_\mathrm{k}$ is computed using LU decomposition.

    (c) If the subspace has been accumulated ($m > 0$), the correction $\mathbf{w}_{\mathrm{k}+1}$ is computed in order to minimize, in a least-square sense, the norm $\|\mathbf{r}_\mathrm{k} - \mathbf{A}\mathbf{w}_{\mathrm{k}+1}\|$, that is

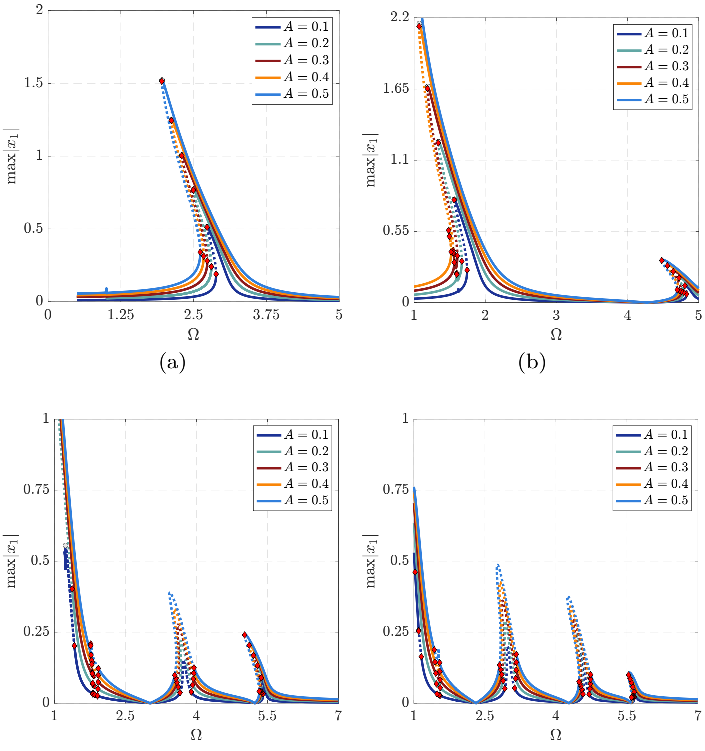

(a) (b)

(c) (d)

Figure 5.45. FRCs for 1DoF (a), 2DoFs (b), 3DoFs (c), and 4DoFs (d) hysteretic mechanical systems having complex hysteresis loop shape shown in Fig. 5.44a, and different amplitudes A, as defined in Eq. (5.5.4), of the input force.

the distance from the solution. This correction is calculated as a linear combination of the residual vectors accumulated in the Krylov subspace.

(d) The solution is updated by adding the acceleration component $\mathbf{w}_{k+1}$ and the standard modified Newton component of the increment $\mathbf{q}_{k+1}$. A new residual $\mathbf{r}_{k+1}$ is calculated, and the subspace is updated with the new residual.

Subsection 5.5.5

Frequency-Response Curves: Stability and Bifurcations

The following sections present the results of the analysis. Specifically, the FRCs for the different DoF systems are discussed, highlighting the key observations related to the amplitude dependence, and the effect of the DoFs' number.

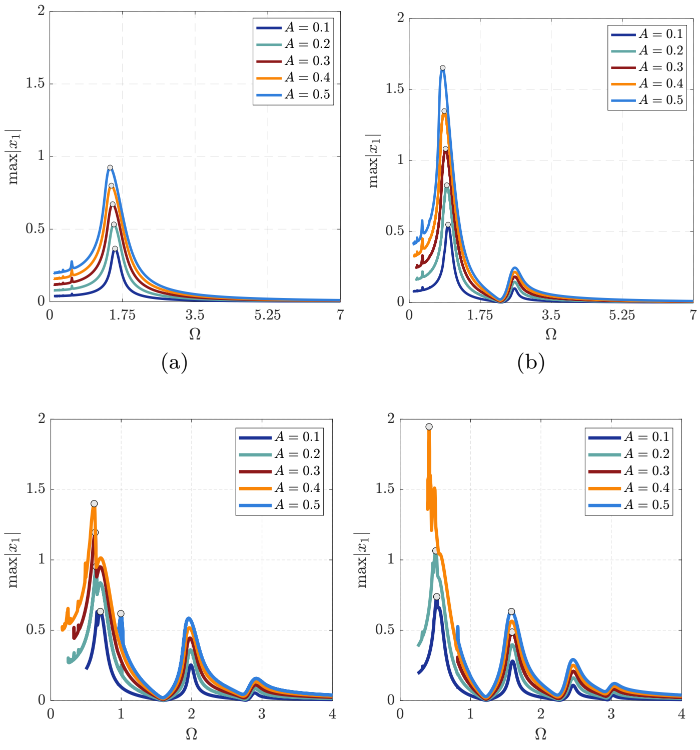

(a) (b) (c) (d)

Figure 5.46. FRCs for 1DoF (a), and 2DoFs (b), 3DoFs (c), and 4DoFs (d) hysteretic mechanical systems having complex hysteresis loop shape shown in Fig. 5.44b, and different amplitudes A, as defined in Eq. (5.5.4), of the input force.

5.5.5.1 Analyzed systems

The study investigates four mechanical systems characterized by rate-independent hysteretic behavior, modeled using the NDVRM+D shown in Section 5.5.2.2. The four analyzed configurations correspond to systems with an increasing numbers of DoFs, from 1 to 4, in which each oscillator exhibits an hysteretic behavior described in Fig. 5.44. We present and discuss the dynamics of these systems under harmonic external forcing, analyzing the resulting periodic solutions obtained using the continuation procedure described in Section 5.5.3.

5.5.5.2 Numerical Analysis and Results

Figure 5.45 (5.46) illustrates the FRCs for mechanical systems exhibiting the rate-independent hysteretic behavior in Fig. 5.44a (5.44b), modeled using the NDVRM+D. The FRCs depict the maximum displacement of the first mass as a function of the excitation frequency Ω, by providing a comprehensive view of the systems' dynamic behavior. The hysteretic elements embedded in the systems strongly influence the observed FRCs, since nonlinear behaviors such as amplitude-dependent resonance shifts, multi-stability, and jump phenomena are observed [19, 97]. Due to its peculiar features, the following analysis focuses specifically on the behavior of the system incorporating hysteretic elements as depicted in Fig. 5.44a.

Amplitude Dependence: The amplitude A of the external forcing significantly affects the dynamic response across all systems. As A increases, the FRCs exhibit higher peak displacements and broader resonance regions, independently from the number of hysteretic elements, indicative of a strong nonlinear behavior. This amplitude dependence highlights the sensitivity of the systems to external forcing intensity and the pronounced role of hysteretic nonlinearity.

Effect of Degrees of Freedom: For the 1DoF system (Fig. 5.45a) the FRC displays a single dominant resonance peak with softening behavior and multiple *fold bifurcation*, characteristic of rate-independent hysteretic systems. This response reflects the simplicity of the system's dynamics combined with strong nonlinear effects. In the case of the 2DoFs system (Fig. 5.45b), the introduction of a second DoF introduces an additional resonance peaks and a more complex bifurcation scenario, broadening the instability region. This behavior is attributed to the interaction between the two coupled oscillators, leading to richer dynamic characteristics. Finally, for the 3DoFs and 4DoFs systems (Figs. 5.45c and 5.45d) as the number of DoFs increases, the FRCs exhibit a progressively intricate structure. This includes multiple resonance peaks and more complex bifurcation scenarios. Notably, it is observed that the introduction of internal masses leads to the emergence of an equal number of completely unstable peaks corresponding to the number of internal masses.

SUBSECTION 5.5.6

Conclusions

The results underscore the critical influence of the number of DoFs on the stability and bifurcation characteristics of hysteretic mechanical systems. The increasing complexity of the FRCs with higher-dimensional configurations reflects the enhanced nonlinear dynamics introduced by additional DoFs. For the 1DoF system, the response is dominated by a single resonance, whereas in higher-dimensional systems, coupling between oscillators introduces additional modes of vibration and nonlinear interactions. Future research endeavors may focus on extending this analysis to investigate additional system configurations and behaviors, as well as exploring the implications of these dynamics in real-world contexts. Such investigations could enhance the understanding of hysteretic systems and inform the development of more robust and efficient engineering solutions.

Section 5.6

Work and Energy Components in Mechanical Systems with Complex Hysteretic Behavior

In this section, using the results provided in Section 4.3.4, we present the comparison of the results obtained by the numerical analyses performed on two SDoF hysteretic mechanical systems in which the nonlinear responses are modeled by means of a rate-independent hysteretic element and using the VRM; the analyses are performed for three specific conditions: (i) free vibration, (ii) oscillations forced by a harmonic load, (iii) oscillations forced by a random load. Specific attention is paid to the evolution of the various components of generalized work and energy components once a steady-state condition, in the case of harmonic force, is reached by the system.

Subsection 5.6.1

Equation of Motion

The selected general family of SDoF hysteretic mechanical systems is illustrated in Fig. 5.47. Such a model is composed of a mass m connected to a rate-independent hysteretic spring. Denoting by u, $\dot{u}$ and $\ddot{u}$ the generalized displacement, velocity, and acceleration, respectively, the equation of motion for the general family of SDoF hysteretic mechanical systems illustrated in Fig. 5.47, can be easily obtained from Newton's second law as:

$$m\ddot{u} + f_{ri}\left(u\right) = p\left(t\right),$$

where f_{ri} is the generalized rate-independent hysteretic force exerted on the rate-independent hysteretic element, assumed to be a function of the generalized displacement u and simulated by using the VRM. Furthermore, p is the time-dependent generalized external force acting on the mass.

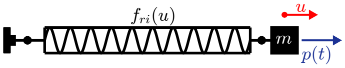

Figure 5.47. SDoF hysteretic mechanical system.

Subsection 5.6.2

Analyzed Hysteretic Mechanical Systems

Two hysteretic mechanical systems are selected:

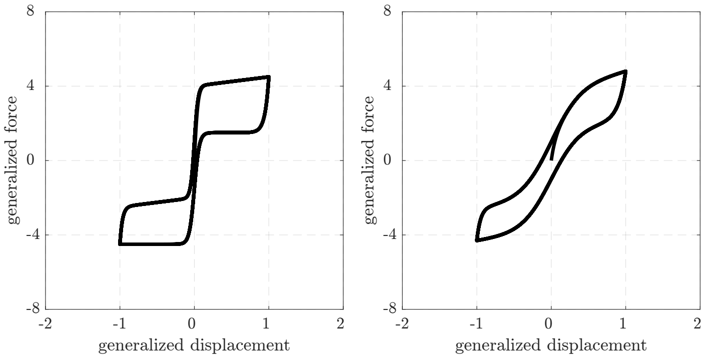

(a)

(b)

Figure 5.48. Complex hysteretic behavior charactering system A (a) and system B (b) simulated by using the VRM parameters in Table 5.14.

1. System A: with hysteretic behavior shown in Fig. 5.48a characterized by an asymmetric flag-shaped hysteresis loop, and belonging to $S3$ category.
2. System B: with hysteretic behavior shown in Fig. 5.48b, characterized by an asymmetric S-shaped hysteresis loop with pinching and belonging to $S4$ category.

Finally, the loops in Fig. 5.48 are simulated using VRM by employing the parameters listed in Table 5.14.

Figure	sgn($\dot{u}$)	k_b	f_0	α	β_1	β_2	γ_1	γ_2	γ_3
5.48a	$+$	0.5	1.0	30	0.0	0.0	1.5	40	0.0
	$-$	0.0	1.5	20	0.0	0.0	1.5	30	0.0
5.48b	$+$	0.5	1.0	20	0.2	1.0	1.5	5.0	0.0
	$-$	0.0	1.0	10	-0.2	-1.0	1.5	5.0	0.0

Table 5.14. VRM parameters adopted to simulate the hysteresis loops in Figure 5.48.

Subsection 5.6.3

Modified Work-Energy Theorem

As shown in Section 4.3.4, the general expression of the MWE theorem for SDoF hysteretic systems states that the sum of the generalized mechanical and internal energy variations of a system is equal to the work done by the generalized external forces acting on the system:

$$\Delta E_M + \Delta E_I = W_p, \tag{5.6.1}$$

where the generalized mechanical energy E_M is equal to the sum of the generalized kinetic E_K and potential E_P energies of the system.

With respect to the hysteretic mechanical system shown in Fig. 5.47, there are no generalized conservative forces so that the generalized potential energy is equal to zero. On the other hand, we know that the variation of the generalized internal energy ΔE_I is related to the generalized work of the non-conservative internal forces W_{nc}^i, that in the general family of mechanical systems under consideration, is represented by the work W_{ri} performed by the generalized force exhibited by the rate-independent hysteretic element; hence, it is possible to write:

$$\Delta E_I = -W_{nc}^i = -W_{ri}.$$

On the other hand, W_p in Eq. (5.6.1), is the generalized work done by the generalized external force $p(t)$ on the mass m. These quantities can be computed as follows:

$$\begin{aligned} W_{ri} &= -\int_{u_i}^{u_f} f_{ri}(u)\,du, \\ W_p &= \int_{u_i}^{u_f} p(t)\,du. \end{aligned}$$

In particular, W_{ri} can be computed in a closed-form for any generalized displacement interval, whereas W_p can be evaluated numerically.

SUBSECTION 5.6.4

Numerical Results

The response of the systems is evaluated by using an explicit, accurate, and computationally efficient time integration method, described in [86], using a time step $\Delta t = 0.001$ s and a unitary mass. The hysteretic model and the solution algorithm have been programmed in MATLAB R2022b and run on a computer having an Intel Core i5 dual-core processor and a CPU at 2.30 GHz with 8 GB of RAM [15].

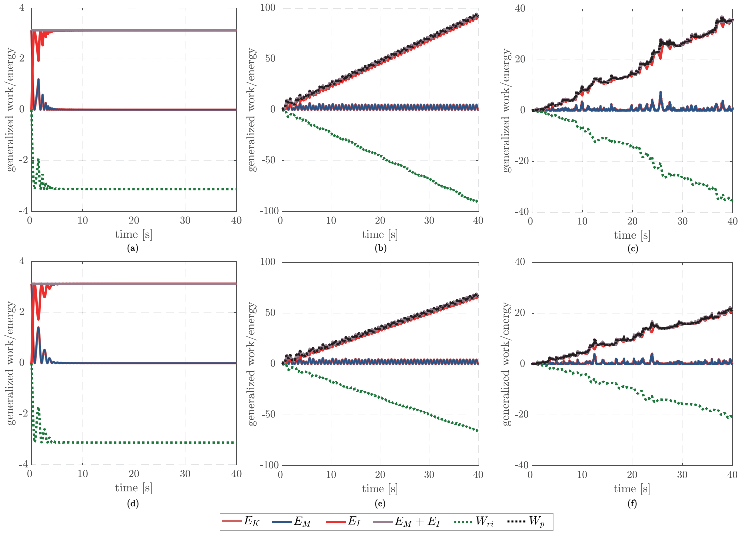

Figure 5.49. Time histories of the generalized energy and work components for the rate-independent hysteretic systems A (a, b, c) and B (d, e, f), obtained for free (a, d), forced harmonic (b, e) and forced random (c, f) vibrations.

5.6.4.1 Free vibrations

To evaluate the free vibration response of the systems under investigation, the following initial conditions were chosen in terms of generalized displacement $u_0 = 0.0$ m and velocity $\dot{u}_0 = 2.5$ m/s, whereas the generalized external force $p(t)$ is considered null. Fig. 5.49a (Fig.5.49d) shows the time history of the various generalized work and energy components for system A (B). In both cases, it can be noted that:

(i) the generalized rate-independent work W_{ri} assumes negative values since the generalized rate-independent hysteretic force f_{ri} tends to bring the mass m back to its equilibrium position;

(ii) the reduction of the generalized mechanical energy E_M can be interpreted as an energy conservation process in which energy is converted into generalized internal energy E_I;

(iii) it can be noted that in the case of free vibrations, the entire amount of generalized mechanical energy, initially supplied to the system due to the initial conditions, has been converted into generalized internal energy through the rate-independent hysteretic phenomena, thus guaranteeing energy conservation;

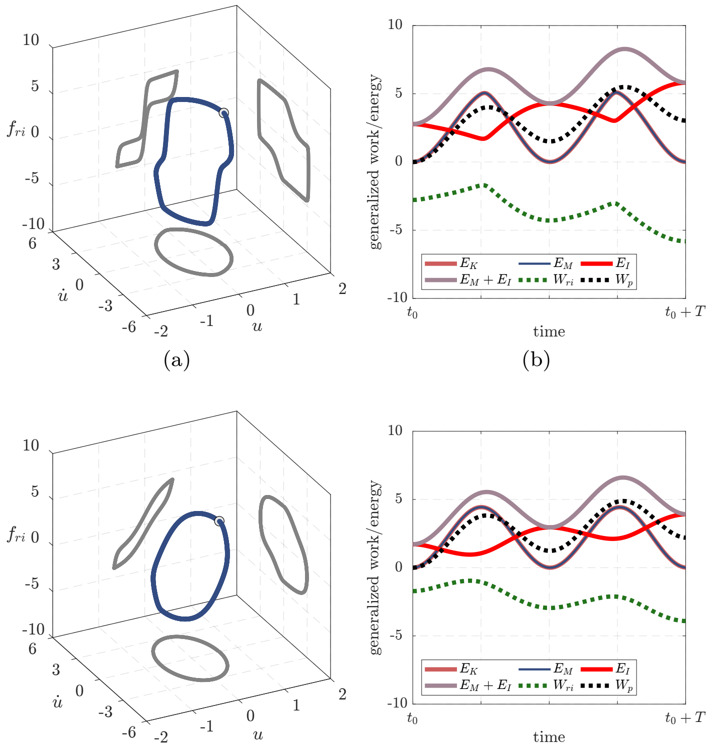

(a) (b)

(c) (d)

Figure 5.50. Steady-state response in the $(u, \dot{u}, f_{ri})$-state-space for the hysteretic mechanical system, and generalized work and energy components over a period T.

(iv) since the generalized external force $p(t)$ is equal to zero, it can be deduced, from Eq. (5.6.1), that the sum between generalized mechanical and internal energy $E_M + E_I$ is constant over time.

5.6.4.2 Forced harmonic vibrations

To evaluate the response of the system in the case of oscillations forced by a harmonic force, initial conditions of zero generalized displacements and velocity are imposed, whereas the load is assumed to be a harmonic function of the following type:

$$p(t) = p_0 \cos(2\pi f_p\, t),$$

where the amplitude is $p_0 = 10$ N and its frequency is $f_p = 0.75$ Hz. Fig. 5.49b (Fig. 5.49e) shows the time history of the various generalized work and energy components for system A (B). In both cases, it can be noted that:

(i) the motion of the mass m is caused by the generalized external work performed by the harmonic load that, as shown in the Figs. 5.49b and 5.49e, is an increasing function over time;

(ii) the generalized mechanical energy and rate-independent work will no longer tend to an asymptotic value, as in the case of the free vibration, but they will assume values able to ensure fulfillment of the MWE theorem, i.e., Eq. (5.6.1);

(iii) as a result of the chosen initial conditions, the sum between generalized mechanical and internal energy $E_M + E_I$ coincides with the generalized work done by the harmonic forcing W_p.

In this case, the time variation of the generalized mechanical energy E_M gives us precious information to distinguish the transition from a transient behavior, in which a reduction of the peaks of the generalized mechanical energy is observed, to a steady-state behavior [32].

Having determined the steady-state response of the two systems under consideration, a further analysis is performed, in which the initial conditions are chosen such that the system is in a steady-state response. In Fig. 5.50 we can see the steady-state responses in the $(u, \dot{u}, f_{ri})$-state-space, with the relative projections for the two analyzed systems (Figs. 5.50a and 5.50c), and time evolution of the generalized work and energy components over a period $T = \frac{1}{f_p}$ (Figs. 5.50b and 5.50d).

5.6.4.3 Forced random vibrations

To evaluate the response of the system in the case of vibrations induced by a random load, initial conditions of zero generalized displacements and velocity are imposed, and a random force modeled as a Gaussian white noise with a variance iwn $= 40$, is applied to the system as external force $p(t)$. Figure 5.49c (Figure 5.49f) shows the time history of the various generalized work and energy components for system A (B).

These latter cases are similar to the harmonic loading ones except for the distinction of transient and steady-state behaviors, which is not possible in this case since the load is not periodic.

Subsection 5.6.5

Conclusions

We have used the MWE theorem to evaluate the generalized work and energy responses of different SDoF hysteretic mechanical systems with complex hysteresis loop shapes simulated by the VRM, in three particular cases: (i) free vibrations, (ii) forced harmonic vibrations and (iii) forced random vibrations.

The performed analyses show valuable information on the time history of the generalized energy components of the systems under consideration, particularly in the case of the steady-state response of a harmonically forced system .

Conclusions

This thesis hopes to contribute to a better understanding of hysteretic mechanical systems by providing a detailed analysis of these systems under time-periodic inputs. By integrating the Vaiana-Rosati model with advanced numerical methods such as the continuation procedures based on Poincaré maps, we have effectively demonstrated the framework's capability to predict complex mechanical behaviors, including steady-state responses, stability, and bifurcation phenomena. The bifurcation analysis conducted, in particular, has proven invaluable for elucidating the dynamics of hysteretic systems under varying loading conditions, providing critical insights that can inform the design of control strategies to mitigate adverse effects associated with hysteresis.

In our investigation of asymmetric hysteretic systems, we have established a clear relationship between the asymmetry of hysteresis loops and the frequency response and stability of the systems. The frequency response analysis highlighted how variations in hysteresis loop shapes significantly influence system performance, particularly when subjected to periodic excitations. Our findings indicate that understanding these asymmetries is crucial for optimizing the dynamic behavior of hysteretic systems in practical applications.

Additionally, the examination of negative stiffness metamaterials introduced a novel perspective on frequency response characteristics. By analyzing this type of metamaterials, we demonstrated that their unique properties can lead to enhanced performance in controlling vibrations and improving stability. This work not only expands the theoretical framework for analyzing hysteretic systems but also provides practical guidance for leveraging metamaterials in engineering applications.

Further, the examination of hysteretic rocking systems revealed how different loop shapes affect frequency response and stability. By carefully selecting hysteresis loop shapes, one can tune system dynamics to enhance resilience in structural design. This work not only expands the theoretical framework for analyzing hysteretic systems but also provides practical guidance for engineering applications.

The findings also underscore the critical impact of dimensionality on the stability and bifurcation characteristics of hysteretic mechanical systems. As the number of degrees of freedom increases, the complexity of the frequency response curves reflects enhanced nonlinear dynamics, which necessitates a more nuanced understanding of system behavior in higher-dimensional configurations.

Finally, the application of the MWE theorem to evaluate generalized work and energy responses across various scenarios has yielded important insights into the energy dynamics of SDoF hysteretic mechanical systems with complex loop shapes. The analyses conducted under free vibrations, forced harmonic vibrations, and forced random vibrations have provided a comprehensive view of how energy components evolve over time, particularly in steady-state conditions.

In summary, this thesis contributes to the field of nonlinear dynamics by providing a robust mathematical framework and innovative approaches for the study of hysteretic mechanical systems. The insights gained from this research lay the groundwork for future investigations and applications, enhancing our understanding of complex hysteretic behaviors and their implications in engineering design and analysis.

APPENDIX

A

Matrix Exponential

In mathematics, the matrix exponential is a matrix function on square matrices analogous to the ordinary exponential function. It is used to solve systems of linear differential equations. The formal definition of the matrix exponential is:

Definition 16

$$e^{\mathbf{A}t} := \sum_{i=0}^{+\infty} \frac{(\mathbf{A}t)^i}{i!}, \tag{A.0.1}$$

where $\mathbf{A} \in \mathbb{R}^{n\times n}$, $t \in \mathbb{R}$ and $\mathbf{A}^0 := \mathbf{I} \in \mathbb{R}^{n\times n}$. The series always converges, so the exponential of $\mathbf{A}t$ is well-defined.

It is easy to note that if we apply the definition in Eq. (A.0.1) to a diagonal matrix $\mathbf{A}$ as follows:

$$\mathbf{A} = \begin{bmatrix} a_{11} & & \\ & \ddots & \\ & & a_{nn} \end{bmatrix},$$

the result is simply a diagonal matrix, whose elements are the exponential of the original elements, namely:

$$e^{\mathbf{A}} = \begin{bmatrix} e^{a_{11}} & & \\ & \ddots & \\ & & e^{a_{nn}} \end{bmatrix}.$$

On the contrary, in case of a full matrix, the matrix exponential is not a simple application of the exponential function to each element of the matrix and the definition in Eq. (A.0.1) must be used to determine its form. For this purpose, the reduction of the matrix $\mathbf{A}$ to its canonical Jordan form can be a straightforward way for the explicit calculation of the matrix exponential. In fact, there exists an invertible matrix $\mathbf{U} \in \mathbb{C}^{n\times n}$, such that $\mathbf{A} = \mathbf{U}\bar{\mathbf{A}}\mathbf{U}^{-1}$, where $\bar{\mathbf{A}}$ is the Jordan canonical form of $\mathbf{A}$. For a matrix expressed in its canonical Jordan form, the following property is fulfilled:

$$e^{\mathbf{A}t} = \mathbf{U}e^{\bar{\mathbf{A}}t}\mathbf{U}^{-1},$$

and due to the diagonal-block-structure of $\mathbf{A}$, the matrix exponential $e^{\mathbf{A}t}$ can easily be computed from Eq. (A.0.1).

The derivative in time of the matrix exponential defined in Eq. (A.0.1) is equal to:

$$\frac{d}{dt}e^{\mathbf{A}t} = \mathbf{A}e^{\mathbf{A}t} = e^{\mathbf{A}t}\mathbf{A},$$

therefore it is now clear why $\mathbf{x}(t) = e^{\mathbf{A}t}\mathbf{b}$ (where $\mathbf{b}$ is an undetermined constant vector) can be chosen as a solution of the linear autonomous system $\dot{\mathbf{x}} = \mathbf{A}\mathbf{x}$. Finally, the imposition of initial conditions leads to $\mathbf{b} = \mathbf{x}_0$.

Let's note that for autonomous systems a shift in time is always allowed, so, in this case, the time t in the matrix exponential actually can be substituted by a time interval from the initial condition. Hence, for a general initial reference time t_0, the correct form for the solution is:

$$\mathbf{x}(t) = e^{\mathbf{A}(t-t_0)}\mathbf{x}(t_0).$$

APPENDIX

B

Notable Laplace Transforms

The fundamental transformations commonly found in engineering systems are listed below:

$$\mathcal{L}\left\{\delta(t)\right\} = 1$$

$$\mathcal{L}\left\{\delta_{-1}(t)\right\} = \mathcal{L}\left\{\int_{-\infty}^{t} \delta(\tau)d\tau\right\} = \mathcal{L}\left\{\int_{0}^{t} \delta(\tau)d\tau\right\} = \frac{1}{s}$$

$$\mathcal{L}\left\{\delta_{-2}(t)\right\} = \mathcal{L}\left\{\int_{-\infty}^{t} \delta_{-1}(\tau)d\tau\right\} = \mathcal{L}\left\{\int_{0}^{\infty} \delta_{-1}(\tau)d\tau\right\} = \frac{1}{s^2}$$

$$\mathcal{L}\left\{\delta_{-3}(t)\right\} = \mathcal{L}\left\{\int_{-\infty}^{t} \delta_{-2}(t)d\tau\right\} = \mathcal{L}\left\{\int_{0}^{t} \delta_{-2}(\tau)d\tau\right\} = \frac{1}{s^3}$$

$$\mathcal{L}\left\{f\delta_{-n}(t)\right\} = \frac{1}{s^n}$$

$$\mathcal{L}\left\{e^{\alpha t}\delta_{-1}(t)\right\} = \frac{1}{s-\alpha}$$

$$\mathcal{L}\left\{te^{\alpha t}\delta_{-1}(t)\right\} = \frac{1}{(s-\alpha)^2}$$

$$\mathcal{L}\left\{\frac{t^n}{n!}e^{\alpha t}\delta_{-1}(t)\right\} = \frac{1}{(s-\alpha)^{n+1}}$$

$$\mathcal{L}\left\{\sin(\omega t)\delta_{-1}(t)\right\} = \frac{\omega}{s^2+\omega^2}$$

$$\mathcal{L}\left\{\cos(\omega t)\delta_{-1}(t)\right\} = \frac{s}{s^2+\omega^2}$$

$$\mathcal{L}\left\{e^{\alpha t}\sin(\omega t)\delta_{-1}(t)\right\} = \frac{\omega}{(s-\alpha)^2+\omega^2}$$

$$\mathcal{L}\left\{e^{\alpha t}\cos(\omega t)\delta_{-1}(t)\right\} = \frac{s-\alpha}{(s-\alpha)^2+\omega^2}$$

$$\mathcal{L}\left\{t\sin(\omega t)\delta_{-1}(t)\right\} = \frac{2\omega s}{\left(s^2+\omega^2\right)^2}$$

$$\mathcal{L}\left\{t\cos(\omega t)\delta_{-1}(t)\right\} = \frac{s^2-\omega^2}{\left(s^2+\omega^2\right)^2}$$

$$\mathcal{L}\left\{te^{\alpha t}\sin(\omega t)\delta_{-1}(t)\right\} = \frac{2\omega(s-\alpha)}{\left[(s-\alpha)^2+\omega^2\right]^2}$$

$$\mathcal{L}\left\{te^{\alpha t}\cos(\omega t)\delta_{-1}(t)\right\} = \frac{(s-\alpha)^2-\omega^2}{\left[(s-\alpha)^2+\omega^2\right]^2}$$

APPENDIX

C

Trigonometric Relationships

Trigonometric expressions useful for *harmonic analysis*:

$$\begin{aligned}
\sin(\alpha)\sin(\beta) &= \frac{1}{2}\left[\cos(\alpha-\beta) - \cos(\alpha+\beta)\right], \\
\cos(\alpha)\cos(\beta) &= \frac{1}{2}\left[\cos(\alpha-\beta) + \cos(\alpha+\beta)\right], \\
\sin(\alpha)\cos(\beta) &= \frac{1}{2}\left[\sin(\alpha-\beta) + \sin(\alpha+\beta)\right].
\end{aligned} \tag{C.0.1}$$

$$\begin{aligned}
\cos^3\alpha = \cos\alpha\left(\cos^2\alpha\right) = \cos\alpha\left[\frac{1+\cos(2\alpha)}{2}\right] &= \\
&= \frac{1}{2}\cos\alpha + \frac{1}{2}\left[\cos\alpha\cos(2\alpha)\right] \\
&= \frac{1}{2}\cos\alpha + \frac{1}{4}\left[\cos(-\alpha) + \cos(3\alpha)\right] \\
&= \frac{1}{2}\cos\alpha + \frac{1}{4}\left[\cos(3\alpha) + \cos\alpha\right] \\
&= \frac{3}{4}\cos\alpha + \frac{1}{4}\cos(3\alpha).
\end{aligned} \tag{C.0.2}$$

$$
\begin{aligned}
\sin^3\alpha = \sin\alpha\left(\sin^2\alpha\right) = \sin\alpha\left[\frac{1-\cos\left(2\alpha\right)}{2}\right] = \\
&= \frac{1}{2}\sin\alpha - \frac{1}{2}\left[\sin\alpha\cos\left(2\alpha\right)\right] \\
&= \frac{1}{2}\sin\alpha - \frac{1}{4}\left[\sin\left(-\alpha\right) + \sin\left(3\alpha\right)\right] \\
&= \frac{1}{2}\sin\alpha - \frac{1}{4}\left[-\sin\alpha + \sin\left(3\alpha\right)\right] \\
&= \frac{3}{4}\sin\alpha - \frac{1}{4}\sin\left(3\alpha\right).
\end{aligned}
\tag{C.0.3}
$$

APPENDIX

D

MDoF Hysteretic Systems Energy Components

For the reader's convenience, we provide the extended form of matrices and vectors presented in Section 4.3.4.

In particular, with reference to the set of N nonlinear equilibrium equations given in Eq. (4.3.21), the constant mass matrix $\overline{\mathbf{M}}$ and the generalized acceleration vector $\ddot{\bar{\mathbf{u}}}(t)$ are:

$$\overline{\mathbf{M}} = \begin{bmatrix} m^{(1)} & \cdots & 0 & \cdots & 0 \\ \vdots & \ddots & \vdots & & \vdots \\ 0 & \cdots & m^{(i)} & \cdots & 0 \\ \vdots & & \vdots & \ddots & \vdots \\ 0 & \cdots & 0 & \cdots & m^{(N)} \end{bmatrix}, \tag{D.0.1}$$

$$\ddot{\bar{\mathbf{u}}}(t) = \begin{Bmatrix} \ddot{\bar{u}}^{(1)}(t) \\ \vdots \\ \ddot{\bar{u}}^{(i)}(t) \\ \vdots \\ \ddot{\bar{u}}^{(N)}(t) \end{Bmatrix}. \tag{D.0.2}$$

In addition, the three generalized internal force vectors $\bar{\mathbf{f}}_e(t)$, $\bar{\mathbf{f}}_{rd}(t)$, and $\bar{\mathbf{f}}_{ri}(t)$, appearing on the left-hand side of Eq. (4.3.21), are given by:

$$\bar{\mathbf{f}}_e(t) = \left\{ \begin{array}{c} f_e^{(1)}(t) - f_e^{(2)}(t) \\ \vdots \\ f_e^{(i)}(t) - f_e^{(i+1)}(t) \\ \vdots \\ f_e^{(N)}(t) \end{array} \right\}, \tag{D.0.3}$$

$$\bar{\mathbf{f}}_{rd}(t) = \left\{ \begin{array}{c} f_{rd}^{(1)}(t) - f_{rd}^{(2)}(t) \\ \vdots \\ f_{rd}^{(i)}(t) - f_{rd}^{(i+1)}(t) \\ \vdots \\ f_{rd}^{(N)}(t) \end{array} \right\}, \tag{D.0.4}$$

$$\bar{\mathbf{f}}_{ri}(t) = \left\{ \begin{array}{c} f_{ri}^{(1)}(t) - f_{ri}^{(2)}(t) \\ \vdots \\ f_{ri}^{(i)}(t) - f_{ri}^{(i+1)}(t) \\ \vdots \\ f_{ri}^{(N)}(t) \end{array} \right\}, \tag{D.0.5}$$

whereas the two generalized external force vectors $\overline{\mathbf{p}}_e(t)$ and $\overline{\mathbf{p}}(t)$, appearing on the right-hand side of Eq. (4.3.21), are:

$$\overline{\mathbf{p}}_e(t) = \left\{ \begin{array}{c} p_e^{(1)}(t) \\ \vdots \\ p_e^{(i)}(t) \\ \vdots \\ p_e^{(N)}(t) \end{array} \right\}, \tag{D.0.6}$$

$$\overline{\mathbf{p}}(t) = \left\{ \begin{array}{c} p^{(1)}(t) \\ \vdots \\ p^{(i)}(t) \\ \vdots \\ p^{(N)}(t) \end{array} \right\}. \tag{D.0.7}$$

As regards the coordinate transformation matrix $\mathbf{T}$, employed in Eq. (4.3.22) and having order $N \times N$, we have:

$$\mathbf{T} = \begin{bmatrix} 1 & \cdots & 0 & \cdots & 0 \\ \vdots & \ddots & \vdots & & \vdots \\ 1 & \cdots & 1 & \cdots & 0 \\ \vdots & & \vdots & \ddots & \vdots \\ 1 & \cdots & 1 & \cdots & 1 \end{bmatrix}. \tag{D.0.8}$$

Furthermore, with regard to the set of N nonlinear equilibrium equations in Eq. (4.3.23), the constant mass matrix $\mathbf{M}$ and the relative generalized acceleration vector $\ddot{\mathbf{u}}(t)$ are:

$$\mathbf{M} = \begin{bmatrix} m^{(1)} + \cdots + m^{(N)} & \cdots & m^{(i)} + \cdots + m^{(N)} & \cdots & m^{(N)} \\ \vdots & \ddots & \vdots & & \vdots \\ m^{(i)} + \ldots + m^{(N)} & \cdots & m^{(i)} + \ldots + m^{(N)} & \cdots & m^{(N)} \\ \vdots & & \vdots & \ddots & \vdots \\ m^{(N)} & \cdots & m^{(N)} & \cdots & m^{(N)} \end{bmatrix}, \tag{D.0.9}$$

$$\ddot{\mathbf{u}}(t) = \left\{ \begin{array}{c} \ddot{u}^{(1)}(t) \\ \vdots \\ \ddot{u}^{(i)}(t) \\ \vdots \\ \ddot{u}^{(N)}(t) \end{array} \right\} = \left\{ \begin{array}{c} \ddot{\bar{u}}^{(1)}(t) \\ \vdots \\ \ddot{\bar{u}}^{(i)}(t) - \ddot{\bar{u}}^{(i-1)}(t) \\ \vdots \\ \ddot{\bar{u}}^{(N)}(t) - \ddot{\bar{u}}^{(N-1)}(t) \end{array} \right\}. \tag{D.0.10}$$

Finally, the three generalized internal force vectors $\mathbf{f}_e(t)$, $\mathbf{f}_{rd}(t)$, and $\mathbf{f}_{ri}(t)$, appearing on the left-hand side of Eq. (4.3.23), are given by:

$$\mathbf{f}_e(t) = \left\{ \begin{array}{c} f_e^{(1)}(t) \\ \vdots \\ f_e^{(i)}(t) \\ \vdots \\ f_e^{(N)}(t) \end{array} \right\}, \tag{D.0.11}$$

$$\mathbf{f}_{rd}(t) = \left\{ \begin{array}{c} f_{rd}^{(1)}(t) \\ \vdots \\ f_{rd}^{(i)}(t) \\ \vdots \\ f_{rd}^{(N)}(t) \end{array} \right\}, \tag{D.0.12}$$

$$\mathbf{f}_{ri}(t) = \begin{Bmatrix} f_{ri}^{(1)}(t) \\ \vdots \\ f_{ri}^{(i)}(t) \\ \vdots \\ f_{ri}^{(N)}(t) \end{Bmatrix}, \tag{D.0.13}$$

whereas the two generalized external force vectors $\mathbf{p}_e(t)$ and $\mathbf{p}(t)$, appearing on the right-hand side of Eq. (4.3.23), are:

$$\mathbf{p}_e(t) = \begin{Bmatrix} p_e^{(1)}(t) + \cdots + p_e^{(N)}(t) \\ \vdots \\ p_e^{(i)}(t) + \cdots + p_e^{(N)}(t) \\ \vdots \\ p_e^{(N)}(t) \end{Bmatrix}, \tag{D.0.14}$$

$$\mathbf{p}(t) = \begin{Bmatrix} p^{(1)}(t) + \cdots + p^{(N)}(t) \\ \vdots \\ p^{(i)}(t) + \cdots + p^{(N)}(t) \\ \vdots \\ p^{(N)}(t) \end{Bmatrix}. \tag{D.0.15}$$

The expressions for the evaluation of the system work components $\widetilde{W}_e$, $\widetilde{W}_{pe}$, $\widetilde{W}_{rd}$, $\widetilde{W}_{ri}$, $\widetilde{W}_p$, presented in Section 4.3.4, can be rewritten as:

$$\widetilde{W}_e = -\int_{\mathbf{u}_i}^{\mathbf{u}_f} \mathbf{f}_e \cdot \mathrm{d}\mathbf{u} = -\sum_{i=1}^{N} \int_{u_i^{(i)}}^{u_f^{(i)}} f_e^{(i)} \, \mathrm{d}u^{(i)} = -\sum_{i=1}^{N} W_e^{(i)}, \tag{D.0.16}$$

$$\widetilde{W}_{pe} = -\int_{\mathbf{T}\mathbf{u}_i}^{\mathbf{T}\mathbf{u}_f} \left[\left(\mathbf{T}^T\right)^{-1} \mathbf{p}_e \right] \cdot \mathrm{d}\left(\mathbf{T}\mathbf{u}\right) = -\sum_{i=1}^{N} \int_{\overline{u}_i^{(i)}}^{\overline{u}_f^{(i)}} p_e^{(i)} \, \mathrm{d}\overline{u}^{(i)} = -\sum_{i=1}^{N} W_{pe}^{(i)}, \tag{D.0.17}$$

$$\widetilde{W}_{rd} = -\int_{\mathbf{u}_i}^{\mathbf{u}_f} \mathbf{f}_{rd} \cdot \mathrm{d}\mathbf{u} = -\sum_{i=1}^{N} \int_{u_i^{(i)}}^{u_f^{(i)}} f_{rd}^{(i)} \, \mathrm{d}u^{(i)} = -\sum_{i=1}^{N} W_{rd}^{(i)}, \tag{D.0.18}$$

$$\widetilde{W}_{ri} = -\int_{\mathbf{u}_i}^{\mathbf{u}_f} \mathbf{f}_{ri} \cdot \mathrm{d}\mathbf{u} = -\sum_{i=1}^{N} \int_{u_i^{(i)}}^{u_f^{(i)}} f_{ri}^{(i)} \, \mathrm{d}u^{(i)} = -\sum_{i=1}^{N} W_{ri}^{(i)}, \tag{D.0.19}$$

$$\widetilde{W}_p = +\int_{\mathbf{T}\mathbf{u}_i}^{\mathbf{T}\mathbf{u}_f} \left[\left(\mathbf{T}^T \right)^{-1} \mathbf{p} \right] \cdot \mathrm{d} \left(\mathbf{T}\mathbf{u} \right) = + \sum_{i=1}^{N} \int_{\overline{u}_i^{(i)}}^{\overline{u}_f^{(i)}} p^{(i)} \, \mathrm{d}\overline{u}^{(i)} = + \sum_{i=1}^{N} \widetilde{W}_p^{(i)}, \tag{D.0.20}$$

in which $W_e^{(i)}$ and $W_{pe}^{(i)}$ are the amounts of work done by the generalized forces acting on the i^{th} internal and external elastic elements, respectively, whereas $W_{rd}^{(i)}$ and $W_{ri}^{(i)}$ represent the amounts of work performed by the generalized forces acting on the i^{th} internal rate-dependent and rate-independent hysteretic elements, respectively. Finally, $\widetilde{W}_p^{(i)}$ is the work done by the generalized external force applied to the i^{th} mass.

Numerical Details

APPENDIX

E

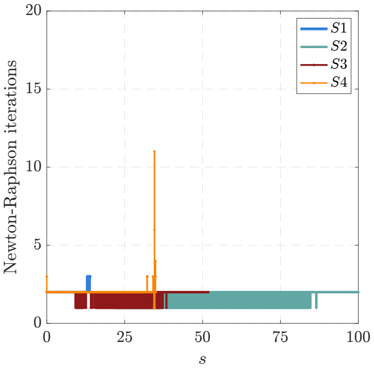

Figure E.1. Number of Newton-Raphson iterations as a function of the arc length s corresponding to the four types of loop shapes analyzed with a forcing amplitude $F = 1$.

In this appendix, we provide a detailed account on the convergence properties of the Newton-Raphson numerical method adopted to solve the system of equation in Eq. (4.3.10), focusing in particular on the number of iterations required to achieve convergence. By presenting key metrics such as the average, minimum and maximum number of iterations required to achieve convergence of the Newton-Raphson method in each numerical experiment (see Table E.1), we intend to provide a broader perspective on the efficiency and reliability of the computational methodology. We believe that this additional level of detail contributes to a deeper assessment of the proposed approach and its suitability for applications. Fig. E.1 illustrates how much the adopted procedure is robust for the four considered hysteresis loop shapes with an amplitude $F = 1$ of the input force. A minimum number of iterations is required for the majority of the

Table E.1. Minimum, maximum, and average number of Newton-Raphson iterations for each PA step corresponding to the FRCs depicted in Fig. 5.4 for different amplitudes of the input force F.

loop shape	F	min	average	max
$S1$	0.5	2	2.1097	29
	0.6	2	2.0811	14
	0.8	2	2.0848	38
	1.0	2	2.0357	3
	1.1	2	2.0273	29
	1.2	1	1.8922	4
$S2$	1.0	1	1.7044	4
	2.0	1	1.7329	3
	3.0	1	1.0501	2
	10.0	1	1.0531	5
	20.0	1	1.0786	44
	30.0	1	1.1166	97
$S3$	0.5	2	2	2
	0.6	2	2	2
	0.8	2	2	2
	1.0	2	2	2
	1.1	1	1.6190	2
	1.2	1	1.3204	2
$S4$	1.0	1	2.0103	11
	2.0	1	2.0301	90
	3.0	1	2.0092	6
	10.0	1	2.0211	23
	20.0	1	1.9862	100
	30.0	1	1.1802	62

analyses, in which occasional instances where a higher number of iterations is needed.

Bibliography

[1] S Alessandri, R Giannini, F Paolacci, M Amoretti, and A Freddo. “Seismic retrofitting of an HV circuit breaker using base isolation with wire ropes. Part 2: Shaking-table test validation”. In: *Engineering Structures* 98 (2015), pp. 263–274.

[2] S Alessandri, R Giannini, F Paolacci, and M Malena. “Seismic retrofitting of an HV circuit breaker using base isolation with wire ropes. Part 1: Preliminary tests and analyses”. In: *Engineering Structures* 98 (2015), pp. 251–262.

[3] V.I. Arnold. *Geometrical Methods in the Theory of Ordinary Differential Equations.* 2nd ed. Grundleheren de Mathematischen Wissenschanften 250. Springer, 1997. ISBN: 3540780386; 9783540780380.

[4] J. Awrejcewicz and L.P. Dzyubak. “Influence of hysteretic dissipation on chaotic responses”. In: *Journal of Sound and Vibration* 284.1 (2005), pp. 513–519.

[5] Thomas T. Baber and Mohammed N. Noori. “Modeling General Hysteresis Behavior and Random Vibration Application”. In: *Journal of Vibration, Acoustics, Stress, and Reliability in Design* 108.4 (1986), pp. 411–420. ISSN: 0739-3717.

[6] Prabakaran Balasubramanian, Giulio Franchini, Giovanni Ferrari, Brian Painter, Kostas Karazis, and Marco Amabili. “Nonlinear vibrations of beams with bilinear hysteresis at supports: interpretation of experimental results”. In: *Journal of Sound and Vibration* 499 (2021), p. 115998.

[7] Paolo Giuseppe Emilio Bolzern, Riccardo Scattolini, Nicola Luigi Schiavoni, et al. *Fondamenti di Controlli Automatici.* McGraw-Hill, 2008.

[8] R Bouc. “Random Excitation of a Non-Linear System with Hysteresis”. In: *Acta Acustica united with Acustica* 17.6 (1966), pp. 357–364.

[9] Robert Bouc. “A mathematical model for hysteresis”. In: *Acta Acustica united with Acustica* 24.1 (1971), pp. 16–25.

[10] Michel Bruneau and Niandi Wang. “Some aspects of energy methods for the inelastic seismic response of ductile SDOF structures”. In: *Engineering Structures* 18.1 (1996), pp. 1–12.

[11] Raffaele Capuano, Davide Pellecchia, Tommaso Coppola, and Nicolò Vaiana. “On the inadequacy of rate-dependent models in simulating asymmetric rate-independent hysteretic phenomena”. In: *European Journal of Mechanics-A/Solids* 102 (2023), p. 105105.

[12] Raffaele Capuano, Nicoló Vaiana, and Biagio Carboni. “A generalized Bouc–Wen model for simulating the quasi-static and dynamic shear responses of helical wire rope isolators”. In: *Nonlinear Dynamics* (2024), pp. 1–15.

[13] Raffaele Capuano, Nicolò Vaiana, Davide Pellecchia, and Luciano Rosati. “A solution algorithm for a modified Bouc-Wen model capable of simulating cyclic softening and pinching phenomena”. In: *IFAC-PapersOnLine* 55.20 (2022), pp. 319–324.

[14] Raffaele Capuano, Nicolò Vaiana, and Luciano Rosati. “Frequency-response curves for rate-independent hysteretic mechanical responses of complex shape”. In: *Nonlinear Dynamics* 112.7 (2024), pp. 5151–5175.

[15] Raffaele Capuano, Nicolò Vaiana, and Luciano Rosati. “Work and energy components in mechanical systems with complex hysteretic behavior”. In: *COMPDYN Proceedings*. 2023. DOI: `10.7712/120123.10540.21081`.

[16] Nicola Carpineto, Walter Lacarbonara, and Fabrizio Vestroni. “Hysteretic tuned mass dampers for structural vibration mitigation”. In: *Journal of Sound and Vibration* 333.5 (2014), pp. 1302–1318.

[17] N Caterino, M Spizzuoco, and A Occhiuzzi. “A semi-active rocking system to enhance the seismic dissipative capability of precast rc columns”. In: *Proceedings of Italian Concrete Days 2016*. Springer. 2018, pp. 261–271.

[18] Nicola Caterino, Christos Thomas Georgakis, M Spizzuoco, and J Chen. “Mitigation of Structural Demand to Wind Turbines: Experimental Investigation of Three Control Strategies”. In: *Proceedings of the XV Conference of the Italian Association for Wind Engineering: IN-VENTO 2018 25*. Springer. 2019, pp. 165–178.

[19] T. K. Caughey. “Sinusoidal Excitation of a System With Bilinear Hysteresis”. In: *Journal of Applied Mechanics* 27.4 (Dec. 1960), pp. 640–643. ISSN: 0021-8936. DOI: `10.1115/1.3644075`. URL: `https://doi.org/10.1115/1.3644075`.

[20] Zhibao Cheng, Zhifei Shi, Antonio Palermo, Hongjun Xiang, Wei Guo, and Alessandro Marzani. “Seismic vibrations attenuation via damped layered periodic foundations”. In: *Engineering Structures* 211 (2020), p. 110427.

[21] A.K. Chopra. *Dynamics of Structures*. Prentice-Hall international series in civil engineering and engineering mechanics. Pearson Education, 2007. ISBN: 9788131713297. URL: `https://books.google.it/books?id=0dU1bDaRyP4C`.

[22] Woo-Jung Chung, Chung-Bang Yun, Nam-Sik Kim, and Ju-Won Seo. “Shaking table and pseudodynamic tests for the evaluation of the seismic performance of base-isolated structures”. In: *Engineering Structures* 21.4 (1999), pp. 365–379. ISSN: 0141-0296.

[23] J Cortés. “Discontinuous Dynamical Systems-A Tutorial on Notions of Solutions, Nonsmooth Analysis, and Stability”. In: *IEEE Control Systems Magazine* (2007).

[24] Jorge Cortes. “Discontinuous dynamical systems”. In: *IEEE Control Systems Magazine* 28.3 (2008), pp. 36–73.

[25] D. De Domenico, D. Losanno, and N. Vaiana. “Experimental tests and numerical modeling of full-scale unbonded fiber reinforced elastomeric isolators (UFREIs) under bidirectional excitation”. In: *Engineering Structures* 274 (2023), p. 115118. ISSN: 0141-0296. DOI: `https://doi.org/10.1016/j.engstruct.2022.115118`.

[26] AM De Leo, G Simoneschi, C Fabrizio, and A Di Egidio. “On the use of a pendulum as mass damper to control the rocking motion of a rigid block with fixed characteristics”. In: *Meccanica* 51 (2016), pp. 2727–2740.

[27] George F Demetriades, Michalakis C Constantinou, and Andrei M Reinhorn. “Study of wire rope systems for seismic protection of equipment in buildings”. In: *Engineering Structures* 15.5 (1993), pp. 321–334.

[28] A Di Egidio, AM de Leo, and A Contento. “Improvement of the dynamic and seismic response of non-structural rocking bodies through the ability to change their geometrical configuration”. In: *Engineering Structures* 275 (2023), p. 115231.

[29] Angelo Di Egidio, Angelo Luongo, and Achille Paolone. “Linear and non-linear interactions between static and dynamic bifurcations of damped planar beams”. In: *International Journal of Non-Linear Mechanics* 42.1 (2007), pp. 88–98.

[30] Moira Di Paolo, Iolanda Nuzzo, Nicola Caterino, and Christos T Georgakis. “A friction-based passive control technique to mitigate wind induced structural demand to wind turbines”. In: *Engineering Structures* 232 (2021), p. 111744.

[31] G. Formica, F. Milicchio, and W. Lacarbonara. “Improving the monodromy matrix computation in pathfollowing schemes for nonsmooth dynamics”. In: *International Journal of Non-Linear Mechanics* (2023), p. 104455.

[32] G. Formica, N. Vaiana, L. Rosati, and W. Lacarbonara. “Pathfollowing of high-dimensional hysteretic systems under periodic forcing”. In: *Nonlinear Dynamics* 103.4 (2021), pp. 3515–3528.

[33] Giovanni Formica, Franco Milicchio, and Walter Lacarbonara. “A Krylov accelerated Newton–Raphson scheme for efficient pseudo-arclength pathfollowing”. In: *International Journal of Non-Linear Mechanics* 145 (2022), p. 104116. ISSN: 0020-7462.

[34] Shufei Gao, Jinxin Gong, and Yunfen Feng. “Equivalent damping for displacement-based seismic design of pile-supported wharves with soil–pile interaction”. In: *Ocean Engineering* 125 (2016), pp. 12–25.

[35] EJ Graesser and FA Cozzarelli. “Shape-memory alloys as new materials for aseismic isolation”. In: *Journal of Engineering Mechanics* 117.11 (1991), pp. 2590–2608.

[36] John Guckenheimer and Philip Holmes. *Nonlinear Oscillations, Dynamical Systems, and Bifurcations of Vector Fields.* Vol. 42. Springer Science & Business Media, 2013.

[37] Louis N Hand and Janet D Finch. *Analytical Mechanics.* Cambridge University Press, 1998.

[38] Enrique Hernández-Montes, Mark A Aschheim, and Luisa María Gil-Martín. "Energy components in nonlinear dynamic response of SDOF systems". In: *Nonlinear Dynamics* 82.1 (2015), pp. 933–945.

[39] Wilfred D Iwan. "The steady-state response of the double bilinear hysteretic model". In: *Journal of Applied Mechanics* 32.4 (1965), pp. 921–925.

[40] Lydik S Jacobsen. "Steady forced vibration as influenced by damping". In: *Trans. ASME-APM* 52.15 (1930), pp. 169–181.

[41] Nicholas P. Jones and III Shenton Harry W. "A Modified, Slowly Varying Parameter Approach for Systems With Impulsive Loadings". In: *Journal of Applied Mechanics* 58.1 (Mar. 1991), pp. 251–258. ISSN: 0021-8936.

[42] Anatole Katok and Boris Hasselblatt. *Introduction to the modern theory of dynamical systems.* 54. Cambridge university press, 1995.

[43] Frederick J Keller, W Edward Gettys, and Malcolm J Skove. *Physics, classical and modern.* McGraw-Hill College, 1993.

[44] Hassan K Khalil. *Nonlinear Systems; 3rd ed.* Upper Saddle River, NJ: Prentice-Hall, 2002.

[45] Masaru Kikuchi and Ian D Aiken. "An analytical hysteresis model for elastomeric seismic isolation bearings". In: *Earthquake Engineering & Structural Dynamics* 26.2 (1997), pp. 215–231.

[46] Yuri A Kuznetsov, Iu A Kuznetsov, and Y Kuznetsov. *Elements of applied bifurcation theory.* Vol. 112. Springer, 1998.

[47] W. Lacarbonara. *Nonlinear Structural Mechanics: Theory, Dynamical Phenomena and Modeling.* Springer Science & Business Media, 2013.

[48] W. Lacarbonara, D. Bernardini, and F. Vestroni. "Nonlinear thermomechanical oscillations of shape-memory devices". In: *International Journal of Solids and Structures* 41.5-6 (2004), pp. 1209–1234.

[49] W. Lacarbonara and F. Vestroni. “Nonclassical responses of oscillators with hysteresis”. In: *Nonlinear Dynamics* 32 (2003), pp. 235–258.

[50] *Poincaré Map-Based Continuation of Periodic Orbits in Dynamic Discontinuous and Hysteretic Systems.* Vol. Volume 7B: 17th Biennial Conference on Mechanical Vibration and Noise. International Design Engineering Technical Conferences and Computers and Information in Engineering Conference. Sept. 1999, pp. 2215–2224.

[51] RS Lakes. “Extreme damping in composite materials with a negative stiffness phase”. In: *Physical Review Letters* 86.13 (2001), p. 2897.

[52] RS Lakes and WJ Drugan. “Dramatically stiffer elastic composite materials due to a negative stiffness phase?” In: *Journal of the Mechanics and Physics of Solids* 50.5 (2002), pp. 979–1009.

[53] Roderic S Lakes, T Lee, A Bersie, and Yun-Che Wang. “Extreme damping in composite materials with negative-stiffness inclusions”. In: *Nature* 410.6828 (2001), pp. 565–567.

[54] C-M Lee and VN Goverdovskiy. “A multi-stage high-speed railroad vibration isolation system with “negative” stiffness”. In: *Journal of Sound and Vibration* 331.4 (2012), pp. 914–921.

[55] C-M Lee, VN Goverdovskiy, and AI Temnikov. “Design of springs with “negative” stiffness to improve vehicle driver vibration isolation”. In: *Journal of Sound and Vibration* 302.4-5 (2007), pp. 865–874.

[56] A. Luongo, G. Rega, and F. Vestroni. “On Nonlinear Dynamics of Planar Shear Indeformable Beams”. In: *Journal of Applied Mechanics* 53.3 (Sept. 1986), pp. 619–624. ISSN: 0021-8936. DOI: `10.1115/1.3171821`.

[57] Angelo Luongo, Manuel Ferretti, and Simona Di Nino. *Stabilità e Biforcazione delle Strutture. Sistemi Statici e Dinamici.* Società Editrice Esculapio, 2022.

[58] Angelo Luongo, Manuel Ferretti, and Simona Di Nino. *Stability and Bifurcation of Structures: Statical and Dynamical Systems.* Springer, 2023.

[59] Angelo Luongo and Daniele Zulli. “Aeroelastic instability analysis of NES-controlled systems via a mixed multiple scale/harmonic balance method”. In: *Journal of Vibration and Control* 20.13 (2014), pp. 1985–1998.

[60] Nicos Makris and Jian Zhang. “Rocking response of anchored blocks under pulse-type motions”. In: *Journal of Engineering Mechanics* 127.5 (2001), pp. 484–493.

[61] FC Moon and Philip J Holmes. “A magnetoelastic strange attractor”. In: *Journal of Sound and Vibration* 65.2 (1979), pp. 275–296.

[62] Ali H Nayfeh and Balakumar Balachandran. *Applied Nonlinear Dynamics: Analytical, Computational, and Experimental Methods*. John Wiley & Sons, 2008.

[63] YQ Ni, JM Ko, CW Wong, and S Zhan. “Modelling and identification of a wire-cable vibration isolator via a cyclic loading test”. In: *Proceedings of the Institution of Mechanical Engineers, Part I: Journal of Systems and Control Engineering* 213.3 (1999), pp. 163–172.

[64] David D Nolte. *Introduction to Modern Dynamics: Chaos, Networks, Space and Time*. Oxford University Press, USA, 2015.

[65] Nobukatsu Okuizumi and Koji Kimura. “Stability and bifurcations of hysteretic systems subjected to principal parametric excitation”. In: *Journal of Sound and Vibration* 324.3 (2009), pp. 940–953.

[66] Haluk Ozdemir. *Nonlinear transient dynamic analysis of yielding structures*. University of California, Berkeley, 1976.

[67] D. Pellecchia, N. Vaiana, M. Spizzuoco, G. Serino, and L. Rosati. “Axial hysteretic behaviour of wire rope isolators: Experiments and modelling”. In: *Materials & Design* 225 (2023), p. 111436.

[68] Daniele Pietrosanti, Maurizio De Angelis, and Agathoklis Giaralis. “Experimental study and numerical modeling of nonlinear dynamic response of SDOF system equipped with tuned mass damper inerter (TMDI) tested on shaking table under harmonic excitation”. In: *International Journal of Mechanical Sciences* 184 (2020), p. 105762.

[69] Ferenc Preisach. “Über die magnetische Nachwirkung”. In: *Zeitschrift für physik* 94.5 (1935), pp. 277–302.

[70] W Ramberg and WR Osgood. “Description of stress-strain curves by three parameters. NACA, Tech”. In: *No902* (1943).

[71] Anil Rao. *Dynamics of Particles and Rigid Bodies: A Systematic Approach.* Cambridge University Press, 2006.

[72] Hermann Riecke. *Methods of Nonlinear Analysis D-12.* 2000.

[73] E Riks. “Some computational aspects of the stability analysis of nonlinear structures”. In: *Computer Methods in Applied Mechanics and Engineering* 47.3 (1984), pp. 219–259.

[74] Marco Rossi. “Dynamics and Stability of Discrete and Continuous Structures: Flutter Instability in Piecewise-smooth Mechanical Systems and Cloaking for Wave Propagation in Kirchhoff Plates”. PhD thesis. Università degli Studi di Trento, 2021.

[75] Apostolos A Sarlis, Dharma Theja R Pasala, MC Constantinou, AM Reinhorn, Satish Nagarajaiah, and DP Taylor. “Negative stiffness device for seismic protection of structures”. In: *Journal of Structural Engineering* 139.7 (2013), pp. 1124–1133.

[76] Michael H Scott and Gregory L Fenves. “Krylov subspace accelerated Newton algorithm: application to dynamic progressive collapse simulation of frames”. In: *Journal of Structural Engineering* 136.5 (2010), pp. 473–480.

[77] Salvatore Sessa, Nicoló Vaiana, Massimo Paradiso, and Luciano Rosati. “An inverse identification strategy for the mechanical parameters of a phenomenological hysteretic constitutive model”. In: *Mechanical Systems and Signal Processing* 139 (2020), p. 106622.

[78] Carlos A.F. Silva, Lionel Manin, Renaud G. Rinaldi, Didier Remond, Etienne Besnier, and Marie-Ange Andrianoely. “Modeling of power losses in poly-V belt transmissions: Hysteresis phenomena (enhanced analysis)”. In: *Mechanism and Machine Theory* 121 (2018), pp. 373–397. ISSN: 0094-114X.

[79] Junho Song and Armen Der Kiureghian. “Generalized Bouc–Wen model for highly asymmetric hysteresis”. In: *Journal of Engineering Mechanics* 132.6 (2006), pp. 610–618.

[80] Steven H Strogatz. *Nonlinear Dynamics and Chaos: With Applications to Physics, Biology, Chemistry, and Engineering.* CRC press, 2018.

[81] Chia-Ming Uang and Vitelmo V Bertero. "Evaluation of seismic energy in structures". In: *Earthquake Engineering & Structural Dynamics* 19.1 (1990), pp. 77–90.

[82] Nicolò Vaiana, Raffaele Capuano, and Luciano Rosati. "Evaluation of path-dependent work and internal energy change for hysteretic mechanical systems". In: *Mechanical Systems and Signal Processing* 186 (2023), p. 109862.

[83] Nicolò Vaiana and Luciano Rosati. "Analytical and differential reformulations of the Vaiana–Rosati model for complex rate-independent mechanical hysteresis phenomena". In: *Mechanical Systems and Signal Processing* 199 (2023), p. 110448.

[84] Nicolò Vaiana and Luciano Rosati. "Classification and unified phenomenological modeling of complex uniaxial rate-independent hysteretic responses". In: *Mechanical Systems and Signal Processing* 182 (2023), p. 109539.

[85] Nicolò Vaiana, Salvatore Sessa, Francesco Marmo, and Luciano Rosati. "A class of uniaxial phenomenological models for simulating hysteretic phenomena in rate-independent mechanical systems and materials". In: *Nonlinear Dynamics* 93 (2018), pp. 1647–1669.

[86] Nicolò Vaiana, Salvatore Sessa, Francesco Marmo, and Luciano Rosati. "Nonlinear dynamic analysis of hysteretic mechanical systems by combining a novel rate-independent model and an explicit time integration method". In: *Nonlinear Dynamics* 98.4 (2019), pp. 2879–2901.

[87] Nicolo Vaiana, Salvatore Sessa, and Luciano Rosati. "A generalized class of uniaxial rate-independent models for simulating asymmetric mechanical hysteresis phenomena". In: *Mechanical Systems and Signal Processing* 146 (2021), p. 106984.

[88] Augusto Visintin. *Differential Models of Hysteresis.* Vol. 111. Springer Science & Business Media, 2013.

[89] Vito Volterra. "Sur la théorie mathématique des phénomènes héréditaires". In: *Journal de Mathématiques Pures et Appliquées* 7 (1928), pp. 249–298.

[90] Chi-Hsiang Wang and Yi-Kwei Wen. “Evaluation of pre-Northridge low-rise steel buildings. I: Modeling”. In: *Journal of Structural Engineering* 126.10 (2000), pp. 1160–1168.

[91] YC Wang and RS Lakes. “Extreme stiffness systems due to negative stiffness elements”. In: *American Journal of Physics* 72.1 (2004), pp. 40–50.

[92] Peter J. Wasilewski. “Magnetic hysteresis in natural materials”. In: *Earth and Planetary Science Letters* 20.1 (1973), pp. 67–72. ISSN: 0012-821X.

[93] Yi-Kwei Wen. “Method for random vibration of hysteretic systems”. In: *Journal of the Engineering Mechanics Division* 102.2 (1976), pp. 249–263.

[94] Stephen Wiggins and Martin Golubitsky. *Introduction to Applied Nonlinear Dynamical Systems and Chaos.* Vol. 2. 3. Springer, 2003.

[95] James Christopher Wohlever. *Symmetry, nonlinear bifurcation analysis, and parallel computation.* Tech. rep. Cornell University, 1996.

[96] CW Wong, YQ Ni, and JM Ko. “Steady-state oscillation of hysteretic differential model. II: Performance analysis”. In: *Journal of Engineering Mechanics* 120.11 (1994), pp. 2299–2325.

[97] CW Wong, YQ Ni, and SL Lau. “Steady-state oscillation of hysteretic differential model. I: Response analysis”. In: *Journal of Engineering Mechanics* 120.11 (1994), pp. 2271–2298.

[98] Jia-Qi Yang, Scott T Smith, Zhenyu Wang, Peng Feng, and Nick Sirach. “Modelling of hysteresis behaviour of moment-resisting timber joints strengthened with FRP composites”. In: *International Journal of Mechanical Sciences* 179 (2020), p. 105593.

[99] Amir A Zadpoor. “Mechanical meta-materials”. In: *Materials Horizons* 3.5 (2016), pp. 371–381.

[100] Jian Zhang and Nicos Makris. “Rocking response of free-standing blocks under cycloidal pulses”. In: *Journal of Engineering Mechanics* 127.5 (2001), pp. 473–483.

[101] Will Zhang, Adela Capilnasiu, and David Nordsletten. “Comparative analysis of nonlinear viscoelastic models across common biomechanical experiments”. In: *Journal of Elasticity* 145.1-2 (2021), pp. 117–152.